Mechanistic Investigation of Photoinitiation Processes via PLP-ESI-MS

Zur Erlangung des akademischen Grades eines
DOKTORS DER NATURWISSENSCHAFTEN
(Dr. rer. nat.)

von der KIT-Fakultät für Chemie und Biowissenschaften
des Karlsruher Instituts für Technologie (KIT)

genehmigte
DISSERTATION
von

Dipl.-Chem. Elena Frick

aus
Mihajlowka (Omsk), Russland

Dekan: Prof. Dr. Willem M. Klopper
Referent: Prof. Dr. Christopher Barner-Kowollik
Koreferent: PD Dr. Andreas-Neil Unterreiner
Tag der mündlichen Prüfung: 22.04.2016

Die vorliegende Arbeit wurde im Zeitraum von Dezember 2012 bis April 2016 unter Anleitung von Prof. Dr. Christopher Barner-Kowollik am Karlsruher Institut für Technologie - Universitätsbereich angefertigt.

Meinen Eltern gewidmet.

Ich bin noch immer verwirrt, aber auf einem höheren Niveau.
Enrico Fermi

Abstract

The present thesis provides insights into the mechanistic details of photoinitiated radical polymerizations as well as the versatility of photoinitiated radical processes. In the first part, the influence of various aromatic substitution patterns on the initiation efficiency of benzoin-type radical photoinitiators is investigated by pulsed-laser polymerization with subsequent electrospray-ionization mass spectrometry (PLP-ESI-MS). Photoinitiators from a library of benzoin derivatives are compared with regard to their initiation efficiency ratios in so-called cocktail experiments. Furthermore, femtosecond spectroscopy and theoretical calculations give additional insight into the molecular dynamics and radical reactivities of the photoinitiators. It is shown that the absorptivity of a photoinitiator is by no means a measure for its initiation efficiency or reactivity. In fact, efficient initiators exhibit a poor absorption behavior at the respective excitation wavelength, resulting from one excited nπ^* singlet state and one or – at the utmost – two nπ^* triplet states. Eventually, benzoin-derivatives with fluorine-substitution at the hydroxyl benzyl position were found to possess the most advantageous initiation efficiency and molecular dynamics.

Next to the investigation of radical photoinitiators, the mechanism of light-initiated copper-mediated reversible-deactivation radical polymerization (photoRDRP) was studied by PLP-ESI-MS. The photoRDRP reaction mixture composition – consisting of monomer, alkyl bromide initiator, copper(II) bromide, and ligand – was varied and irradiated in a PLP setup and the generated polymer was analyzed by high resolution mass spectrometry. The variation of the reactant composition and omission of single components provided information on how the species react upon irradiation with light as well as how the reactants interact with each other. As a result, a new mechanism of photoRDRP is postulated. In addition, the initiating species are unambiguously identified. The generation of initiating radicals is performed via UV light-induced bond scission of the alkyl bromide initiator, giving rise to propagating chains. The main pathway for the generation of copper(I) activator moieties is the reduction of copper(II) species by the amine ligand. The ligand can thereby serve as a reducing agent in its ground state as well as in its photolytically excited state.

A synthetic application of the photoinitiator-based radical generation process for the formation of single-chain nanoparticles (SCNPs) is introduced in the final part of the current work. Photoinitiator-functionalized polymers were synthesized to yield macromolecules that generate radicals along their chain upon irradiation with UV light. High dilution and subsequent irradiation of such single chains was envisaged to result in the effective formation of intramolecular bonds via radical combination events and the collapse of the chain into a nanoparticle. Employing a fast and efficient radical combination reaction was considered as an ideal alternative for the delicate procedures and synthetic pathways that are usually necessary to generate SCNPs. However, although a range of experimental parameters such as solvent nature, irradiation intensity, time, and wavelength as well as photoinitiator density were varied, the radical combination reaction did not result in an efficient intramolecular folding of the chains. Crosslinking of the polymer chains and radical abstraction reactions occured, resulting in a mixture of crosslinked and folded polymer chains as well as small molecules as side products.

Zusammenfassung

Die vorliegende Arbeit gibt einen Einblick in die mechanistischen Details und die Vielseitigkeit photoinitiierter radikalischer Polymerisationen. Im ersten Teil wird der Einfluss der aromatischen Substitution auf die Initiierungseffizienz von radikalischen Photoinitiatoren des Benzoin-Typs untersucht. Dabei wurden Polymere mittels gepulster Laserpolymerisation synthetisiert und anschließend durch Elektrosprayionisations-Massenspektrometrie (PLP-ESI-MS) untersucht. Eine Auswahl von Photoinitiatoren des Benzoin-Typs wurde hinsichtlich ihrer Initiierungseffizienz in sogenannten Cocktail-Experimenten verglichen. Femtosekundenspektroskopie und theoretische Berechnungen vermittelten einen zusätzlichen Einblick in die vorherrschende Moleküldynamik sowie die Radikalreaktivitäten der Photoinitiatoren. Die Zusammenfassung der Ergebnisse ergibt ein Bild wie das Substitutionsmuster des Benzoins charakteristische Moleküleigenschaften wie die Initiierungseffizienz, Extinktionskoeffizient, Anregungszustände und Radikalreaktivitäten beeinflusst. Dabei wird aufgezeigt, dass die Absorption eines Photoinitiators in keinem Fall als Maß für seine Initiierungseffizienz angesehen werden darf. Tatsächlich zeigen effiziente Initiatoren eine schwache Absorption bei der entsprechenden Anregungswellenlänge, als Folge eines elektronisch angeregten $n\pi^*$ Singulett-Zustandes sowie eines oder höchstens zweier $n\pi^*$ Triplett-Zustände. Desweiteren wurden bei Benzoin-Derivaten mit Fluorsubstitution in Hydroxybenzylposition eine günstige Initiierungseffizienz sowie Molekulardynamik gefunden.

Neben radikalischen Photoinitiatoren wurde der Mechanismus der photoinitiierten Kupfer-vermittelten Reversiblen Deaktivierungspolymerisation (engl. reversible-deactivation radical polymerization, photoRDRP) durch PLP-ESI-MS untersucht. Dabei wurde die Zusammensetzung einer photoRDRP Rektionsmischung – bestehend aus Monomer, Alkylbromid-Initiator, Kupfer(II)bromid und Ligand – variiert und mittels PLP polymerisiert. Das entstandene Polymer wurde massenspektrometrisch analysiert. Die Variation der Zusammensetzung und das gezielte Auslassen bestimmter Komponenten gibt Auskunft darüber wie sich die Reaktanten unter Bestrahlung mit Licht verhalten sowie über die jeweiligen gegenseitigen Wechselwirkungen. Zusätzlich konnten die initierenden Spezies eindeutig ermittelt werden. Durch Betrachtung aller Teilreaktionen wird schließlich ein neuer photoRDRP Mechanismus postuliert. Die Bildung von initiierenden Radikalen erfolgt durch den Licht-induzierten Bindungsbruch am Alkylbromid-Initiator, das die Bildung von propagierenden Ketten zur Folge hat. Den bedeutendsten Beitrag zur Bildung von Kupfer(I)-Aktivatorspezies stellt die Reduktion von Kupfer(II)-Komplexen durch den Aminliganden dar. Der Ligand kann dabei im elektronischen Grundzustand sowie im photochemisch angeregten Zustand als Reduktionsmittel agieren.

Im abschließenden Teil dieser Arbeit wird die Photoinitiator-basierte Radikalbildung auf dem Gebiet der Einzelkettennanopartikel (engl. single-chain nanoparticle, SCNP) angewendet. Photoinitiator-funktionalisierte Polymere wurden mit dem Ziel synthetisiert, Makromoleküle zu erhalten, die unter Bestrahlung mit Licht Radikale entlang ihrer Kette ausbilden. Durch hohe Verdünnung und eine anschließende Bestrahlung solcher Einzelketten sollte die intramolekulare Bildung von kovalenten Bindungen durch radikalische Kombinationsreaktionen erfolgen. Die daraus resultierende Faltung der Kette sollte zwangsläufig zur Bildung eines Nanopartikels führen. Da üblicherweise eine komplexe Durchführung und Synthese für die Herstellung von SCNPs erforderlich ist, wurde die Anwendung der schnellen und effizienten radikalischen Kombinationsreaktion als eine ideale Alternative hierfür betrachtet. Trotz der Anpassung von einer Reihe von experimentellen Parametern wie Lösungsmittel, Bestrahlungsintensität und -zeit, Wellenlänge und Photoinitiatordichte, konnte keine effiziente intramolekulare Faltung der Ketten erzielt werden. Vernetzungen der Polymerketten und radikalische Abstraktionsreaktionen hatten zur Folge, dass sich eine Mischung von vernetzten und gefalteten Polymeren und kleinen Molekülen als Nebenprodukte bildete.

Publications

Publications Arising from this Thesis

- *Toward a Quantitative Description of Radical Photoinitiator Structure-Reactivity Correlations*
  Frick, E.; Schweigert, C.; Noble, B. B.; Ernst, H. A.; Lauer, A.; Liang, Y.; Voll, D.; Coote, M. L.; Unterreiner, A.-N.; Barner-Kowollik, C. *Macromolecules* **2016**, *49*, 80-89.

- *Enlightening the Mechanism of Copper-Mediated PhotoRDRP via High-Resolution Mass Spectrometry*
  Frick, E.; Anastasaki, A.; Haddleton, D.; Barner-Kowollik, C. *J. Am. Chem. Soc.* **2015**, *137*, 6889-6896.

- *Studying the Polymerization Initiation Efficiency of Acetophenone-Type Initiators via PLP-ESI-MS and Femtosecond Spectroscopy*
  Frick, E.; Ernst, H. A.; Voll, D.; Wolf, T. J. A.; Unterreiner, A.-N.; Barner-Kowollik, C. *Polym. Chem.* **2014**, *5*, 5053-5068.

Other Publications

- *Systematic Assessment of the Photochemical Stability of Photoinitiator-Derived Macromolecular Chain Termini*
  Lauer, A.; Fast, D. E.; Kelterer, A.-M.; Frick, E.; Neshchadin, D.; Voll, D.; Gescheid, G.; Barner-Kowollik, C. *Macromolecules* **2015**, *48*, 8451-8460.

- *Investigation of Electrochemically Mediated Atom-Transfer Radical Polymerization*
  Magenau, A. J. D.; Bortolamei, N.; Frick, E.; Park, S.; Gennaro, A.; Matyjaszweski, K. *Macromolecules* **2013**, *46*, 4346-4353.

- *Rapid UV Light-Triggered Macromolecular Click Conjugations via the Use of o-Quinodimethanes*
  Gruendling, T.; Oehlenschlaeger, K. K.; Frick, E.; Glassner, M.; Schmid, C.; Barner-Kowollik, C. *Macromol. Rapid Commun.* **2011**, *32*, 807-812.

Conference Contributions

- *Enlightening the Mechanism of PhotoRDRP via High-Resolution Mass Spectrometry*
  Oral presentation at the Photopolymerization Fundamentals Meeting, Boulder, CO, USA
  13th - 16th September 2015

- *Toward a Quantitative Description of Benzoin-Type Photoinitiator Structure-Reactivity Correlations*
  Poster at the Photopolymerization Fundamentals Meeting, Boulder, CO, USA
  13th - 16th September 2015

- *Quantitative Comparison of Photoinitiators Using PLP-ESI-MS and Femtosecond Pump-Probe Spectroscopy*
  Poster at the Precision Polymer Materials (P2M), Gent, Belgium
  25th - 28th August 2013

Contents

Abstract I

Zusammenfassung III

Publications V

Contents VII

1. Introduction XI

2. Theory and Background 3
- 2.1. Radical Polymerization 3
  - 2.1.1. Free Radical Polymerization 3
  - 2.1.2. Reversible-Deactivation Radical Polymerization (RDRP) 4
  - 2.1.3. Atom-Transfer Radical Polymerization (ATRP) 5
- 2.2. Photoinitiated Free Radical Polymerization 9
  - 2.2.1. Radical Photoinitiators 10
- 2.3. Physical Processes in a Molecule upon Irradiation 13
  - 2.3.1. Jablonski Diagram 13
  - 2.3.2. Franck-Condon Principle 15
  - 2.3.3. Excited States 15
  - 2.3.4. Molecular Electronic Transitions 16
  - 2.3.5. Beer-Lambert's Law 16
  - 2.3.6. Photochemical Processes in a Photoinitiator 17
- 2.4. Lasers 19
- 2.5. Mass Spectrometry 22
  - 2.5.1. Ionization Methods 22
  - 2.5.2. Mass Separation 23
  - 2.5.3. Collision-Induced Decay 26
  - 2.5.4. Resolution and Mass Accuracy 26
  - 2.5.5. Mass Spectrometry on Polymers 27
- 2.6. Investigation of Photoinitiated Polymerizations via PLP-ESI-MS 29
- 2.7. Femtosecond Spectroscopy 32
  - 2.7.1. Investigation of Photoinitiators by fs Spectroscopy 33
- 2.8. Single-Chain Nanoparticles and their Characterization 34
  - 2.8.1. Single-Chain Nanoparticles 34
  - 2.8.2. Characterization of SNCPs 35

3. Photoinitiator Investigation 39
- 3.1. Initiation Efficiencies of MMMP, Benzoin, and 4MB 40
  - 3.1.1. Initiation Efficiency Evaluation via PLP-ESI-MS 40
  - 3.1.2. Ionization Enhancement Study 42
  - 3.1.3. Evaluation of ESI-MS Data for Quantitative Comparison of Initiator Fragments 43
  - 3.1.4. Ionization of MMMP-initiated Polymer 48

3.1.5. Femtosecond Spectroscopy and Theoretical Methods 50
3.1.6. Conclusions 53
3.2. Investigation of Structure-Reactivity Correlations for Benzoin-Type Photoinitiators 55
3.2.1. Photoinitiator Synthesis 56
3.2.2. UV-Vis Spectroscopic Evaluation 57
3.2.3. Initiation Efficiencies via PLP-ESI-MS 57
3.2.4. Additional Analytical Methods 58
3.2.5. Combined Photoinitiator Analysis 61
3.2.6. Critical Evaluation of the PLP-ESI-MS Method 65
3.2.7. Summary and Conclusion 65

4. Mechanistic Investigation of Copper-Mediated PhotoRDRP 67
4.1. Stepwise Mechanism Elucidation via PLP-ESI-MS 67
4.1.1. PLP Experiments 69
4.2. The Mechanism of PhotoRDRP 73
4.2.1. The Impact of the Ligand 75
4.2.2. The Significance of UV-Vis Spectra for the Mechanistic Elucidation . . 76
4.3. Summary and Conclusions 77

5. Photoinitiator-Based Single-Chain Nanoparticle Formation 79
5.1. Introduction of Photoinitiator Units along the Chain 80
5.2. Irradiation Experiments 81
5.2.1. Variation of the Solvent Mixture and Polymer Concentration 81
5.2.2. Addition of Radical Inhibitor 87
5.2.3. Variation of the DCM/Diethyl Ether Solvent Mixture 88
5.2.4. Variation of Irradiation Intensity and Time 89
5.2.5. Variation of the Precursor Chain Length 90
5.2.6. Irradiation at Higher Dilution and Lower Temperature 91
5.2.7. Variation of the Normalization Method 91
5.2.8. Variation of Irradiation Wavelength 92
5.2.9. Performance of Test Reactions 93
5.3. Characterization via DOSY 94
5.4. Conclusions and Outlook 97

6. Conclusions and Outlook 101

7. Experimental Section 103
7.1. Photoinitiator Investigation 103
7.1.1. Materials and Instrumentation 103
7.1.2. Syntheses 107
7.2. PhotoRDRP 110
7.2.1. Materials and Instrumentation 110
7.3. SCNP Formation 112
7.3.1. Materials and Instrumentation 112
7.3.2. Synthesis 113

Bibliography 117

A. Appendix **127**

Abbreviations **135**

Curriculum Vitae **139**

Acknowledgements **141**

1

Introduction

The first reported photochemical reaction used by mankind dates back over 4000 years: The preparation of mummies in ancient Egypt involved a light-induced crosslinking polymerization. The linen strips that were wrapped around the mummies were soaked in bitumen from Judea – containing unsaturated compounds – and were subsequently hardened under sunlight.[1] Likewise, the main industrial application of photochemistry today is the light-induced polymerization and crosslinking of materials. In nature, photochemistry supports the existence of life on Earth through the formation of oxygen and organic substances from carbon dioxide and water, based on photosynthesis.[2] An aerobic atmosphere as well as the growth of plants, e.g., food for living organisms on Earth, results from this photoinitiated reaction. This extremely efficient reaction summarizes the benefits of photoinitiated reactions compared to thermally initiated reactions: They are fast and can be performed under mild conditions, at low as well as high temperatures and they can be spatially and temporally controlled. Therefore, the application of photochemical processes is not only beneficial from an environmental point of view, but also based on economic reasons. Logically, photochemistry has thus been employed for decades in industrial as well as daily-life applications.[3,4] For instance, in the print and automotive industries, the UV light-induced curing of inks and coatings is achieved via photocuring of a mixture of photoinitiator, monomers, and dyes. In addition, the yearly visit of a dentist might end with applied photochemistry: dental fillings – so-called dental composites – consist of a mixture of monomer, inorganic components, and photoinitiator and are cured photochemically.[5]

The common component of the aforementioned systems, the photoinitiator, plays a major role in the described processes. Enhancing the efficiency of homolytic cleavage as well as the reactivity of the radicals formed from a photoinitiator is of high importance for industrial applications. Better photoinitiators require reduced light intensities and irradiation times, thus lower energy consumption, and can be used in lesser amount, thereby saving costs. In addition, a lower amount of initially employed photoinitiator species may result in a smaller number of residual and unreacted initiator moieties in the final product. Undesirable effects arising from residual photoinitiators in a product could be reduced to a minimum. For instance, the amount of photoinitiator migration from food packaging into foodstuff, as repeatedly reported[6–8] could be decreased.

Improving the performance of photoinitiators is of high interest. However, the factors that determine their efficiency are to date not well understood. The development of new photoinitiators is mainly based on a trial-and-error procedure and the prediction of their performance is primarily estimated by absorption behavior.[9–11] The current dissertation puts this procedure into question. In the first chapter, the initiation efficiencies of benzoin-type photoinitiators are investigated from a trifold perspective. Firstly, the focus is placed on the influence of the aromatic substituents on the photoinitiating efficiency. Here, pulsed-laser polymerization coupled with electrospray-ionization mass spectrometry (PLP-ESI-MS) turned out as a powerful tool for detecting and comparing the initiation behavior of single initiator fragments. Secondly, the molecular dynamics are investigated for each substance, highlighting the underlying factors for good or poor initiation and the effects of various substitution patterns. Finally, the actual reactivity of the initiating radical fragments is investigated theoretically. Such an in-depth analysis of photoinitiators gives an insight into the processes that occur upon irradiation. The questions "How can radical formation be enhanced?" or "Which substituent should be selected for high radical reactivity?" are discussed in detail in the current work.

The spectrum of photoinitiated polymerizations is not only governed by photoinitiator-based processes. Various light-induced chemical reactions can lead to a radical polymerization. For instance, light-triggered electron-transfer reactions of organic as well as metal-containing compounds can result in the formation of initiating radicals.[12–14] In addition, photopolymerizations initiated by a different mechanism than by photoinitiator dissociation may still benefit from the same advantages. A newly discovered photoinitiated polymerization is the photoinitiated copper-mediated RDRP (photoRDRP).[15] While the thermally initiated copper-mediated RDRP has been studied and utilized for decades in research, its light-triggered version is in its infancy.[16,17] Particularly, the actual mechanism for the formation of radicals as well as the generation of copper(I) species from copper(II) species – triggered by light – remained unclear. However, a polymerization process can only be improved regarding its polymerization rate and product output if the rate determining steps are identified. The current work seeks to unravel the processes that occur in a photoRDRP reaction and, thus enlightening its mechanism. Once more, PLP-ESI-MS is employed: PLP enables the generation of short polymer chains which can be subsequently analyzed via mass spectrometry. The advantage of mass spectrometric analysis is that the exact molecular composition of the polymer chains as well as the respective initiating fragments can be determined. In the progress of the current work, the questions on how light can play the major role in the radical generation step as well as the reduction step of the copper(I) species will be addressed.

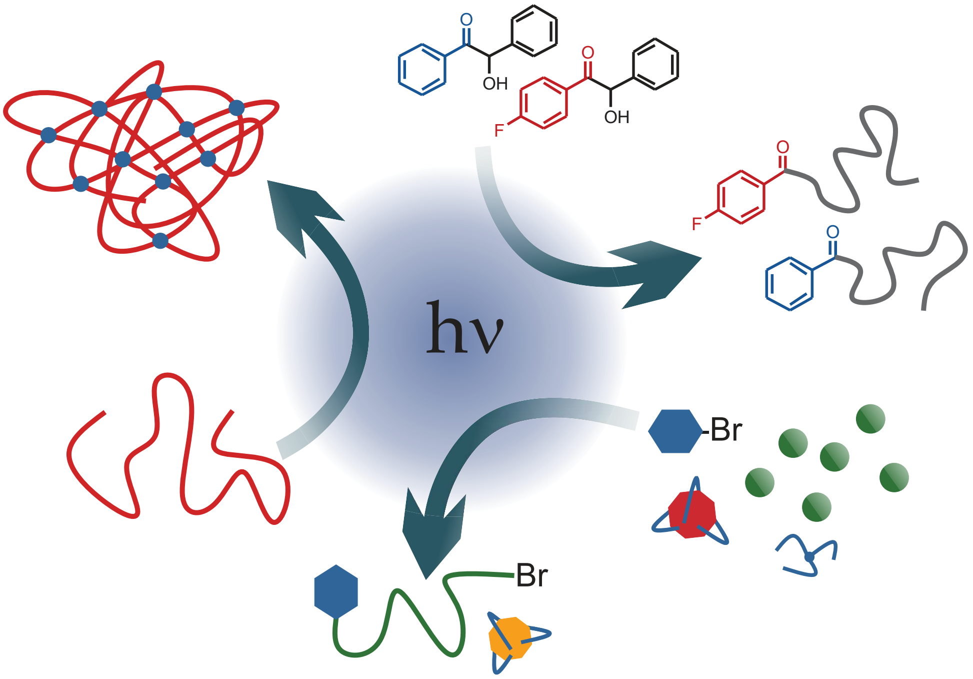

Figure 1.1.: Overview of the projects addressed in the current dissertation.

The third part of this dissertation focuses on the application of radical photoinitiators in the sophisticated field of single-chain nanoparticles (SCNPs). Thereby, the combination reaction between two photoinitiator radicals is investigated regarding its synthetic ability to develop intramolecular bonds along a single polymer chain. High dilution and subsequent irradiation of a photoinitiator-functionalized polymer is supposed to form so-called SCNPs, nanoparticles that are highly defined regarding their molar mass, particle size, and functionality.[18] The target is to employ the very fast radical combination reaction for a process that to date has only been realized by delicate procedures, numerous synthetic steps, and – in some cases – long reaction times.[18] In addition, the purpose of employing radical photoinitiators for SCNP formation is to demonstrate their versatile character.

Figure 1.1 illustrates an overview of the three projects addressed in the current dissertation.

2

Theory and Background

2.1. Radical Polymerization

2.1.1. Free Radical Polymerization

Free radical polymerization (FRP) is a very versatile polymerization technique and of high industrial significance. Many different polymers can be produced by this technique due to its applicability to a wide range of monomers, its high tolerance toward many chemical functionalities, and the various methods that can be employed to initiate the polymerization. The process of a free radical polymerization, as illustrated in Figure 2.1, consists of four fundamental reaction steps: 1) initiation, 2) propagation, 3) termination, and 4) chain transfer.[19] Before the actual initiation reaction occurs, the initiator dissociates into two radicals that can initiate the radical polymerization of vinylic monomers by adding onto their double bond. During this step the radical function is transferred to the monomer.
There are several possibilities to generate initiating free radicals that can react with monomer. Decomposition of an initiator molecule into two radicals can be accomplished via thermal degradation, UV light irradiation, or through a redox reaction for instance. Typical values for the rate of dissociation k_d are in the order of 10^{-1} to 10^{-6} s^{-1} and vary with the reaction conditions. For further information on the UV light-initiated radical polymerization and – most importantly – the photoinitiator structure, refer to section 2.2.

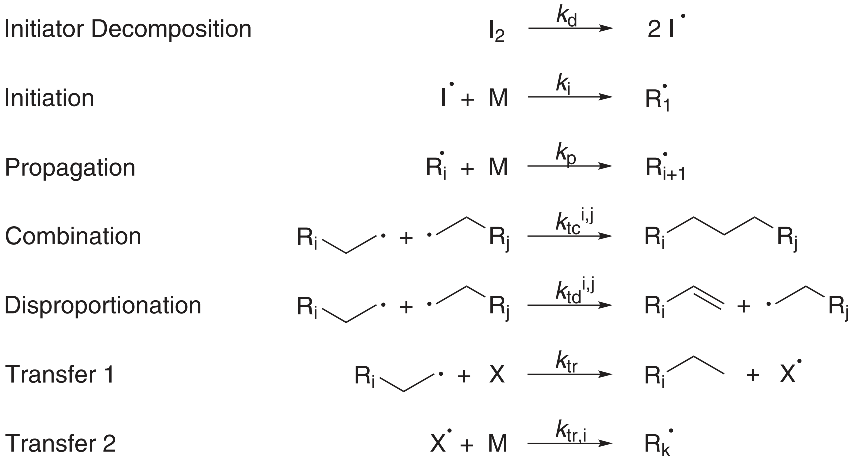
Initiator Decomposition
Initiation
Propagation
Combination
Disproportionation
Transfer 1
Transfer 2
$I_2 \xrightarrow{k_d} 2\,I^\bullet$
$I^\bullet + M \xrightarrow{k_i} R_1^\bullet$
$R_i^\bullet + M \xrightarrow{k_p} R_{i+1}^\bullet$
$k_{tc}^{i,j}$
$k_{td}^{i,j}$
k_{tr}
$X^\bullet + M \xrightarrow{k_{tr,i}} R_k^\bullet$
R_i
R_j
X

Figure 2.1.: The mechanism of free radical polymerization including the initiation step, propagation, termination via combination or disproportionation, and the radical transfer step.

During the following propagation reaction the polymer is formed by successive additions of monomer units to the radical chain end functionality. The propagation rate coefficient k_p characterizes the addition reaction of one monomer radical to another monomer. Thereby the polymerization rate is highly dependent on the stability of the formed radicals. A slow propagation rate is associated with stable radicals, such as styrene or methyl methacrylate, and is in the order of $k_p = 10^2$ L·mol^{-1}·s^{-1}. Whereas unstable radicals, such as acrylates, imply a fast polymerization with a k_p of close to 10^4 L·mol^{-1}·s^{-1}. In general, monomers that can be readily transformed into a radical species, due to their high stability, show a fast initiation rate yet a slow polymerization rate. The opposite, a high reactivity, is the case for monomers whose radical analog is difficult to form. The rate coefficient k_p solely depends on the chemical structure of the monomer and the reaction temperature. However, for very high conversions diffusion control can be observed, originating from the high viscosity of the reaction mixture having a major impact on the propagation rate.

The growth of a polymer chain is maintained by the propagation reaction. The termination reaction limits the growth and is the result of the reaction of two radical chain ends. Two possible termination pathways exist: the combination and the disproportionation reaction. The combination reaction of two chains results in the formation of a single, so-called "dead" polymer chain, while the disproportionation reaction generates one dead polymer chain and one polymer chain carrying a double bond functionality that is able to further participate in the polymerization step. Most monomers undergo both disproportionation as well as combination steps. However, a high steric hindrance closely located to the double bond of the monomer, e.g., as it is the case for methyl methacrylate, promotes the disproportionation reaction, whereas monomers with less sterically hindered double bonds, such as styrene, rather undergo combination reactions.[20–22]

The approach of two polymeric chains in the reaction solution, and therefore their termination reaction, is diffusion-controlled. Hence, the termination rate coefficient, k_t, is mainly influenced by the viscosity of the reaction solution. Typical values for k_t are in the order of 10^6-10^8 L·mol^{-1}·s^{-1}, depending on several parameters such as conversion, temperature, and – importantly – the length of the polymer chains. Besides the three aforementioned reactions – initiation, propagation, and termination – the transfer reaction is the fourth event that can occur in a radical polymerization. During the transfer step the propagating radical is transferred to another species, such as another monomer molecule, a polymer chain, solvent, or a transfer agent that was added intentionally. The transfer reaction generally leads to a lower average molar mass or leads to branching along the polymer chain. Since no radical species is eliminated, the transfer reaction does not decrease the total radical concentration in the reaction solution. In fact, the transfer reaction in radical polymerizations is frequently used in order to introduce control over the molar mass or the topology of polymers.

Considering the mass of polymer that is industrially produced every year, FRP is the most important polymerization technique. However, it entails a range of disadvantages such as the lack of control over molar mass, dispersity, topology, and the exact chemical functionality of the polymer end group. Consequently, advanced polymerization techniques have been developed in order to address these issues. The development of reversible-deactivation radical polymerization (RDRP) techniques, formerly known as controlled/living radical polymerization, serve as important tools to satisfy the aforementioned requirements for well-defined polymers. In the following the general concept of RDRP will be introduced.

2.1.2. Reversible-Deactivation Radical Polymerization (RDRP)

As mentioned in the previous section, the main disadvantage of FRP is the lack of control over molar mass, dispersity, and end group functionality. The main cause for these effects is the occurrence of the termination reaction, leading to broad dispersities and accumulation of dead chains that cannot be functionalized in subsequent synthetic steps. Consequently, the elimination of the termination reaction can serve as an instrument to gain control over the structure and chemical character of a polymer. Various polymerization techniques, formerly known as controlled/living radical polymerizations, have been developed in the past decades targeting the elimination of the termination reaction and producing polymers with defined end groups that can be functionalized in further synthetic steps. The mechanism of these techniques is mainly based on the concept of a reversible deactivation step of the radical chain. Therefore, they are summarized as reversible-deactivation radical polymerizations (RDRP). In an ideal living polymerization, termination and transfer reactions are completely absent, thus resulting in a narrow molar mass distribution.[23–25] However, in the reality of a radical polymerization, termination events can never be eliminated entirely. Thus, radical polymerizations with a living character, i.e., when terminated polymer chains do not influence the final product and are not detectable, are referred to as RDRP instead of living polymerizations. Typical RDRP techniques fulfill the following criteria: a fast and complete initiation process, a linear evolution of molar mass with monomer conversion, low dispersities (typically $Đ < 1.2$), and chemically defined end groups that can be functionalized in a subsequent synthetic step.

Two main techniques are used in order to decrease the occurence of termination events in a radical polymerization. On the one hand the absolute concentration of radicals in the reaction mixture can be reduced through the reversible termination of radical chain ends. A lower number of radicals in a reaction minimizes the probability of their collision and, thus, of termination events. This mechanistic approach is applied in nitroxide-mediated polymerization (NMP), using a nitroxide species to reversibly terminate a radical chain end. The release of the radical chain as well as the original nitroxide species occurs at elevated temperatures (80-100℃).[26–29] Another important technique that follows the approach of reducing the number of radicals in the polymerization is the atom-transfer radical polymerization (ATRP) and will be described in the following section. An alternative approach, on the other hand, to reduce radical termination products in a polymerization is to introduce a transfer agent that performs a reversible chain transfer reaction. This technique, known as the reversible addition fragmentation chain transfer (RAFT) polymerizations,[30–32] has the advantage of not decreasing the absolute number of radicals in the reaction solution and, thus, maintaining a high polymerization rate. Important transfer agents for RAFT polymerizations, so-called RAFT agents, are dithiocarbonates, trithiocarbonates as well as xanthates. In the current work, since NMP and RAFT were not employed, a detailed focus is placed on ATRP.

2.1.3. Atom-Transfer Radical Polymerization (ATRP)

Among the previously described techniques in the field of RDRP, the atom-transfer radical polymerization (ATRP)[33] and the mechanistically related single electron transfer living radical polymerization (SET-LRP)[34] [35] are two of the most popular methods of RDRP. Due to their related mechanisms and identical products, only ATRP is described in detail here.[36–39]

The nearly full elimination of termination events in ATRP is achieved by the decrease of the number of radicals in the reaction mixture. Thereby, a dormant/active interchange is employed based on a redox equilibrium in which a transition metal complex (M_nX/L) activates an alkyl halide ($P_n - X$) generating alkyl radicals and the metal complex in a higher oxidation state ($M_n^{+1}X_2/L$) (refer to Figure 2.2). Mostly, copper complexes serve as catalysts and bromine as the transferred halogen. The lower oxidation state complex Cu^IBr/L is commonly referred to as the activator and $Cu^{II}Br_2/L$ as the deactivator. The activator species abstracts a halogen atom from the alkyl halide, forming the deactivator and a radical species that can initiate a polymerization. In classical ATRP the activator is regenerated through the reaction of $Cu^{II}Br_2/L$ with a propagating radical.

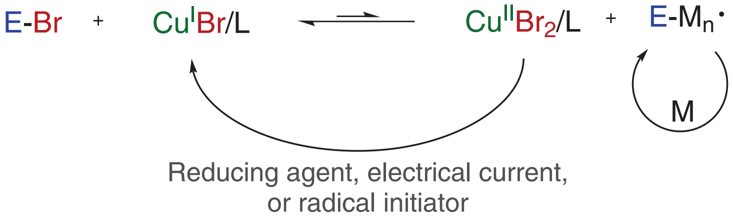

Figure 2.2.: The mechanism of atom-transfer radical polymerization with activator regeneration.

An equilibrium between the growing radical chains and dormant halide-capped chains maintains a low radical concentration and enables the formation of polymers with high end group fidelities and low dispersities. Provided that the activation rate coefficient k_a (with typical values in the order of 1 $L{\cdot}mol^{-1}{\cdot}s^{-1}$) is orders of magnitude lower than the deactivation rate coefficient k_{da} (typically around 10^7 $L{\cdot}mol^{-1}{\cdot}s^{-1}$), an adequate equilibrium and therefore a good control over the polymer characteristics can be achieved. The ATRP initiator, an alkyl halide that can have various activating substituents in α-position of the halide, has to be chosen according to the monomer reactivity. Furthermore, the chosen ligand plays an important role for the activation rate. Both the initiator and ligand have to be chosen carefully in order to have an ATRP with a high initiation rate as well as a fast polymerization rate.[40] A selection of commonly used ATRP initiators and ligands is illustrated in Figure 2.3.

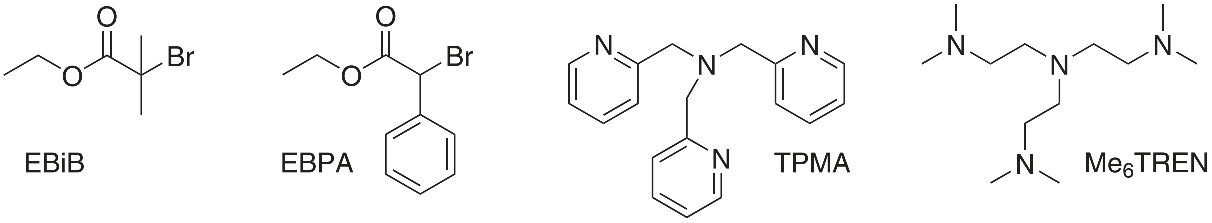

Figure 2.3.: Commonly used initiators and ligands for ATRP: ethyl $\alpha-$bromoisobutyrate (EBiB), ethyl $\alpha-$bromophenylacetate (EBPA), tris(2−pyridylmethyl)amine (TPMA), and tris[2−(dimethylamino)ethyl]amine (Me$_6$TREN).

In the past decade a wide range of advanced ATRP techniques have been developed that continuously regenerate the activator by, for instance, the addition of reducing agents (activator regenerated by electron transfer, ARGET ATRP)[41] or radical initiators (initiators for continuous activator regeneration, ICAR ATRP).[42][43] The described techniques allow it to perform the ATRP reaction starting from the catalyst in its higher oxidation state $Cu^{II}X_2/L$ that is, compared to $Cu^{I}X/L$, not sensitive to oxygen and therefore easier to handle. In the course of the reaction, Cu^{II} deactivator species are reduced to Cu^{I} activator species by, for instance, the added reducing agent. Hence, the sensitivity of ATRP toward oxygen could be significantly diminished as well as the amount of catalyst in the reaction reduced.[44][41] Recently, external stimuli on the redox equilibrium of the copper catalyst have been extensively investigated. Thereby the application of, for instance, an electrochemical input in order to continuously regenerate the activator (the catalyst in its lower oxidation state $Cu^{I}X/L$) throughout the reaction process marked an important milestone in the development of advanced RDRP techniques.[45][46]

In the last years the investigation of the influence of light on the redox equilibrium lead to the introduction of photoRDRP (herein, both photoATRP and photoLRP are included),[15–17,47–50] the latest advancement in ATRP and SET-LRP. For the first time, Guan and Smart[15] discovered the beneficial influence of light on the polymerization rates and final monomer conversion in an ATRP performed under visible light compared to an ATRP conducted under dark conditions. The actual initiation of an ATRP by light was reported for the first time by Tasdelen *et al.* Thereby, the copper catalyst in its highest oxidation state $Cu^{II}Br_2/L$ was employed, indicating that light can trigger its reduction toward $Cu^{I}Br/L$. The photochemical initiation of an ATRP represents an elegant type of RDRP, combining control over molar mass and dispersity with the benefits of light-triggered reactions, i.e., allowing spatial and temporal control over the polymerization process. Recently, Jordan and coworkers showed that even ambient laboratory light has a significant positive influence on several ATRP techniques by increasing the polymerization rate and final monomer conversions.[51]

Despite the utilization of photoRDRP, its mechanism remained rather unclear. Lately, attempts were made by Haddleton and colleagues and Matyjaszewski and coworkers to clarify how $Cu^{II}Br_2/L$ can be reduced toward $Cu^{I}Br/L$ by light and which role the ligand (L) and initiator (R-X) play in this process.[16,17] The first attempt to elucidate the mechanism of photoRDRP was performed by Haddleton and coworkers.[16] In their study, using acrylate monomers and Me_6TREN as the ligand, single components of the RDRP mixture were systematically omitted in order to clarify their role in the complete photochemically driven process. Their experiments showed that for the successful initiation and maintenance of a well-controlled polymerization, an aliphatic tertiary amine σ-donor ligand in excess relative to Cu^{II} is required. In the proposed mechanism free Me_6TREN is photoactivated, performing an outer-sphere single-electron transfer (OSET) to an alkyl halide initiator, leading to a C-Br bond scission of the latter. The resulting radicals can subsequently initiate the polymerization. Based on the presence of the deactivator $Cu^{II}Br_2/Me_6TREN$, the ATRP redox equilibrium (as illustrated in Figure 2.4) can be established through the reaction with propagating radicals, forming the $Cu^{I}Br/Me_6TREN$ activator species. Additionally, Me_6TREN radical cations and bromide anions are proposed to be formed in the OSET reaction and being involved in the generation of $Cu^{II}Br_2/Me_6TREN$ after oxidation of $Cu^{I}Br/Me_6TREN$. However, in the mechanism of Haddleton and coworkers the deactivation process with $Cu^{II}Br_2/Me_6TREN$ is proposed as the exclusive pathway to form $Cu^{I}Br/Me_6TREN$ species. Thus, it is not entirely ensured how a high polymerization rate can be maintained when solely the propagating radicals can contribute to the formation of the activator.

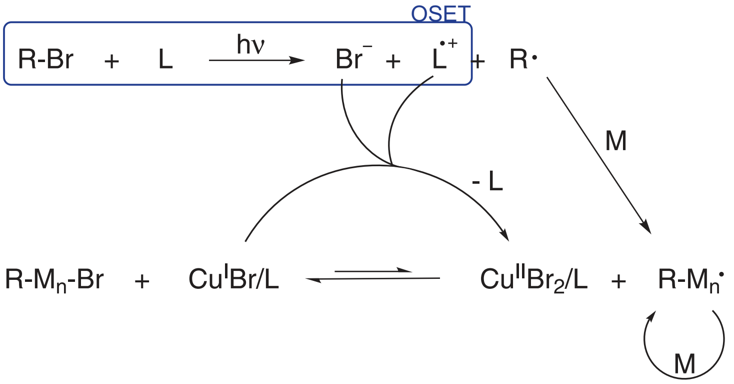

Figure 2.4.: The mechanism of photoRDRP proposed by Haddleton *et al.*[16]

In the following mechanistic study on photoATRP, carried out by Matyjaszewski and coworkers, a similar approach was taken.[17] Thereby, all reaction pathways that appear plausible were studied both experimentally and with simulation kinetic techniques. For various reactions rate coefficients were derived from rate/conversion fittings and employed for simulations. Hence, pathways for radical generation and formation of $Cu^{I}Br/Me_{6}TREN$ were simulated. In their proposed mechanism, that is illustrated in Figure 2.5, the photochemical reduction of Cu^{II} species by free ligand and generation of their radical cations is the main pathway for the formation of activator. A synergistic reaction between ATRP initiator and ligand leads to the formation of radicals, able to initiate a polymerization. However, only a small contribution is assigned to the latter process, more precisely being 1 order of magnitude slower than the reduction of deactivator. Therefore, as is the case for the proposed mechanism by Haddleton and coworkers, it is not fully understood how a sufficient amount of initiating radicals is generated photochemically in order to rapidly initiate the polymerization process.

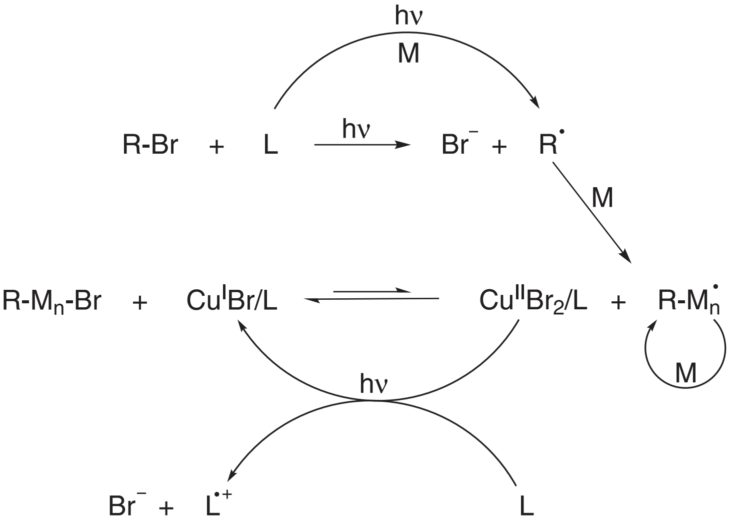

Figure 2.5.: The mechanism of photoRDRP proposed by Matyjaszewski *et al.*[17]

Considering the aforementioned studies, it can be assumed that a photochemical process is involved in the reduction of Cu^{II} species. Furthermore, the involvement of the initiator and/or ligand in this process is likely. However, both studies lack detailed mechanistic information about how the individual compounds are involved in the photochemical process. An elucidation of the involved structures by nuclear magnetic resonance spectroscopy (NMR), mass spectrometry, or similar exact techniques is missing. In chapter 4, the verification of the photoRDRP mechanism on a molecular level will be presented. Thereby, pulsed-laser polymerization (PLP) was employed and the resulting products were subsequently analyzed by high resolution electrospray ionization mass spectrometry (ESI-MS).

2.2. Photoinitiated Free Radical Polymerization

In addition to thermally initiated free radical polymerization, photochemically initiated FRP, schematically illustrated in Figure 2.6, plays an important role in research as well as in industrial applications. A wide range of coatings, for instance in the automotive industry, inks or adhesives are based on the initiation of an FRP by photochemical means.[52] [53] In addition, dental fillings are cured photochemically, applying a resin that consists of a monomer mixture and radical photoinitiator.[5] Furthermore, photoinitiated FRP is employed in the highly advanced fields of 3D printing[54] and photolithography, a process that is employed for the fabrication of micropatterns.[55] All these applications have one common component, the radical photoinitiator. In the following section typical photoinitiators and their physical properties will be discussed.

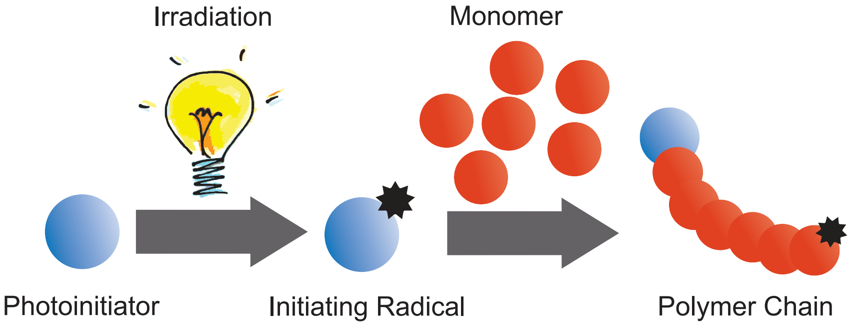

Figure 2.6.: Illustration of photoinitiated radical polymerization, reproduced from ref.[4] with permission, ©2010 American Chemical Society.

The most striking advantage of photopolymerizations compared to thermally initiated polymerizations is the possibility to perform the reaction at ambient temperature and even below. Fewer side reactions such as chain transfer occur when lower temperatures are applied, but also the polymerization of monomers with a low ceiling temperature can be performed, without the risk of depolymerization to occur. For practical reasons, the photochemical curing of large coated surfaces or small structures is easier to realize than thermal curing. For an even heating of a large surface appropriate industrial furnaces are necessary. Whereas the light-induced curing can be performed by light sources that are less energy-consuming. Furthermore, in application areas where high temperatures can not be applied, such as biological media, for instance in the presence of enzymes, or in dental fillings, photopolymerizations are more applicable.[4]

Pulsed-Laser Polymerization

Pulsed-laser polymerization (PLP) is a polymerization technique that applies consecutive short laser pulses (≈ 10 ns) in order to initiate a polymerization. When the laser beam hits the sample, a large amount of radicals is formed by the photointiator molecules that can add onto a monomer, commencing the propagation reaction during the subsequent dark phase before the next laser pulse. Next to propagation, the radicals that are formed via a laser pulse can add onto a propagating polymer chain and thus lead to its termination by combination or disproportionation. During the time intervals between two consecutive laser pulses (the dark phases) the polymer chains can propagate and terminate like in a continuously initiated FRP via disproportionation and combination. Most propagating chains are terminated by new radicals that are formed by a laser pulse. However, a small amount of radicals survives and can propagate in a second or even third dark phase. The variation of the laser pulse frequency (typically in the range of 1-500 Hz), i.e., the duration of the dark phase, allows for the control of the polymer chain length.[56]

The benefit of PLP compared to conventional FRP is that it generates relatively short polymer chains while still performing photoinitiated FRP. Short polymer chains have the advantage that they can be analyzed by mass spectrometric techniques such as electrospray ionization mass spectrometry (ESI-MS) that is described in section 2.5. PLP was described for the first time by Sokolov and coworkers[57,58] and was further improved by Olaj and coworkers.[59,60] It is mainly used for the determination of propagation rate coefficients k_p.[61–63] For this purpose, the principle that some radicals survive a laser pulse and propagate for a second or even third dark phase is exploited. Most polymer chains that are generated by PLP propagated for one dark phase, some propagated for two dark phases and only a few for three. Thus, their molecular weights (M_1, M_2, M_3, M_i) are characteristic and increase constantly after each dark phase, i.e., $M_i = i \cdot M_1$. The size exclusion chromatogramm of a polymer, that was synthesized in such way, has a characteristic shape, showing at least two inflection points (L_i, determined by the maxima in the first derivative). The propagation rate coefficient can be determined from these inflection points according to Equation 2.1.

$$L_i = \frac{M_i}{MW_M} = i \cdot k_p \cdot c_M \cdot t_0 \text{ with } i = 1, 2, 3... \tag{2.1}$$

L_i is the degree of polymerization, M_i is the molecular weight at the inflection point number i and is determined by size-exclusion chromatography (SEC), MW_M ist the molecular weight of the monomer, c_M is the monomer concentration, and t_0 is the time between two subsequent laser pulses. In Equation 2.1 only i and t_0 can be determined, thus, in order to identify k_p, the monomer concentration c_M is assumed to be constant. However, this assumption is only valid for very low monomer conversions (up to 1-3 %).

2.2.1. Radical Photoinitiators

The photoinitiator plays a major role in a photopolymerization, since it acts in its very first step by generating radicals upon absorption of a photon. A photoinitiator, or a photoinitiator system, is defined as a molecule or a combination of molecules that absorb light and form radicals that can add onto a monomer double bond, generating a radical that can further propagate.[9] A wide range of different photoinitiators and photoinitiator systems has been developed in the past decades, offering different properties such as absorptivity, reactivity, storage stability, migration ability, toxicity etc. Thus, in order to select the right photoinitiator for industrial applications, many parameters have to be considered beforehand. In the following, the main classes of photoinitiators will be introduced.

Photoinitiator Type I and Type II

Radical photoinititors are classified as Type I and Type II initiators. Their distinct mechanistic differences are illustrated in Figure 2.7. Photoinitiators of the Type I absorb light of a certain wavelength, leading to an excited singlet state that can be transformed into a triplet state after intersystem crossing (ISC) The subsequent α-cleavage forms radicals without the interaction with other species and is often referred to as a Norrish Type I reaction.[64,65] Simply, the same molecule that is photochemically excited, forms a radical that initiates the polymerization. Most Type I initiators are aromatic carbonyl compounds and can be functionalized with various substituents. Typical Type I initiators are benzoins, acetophenons, benzils, acylphosphines oxides, or acylgermanes.[66] Direct photocleavage after the absorption of light is possible due to the low CO-alkyl bond energy of 272-293 kJ·mol^{-1}, since UV light provides energy in the range of 293-335 kJ·mol^{-1}.[3] The advantages of employing Type I photoinitiators are their high quantum yields and reactivities. For applications with styrene as the monomer, these photoinitiators are particularly useful, due to their low sensitivity to triplet quenchers.[67] Furthermore, due to the monomolecular kinetics of the radical formation, i.e., being independent of added compounds, a higher radical output can be achieved. The disadvantage of some photoinitiator Type I species is their relatively low thermal stability.

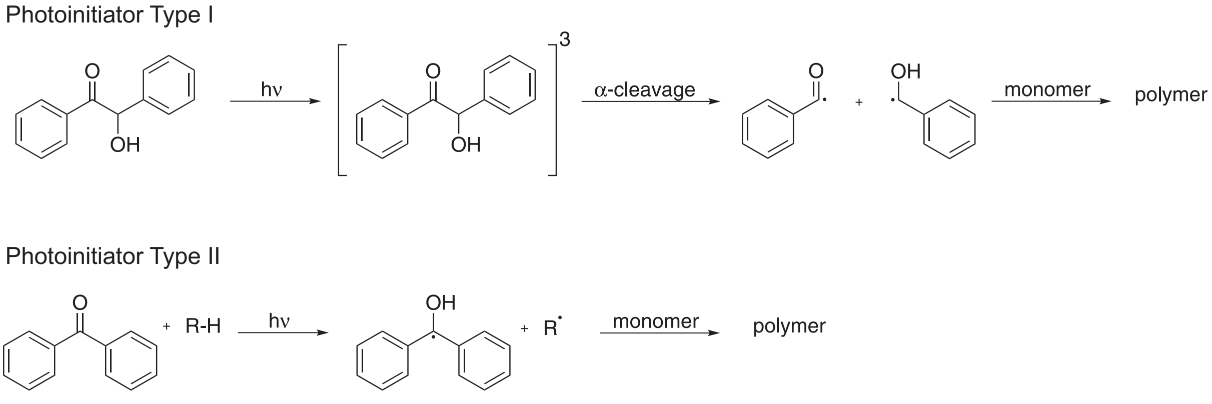

Figure 2.7.: Illustration of the mechanistic differences between the photoinitiator types I and II.

Photoinitiators of the Type II form radicals via a bimolecular process. The light-absorbing photoinitiator species form an electronically excited state. A direct bond scission after absorbance of a photon cannot be performed, since the CO-aryl bond energy (335-377 kJ·mol^{-1}) is too high to be cleaved. The molecule in its excited state does not form a radical sufficiently reactive to add onto a monomer double bond. Therefore, a co-initiator that acts as a H-donor, is employed. It reacts with the excited photoinitiator by creating a reactive radical that initiates the polymerization. Commonly, tertiary amines are employed as co-initiators. After the hydrogen abstraction, the photoinitiator forms a radical that is not reactive enough to act as an initiator. Although photoinitiators of the Type II are widely used, their application bears some disadvantages. Firstly, the use of highly volatile and odorous alkylamines leads to various application problems. Secondly, the bimolecular process is more sensitive to quenching of the excited photoinitiator by oxygen or monomer. In general, a slower initiation process is observed for Type II photoinitiators. Commonly used photoinitiators of this type are acetophenones, benzophenones, and thioxanthones.[10,68,69]

Figure 2.8 shows typical photoinitiators from both categories, Type I and II, pointing out their structural variety. In the following, some characteristic properties for each of the depicted photoinitiator derivatives will be described.

- **Benzoins** are efficient low-cost Type I photoinitiators for the production of polyester/ styrene coatings in, for instance, wood coatings.[70,71] Functionalization has a strong influence on their initiating behavior.

- **Benzil** alone is a poor Type I photoinitiator for FRP. However, the addition of amines as co-initiators can increase its efficiency.[72,73]

- **α-Hydroxy ketones** are highly efficient photoinitiators for photocuring applications such as coatings.[74]

- **α-Aminoketones** form a large amount of radicals under UV light irradiation.[75]
- **Bis(acyl)phosphine oxides** are very efficient photoinitiators with a high thermal stability. The formed phosphonyl radicals are highly reactive due to the high electron density at the phosphorus atom. The resulting pyramidal radical structure provides good steric conditions for the addition to a monomer.[76–78]
- **Acylgermanes** are newly developed initiators for FRP at visible light and applications for dental materials.[4,79–81]
- **Acetophenone** derivatives are efficient Type II photoinitiators, especially for applications in micellar solutions.[82,83]
- **Thioxanthones** are commonly employed Type II intiators. Some derivates do not require an added co-initiator and are thus called one-component photoinitiators.[4,84–86]
- **Camphorquinones** are Type II initiators commonly used in dental resin composites.[87,88]

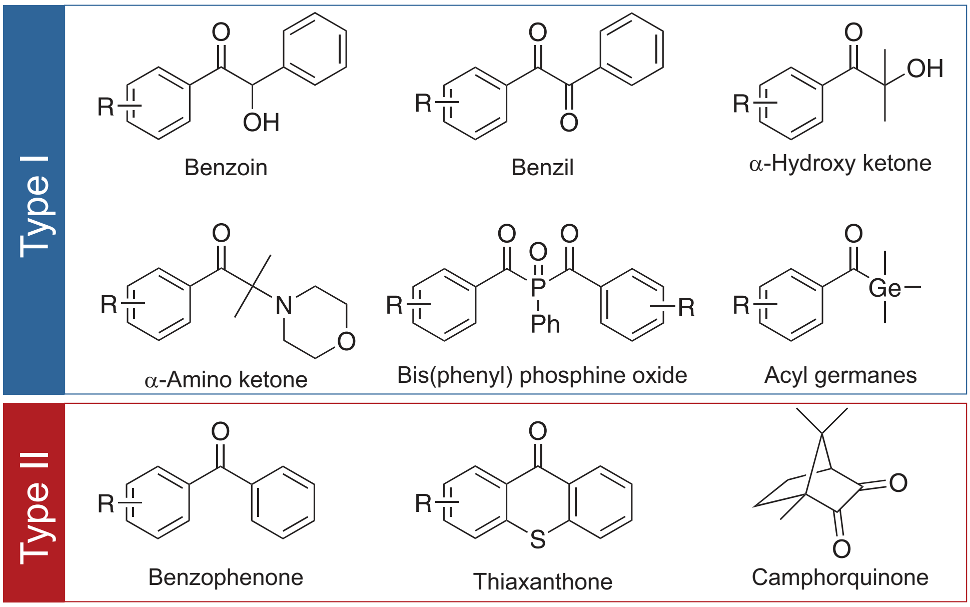

Figure 2.8.: Commonly employed photoinitiators of both Type I and Type II categories.

The design of new photoinitiators is part of ongoing research focusing on improving the performance of photoinitiators regarding the monomer conversion, quantum yield, the initiation at visible light,[11,69,70] and thermal and photochemical stability of the resulting end groups.[89] When designing new photoinitiators, a small change in the molecular structure can have a strong influence on its physical properties and its dynamics. In the following an insight into the processes that can occur in a molecule, especially in a photoinitiator, upon irradiation with light will be given.

2.3. Physical Processes in a Molecule upon Irradiation

Fundamental research by Planck[90] and Einstein[91] gave insight into the character of light and the physical processes that can occur in a molecule after absorption of a photon. Planck postulated that the oscillator energy in a black body is quantized and can be described by

$$E = nh\nu$$

where n is an integer (1,2,3...), h is the Planck's constant, and ν is the frequency of the oscillator. Planck's postulate was used by Einstein for the explanation of the photoelectric effect, the phenomenon that metals emit electrons when irradiated. Based on the principle of absorption of single light quanta, the concept of the quantum yield was introduced in photochemical reactions, being the number of chemically modified molecules per absorbed photon.

2.3.1. Jablonski Diagram

A molecule that absorbs a photon generally performs a transition from the singlet ground state (S_0) into an excited singlet state (S_n). Once in the excited state, the molecule can perform a range of transitions such as

- Vibrational relaxation into the lowest state of vibration of an excited singlet state
- Radiationless deactivation into a lower electronic singlet state or back to the singlet ground state S_0 by internal conversion (IC) and subsequent vibrational relaxation
- Emission of light via fluorescence and, thus, a transition into the singlet ground state S_0
- Radiationless transition from an excited singlet state S_n into an energetically lower triplet state T_n via intersystem crossing (ISC), thereby performing a forbidden change of multiplicity
- Vibrational relaxation from a vibrationally excited triplet state into the lowest vibrational state of this triplet
- After performance of an ISC, returning to the singlet state S_0 by emission of light via phosphorescence, thereby performing a change of multiplicity

These processes can be summarized in a so-called Jablonski Diagram, illustrated in Figure 2.9. Jablonski was the first to introduce the concept of a "metastable energy level M, situated lower than the level F, reached immediately after absorption".[92] Thereby level M implies the triplet state T_1 that is energetically lower than the excited singlet state S_1 (level F). The Jablonski diagramm gives a good overview over the possible processes that can occur in a photochemically excited molecule. However, it serves only as a simplification. The actual photochemical processes can be more complex. A combination of radiationless transitions, light absorption and emission, vibrational relaxation, and the interaction with other nearby species by collision can play a role in the conversion of energy.

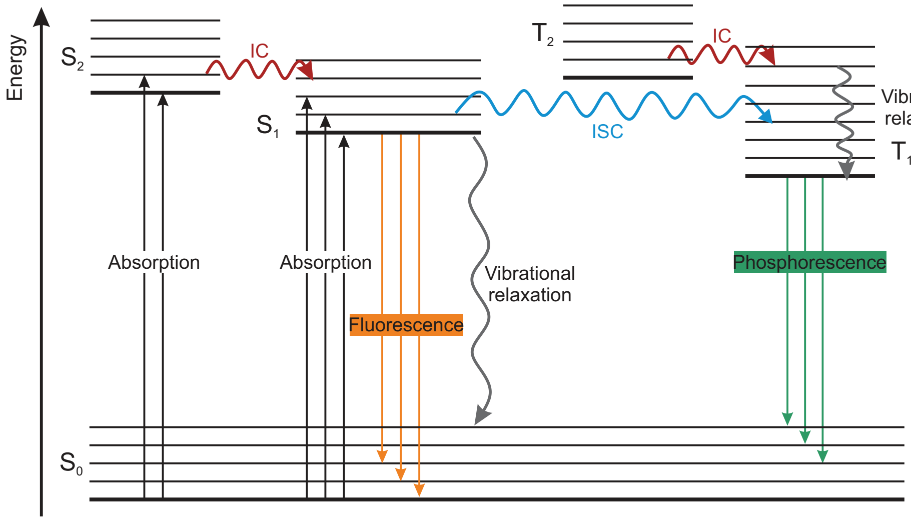

Figure 2.9.: Possible electronic and vibrational transfers for a molecule summarized in a Jablonski diagram. Absorption and emission of light are illustrated by straight vertical arrows. Radiationless transitions are displayed by horizontal wavy arrows.

Internal Conversion and Intersystem Crossing

The radiationless transitions internal conversion (IC) and intersystem crossing (ISC) occur between isoenergetical vibrational levels of two different electronic states. During the transitions, no change in energy occurs and no photon is emitted. IC occurs between two states of the same multiplicity (singlet-singlet or triplet-triplet) and at crossing points of two potential energy curves. After the very fast IC process (on the ps time scale), the system can perform vibrational relaxation and transform the photochemical energy into heat. A molecule in an excited singlet state can also perform an ISC to reach an excited triplet state and subsequently relax through vibrational energy output to an energetically lower state. Since the multiplicity changes during ISC, this process is a forbidden spin transition and thus occurs less likely than IC. The time range of ISC is on the picoseconds scale.

Fluorescence and Phosphorescence

Fluorescence and phosphorescence are both luminescence processes that allow a system to reach an energetically lower state via the emission of light. Fluorescence is a fast transition between an excited singlet state and a ground singlet state. Since no change in multiplicity takes place, unlike for phosphorescence, fluorescence occurs on a short timescale (in the range of nanoseconds). A system in an excited triplet state can perform phosphorescence to reach the singlet ground state. The system emits light and changes its multiplicity from singlet to triplet. Since the latter is a forbidden spin transition, phosphorescence occurs on a much longer timescale than fluorescence and is less likely. Both fluorescence and phosphorescence are subject to the Kasha-Vavilov rule,[93] stating that the quantum yield of luminescence is independent of the excitation wavelength. The reason for this effect is that excited molecules usually decay to their lowest vibrational level of the electronically excited state, before performing luminescence. However, this rule is violated by some molecules.

2.3.2. Franck-Condon Principle

Upon absorption of a photon, a molecule performs vibronic transitions, i.e., it changes its vibrational and electronic states simultaneously. The intensity – and thus probability – of such vibronic transitions is governed by the so-called Franck-Condon principle,[94,95] stating that, during an electronic transition, a change in the vibronic state occurs more likely with a stronger overlap of the two vibrational wave functions. The principle assumes that an electronic transition occurs while the position of the molecules' nuclei remains steady, resulting in vertical transitions in the energy diagram, illustrated in Figure 2.10. Changes in the electronic states are instantaneous while the vibrational levels take up an equilibrium state on a much larger time scale, changing the bond length of the electronically excited molecule. After the electronic transition, the molecules immediately begin relaxation into their lowest state. If the molecule is dissolved in a solvent, its environment has an important impact on the relaxation time due to the interaction between solute and solvent species.

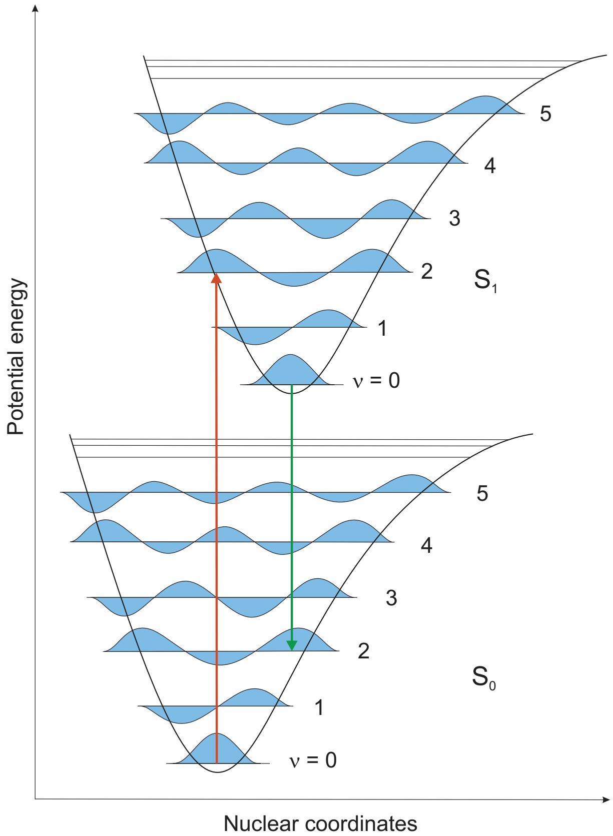

Figure 2.10.: Diagram illustrating the Franck-Condon principle. Electronic transitions appear as vertical transitions, while the nuclear coordinates remain steady. The transitions occur between electronic states with the highest overlap of the vibrational wave functions (image adapted from ref.[96] ©Wiley-VCH Verlag GmbH & Co. KGaA, reproduced with permission).

2.3.3. Excited States

A molecule in its ground state has certain properties, such as energy content, bond strength and length, ionization potential, distribution of charge, a tendency to structural rearrangements, and many more. These properties depend on the electronic structure within a molecule, i.e., on the distribution of electrons in the molecular orbitals.[97] A molecule in its excited state underwent an electronic transition and, thus, changed its distribution of electrons. Therefore, an excited state should be considered as a new chemical species, not just a species with a higher energy content. Excited states have a transient character, since they are created by an external stimuli and can be quenched (deactivated) in a multitude of ways. Their reactivity thus depends strongly on the accessibility of various deactivation pathways. If no bimolecular deactivation takes place, the decay of the excited state occurs with a first-order rate coefficient k, defining the lifetime τ of the excited state:

$$\tau = \frac{1}{k} \tag{2.2}$$

Typical lifetimes can range from 10^{-12}-10 s and can be measured by detecting the decay of a certain property such as the emission intensity, for instance by femtosecond spectroscopy (see 2.7). The higher energy content of the excited state can be used for performing chemical reactions that afford a higher activation energy. An example for the conversion of light into chemical energy is natural photosynthesis.[2,97]

2.3.4. Molecular Electronic Transitions

The electrons that perform transitions in an irradiated organic molecule originate mostly from 2s and 2p orbitals of the carbon atoms. Their interaction in a molecular bond results in the formation of bonding σ and π, non-bonding n, and anti-bonding σ^* and π^* orbitals. If heteroatoms such as oxygen, nitrogen, or halogens are present, electrons (lone pairs) that are not involved in bond formation, occupy non-bonding orbitals and are referred to as n orbitals. The lowest energy transition that an electron in an irradiated molecule can perform is the excitation from the highest occupied molecular orbital (HOMO) into the lowest unoccupied molecular orbital (LUMO). Due to the presence of σ, π, and n orbitals, several electron transitions can be observed and will be described in the following.[10,98,99]

σ to σ^* transitions are performed between the highest bonding electron pair (σ) and the lowest antibonding electron pair (σ^*) and are observed mainly for saturated hydrocarbons. Their absorption can be found below 190 nm.

n to π^* transitions can be observed if free electrons, that are likely to occupy the HOMO, are present. Due to the spatial separation between n and π orbitals and the resulting poor overlapping, transitions between localized n orbitals and delocalized π^* orbitals are forbidden. Hence, nπ^* transitions show a week intensity with molar extinction coefficients of ε = 5-200 L·mol^{-1}·cm^{-1}.

π to π^* transitions occur in molecules in which π electrons are involved in bond formation, for instance in aromatic systems. The energy of $\pi\pi^*$ transitions (the energy gap) decreases with increasing length of the conjugated system of the molecule. Typical molar exctinction coefficients are in the range of ε = 10-10^5 L·mol^{-1}·cm^{-1}.

Charge-Transfer (CT) transitions can be observed in strongly polarized molecules with delocalized molecular orbitals. Upon excitation, the energy is delocalized over the entire molecule. Typical molar extinction coefficients are very high and the absorption is red-shifted compared to non-polarized molecules.

In Figure 2.11, the different absorption ranges for the aforementioned transitions are illustrated.

2.3.5. Beer-Lambert's Law

The Beer-Lambert's law describes the attenuation of a light beam on its way through a medium containing a light absorbing species, depending on the concentration of the species and the

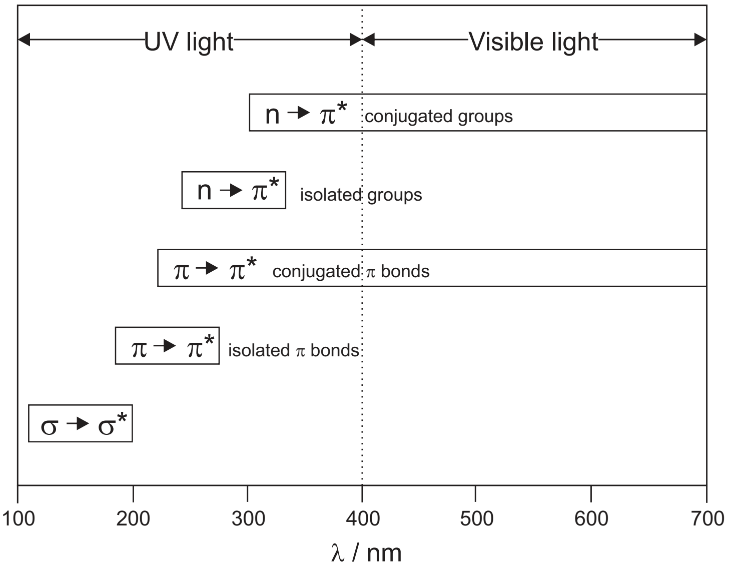

Figure 2.11.: Illustration of the absorption wavelengths for the main electronic transitions in organic molecules (image adapted from ref.[99]).

length of the pathway. It is used for the determination of the extinction coefficient ε_λ, a parameter that describes the ability of a molecule to absorb light at a certain wavelength and can be described by Equation 2.3.

$$lg\left(\frac{I_0}{I}\right) = \varepsilon_\lambda \cdot c \cdot d \tag{2.3}$$

Thereby, I_0 is the light intensity before and I the light intensity after passing through the medium, c is the concentration of the absorbing species, and d is the distance that the light is passing on its way through the medium.

2.3.6. Photochemical Processes in a Photoinitiator

Photoinitiators are expected to have a high quantum yield and to form a large amount of reactive radicals. Therefore, fluorescence and phosphorescence are not desired. Low rates of IC as the main deactivation pathway and high ISC rates are favored, since radicals are formed from an excited triplet state. A high absorbance of the photoinitiator is preferred, since it reflects how many photons of a certain wavelength can be absorbed. As will be shown in the further course of this work, the absorbance alone is not sufficient for determining the quality of a photoinitiator. The main electronic transitions that can be encountered for photoinitiators are nπ^* and $\pi\pi^*$ transitions, whereas $\sigma\sigma^*$ transitions are rarely found. The dissociation into two radicals after photochemical excitation (photodissociation) occurs favorably in molecules with a localized excitation energy. The latter is given for nπ^* states. Thus, photodissociation into radicals is mostly performed after initial nπ^* transitions.[10] Furthermore, triplet states are favored for photodissociation due to their longer lifetimes (μs) compared to singlet states (ps). On the other hand, $\pi\pi^*$ transitions do not lead to photodissociation.

In order to form a high amount of radicals, the rate of ISC should be high. The El-Sayed rule[97,100] describes that the rate of ISC is high if a change in orbital type is involved during the transition and is illustrated by:

$$^{1}(n\pi^{*}) \longleftrightarrow^{3} (\pi\pi^{*}) \qquad ^{3}(n\pi^{*}) \longleftrightarrow^{1} (\pi\pi^{*}) \qquad \textbf{allowed}\text{ processes} \tag{2.4}$$

$$^{1}(n\pi^{*}) \longleftrightarrow^{3} (n\pi^{*}) \qquad ^{1}(\pi\pi^{*}) \longleftrightarrow^{3} (\pi\pi^{*}) \qquad \textbf{forbidden}\text{ processes} \tag{2.5}$$

Additionally, the energy gap between the states involved in ISC is crucial for the rate. The ISC rate decreases exponentially with increasing energy gap.[101]
The reactive excited states of ketones and aldehydes (structures in typical photoinitiators) are the $^{1}(n\pi^{*})$ and $^{3}(n\pi^{*})$ states. After ISC, most of photoreactions originate from the $^{3}(n\pi^{*})$ state. The $n\pi^{*}$ state of a C=O group of a photoiniaitor can be described in the simplest way as a non-bonding n orbital localized at the oxygen atom and an anti-bonding π^{*} orbital delocalized over the carbon and oxygen atom. The $n\pi^{*}$ state can have a $\pi\pi^{*}$ character, if other $\pi\pi^{*}$ states with similar energy and equal multiplicity are in close proximity. Such a mixed character can affect the reaction rate. However, it does not affect the reaction type. During the radical fragmentation, referred to as Norrish Type I reaction, the C=O bond cleaves homolytically in α-position. Thereby, the half-filled n orbital, localized at the oxygen atom, serves as an electrophilic site, accepting an electron from the C-H bond. The cleavage results in the formation of two radicals, as illustrated in Figure 2.12.

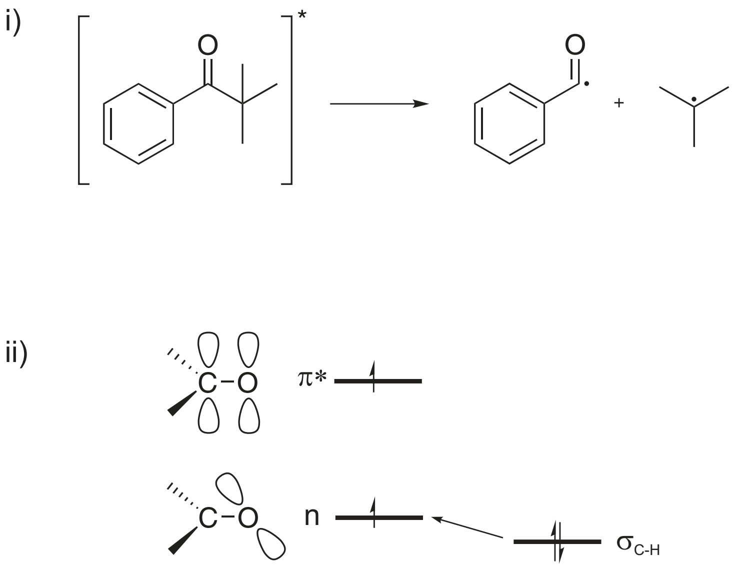

Figure 2.12.: Illustration of the Norrish Type I reaction, i), and the corresponding transition of an electron from the C-H bond to the non-bonding n orbital of the oxygen atom, ii), image adapted from ref.[97] ©Wiley-VCH Verlag GmbH & Co. KGaA, reproduced with permission.

2.4. Lasers

Laser is an abbreviation for *light amplification for stimulated emission of radiation* and is a light source that emits monochromatic and coherent radiation of variable wavelength and energy. The light beam consists of a continuous wave (cw laser) or consecutive laser pulses (pulsed laser) with very short time periods between the pulses (10^{-6}-10^{-15} s). A large range of different laser types, differing in wavelength, energy output, and amplification medium has been developed in the past decades. However, the working principle remains the same and is based on a stimulated emission of photons that can only occur in the case of a *population inversion*, i.e., a state at which more species exist in their excited state than in their ground state. Stimulated emission takes place when an excited species A* interacts with a photon and, while emitting two photons, returns to the ground state A.

$$A^* + h\nu \rightarrow A + 2\,h\nu \tag{2.6}$$

For a two-level system, the concentration of excited states A* is negligible compared to species A in their ground state, as described by the Boltzmann distribution

$$\frac{N_1}{N_0} = exp\left(\frac{-\Delta E}{k_B T}\right) \tag{2.7}$$

where N_1 and N_0 are the populations of the excited state and the ground state, respectively. The energy gap between the two states is given by ΔE and the Boltzmann constant and the temperature by k_B and T. N_1 can thus never become larger than N_0. Therefore, the absorption of a photon occurs mainly by species A. However, if population inversion is achieved, the concentration of A* is higher than of A and stimulated emission can occur. In order to achieve the latter, a three-level or four-level laser system is necessary, as illustrated in Figure 2.13.

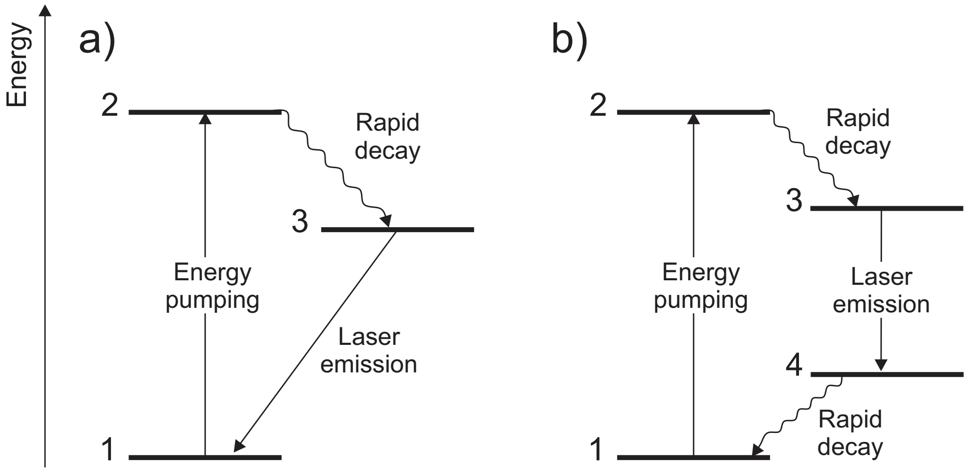

Figure 2.13.: Schematic illustration of a three-level, a), and a four-level laser system, b), image adapted from ref.[97] ©Wiley-VCH Verlag GmbH & Co. KGaA, reproduced with permission.

In a three-level laser the population inversion is achieved after excitation of the system and a subsequent rapid decay, for instance through internal conversion or intersystem crossing into a third state that is energetically lower than the excited state and has a relatively long lifetime, compared to state 2. As soon as the population of state 3 exceeds that of the ground state (see Figure 2.13), spontaneous emission from state 3 triggers stimulated emission and thus light amplification. In a four-level laser the system does not return into the ground state after the stimulated emission, but into a fourth level – energetically higher than the ground state – that is scarcely populated. Four-level lasers are thus more efficient than three-level systems. An example for a three-level laser is the ruby laser with dispersed Cr^{3+} ions in Al_2O_3 in the shape of a glass rod. The emitted light is in the visible range and has a wavelength of 649 nm. The Nd:YAG laser is an example for a four-level laser system that uses dispersed Nd^{3+} ions in a $Y_3Al_5O_{12}$ crystall, called YAG (= yttrium aluminum garnet). Its emission wavelenth is 1064 nm and is located in the IR range. Both, Cr^{3+} and Nd^{3+} ions are pumped by a flash lamp into upper excited states that decay rapidly into energetically lower states with a longer lifetime. In order to produce a coherent laser beam, a special setup is utilized (see Figure 2.14): the active laser material is placed between two mirrors, of which one is entirely reflecting and one is partially reflecting (approx. 1%). An energy source, such as a flash lamp, is employed to "pump" the laser material into an excited state and hence achieve the population inversion. The photons emitted by stimulated emission propagate along the axis of the two mirrors, resulting in a collimated laser beam that can emerge through the partially reflecting mirror to the outside.

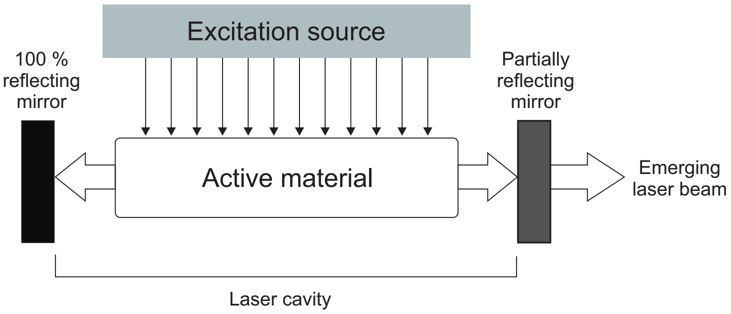

Figure 2.14.: A schematic illustration of a laser setup, image adapted from ref.[97] ©Wiley-VCH Verlag GmbH & Co. KGaA, reproduced with permission.

Due to the propagation of the photons between the mirrors in the laser cavity, the length L of the cavity has a strong impact on the wavelength λ of the outcoming laser beam, described by

$$L = n\frac{1}{2}\lambda \tag{2.8}$$

with n being an integer. Another popular laser type is the excimer laser (also called exciplex laser) employing a gas mixture as the active material. An excimer is an excited dimer and can only exist in its excited state. Therefore, the population inversion is given by the lack of an occupied ground state. Excimers are formed by a halogen and a noble gas, for instance $XeF\cdot$ from a mixture of Xe and F_2, after an excitation pulse conducted by an electrical discharge. Excimer lasers usually emit light in the UV range, yet the exact wavelength is depending on the used molecules. A $XeF*$ laser operates at a wavelength of 351 nm.

Femtosecond Lasers

Femtosecond lasers are so-called ultrashort pulse lasers with pulse lengths in the domain of picoseconds to femtoseconds (10^{-12}-10^{-15} s). Ultrashort pulse lasers are Ti:Sapphire lasers, using Ti^{3+} ions in a Al_2O_3 corundum structure as the amplifying medium. In order to achieve ultrashort pulses a mode-locking is employed that forces all the modes inside the laser cavity to interfere contructively in one point and form an intense and ultrashort pulse. This self-focusing of the laser beam is based on the Kerr effect that uses the change of the refractive index of a medium when an electric field is applied.[102,103] In contrast to laser pulses longer than femtoseconds or cw lasers, the bandwidth of femtosecond lasers is larger. In analogy to the uncertainty principle

$$\Delta x \cdot \Delta p \geq \frac{\hbar}{2} \tag{2.9}$$

the laser pulse length can be written in relation to its frequency width as

$$\Delta \omega \cdot \Delta t \approx \frac{\hbar}{2} \tag{2.10}$$

Thus, the bandwidth of an outgoing laser beam becomes larger with shorter pulse duration. Such short laser pulses are employed for instance for the investigation of molecular processes on a short timescale, such as the relaxation of a molecule upon absorption of a photon.

2.5. Mass Spectrometry

Mass spectrometry is an analytical technique that generates ions from organic (or inorganic) compounds by variable methods, separates the ions according to their mass-to-charge ratio (m/z) and detects them in respect to their m/z and their abundance in the sample. The analyte may be ionized in different ways, such as by a laser beam, an electric field, or an electron beam. The detected ions can be single atoms, atom clusters, molecules or fragments of the analyte. A mass spectrometer consists of the following basic components: an ion source, a mass analyzer, and a detector. All three components can be varied depending on the character of the analyte, thus mass spectrometry is one of the most versatile and important analytical methods. The mass-to-charge ratio m/z is dimensionless by definition, since the dimensionless mass number m and the number of the elementary charge z is used. The analyte is mostly singly charged ($z = 1$), yet depending on the constitution of the analyzed molecule it can be up to two, three, or even four. If the charge is one, m/z directly corresponds to the molecular weight of the analyte. In the following the three main components of a mass spectrometer will be described briefly, thereby the focus will be placed on mass spectrometry in the field of polymer chemistry. A detailed discussion can be found in the literature.[104–106]

2.5.1. Ionization Methods

A mass analyzer can only handle charged species that have been produced from neutral atoms, molecules, or, in some cases, radicals. Therefore, ionization is the first step on the way to a mass spectrum and a wide range of different techniques has been developed in the past decades. However, for the analysis of polymers, only two techniques are commonly used: electrospray ionization (ESI)[107] and matrix-assisted laser desorption ionization (MALDI).[108,109] Both methods are "soft" ionization techniques, i.e., not leading to a fragmentation of the analyte as it is the case for ionization via electrons. In the following, the ESI process will be explained in detail.

Electrospray Ionization

The process of electrospray ionization[104,105,110] (ESI) begins with the transfer of the analyte solution, typically in a solvent mixture such as THF/methanol or DCM/methanol with approx. 100 μM of salt (for instance sodium tetrafluoroacetate), through a capillary that is held at a high potential (approx. 4 kV). The latter results in the formation of highly charged solvent droplets and a so-called Taylor cone, an elliptically shaped solvent cone at the outlet of the nozzle, as illustrated in Figure 2.15. The electrostatic force pulls out liquid and droplets from the nozzle as an aerosol. If a positive ΔV is applied, the droplets contain an excess of positive charge, thus leading to positively charged molecules. A negative ΔV leads to negatively charged analyte molecules. Usually, an additional coaxial gas flow, such as nitrogen, is used in order to promote nebulization. The solvent evaporates from the droplets into the ion chamber at atmospheric pressure until the charge on the outsideof the droplet reaches a limit at which the repulsive forces between equal charges exceed the cohesive forces of the solvent, the so-called Rayleigh limit:[110]

$$Q_R = 8\pi \left(\varepsilon_0 \gamma {R_R}^3\right)^{\frac{1}{2}} \tag{2.11}$$

where Q_R is the number of surface charges on droplets with the radius R_r, ε_0 being the permittivity of the solvent and γ the liquid surface tension. At this point consecutive coulombic explosions lead to the reduction of droplet sizes and finally the formation of unsolvated charged polymer molecules, carrying one or sometimes two ions of the salt that was added to the analyte solution. The polymer molecules are then introduced through the skimmer into the mass analyzer as an ion beam. The ions are accelerated by the electric field on their way to the skimmer where they enter the mass analyzer (see 2.5.2). The ions can be described as $[P + zCation]^{z+}$ or $[P + zH]^{z+}$, for the case of proton ionization, with z being the number of the charge. Cations are assumed to locate themselfs along the backbone of the polymer chain or, if such groups are present in the polymer, on polar functionalities such as hydroxy groups. Proton ionization can occur on sites with high Lewis basicity, for instance on amine groups.[105] The addition of salt to the analyte solution and the choice of solvent can have a major impact on the ionization process. However, the exact influence of the single parameters is not yet fully understood.[111,112]

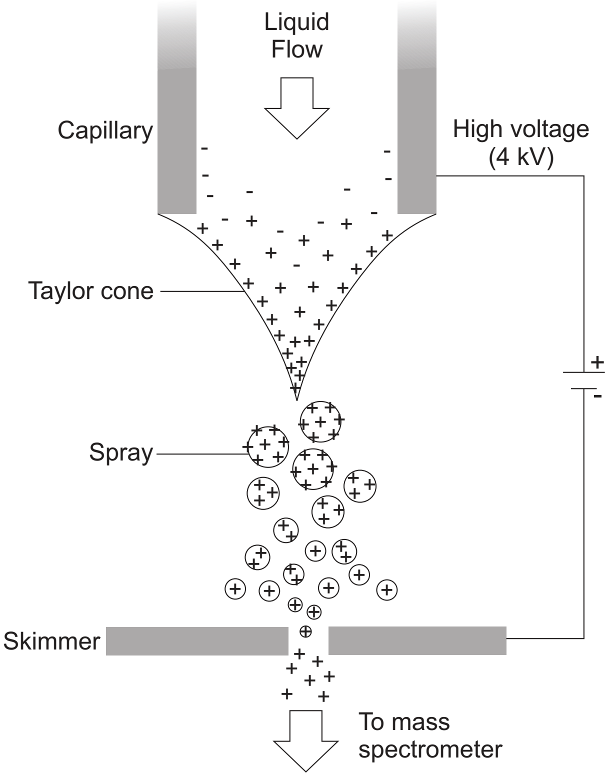

Figure 2.15.: The electrospray ionization process for positively charged molecules in a schematic illustration (adapted from ref.[110] ©2002 American Chemical Society).

2.5.2. Mass Separation

The ion source is not only producing an ion beam that can enter the mass analyzer. Based on the applied electric field it also imports a kinetic Energy E_{kin} to each ion. As soon as the ions pass the skimmer, they enter a field-free region. Various methods have been developed in order to separate the ion beam according to the mass of the ions, such as the time-of-flight (TOF) analyzer, the quadrupole ion trap, and the orbitrap. In the following each of these methods will be introduced briefly.

Time-of-Flight

The principle of the time-of-flight (TOF) analyzer[104,113] is based on the fact that all ions entering the mass analyzer at a certain point have the same kinetic energy. On their way to the detector they pass a pathway of the same length, thereby the lighter ions will arrive earlier at the detector than the heavier ions, as illustrated in Figure 2.16. This techniques demands for a pulsed ion beam, as provided by MALDI. The kinetic Energy E_{kin} that the ions gain during their acceleration equals the energy uptake E_{el} based on the applied electric field with the voltage U being

$$E_{kin} = \frac{1}{2} m_i v^2 = zeU = E_{el} \tag{2.12}$$

with z being the integer number of electron charges e. When assuming that the ions were in rest before acceleration, the approximation for their velocity when entering the mass analyzer yields

$$v = \sqrt{\frac{2ezU}{m_i}} \tag{2.13}$$

Knowing the length of the pathway s through the mass analyzer to the detector and the time t the ions need to cross the mass separator, the ion mass m_i can be determined with

$$t = \frac{s}{\sqrt{\frac{2ezU}{m_i}}} \tag{2.14}$$

and hence the ratio m_i/z with

$$\frac{m_i}{z} = \frac{2eUt^2}{s^2} \tag{2.15}$$

Disadvantages of the TOF mass analyzer are their relatively large size and their limitation toward pulsed ion formation. However, their high abundance sensitivity and their (theoretically) unlimited mass range (> 100 000) are beneficial.

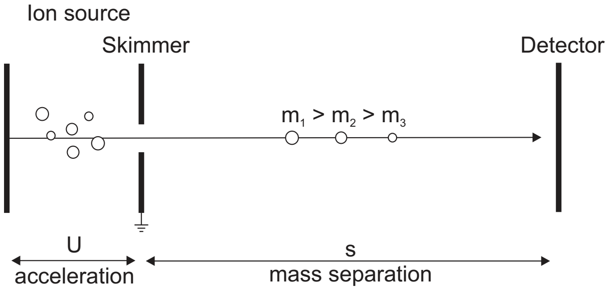

Figure 2.16.: A schematic illustration of the TOF process, separating masses by their flight time through the mass analyzer (adapted from ref.[104] with permission of Springer).

Quadrupole Ion Trap

A quadrupole ion trap consists of four cylindrical electric rods mounted in a square configuration (xy-plane) and extending into the z-direction. Opposite rods are electrically connected and carry the same potential, respectively. The applied voltage consists of a direct current (DC) voltage U and a radiofrequency (rf) voltage V with the frequency ω. The total potential Φ_0 is thus given by

$$\Phi_0 = U + V cos\omega t \tag{2.16}$$

for the x- as well for the y-axis. Ions are accelerated in the z-axis before entering the quadrupole in which they experience an electrical field combined from the two rod pairs, carrying opposite polarity, as illustrated in Figure 2.17. Cations are drawn towards the negatively charged rods and anions vice versa. If the rods change their sign of polarity periodically, before the cation hits the rod surface and thus discharges, the ion is held at a constantly oscillating distance and crosses the quadrupole along a z-trajectory towards the detector. The frequency of change in current determines if the ions can pass the quadrupole rods or if they collide with the electrodes. For each ion mass a set of U, V, and ω exists that enables the ions to pass the ion trap and hit the detector. The quadrupole scans the sample for each m/z value and thus acts as a mass filter. The relatively low costs and space requirements of a quadrupole mass analyzer are beneficial. However, the relatively low mass range (up to 4000) and the low mass resolution (up to 1000) limit their application.

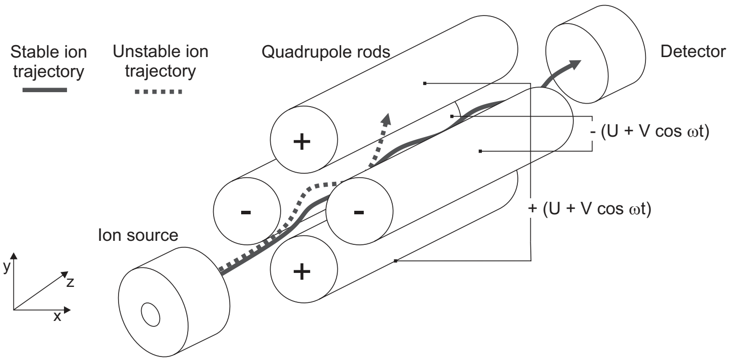

Figure 2.17.: A schematic illustration of the quadrupole ion trap, acting as a mass filter by periodically changing the sign of polarity of the electric rods, the path of the ions is represented by grey lines (adapted from ref.[105], ©Wiley-VCH Verlag GmbH & Co. KGaA, reproduced with permission.).

Orbitrap

The orbitrap is the newest technique to analyze ion masses, providing very high resolutions. In the orbitrap the ions are trapped on radial trajectories around a central spindle electrode, surrounded by an outer coaxial barrel-like electrode, as illustrated in Figure 2.18. The ions – injected tangentially to the inner electrode – are orbitally trapped around the latter producing an electric field with a frequency proportional to their $m/z^{0.5}$, independent of their energy and spatial spread. The ion frequencies are measured at the inner electrode by the acquisition of image current transients in the time-domain and are processed by fast Fourier transformation (FFT) into a frequency-domain signal, in order to obtain a mass spectrum.[105,114,115] Unlike the quadrupole ion trap the orbitrap does not apply magnetic or rf fields, but utilizes solely an electric field to trap the ions.

Resolutions of up to 150 000[115] can be achieved using an orbitrap, placing it among the most powerful instruments available today. Further advantages of an orbitrap are their high abundance sensitivity, small size, and moderate cost.

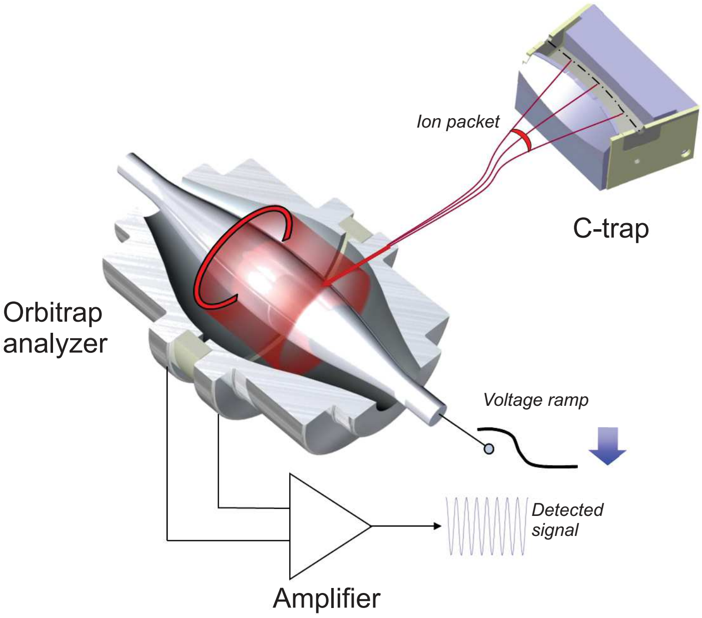

Figure 2.18.: Illustration[1] of the orbitrap: the red lines symbolize the pathway of the ions around the inner electrode, trapped electrostatically.

2.5.3. Collision-Induced Decay

Ions that have been trapped by a mass analyzer, such as a quadrupole or an orbitrap, can be isolated and bombarded with neutral gas atoms (He, Ar, or N_2) in order to induce a decay in the molecular structure of the ion and to detect characteristic fragments of the analyte. Such a collision-induced decay (CID) can help to elucidate the structure of a molecule, for instance giving information about functional groups that where cleaved off during the collision. The bombardment energy can be changed by varying the kinetic energy of the gas atoms.

2.5.4. Resolution and Mass Accuracy

The ability of a mass spectrometer to obtain sharp signals and exact m/z values is of crucial importance for the investigation of reactions and the elucidation of a molecules' structure. The separation of neighbouring peaks is defined as the *resolving power* or *resolution*. The resolution R is specified by the ratio of the measured mass m and the difference in mass Δm, defined as the peak width at a specific peak height.[104]

$$R = \frac{m}{\Delta m} \tag{2.17}$$

A high resolution is frequently confused with a high mass accuracy. However, a measurement that was performed at high resolution does not necessarily imply measuring the accurate mass. Mass accuracy is defined as the difference between the measured mass and the calculated exact mass of a molecule and can be given by absolute values (in atomic mass units amu) or in relative mass accuracy in ppm. The orbitrap (2.5.2) is a mass spectrometer with a high resolution as well as a high mass accuracy and serves as a powerful tool for investigating the mechanistic aspects of a reaction.

---

[1] Image from Thermo Fisher Scientific

2.5.5. Mass Spectrometry on Polymers

Soft ionization techniques such as ESI and MALDI enabled the application of mass spectrometry for polymers, due to their non-destructive character and tolerance toward high molecular weights. The exact determination of the polymer mass gives valuable information about its structure. Thus, the polymer end groups, i.e., the initiating fragment as well as termination event can be undoubtedly determined. Therefore, the application of mass spectrometry plays a paramount role in the mechanistic investigation of a polymerization.[116] The mass spectrum of a polymer is entirely different compared to a small molecule. The distributive character of a polymer is reflected in its mass spectrum, which is comprised of a multitude of peaks with a mass difference corresponding to the monomer mass. Thereby, each peak – given the synthesis was carried out by radical polymerization – gives information about which event led to the termination of the polymer chain. Polymer chains terminated by combination show peaks with a classical staircase-like pattern, caused by the different number of heavy isotopes (^{2}H and ^{13}C) that chains with a certain length contain. Polymer chains terminated by disproportionation can be identified by their characteristic peak clusters, consisting of two peaks (each of them showing the staircase-like pattern) with a mass difference of 2 Da. The signal is comprised of both double bond-carrying and proton-carrying polymer chains resulting from the disproportionation reaction. These clusters have the characteristic shape that can be described as "high-low-very high-low" and can be readily identified in a mass spectrum. In case the analyzed polymer was synthesized by ATRP (see 2.1.3), the polymer chain is terminated with a bromine group in ω-position. Due to the two isotopes of bromine (^{79}Br and ^{81}Br) with nearly equal abundance, the peaks of bromine-terminated polymers exhibit a typical shape, similar to disproportionation peaks, described as "high-low-high-low".

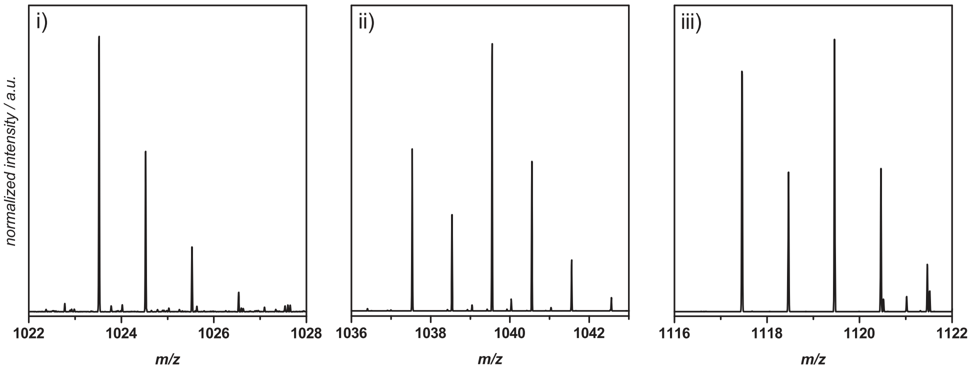

Figure 2.19.: Comparison of the characteristic peak patterns of i) combination products, ii) disproportionation products, and iii) bromine-terminated polymer chains in a mass spectrum.

Mass spectrometry is not only used for analyzing the molecular structure of a polymer, but also for the determination of the reaction progress and conversion, for instance for end group modifications. Thereby, the height or the integral of the starting material peak as well as the product peak are monitored with reaction time. This technique has been applied for the monitoring of for instance polymer conjugation reactions based on photoenol click chemistries,[117] end group modifications via azirines,[118] or NITEC chemistry.[119]

However, the quantitative determination of a reaction conversion by mass spectrometry should always be treated with caution. The ionization behavior of a molecule is strongly dependent on its functional groups and can vary immensely with (apparently) small variations in the molecular structure. For polymers it has to be considered that not only the polymer backbone is of high importance for the ionization, yet also the structure of the end groups. A major change in the electronic structure of the polymer end group during the investigated reaction can lead to a strongly increased or decreased ionization ability, leading to falsified conversion results. Thus, quantitative mass spectrometry can only be applied for polymers with identical polymer backbones and similar end groups.

Another important application of mass spectrometry was shown by Gruendling *et al.* for the determination of accurate and absolute molar mass distributions as well as the absolute concentrations for individual polymer compounds in their respective mixtures.[120,121] Thereby, polymers with the same backbone, i.e., consisting of the same monomer, yet different end groups could be separated and their concentration in the mixture was determined by the online coupling of size exclusion chromatography and ESI-MS (SEC-ESI-MS), combined with a data processing algorithm that is based on the maximum entropy principle. In detail, an analytic run by SEC-ESI-MS gives two data streams. On the one hand, the signal detected by the RI detector of the size-exclusion chromatogram gives a total mass concentration of polymer $S(V_R)$ in the eluent at the elution volume V_R. On the other hand, the mass spectrometer detects a data set consisting of the total ion count for a certain m/z range at a specific elution volume V_R, giving so-called single oligomer profiles (SOP's). Tung's equation describes the relationship between the signal $S(V_R)$ of the RI detector and the total mass weighted molar mass distribution $w_{tot}(n)$ of a polymer mixture:

$$S(V_R) = \int_1^\infty G(V_R, n) w_{tot}(n) dn \tag{2.18}$$

with $G(V_R, n)$ as the calibration and broadening function of the chromatographic system. Based on an algorithm, the molar mass distribution w_i of a single species is subsequently calculated. For a detailed discribtion of the calculation process, the reader is referred to literature.[120,121] With the described procedure, binary and ternary mixtures of pMMA polymers can be analyzed regarding their individual concentration.

Mass spectrometry plays a significant role in the current work. As described in the following section, ESI-MS was employed for the comparison of initiation efficiencies of radical photoinitiators and for the mechanistic investigation of photoinitiated RDRP (see section 2.1.3).

2.6. Investigation of Photoinitiated Polymerizations via PLP-ESI-MS

Polymerizations initiated by radical photoinitiators result in polymers that carry the initiating fragment in α-position and the corresponding terminating group (depending on the termination type) in ω-position. For monomers such as methyl methacrylate (MMA), undergoing disproportionation as the preferred termination event, the resulting polymer chains are highly uniform. Additionally, poly(methyl methacrylates) (pMMA) posses a multitude of polar groups, resulting in a high ionizability, making it an ideal polymer for analysis by mass spectrometry. Both properties help in the investigation of photoinitiated polymerization processes, due to the uniformity of the resulting products and the facile determination of their molecular structure. The actual initiating fragment that commenced the growth of the polymer chain, can be readily identified. The initiation performance of photoinitiators can thus be compared based on their relative incorporation propensity into the chain termini. Thereby PLP-ESI-MS, the combination of PLP (see 2.2) for polymer synthesis and ESI-MS for the analysis of the polymer chains, serves as a powerful tool for the investigation of photoinitiation mechanisms and the initiation ability of photoinitiators.[122–129]

For the quantitative investigation of photoinitiation abilities of radical fragments, PLP-ESI-MS was employed for the first time by Günzler *et al.*[122] for the comparison of the two photoinitiators benzoin (2-hydroxy-1,2-diphenylethanone) and mesitil (1,2-dimesitylethane-1,2-dione), illustrated in Figure 2.20. Thereby it was shown that, at an excitation wavelength of 351 nm, the mesitoyl radical shows a 8.6 times lower initiation ability compared to the benzoyl radical generated by benzoin. This observation was even more surprising as mesitil shows a 10-fold higher absorbance at the excitation wavelength than benzoin. Intuitively, a higher initiation ability would be expected for mesitil.

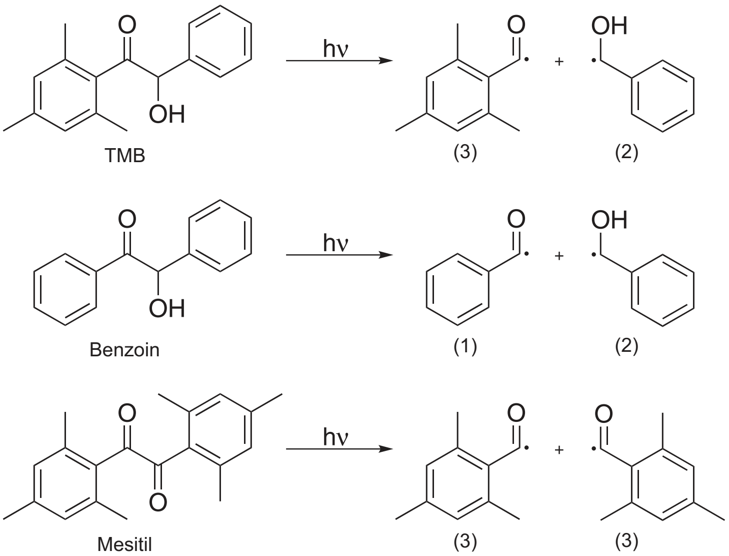

Figure 2.20.: The three photoinitiators TMB, benzoin, and mesitil that where compared regarding their initiation efficiency (by Günzler *et al.*[122]) and the origin dependence of the initiating fragment trimethylbenzoyl (3) by Voll *et al.*[123]

Subsequently, an investigation was carried out determining whether the initiation ability of the initiating radical fragment is origin dependent. Therefore, a so-called cocktail experiment was performed with 2,4,6-trimethylbenzoin (TMB), benzoin, and mesitil as the photoinitiators.[123] The mesitoyl fragment (3), originating from TMB was demonstrated to be less effective in intiating a polymerization compared to the benzoyl fragment (1), yet, only by a factor of 3. Thus, not only the radical fragment, but its originating photoinitiator structure determines the initiation ability.

In a further study[124] the contribution of methyl substitution on the initiation efficiency of a benzoyl radical fragment was investigated, analyzing six different photoinitiators with an increasing number of methyl substituents at the benzoyl group, as illustrated in Figure 2.21. Thereby, all six photoinitiators were irradiated in an equimolar ratio in a PLP experiment with MMA. The resulting polymer mixture, containing polymer chains carrying six different chain termini, was analyzed by ESI-MS. The chain with the highest peak intensity was correlated with the highest initiation efficiency for the corresponding initiating fragment. It was found that 28% of all chains were initiated by the benzoyl fragment of benzoin, 27% by the corresponding fragment of A, 22% by B, 11% by C, 4% by D, and 9% by E.

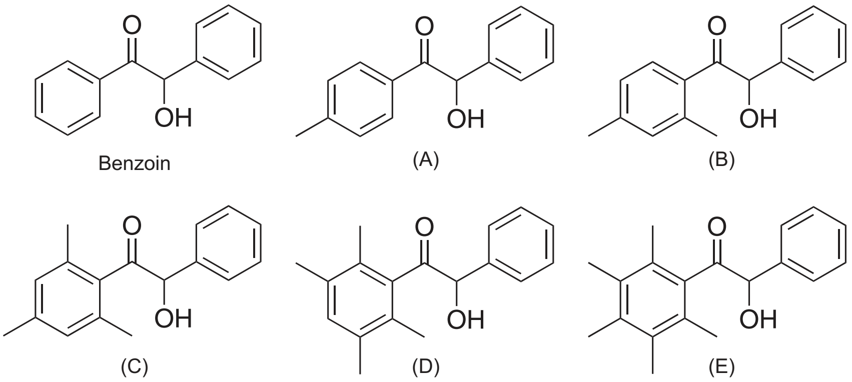

Figure 2.21.: Benzoin-type photoinitiators with an increasing number of methyl substituents at their benzoyl group that were investigated regarding their initiation efficiency by Voll *et al.*[124]

Next to the initiation efficiency of photoinitiators, the PLP-ESI-MS technique can be employed for mechanistic investigations of photochemical processes, such as light-triggered conversion of polymer end groups. In a study by Voll *et al.*[126] the UV light-induced transformation of benzoin-derived polymer end groups was elucidated. It was found that under UV irradiation the aforementioned benzoyl end group performs a Norrish Type I or a Norrish Type II reaction, resulting in the cleavage of the aromatic end group and the loss of functionality, as illustrated in Figure 2.22. The study was further supported by chemically induced dynamic nuclear polarization-nuclear magnetic resonance spectroscopy (CIDNP-NMR), in order to identify the radical fragments involved in the cleavage.

A related study by Lauer *et al.*[89] investigated the influence of methyl-substitution on the tendency for the aforementioned UV-induced cleavage process. Eight benzoin-type photoinitiators with varying methyl-substitution were employed, whereas only polymer end groups with a methyl group in ortho-position showed no cleavage tendency. Thus, in order to increase the UV light stability of benzoin-type derived polymer end groups, an introduction of a methyl substituent in ortho-position is proposed.

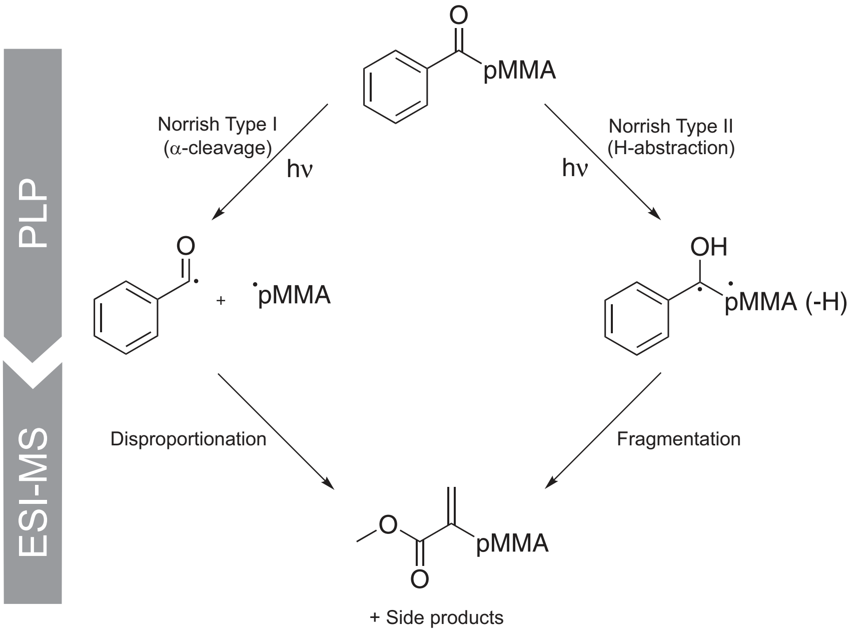
PLP
ESI-MS
pMMA
Norrish Type I
(α-cleavage)
hν
Norrish Type II
(H-abstraction)
hν
O
+
•pMMA
OH
pMMA (-H)
Disproportionation
Fragmentation
pMMA
+ Side products

Figure 2.22.: Overview of the UV light-induced transformation of polymer end groups derived from benzoin, investigated by Voll *et al.*[126] and Lauer *et al.*[89]

2.7. Femtosecond Spectroscopy

The investigation of photophysical and photochemical processes requires a deep understanding of the underlying mechanisms in a molecule upon absorption of light and the character of the resulting excited states (see 2.3.3). Since the evolution of the latter occurs on an ultrafast timescale, time-resolved spectroscopic techniques such as femtosecond (fs) spectroscopy have become an important tool for the elucidation of molecular dynamics. The fs pump-probe absorption spectroscopy gives valuable information about the occuring processes, relaxation channels, and the corresponding lifetimes of a photochemically excited system and will be briefly described in the following.[130,131]

As illustrated in Figure 2.23, in a common fs pump-probe experiment the fs laser pulse is split up into a path to generate a so-called pump pulse and a second path in order to generate a probe pulse. Both pulses are redirected into the measured sample, whereas the probe pulse is passing through an optical delay line before entering the sample in order to enable a time delay of the pulse. As the pump pulse passes through the sample it excites the molecules into a higher electronic state. The subsequent probe pulse penetrates the excited sample and acts as a detector for the proceeding changes of the molecular system after pumping. The delay time between pump and probe pulse can be varied by the delay line in order to monitor the evolution of the excited state with time.

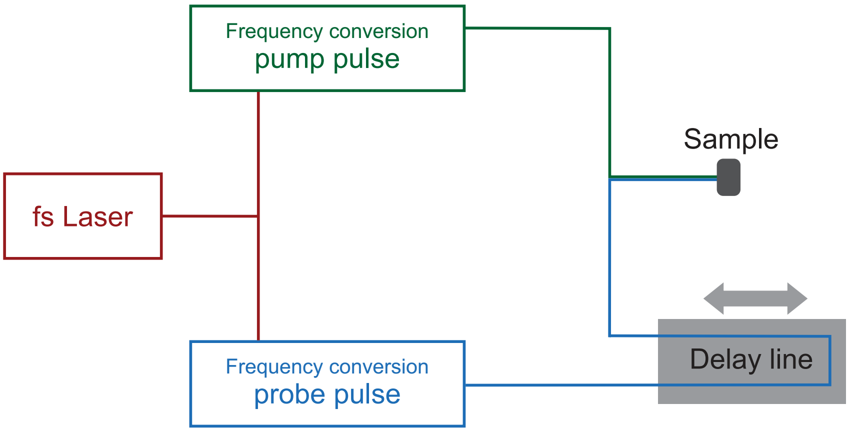

Figure 2.23.: Illustration of the setup of a fs pump-probe experiment, image adapted from ref.[130]

Both pump and probe pulse can be varied in their wavelength range. However, for the probe pulse it is possible to cover a wide spectral region (white light continuum) that gives an overview over the complete wavelengths. The transmission of the excited species is detected by measuring the transmitted light of the sample in the ground state (unexcited) and after the pump pulse (excited). Thereby, the transient absorbance (TA) is measured as the change in optical density ΔOD with time and wavelength of the probe light, described by

$$\Delta OD(\lambda,t) = log\left(\frac{I_0}{I(\lambda,t)}\right) - \Delta OD_0 \tag{2.19}$$

Thereby, $I(\lambda,t)$ is the transmitted light intensity of the excited sample, detected after the pump pulse, and I_0 the time-independent light intensity of the sample, without previous excitation. The change in optical density ΔOD can be positive or negative. If an excited state is absorbing photons of the pump pulse, the resulting ΔOD becomes positive. However, the pump pulse can also lead to the stimulated emission of a photon by the excited state, resulting in a negative ΔOD.

The transient absorption shows the dynamics of the excited states in the samples and, in case α-cleavage occurs, the formation of radicals. However, the termination of photoinitiator radicals has not yet been observed. Radicals originating from triplet states, as is the case for photoinitiator radicals, have to perform a spin flip before being able to recombine. This forbidden process takes place on the timescale of μs and is thus too slow to be observed by fs spectroscopy.[130]

2.7.1. Investigation of Photoinitiators by fs Spectroscopy

Femtosecond spectroscopy has already been successfully applied for the investigation of the dynamics of the three photoinitiators benzoin, TMB, and mesitil (as shown in Figure 2.20)[132] and the results were correlated to the initiation efficiency comparison carried out by PLP-ESI-MS.[123] Thereby, it was found that benzoin and TMB show similar properties regarding their excited state dynamics. Both, benzoin and TMB, perform a rapid ISC after excitation into the S_1 state on a timescale that can compete with fast IC processes. The fast ISC is caused by the presence of an excited triplet state T_n in close energetic proximity, making an ISC the preferred deactivation pathway of S_1. Mesitil, in contrast to benzoin and TMB, is excited into the S_2 state with no available isoenergetic triplet state for ISC. In this case, IC is the main deactivation pathway, resulting in small ISC rates and thus in a small amount of formed radicals. These results could be correlated to the poor initiation efficiency of mesitil found in PLP-ESI-MS experiments. Hence, the efficiency of the ISC process is a crucial parameter for the efficiency of a photoinitiator. This study testified the unique character of the combination of femtosecond spectroscopy and PLP-ESI-MS as a valuable tool for the investigation of photoinitiators.

2.8. Single-Chain Nanoparticles and their Characterization

Single-chain nanoparticles (SCNPs) are three-dimensional structures that are formed by polymers consisting of a single chain.[18] This technology aims at mimicking the behavior of naturally occurring single-chain architectures, such as proteins in their three-dimensional structure, by means of synthetic polymers. Since a side project of the current work focused on the formation of SCNPs on the basis of photoinitiators, some current synthetic approaches for the creation of SCNPs are discussed in the following section, together with suitable characterization methods.

2.8.1. Single-Chain Nanoparticles

The three-dimensional structure of an SCNP can be imparted to single polymer chains by either the collapse of the chain through interactions of functionalities within the side groups (repeating unit folding) or the placement of recognition units at predetermined places along the polymer chain (selective point folding). To this day, single-chain folding was achieved, for instance, by means of mutually orthogonal hydrogen bonding recognition units,[133] reversible disulfide bonds,[134] metal-ligand-complexation,[135,136] or cyclodextrin host-guest chemistry.[137] As an example, the SCNP formation based on the two pairs of mutually orthogonal recognition species thymine and diaminopyridine (three-point interaction) as well as cyanuric acid and Hamilton wedge (six-point interaction) is illustrated in Figure 2.24.[133] The folding and the intramolecular interaction is thereby induced by a high dilution of the single chain. High dilution is a crucial requirement in order to favor intramolecular bonding formation and to avoid the respective intermolecular reaction that would lead to crosslinking.

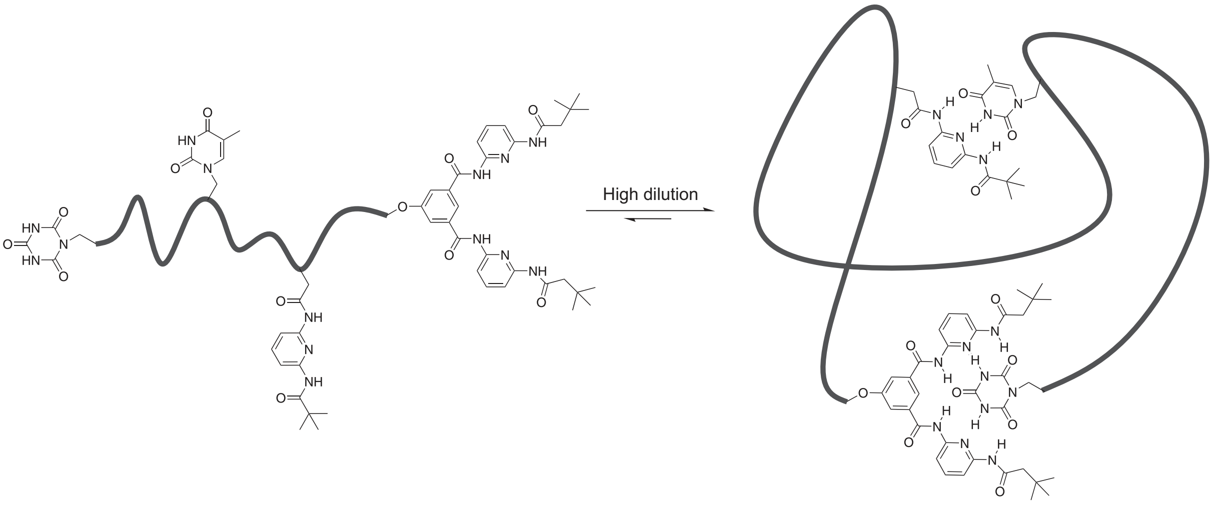

Figure 2.24.: Single-chain nanoparticle formation, mimicking natural protein structures, on the basis of two mutually orthogonal recognition pairs: thymine-diaminopyridine and cyanuric acid Hamilton wedge. The image was reproduced from ref.[133] with permission of The Royal Society of Chemistry.

In general, the folding into SCNPs can be performed by means of a wide range of methods. Thereby, irreversible and reversible formation of covalent bonds, noncovalent bond formation (such as the described hydrogen bonding), and complexation methods can be employed. The functional groups that interact with each other are usually introduced during the polymerization process. However, post-polymerization modifications are another possible pathway. For the synthesis of the single chains, that are subsequently undergoing the folding process, the RDRP techniques (see chapter 2.1.2) play an important role, since highly defined end groups and chain lengths are necessary. Therefore, ATRP, NMP, and RAFT are the preferred polymerization methods.

In order to verify the successful folding of a chain, their in-depth characterization is essential. In the following, selected characterization methods for SCNPs will be introduced briefly.

2.8.2. Characterization of SNCPs

Providing evidence for the successful folding of a single chain into a SCNP and its characterization is a crucial issue in the SCNP field. In general, no analytical technique is sufficient on its own for the unambiguous proof of SCNP formation. Therefore, a combination of different techniques is utilized for an in-depth characterization. The most important techniques are size-exclusion chromatography (SEC), dynamic light scattering (DLS), and nuclear magnetic resonance spectroscopic techniques, especially the diffusion ordered spectroscopy (DOSY). In the following, SEC and DOSY will be described briefly.

Size-Exclusion Chromatography (SEC)

Size-exclusion chromatography (SEC) is an analytical technique that separates macromolecules according to their hydrodynamic radii and became a standard technique for the determination of the molar mass and distribution of polymers. The separation is performed on columns filled with a porous crosslinked material (the gel), that is swollen with a solvent, the so-called eluent (for instance THF or DMSO). The latter flows through the system with a constant speed. The analyzed polymer is introduced into the eluent as a diluted solution. On its pathway through the column, it passes the pores of the gel with various pore sizes. Polymer chains with a large hydrodynamic radius can only access those pores that are large enough for the macromolecule to enter. However, small polymer chains can access more pores than large polymers. Their diffusion through the columns takes more time. The detectors, usually measuring the refractive index (RI) or the UV absorbance of the eluent, are placed after the columns and detect the large polymer chains earlier than the short polymer chains. In such way, the polymer sample is separated by size. For the determination of the molar mass of a polymer, a calibration has to be performed beforehand.

The application of SEC for the detection of SCNP formation is based on the fact that the hydrodynamic radius of a single polymer chain is decreasing after its folding into an SCNP. Thus, a shift in the chromatogram towards longer elution times, i.e., smaller molar masses is observed.

Diffusion Ordered Spectroscopy (DOSY)

The diffusion ordered spectroscopy (DOSY) is an NMR technique that, as implied by its name, measures the translational diffusion coefficient of a molecule in solution.[138,139] A spherical particle with the hydrodynamic radius R_h in a medium with the viscosity η exhibits a diffusion coefficient D, as described by the Stokes-Einstein relation:

$$D = \frac{k_B T}{6\pi\eta R_h} \tag{2.20}$$

with k_b and T as the Boltzmann constant and the temperature, respectively. Since the hydrodynamic radius of a particle is directly correlated with the diffusion coefficient, DOSY serves as a powerful tool for the characterization of SCNPs due to the decrase of the chains' radius after folding

The basic principle of DOSY is the possibility to label the position of a spin with the Larmor frequency of a pulsed magnetic field. Thereby, the measured sample is exposed to multiple pulses and a series of spin echo spectra with varying field gradient strengths and signal decays is recorded.
After a first pulse, the time Δ is given to the molecule for the diffusion process. The second pulse thus can be employed for decoding the molecules' position after the time Δ. The intensity of the measured signal will depend on the time Δ (diffusion time), and the gradient parameters G and δ, the strength and duration, respectively. Thereby, the signal experiences an attenuation that can be described by Equation 2.21 with the gyromagnetic constant γ of the nucleus.

$$I = I_0 exp\left[-\gamma^2 G^2 \delta^2 (\Delta - \frac{\delta}{3}) D\right] \tag{2.21}$$

When a static magnetic field with the strength B_0 is applied in the z-direction, the nuclear spin precesses with an angular frequency ω_0, that is referred to as the Larmor frequency, described through

$$\omega_0 = \gamma B_0 \tag{2.22}$$

with γ being the gyromagnetic ratio of the nucleus. The magnetic field in z-direction is spatially homogenous and so is ω. However, when an additional magnetic field gradient G is applied, ω becomes spatially dependent.
One of the simplest DOSY experiments is the pulsed field gradient (PFG) sequence, introduced by Stejskal and Tanner[140] and illustrated in Figure 2.25. Thereby, a 90° pulse is applied, that rotates the magnetization into the x,y-plane. After the time t_1, a gradient pulse G is applied for a duration δ. At the end of the time period Δ, the spin experiences a phase shift. Subsequently, a 180° pulse is applied, resulting in the reverse of the precession direction. After the time period $t_1 + \Delta$, a second pulse G is applied with the same magnitude and duration.

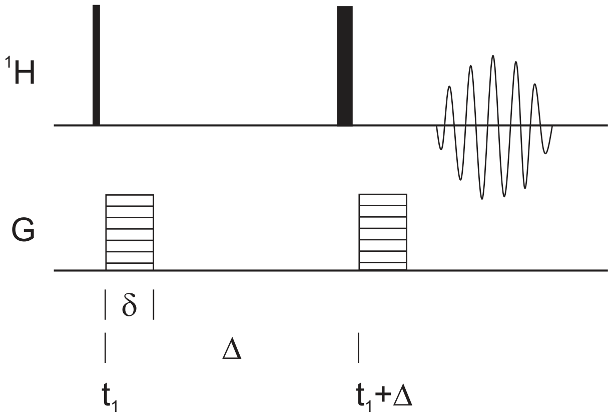

Figure 2.25.: Schematic illustration of the pulsed field gradient (PFG) sequences as the easiest example for a DOSY experiment. Imaged adapted from ref.[139], ©1999, with permission from Elsevier.

If at this point the molecules in the sample did not diffuse along the z-axis since the first pulse, the two pulses cancel each other out, resulting in a refocusing of the spins and a signal with maximum intensity. However, since the molecules do diffuse along the z-axis, the dephasing that results from the applied pulses is proportional to the displacement during the time Δ. Hence, due to the movement of the molecules, i.e., the nuclei, the second pulse cannot refocus the spins and an attenuated signal is recorded, see Equation 2.21.
As already mentioned, the described PFG experiment is a very simple version of DOSY experiments and it bears various disadvantages. Advanced DOSY techniques, for instance, apply several pulses with different magnitudes, such as the bi-polar longitudinal eddy current delay (BPLED) pulse sequence. For a detailed discussion of this advanced technique, the reader is referred to the literature.[138,139]

3

Photoinitiator Investigation

As described in 2.2.1, photoinitiators play a fundamental role in many industrial applications. Their initiation efficiency not only determines the amount of employed photoinitiator and irradiation time, but additionally the energy costs arising from the production process. Thus, the knowledge of a photoinitiators' initiation efficiency is of paramount importance.

The key factors that determine the efficiency of photoinitiators are their absorption behavior, their fast radical cleavage, and the high reactivity of the generated radicals. Thus, the comparison of photoinitiators can be performed in manifold ways. In the past, a closer look at the absorbance of photoinitiators in the UV-vis region,[141–143] their initiation quantum yield,[144,145] and their polymerization rate and final monomer conversion has been taken.[141–143,146,147] For the investigation of photoinitiators, a wide range of techniques that evaluate their photochemical properties can be employed. Steady-state photolysis,[142,143] fluorescence probe techniques[144] and real-time IR spectroscopic evaluation[141–143,146] are just a few examples. Furthermore, an advanced technique for the investigation of photoinitiators is the time-resolved laser flash spectroscopy with detection through UV-vis, IR, and ESR. It was employed by Turro and co-workers,[74] focusing on the photochemical behavior of photoinitiators and the mechanistic aspects of their radical formation. The formation of radical initiator species can thereby be followed by ESR spectroscopy.[141–143]

In order to compare the initiation efficiency of photoinitiators on a quantitative scale, PLP-ESI-MS proved to be an excellent tool. It enables the investigation of specific photoinitiator fragments and provides valuable information about the initiation mechanism. Furthermore, very small amounts of photoinitiator and polymer are necessary for the investigation. The polymerization is initiated by a pulsed laser system and the polymer is subsequently analyzed by ESI-MS. PLP-ESI-MS can be accompanied by the use of femtosecond spectroscopy and theoretical calculation methods, allowing for a detailed investigation of the molecular dynamics of a photoinitiator and the reactivity of the respective radical fragments.[132] In the current chapter, that is divided in two main sections, the focus is on benzoin-type photoinitiators and their respective derivatives. Based on benzoin as the basic structure, a wide range of structurally different photoinitiators are compared in their initiation efficiency towards methyl methacrylate (MMA). In addition, femtosecond spectroscopy and theoretical calculation methods accompany the results. Summarizing the viewpoints from both experimental and theoretical parts leads to an in-depth discussion of the reactivity of photoinitiator fragments.

Parts of this chapter were reproduced from E. Frick, H. A. Ernst, D. Voll, T. J. A. Wolf, A.-N. Unterreiner, C. Barner-Kowollik, *Polym. Chem.* **2014**, *5*, 5053-5068 and E. Frick, C. Schweigert, B. B. Noble, H. A. Ernst, A. Lauer, Y. Liang, D. Voll, M. L. Coote, A.-N. Unterreiner, C. Barner-Kowollik, *Macromolecules* **2016**, *49*, 80-89. DFT Calculations and femtosecond experiments from section 3.1 were performed by Hanna A. Ernst and Thomas J. A. Wolf. Femtosecond experiments from section 3.2 were performed by Caroline Schweigert. Calculations in section 3.2 were performed by Benjamin B. Noble.

3.1. Initiation Efficiencies of MMMP, Benzoin, and 4MB

The photoinitiator 2-methyl-4'-(methylthio)-2-morpholinopropiophenone (MMMP) is widely used in industrial applications and is referred to as a nearly ideal photoinitiator, being able to form two radical fragments at the same time, both of equal initiation ability.[75] However, this statement has not yet been verified, i.e., the initiation efficiency of the two radicals formed after the radical cleavage of MMMP has not been investigated quantitatively. Therefore, in the study introduced in this chapter, the initiation efficiency of the radical fragments of MMMP, T and N, are compared to the radical fragment B of benzoin, and MB of 4-methyl benzoin (4MB), as shown in Figure 3.1.

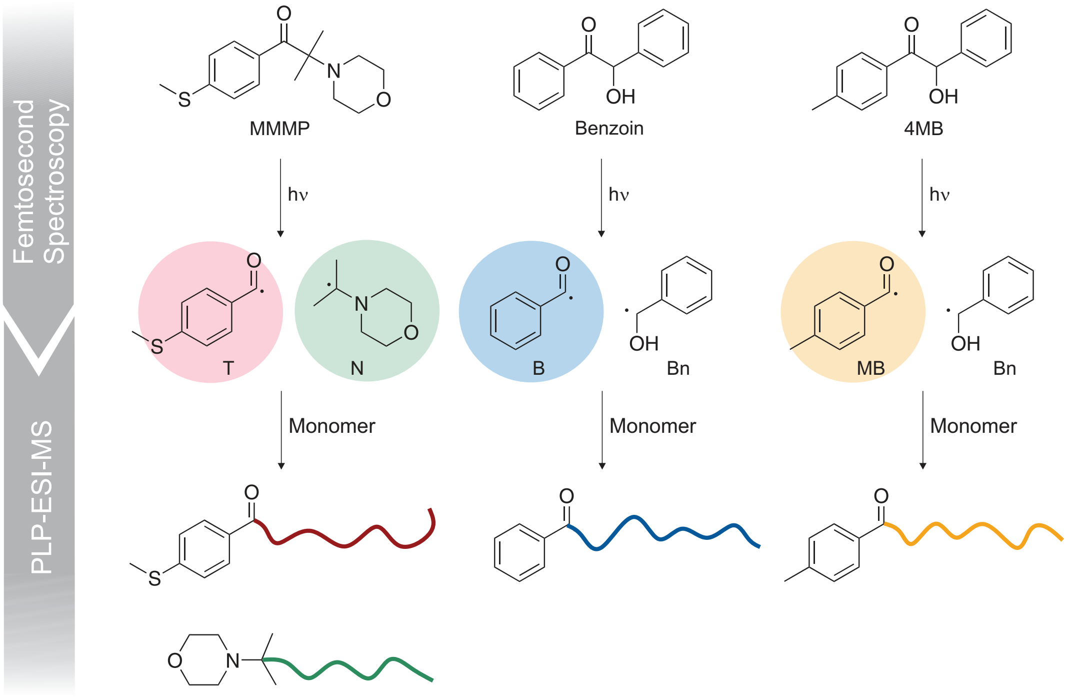

Figure 3.1.: The three photoinitiators MMMP, Bz, and 4MB, and their photolytic decomposition into radical fragments after UV light irradiation at 351 nm.

Benzoin, a commonly employed photoinitiator, is utilized as a reference due to its structural simplicity and good initiation performance. However, photoinitiators with a benzoyl radical cannot be compared to benzoin in their initiation efficiency due to the isobaric overlap of the fragments in mass spectrometric analysis. 4MB, due to its methyl-substitution, is beneficial for such cases and was thus selected as a second reference initiator. The second radical fragment Bn, formed by both benzoin and 4MB, is not subject of this study, since its initiation efficiency is negligible.

3.1.1. Initiation Efficiency Evaluation via PLP-ESI-MS

The comparison of the aforementioned initiators was performed via a combination of pulsed-laser polymerization and subsequent analysis via electrospray-ionization mass spectrometry (PLP-ESI-MS), a previously established technique for the quantitative analysis of initiation efficiencies.[122–125] PLP-ESI-MS provides quantitative insight into the incorporation propensity of radical fragments during a photoinitiated FRP. Therefore, in a first step, polymerizations via PLP were carried out, employing a pulsed laser system at a wavelength of 351 nm. In order to compare photoinitiator fragments, various mixtures of two photoinitiators were irradiated in the PLP experiments. Thereby, different molar ratios of the two photoinitiators that are simultaneously present in the solution were employed. The subsequent post-mortem analysis of the generated polymer products was performed via ESI-MS in order to determine the extent of incorporation of the initiator radicals into the polymer chains. This so-called "cocktail experiment" technique allows for the quantitative determination of the initiation efficiency of the compared radical fragments. All products that can be found in the mass spectra are shown in Figure 3.2.

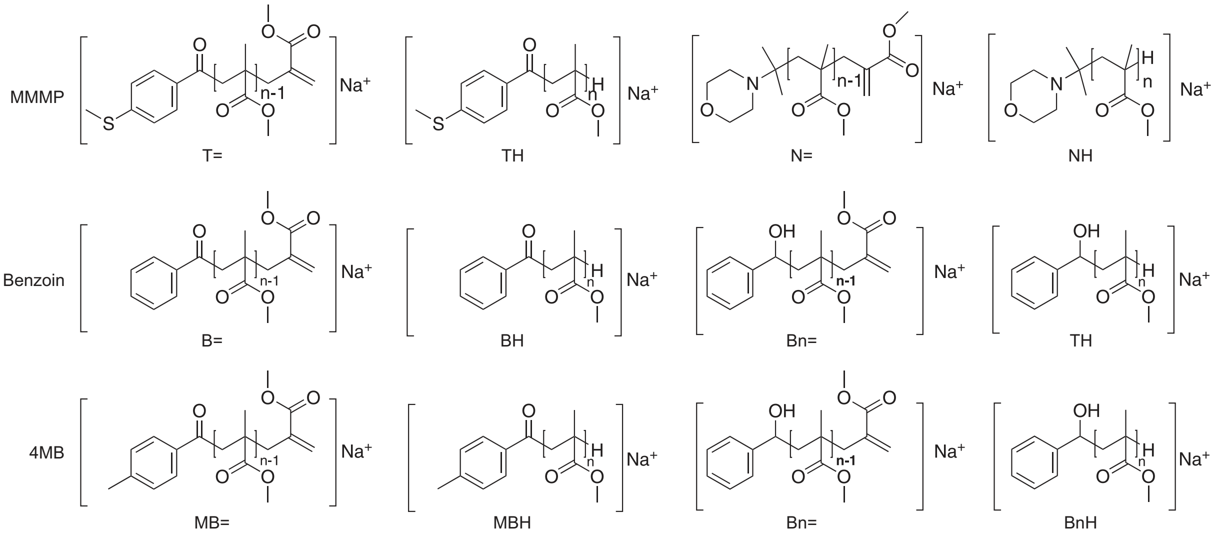

Figure 3.2.: All disproportionation products found in the mass spectra for MMMP, benzoin, and 4MB. For the sake of clarity, recombination products are omitted.

Previously, the comparison of the two initiators MMMP and benzoin could not be carried out via PLP-ESI-MS, due to the overlap of the mass spectrometric peaks originating from the benzoyl radical fragment (B), ionized with Na^+ ions, and the *N*-isopropyl morpholino radical fragment (N) ionized with H^+ (along with Na^+ ionization) during the ESI process. In the context of the present work, a new protocol was developed for the suppression of H^+ ionization of the morpholino moiety (fragment N) during the ESI process, enabling the comparison of MMMP and benzoin via PLP-ESI-MS.

Next to the investigation via PLP-ESI-MS, femtosecond transient absorption (TA) spectroscopy and density functional theory (DFT) methods were employed in order to enlarge the investigative viewpoint toward the very first steps of the photoinitiators upon absorption of a photon. Thereby, the excited state properties of MMMP, Benzoin, and 4MB and their respective relaxation mechanisms were studied. The high performance of such a combination was shown in a previous study by Wolf and Voll *et al.*,[132] resulting in the identification of the important factors leading to an efficient initiation step and thus high incorporation rates of radical fragments. In the study presented in this chapter, the four different radical fragments T, N, B, and MB, illustrated in Figure 3.1, were compared regarding their initiation efficiency and a deeper insight into their dynamics upon irradiation was achieved.

3.1.2. Ionization Enhancement Study

In the ESI-MS analysis of MMMP-initiated polymer samples performed in common solvent mixtures (such as THF/methanol or DCM/methanol), chains carrying the morpholino fragment (N) show an ionization with H^+ next to the desired ionization with Na^+. The exact masses of MMMP- and benzoin-initiated polymer chains, respectively, show isobaric overlap for the H^+ ionized disproportionation products originating from the N fragment, $[NH]^{H+}$ and the corresponding Na^+ ionized polymer chains initiated by the benzoyl fragment B, $[BH]^{Na+}$. Thus, in order to perform a quantitative comparison of MMMP and benzoin, the H^+ ionization of the morpholino-initiated chains during the ESI process needs to be suppressed.

Therefore, the first focus was set on reducing the ionization with H^+, most probably occuring at the nitrogen atom of the morpholino group, to a minimum. The influence of the salt concentration (0-500 μM NaTFA), the capillary temperature (270-320°C), the capillary voltage (4-8 kV), and the solvent mixture (THF/methanol (3/2), DCM/methanol (3/1), MeCN/methanol (3/1), toluene/methanol (3/2, v/v, respectively)) was assessed. Figures 3.3 and 3.4 show the respective results.

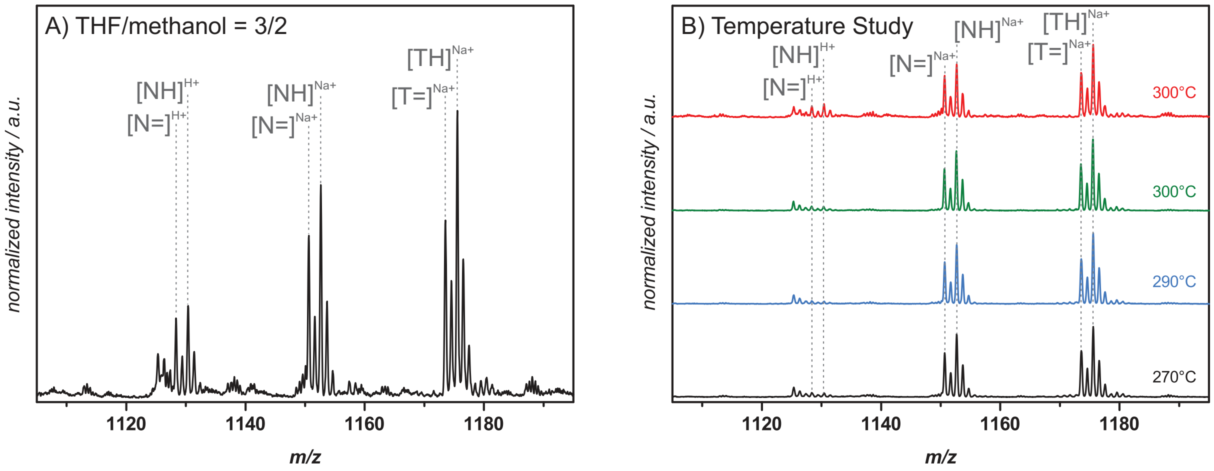

Figure 3.3.: Variation of specific parameters in order to suppress H^+ ionization of polymer chains carrying a morpholino end group (N= and NH). A) Mass spectrum of MMMP-initiated pMMA in THF/methanol (3/2). H^+ and Na^+ionization occur. B) The variation of the capillary temperature shows a slight decrease of H^+ ionization towards lower temperatures, yet no full suppression.

Variation of the capillary temperature or voltage in a solvent mixture of THF/methanol (3/2) resulted in no significant change in H^+ ionization compared to Na^+ ionization. Moreover, the extent of H^+ ionization seemed to be irreproducible and changed arbitrarily. Finally, changing the solvent mixture to toluene/methanol (3/2) and adding 300 μM of NaTFA resulted in a successful and reproducible suppression of H^+ ionization.

The positive influence of toluene on suppressing H^+ ionization may be a result from its very low permittivity ($\varepsilon_r = 2.38$) compared to that of THF ($\varepsilon_r = 7.52$), DCM ($\varepsilon_r = 8.93$), or MeCN ($\varepsilon_r = 36.64$).[148] A high permittivity solvent can result in a distinct field weakening effect during the ESI process, based on the orientation of the droplet in the charged field and thus in a support of H^+ ionization. Additionally, the solvent can have an influence on the pK_a value of the morpholino group, that has a large impact on its ionization behavior. The critical evaluation of the mass spectra depicted in Figure 3.3 and 3.4 one can identify that the H^+ ionization behavior

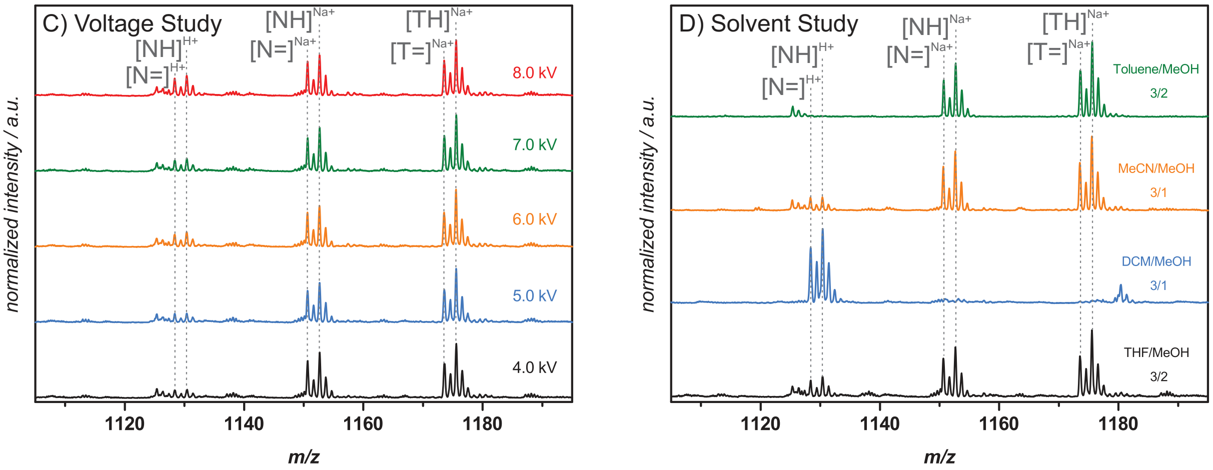

Figure 3.4.: Variation of specific parameters in order to suppress H^+ ionization of polymer chains carrying a morpholino end group (N= and NH). C) Variation of the capillary voltage shows, similar to B), a slight decrease of H^+ ionization, yet no full suppression. D) A solvent study with different solvent mixtures indicates full elimination of H^+ ionization for toluene/methanol (3/2).

in the different solvent mixtures does not follow their permittivity trend. The value of ε_r of acetonitrile is higher than of DCM. Yet, significantly more H^+ ionization can be observed for the DCM/methanol solvent mixture than for MeCN/methanol. Thus, next to the permittivity, other parameters appear to have an impact on the extent of H^+ ionization.

3.1.3. Evaluation of ESI-MS Data for Quantitative Comparison of Initiator Fragments

After the polymerization of methacrylates via PLP, the polymer sample mainly consists of disproportionation products and only small amounts of combination products can be identified. Analysis of the latter provides no information regarding which fragment served as the initiating radical for the polymerization, since both polymer end groups are initiator fragments. Thus, only the disproportionation products contain the information on which photoinitiator fragment initiated the polymerization and which specific fragment performed better in the initiating step.

A disproportionation step during a polymerization results in the formation of two different polymer chains: one chain carrying a double bond at its end group and another chain carrying a hydrogen at the former radical site. Thus, as already described in 2.5.5, disproportionation peaks in a mass spectrum occur in pairs with a mass difference of 2 Da between the respective peaks. In the present thesis, the disproportionation peaks are labeled as "XH" and "X=", where X defines the chemical nature of the initiating fragment, i.e., the α-position of the polymer (B, T, N, or MB for benzoin, MMMP, and 4MB, respectively). "H" and "=" define the role of the polymer chain in the H-abstraction during the disproportionation step, giving information about the functionality of the polymer at the ω-position.

For the quantitative comparison of the initiation efficiency of MMMP, benzoin, and 4MB, the peak heights Δh of the polymer signals of each repeating unit, as illustrated in Figure 3.5, are evaluated. Only the "H=" peak, i.e., the first peak of each disproportionation peak cluster is utilized, since it shows no isobaric overlap with other major product peaks.

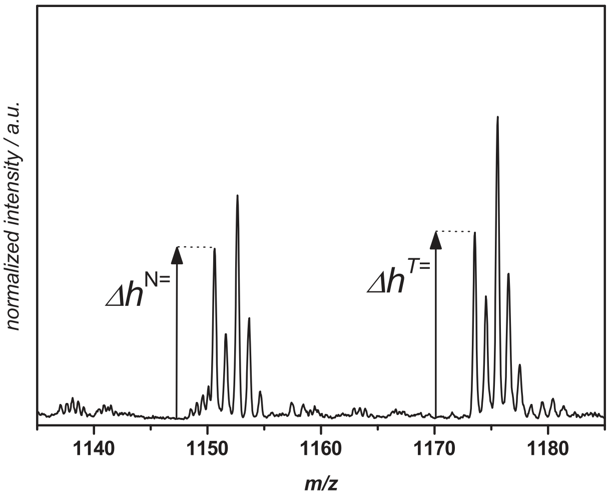

Figure 3.5.: Zoom into the ESI-MS spectrum of pMMA initiated by MMMP showing the disproportionation peaks [N] and [T], associated with polymer chains initiated by the fragments N and T of MMMP. The peak height Δh that is employed for the evaluation of the spectra is shown exemplarily.

The peak heights are utilized for the calculation of the mole fraction $F^{X}(i)$ of a disproportionation product with the end group X, corresponding to the respective initiating fragment, for the number i of the repeating unit. Assuming two different initiating fragments (X_1 and X_2) compete in one PLP experiment, the mole fraction $F^{X_1}(i)$ for the chains initiated by the fragment X_1 can be described by

$$F^{X_1}(i) = \frac{\Delta h^{X_1}(i)}{\Delta h^{X_1}(i) + \Delta h^{X_2}(i)} \tag{3.1}$$

$F^{X_1}(i)$ is a direct correlation to the relative number of polymer chains initiated by the fragment X_1 that can be found in the PLP sample. It is assumed that, starting from a $DP_n \geq 2$, the chemical nature of the initiating fragment has no influence on the propagation rate of the monomer. Thus, the end group X is equally distributed over all chain lengths. Plotting the $F^{X_1}(i)$ values for a fragment X versus the chain length i, i.e., the degree of polymerization DP_n, illustrates the distribution of the fragment X over the polymer chains as they are detected in the ESI-MS.

In an ideal case, the gradient of such a plot is close to zero, showing a constant $F^{X_1}(i)$ value for each chain length and thus representing a chain length-independent ESI process. However, in some cases a chain length-dependent ionization occurs and can be recognized by an increasing or decreasing evolution of $F^{X_1}(i)$, indicating a mass-biased ESI process. In order to overcome the mass tampering, Günzler *et al.*[122] established a method that allows the mass-bias free evaluation of the peak heights. In this approach, $G^{X_1}(i)$ is the ratio of the peak heights Δh^{X_1} and Δh^{X_2}, originating from the two radical fragments X_1 and X_2 that are to be compared in their initiation efficiency. Three different ratios G, G', and G'' are to be compiled: one ratio for the considered repeating unit i, one for the preceding repeating unit $i-1$, and one for the following repeating unit $i+1$, respectively.

$$G^{X_1}(i) = \frac{\Delta h^{X_1}(i)}{\Delta h^{X_2}(i)} \tag{3.2}$$

$$G'^{X_1}(i,i-1) = \frac{\Delta h^{X_1}(i)}{\Delta h^{X_2}(i-1)} \tag{3.3}$$

$$G''^{X_1}(i,i+1) = \frac{\Delta h^{X_1}(i)}{\Delta h^{X_2}(i+1)} \tag{3.4}$$

Thereby, after averaging G, G', and G'', a mass-bias free ratio of two disproportionation peaks, $G^{X_1}_{m/z,0}$, is obtained

$$G^{X_1}_{m/z,0} = \frac{G^{X_1}(i) + G'^{X_1}(i,i-1) + G''^{X_1}(i,i+1)}{3} \tag{3.5}$$

Plotting $G^{X_1}_{m/z,0}$ against the molar ratio of the photoinitiators in the polymerization mixture results in a linear trend serving as a tool for quantitatively determining the initiation efficiency of the two compared initiator fragments X_1 and X_2. The ratio X_1/X_2 at which the $G^{X_1}_{m/z,0}$ value equals 1, is the initiator ratio that has to be employed in order to achieve equal initiation probability for both fragments. Consequently, this ratio correlates with the quantitative initiation efficiency ratio of the compared fragments. In the following section the initiation efficiency ratios for the initiating fragments of MMMP, benzoin, and 4MB will be discussed in detail. Table 3.1 gives an overview over all compiled initiation efficiency ratios.

Comparison of MMMP and Benzoin

The two radical fragments T and N of MMMP were compared to the benzoyl fragment B of benzoin based on the aforementioned evaluation technique. The plot of the mass-bias free ratio $G^{X_1}_{m/z,0}$ against the MMMP/benzoin ratio, illustrated in Figure 3.6, follows a constant gradient. The $G^{X_1}_{m/z,0}$ value for the T fragment equals 1 for an initiator ratio of MMMP/benzoin = 1.6. For the N fragment of MMMP $G^{X_1}_{m/z,0}$ equals 1 for a ratio of MMMP/benzoin = 2.2. Consequently, an equal number of polymer chains are initiated by T (or N) and B fragments, when a photoinitiator mixture of MMMP/benzoin in the molar ratio of 1.6/1 (or 2.2/1) is applied, respectively. Hence, the benzoyl fragment B of benzoin exhibits a 1.6 times higher initiation efficiency than the T fragment and a 2.2 times higher efficiency than the N fragment of MMMP.

Comparison of MMMP and 4MB

The initiation efficiency of the fragments T and N were additionally compared to the methyl-substituted benzoyl fragment MB of 4MB. In contrast to benzoin, the initiating fragment of 4MB shows a lower initiation efficiency than both the T as well as N fragment of MMMP. The mass-bias free ratio for the T fragment equals 1 for an initiator ratio of MMMP/4MB = 0.7. For the N fragment an initiator ratio of MMMP/4MB = 0.9 has to employed in order to achieve equal initiation propensity, as illustrated in Figure 3.7. Thus, for the fragments T and MB an initiation efficiency ratio of T/MB = 1/0.7 is found, implying a 1.4 times higher initiation efficiency for T compared to MB. For N and MB a ratio of N/MB = 1/0.9 was found, hence the fragment N being 1.1 times more efficient than MB.

Comparison of Benzoin and 4MB

Finally, a third comparison – benzoin and 4MB – was carried out, completing the investigation of the three initiators. For both, benzoin and 4MB only the respective benzoyl can be compared

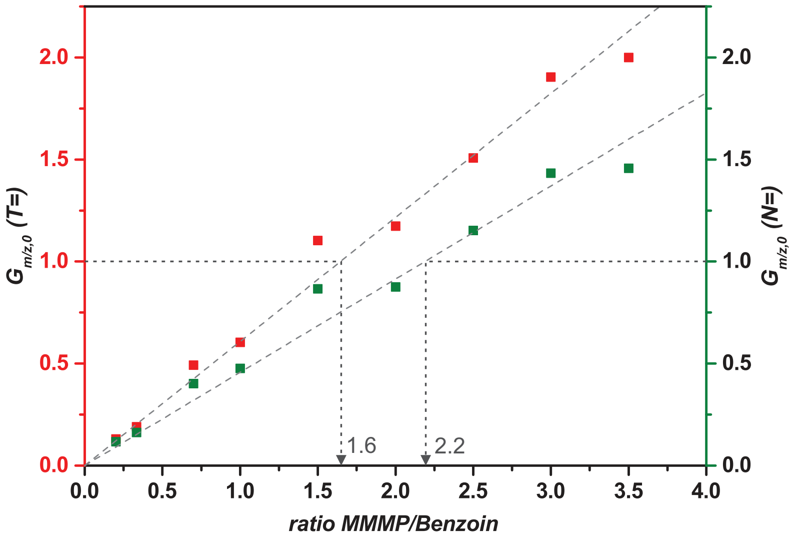

Figure 3.6.: The mass bias-free ratio of the disproportionation products is plotted versus the molar ratio of the photoinitiators MMMP and benzoin. $G_{m/z,0}^{X_1}$ equals 1 for a ratio of 1.6 for the T fragment and 2.2 for the N fragment, respectively.

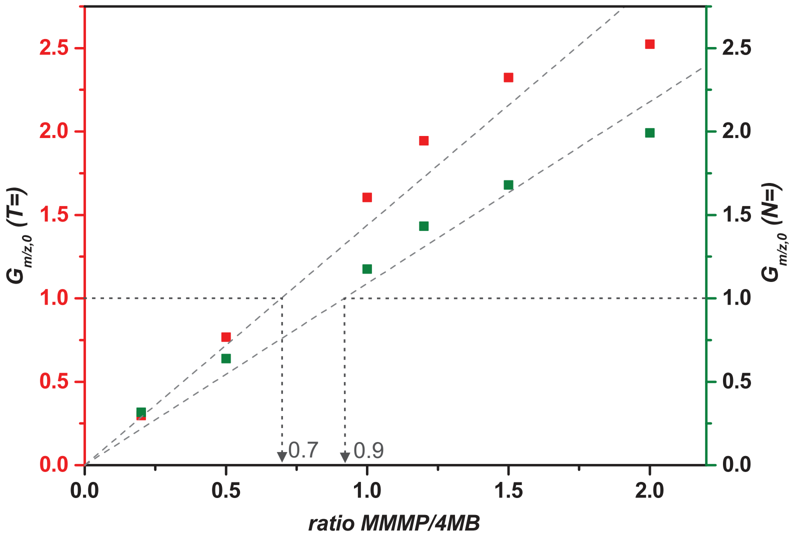

Figure 3.7.: The mass bias-free ratio of the disproportionation products is plotted versus the molar ratio of the photoinitiators MMMP and 4MB. $G_{m/z,0}^{X_1}$ equals 1 for a ratio of MMMP/4MB = 0.7 for the T fragment and MMMP/4MB = 0.9 for the N fragment, respectively.

since the peaks of the second fragment, Bn, show isobaric overlap and thus cannot be evaluated. Yet, the initiation ability of this fragment is negligible, since its activity during the PLP experiment is limited mainly to termination events. As illustrated in Figure 3.8, for the comparison of the fragments B and MB the mass-bias free ratio equals 1 at a ratio of benzoin/4MB = 0.86. Thus, the benzoyl fragment of benzoin shows a 1.2 times higher initiation efficiency than the respective methyl-substituted fragment.

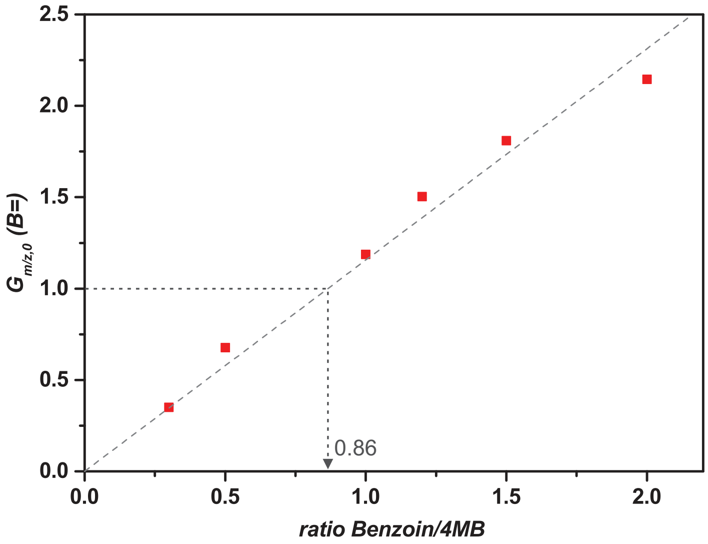

Figure 3.8.: The mass bias-free ratio of the disproportionation products is plotted versus the molar ratio of the photoinitiators benzoin and 4MB. $G_{m/z,0}^{X_1}$ equals 1 for a ratio of benzoin/4MB = 0.86 for the benzoyl fragment of benzoin.

Trio Experiment: Comparison of MMMP, Benzoin, and 4MB

The previously described experiments comparing two initiators, respectively, were completed by a trio cocktail experiment containing all three initiators MMMP, benzoin as well as 4MB in one PLP experiment. The corresponding mass spectrum is shown in Figure 3.9. The spectrum illustrates the strong initiation efficiency of the B fragment. The peaks of benzoyl-initiated polymer chains clearly surpass the respective peaks originating from the fragments T, N, and MB, according to the evaluation of their initiation efficiencies ratios. At the same time, the peak heights from T- and MB-initiated chains show similar values.

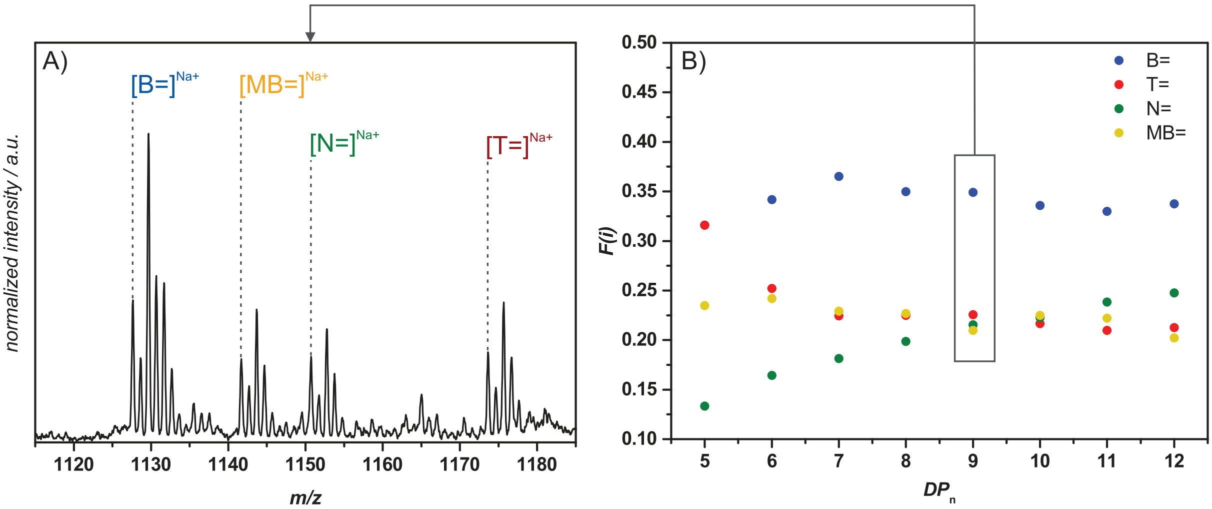

Figure 3.9.: Results of the trio experiment with MMMP, benzoin, and 4MB. A) shows the mass spectrum of the corresponding PLP experiment containing all three initiators. B) shows the $F^X(i)$ plot, illustrating the molar fractions of the polymer chains initiated by the fragments B, T, N, and MB, respectively. The highlighted molar fractions are represented in the mass spectrum in A).

Compared Fragments	Initiation Efficiencies
B : T	1 : 0.63
B : N	1 : 0.45
B : MB	1 : 0.86
T : MB	1 : 0.70
N : MB	1 : 0.90

Table 3.1.: Initiation efficiencies derived from PLP-ESI-MS experiments of MMMP, benzoin, and 4MB.

3.1.4. Ionization of MMMP-initiated Polymer

As described above, the mole fractions $F^X(i)$ of specific peaks have an ideally constant gradient of zero when plotting against the polymer chain length. A chain-length independent ionization takes place in such a case. However, the $F^X(i)$ values of the T- and N-initiated disproportionation peaks show a deviation, as illustrated in Figure 3.10. The declining $F^X(i)$ values observed for T-initiated chains (with increasing DP_n) and the inclining values for the N-initiated chains correspond to their relative decrease in peak intensity in the mass spectrum. One might assume that this behavior reflects the tendency of the T fragment to generate shorter polymer chains than the N fragment. However, the influence of the initiator group at the α-end of the polymer on the propagation rate of the radical ω-end can be excluded for $DP_n > 2$, where penultimate effects are negligible.[149] Thus, an equal propagation rate can be assumed for all growing polymer chains during a PLP experiment.

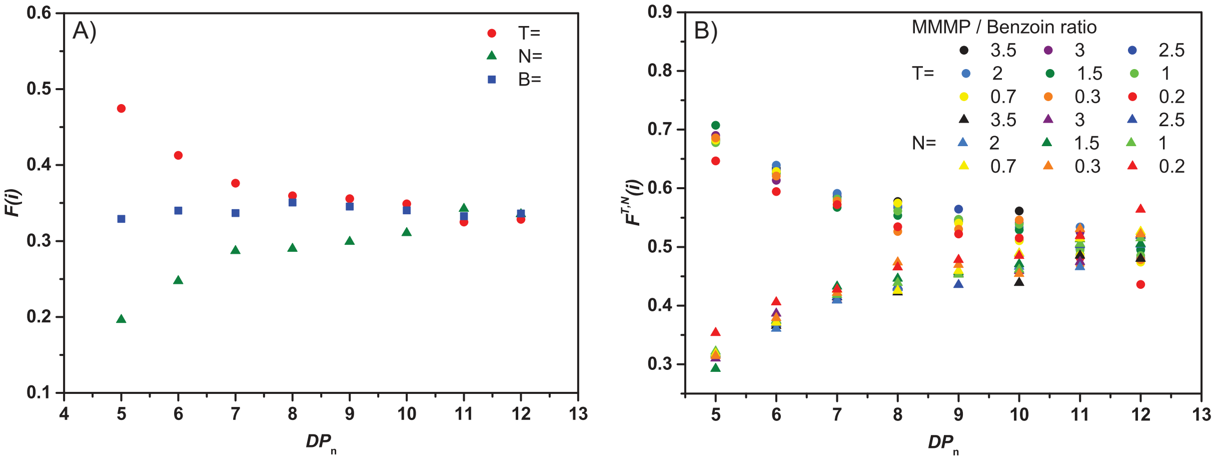

Figure 3.10.: A) Plot of the mole fractions of T-, N-, and B-initiated disproportionation products versus the degree of polymerization for the molar ratio of MMMP/benzoin = 1.5. B) Plot of the mole fractions of T- and N-initiated disproportionation products for different initiator ratios, without the influence of B-initiated chains.

The observed decline of $F^X(i)$ values is a sign for a chain length-dependent ionization of the polymer chains. With increasing DP_n, the ionization of T-initiated chains decreases and the ionization improves for chains carrying the N fragment. Simultaneously, the ionization behavior of B-initiated disproportionation products remains constant. In order to exclude the influence of the disproportionation peaks originating from the B fragment, the mole fractions $F^T(i)$ and $F^N(i)$, not including the B-initiated signals, were plotted versus the DP_n.

$$F^T(i) = \frac{\Delta h^{T=}(i)}{\Delta h^{T=}(i) + \Delta h^{N=}(i)} \tag{3.6}$$

$$F^N(i) = \frac{\Delta h^{N=}(i)}{\Delta h^{N=}(i) + \Delta h^{T=}(i)} \tag{3.7}$$

As illustrated in Figure 3.10 (right), an asymptotic behavior for $F^T(i)$ and $F^N(i)$ can be observed. For short polymer chains, the T-initiated chains are the main products, whereas the N-initiated chains appear as a side product with very low peak intensities. With growing chain length, the proportions of N-initiated and T-initiated chains both approach a molar fraction of close to 0.5. Most probably, this asymptotic behavior is caused by the morpholino (N) fragment due to its differing chemical structure compared to the other fragments T, B, and MB. Poor solubility in the employed toluene/methanol solvent mixture or poor ionization with Na^+ based on the influence of the N group can cause such a behavior. With the lengthening of the polymer chain, the negative influence of the morpholino group is diminished, since with the growing number the monomer units become more dominant.

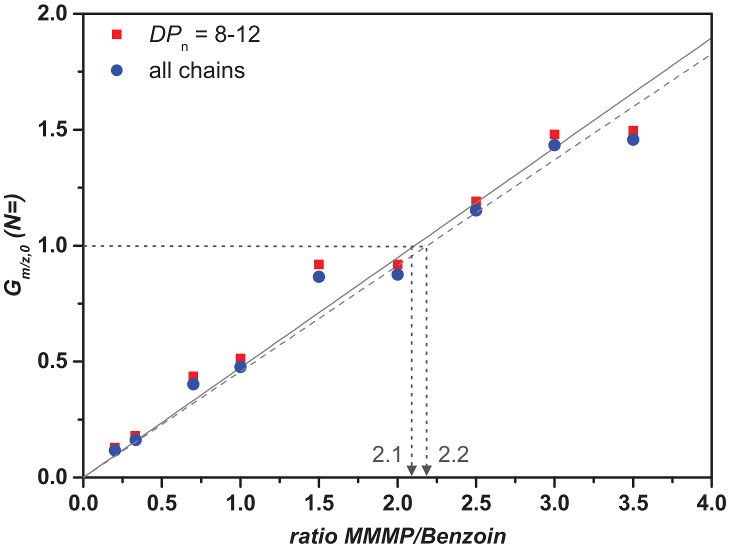

Figure 3.11.: The mass bias-free ratio of the N-initiated disproportionation products is plotted versus the molar ratio of the photoinitiators MMMP and benzoin for both, chains with a DP_n of 8-12 and for all chain lengths. No significant difference can be detected.

The fact that for long polymer chains the molar fractions of T- and N-initiated disproportionation products become equal indicates that both MMMP fragments T and N most probably exhibit an equal intitiation efficiency. Consequently, the quantitative comparison of the initiation efficiency for the MMMP fragments with B and MB could be questioned. In order to verify the initiation efficiency ratios, a corrected mass bias-free ratio $G_{m/z,0}$ was assessed by selecting only those polymer chains with a DP_n of 8-12. The result is illustrated in Figure 3.11. With this new approach the influence of the short chains is reduced. However, no significant difference for the initiation efficiency ratios was detected. Both approaches, taking all chains into account or only the long ones, lead to very similar results. The applicability of the mass bias-free evaluation is thus verified.

	$\varepsilon/(10^3\ \mathrm{L{\cdot}mol^{-1}{\cdot}cm^{-1}})$	
	351 nm	325 nm
MMMP	0.354	3.571
Benzoin	0.110	0.311
4MB	0.245	0.669

Table 3.2.: Extinction coefficents for MMMP, benzoin, and 4MB for both wavelengths employed in the PLP experiments and femtosecond spectroscopy, respectively.

3.1.5. Femtosecond Spectroscopy and Theoretical Methods

UV-Vis Spectroscopy

A closer look into the extinction of the initiators MMMP, benzoin, and 4MB shows that the structurally similar species benzoin and 4MB exhibit a similar absorption behavior, whereas the absorption of MMMP differs strongly. As illustrated in Figure 3.12, both benzoin and 4MB show a weak absorption centered around 320 nm and a strong absorption below 250 nm. Benzoin exhibits two weak shoulders around 284 nm and 292 nm, respectively, whereas 4MB shows shoulder at 257 nm. In contrast, MMMP shows a strong extinction at 304 nm and a small shoulder around 350 nm. The excitation wavelengths in the PLP experiments (350 nm) and the pump pulse wavelength employed in the femtosecond spectroscopy (325 nm) are assigned in the spectrum. For the femtosecond spectroscopy, a lower wavelength was chosen, since the signal-to-noise ratio was very low at 351 nm. At 325 nm the excitation probability is increased, resulting in a significantly higher quality of the transient spectra.

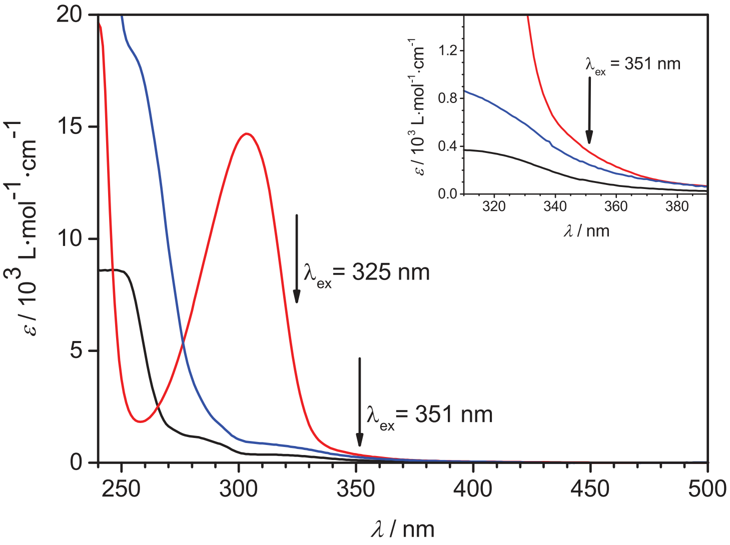

Figure 3.12.: Wavelength dependent extinction of MMMP (red), benzoin (black), and 4MB (blue) in MIB as the solvent. The excitation wavelengths during PLP experiments and femtosecond spectroscopy are assigned.

The determined extinction coefficients of MMMP, benzoin, and 4MB at both wavelengths are listed in Table 3.2. MIB was chosen as the solvent for measuring the extinction coefficient as well as for the transient spectra. Due to its structural similarity to MMA, that is employed in the PLP experiments, MIB is an ideal substitute for the monomer.

As Table 3.2 shows, the extinction coefficients of MMMP at both wavelengths are higher than those of benzoin and 4MB. However, as already pointed out in a previous study,[132] the

extinction coefficient at the employed excitation wavalength is not a sufficient measure for the initiation efficiencies. Further extensive investigations have to be carried out in order to understand the underlying processes that result in differing initiator performances.
A closer look into the absorption spectra in Figure 3.12 shows that both excitations of benzoin and 4MB (at 325 nm and 351 nm) correspond to the excitation into their first weak absorption bands. Yet, for MMMP the excitation into higher excited states is assumed for both wavelengths, due to its strong absorption band (at 304 nm) and the shoulder at 350 nm.

Femtosecond Spectroscopy

Femtosecond spectroscopy[1] was carried out in order to deeper understand the processes in the initiators MMMP, benzoin, and 4MB upon irradiation and the determining parameters for a high or low initiation efficiency.
As mentioned in the previous section, the transient spectra were recorded at a pump wavelength of 325 nm, due to higher signal intensities compared to the wavelength of 351 nm. Figures 3.13 and 3.14 illustrate the transient absorption spectra of MMMP, benzoin, and 4MB at 325 nm. In the case of benzoin and 4MB the spectra exhibit a similar structure with a dominant absorption between 430 nm and 540 nm. Thereby, 4MB shows a slower absorption decay than benzoin. In contrast to benzoin and 4MB, MMMP clearly shows two proximate absorption bands. One absorption band (at 520 nm) appears at time zero and decays within 1.8 ns, i.e., within the experimental time frame. The second band (at 464 nm) appears at a later point, its decrease exceeds the experimental time frame. Both the decrease of the fist absorption band and the increase of the second band exhibit comparable time scales. Thus, the depopulation of the excited states – demonstrated by the decreasing first absorption band – can be directly correlated with the population of a second excited state, expressed by the increase of the second absorption band.

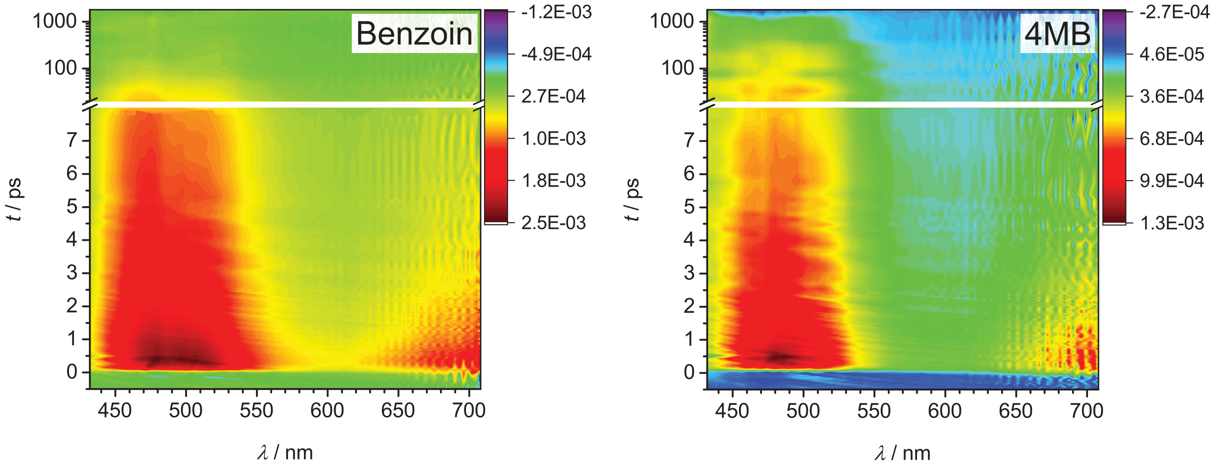

Figure 3.13.: Transient absorption spectra of benzoin and 4MB, recorded in MIB at a pump wavelength of 325 nm.

The TA spectra illustrated in Figure 3.13 and 3.14 were fitted by multiexponential functions, such as the function

---

[1] Experiments were carried out by Hanna A. Ernst and Thomas J. A. Wolf in the frame of a collaboration with PD Dr. Andreas-Neil Unterreiner, Physical Chemistry, Karlsruhe Institute of Technology

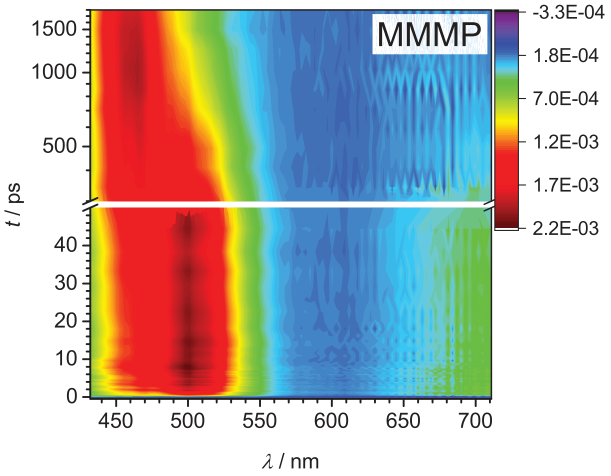

Figure 3.14.: Transient absorption spectra of MMMP, recorded in MIB at a pump wavelength of 325 nm.

$$\Delta OD(\lambda,\tau) = \frac{1}{2}\left[1 + erf(2\sqrt{ln\,2}\frac{\tau}{\tau_0})\right]\sum_{i=1}^{n} A_i(\lambda)exp(-\frac{\tau}{\tau_i}) \tag{3.8}$$

with the wavelength-dependent amplitudes A_i and time constants τ_i. The resulting time constants that were obtained by global fitting can be found in Table 3.3.

	Benzoin	4MB	MMMP
τ_1	2.5 ps ± 0.1 ps	2.5 ps ± 0.1 ps	1.1 ps ± 0.1 ps
τ_2	(50-80) ps	(150-350) ps	57 ps ± 6 ps
τ_3	> 1.8 ns	> 1.8 ns	(450-650) ps
τ_4	–	–	> 1.8 ns

Table 3.3.: Time constants obtained by multiexponential fits for benzoin, 4MB, and MMMP at a pump wavelength of 325 nm.

The determined time constants can be assigned to the following processes:
τ_1 (in case of benzoin and 4MB) corresponds to the spectral signature of the S_1 state and comprises both ISC and IC. It can be intrepreted as $\tau_1 = (\tau_{IC} \cdot \tau_{ISC})/(\tau_{IC} + \tau_{ISC})$.
τ_2 corresponds to the spectral signature of the T_1 state.
τ_3 (in case of benzoin and 4MB) corresponds to the spectral signature of the generated radicals.
τ_3 (in case of MMMP) corresponds to the ISC from the S_1 state.
τ_4 corresponds to the triplet lifetime and radical cleavage of MMMP.
An analysis of the time constants exhibits similarities for benzoin and 4MB and a clear discrepancy to the behavior of MMMP. Additional theoretical methods serve as a valuable supplement in order to understand and interpret the TA spectra. Therefore, DFT calculations were employed to determine the optimized geometries of the three photoinitiators and the respective ground state energies. For a detailed discussion of the minimum geometries, the reader is referred to the respective works of Thomas J. A. Wolf[130] and Hanna A. Ernst.[131]
As described in section 2.3.6, Type I photoinitiators perform radical cleavage after successful ISC into a triplet state. Therefore, ISC is a crucial step for the overall performance of a photoinitiator. The El-Sayed rule (see 2.3.6) predicts that $^1(n\pi^*)$ states easily perform an ISC into $^3(\pi\pi^*)$ states. However, next to the change in multiplicity it is also important to consider the energy gap

between the singlet and triplet states that are involved in the ISC. For all three initiators the smallest energy gaps are found between the S_1 and T_2 states. The involved orbitals in the T_2 state exhibit a partial $^3(\pi\pi^*)$ character. In the following, the major findings are summarized briefly. As a consequence of their similar behavior, benzoin and 4MB are jointly discussed.

Benzoin and 4MB

- Almost total decay of the TA within 100 ps
- Fast decay of the TA results in the formation of radicals after ISC
- Excitation takes place into the S_1 state
- The ISC takes place between the S_1 and T_2 states in a time range of 2-3 ps for both benzoin and 4MB
- 4MB shows a 3.4 times higher capability toward radical formation compared to benzoin
- 4MB shows a longer time constant associated with radical cleavage compared to benzoin

MMMP

- More complex mechanism than for benzoin and 4MB
- Excitation takes place into the S_1 and S_2 states
- The ISC takes place from the S_1 into the T_2
- The first absorption band in the TA spectra is assigned to singlet-singlet absorption of the S_1 state
- The second absorption band is assigned to triplet-triplet absorption of the T_1 state
- The triplet states exhibit long lifetimes (> 2 ns), radical cleavage products are not observable
- ISC and radical cleavage is performed on a larger timescale compared to benzoin and 4MB
- A high ISC efficiency of 94% is determined and thus a high radical formation capability

3.1.6. Conclusions

As a consequence of the above listed findings, a higher capability for radical formation was found for both MMMP and 4MB compared to benzoin. However, benzoin showed the highest initiation efficiency in the PLP-ESI-MS experiments. One of the reasons for the lower initiation efficiency of MMMP, as observed in the PLP-ESI-MS experiments, could be its strong triplet-triplet absorption, resulting from triplet states with long lifetimes. For 4MB, the radical cleavage takes place on a longer time scale compared to benzoin and can thus be a reason for its lower initiation efficiency. Another important factor that was not analyzed in this study, is the radical reactivity of the generated initiator fragments. The importance of this effect, together with other factors, will be discussed in more detail in the following chapter.

The present study has shown that the extinction coefficient at the excitation wavelength is a poor measure for the initiation efficiency of the respective photoinitiator radicals. Furthermore, the ISC efficiency and lifetimes of the resulting triplet states is better suited for estimating the initiation efficiencies. In addition, the different reactivities of the generated initiator radicals towards the utilized monomer has to be taken into account.

3.2. Investigation of Structure-Reactivity Correlations for Benzoin-Type Photoinitiators

Typically, the first look at the absorption spectrum of a photoinitiator tempts chemists, without the background knowledge about photochemical processes, to estimate the reactivity of the molecule at a specific wavelength. Thereby, the simple idea that molecules with high extinction coefficients absorb a large number of photons are excited with a high probability and, as a consequence, perform radical bond cleavage in high yields, is the basis for such assumptions. It results in the frequent conclusion that good photoinitiators exhibit high absorptivities at the respective irradiation wavelength. The current thesis shows that this approach is highly questionable, since the absorption of light entails a multitude of relaxation pathways and the radical cleavage is just one of them, as discussed in 2.3. In an excited molecule, several processes are in competition. Finally, after the generation of radicals, their respective reactivity is of high importance. A large number of formed radicals has no effect if their reactivity toward the monomer double bond is limited.

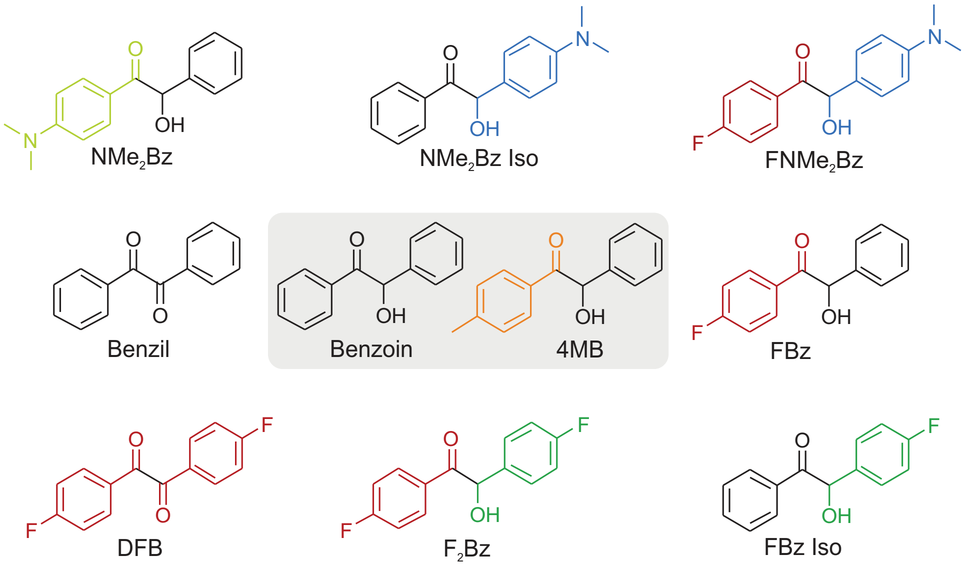

Figure 3.15.: Photoinitiator library: overview of the analyzed photoinitiators with varied substitution. Benzoin and 4MB served as comparison species.

As shown in the previous section, the quantitative investigation of initiation efficiencies of photoinitiator fragments can be performed by the powerful combination of PLP-ESI-MS and femtosecond spectroscopy. In this chapter the focus is on the influence of the substitution of a benzoin-type photoinitiator on its initiaiton efficiency and photochemical behavior. The enhancement of the initiation efficiency of benzoin is the aim of the present study. However, creating an instruction for a "tailormade" photoinitiator that fulfills specific requirements is the long-term aim.

On the basis of the benzoin structure, a library of photoinitiators with various substitution was synthesized, as illustrated in Figure 3.15. Substituents with an electron donating or withdrawing effect were incorporated, such as methyl, dimethylamine, and fluorine, respectively. The substituents were placed at the aromatic ring alongside the carbonyl or the hydroxyl group. Next to benzoin, the photoinitiator library was extended to benzil and its substituted derivative difluorobenzil (DFB). The substitution along the aromatic ring causes a change in the elctronic structure of the molecule, having an important impact on its photochemical behavior and the

reactivity of the generated radicals. The choice of substituents was thereby made based on their red-shifting influence on the absorption compared to the original benzoin structure.
Similar to the previous chapter, the photoinitiators were investigated by the combination of PLP-ESI-MS, TA spectroscopy, and quantum chemical calculations. However, in this study the rate coefficients of the generated radicals for their addition to MMA were additionally determined. Finally, the summarized results provide an insight into the correlation between the structure of a photoinitiator and its reactivity.

3.2.1. Photoinitiator Synthesis

The benzoin derivatives illustrated in Figure 3.15 were obtained by three synthetic routes. NMe_2Bz Iso and $FNMe_2Bz$ were synthesized via electrophilic aromatic substitution, starting from the respective phenylglyoxal monohydrates that react with the electron-rich benzene ring of *N*,*N*-dimethylanilin in a straightforward fashion.
The synthesis of FBz Iso and F_2Bz was performed via cyanide-catalyzed benzoin condensation of fluorobenzaldehyde (for F_2Bz) and fluorobenzaldehyde and benzaldehyde (for FBz Iso). During the synthesis, asymmetric benzoins are known to form a product mixture consisting of one main product that is the thermodynamically stable regioisomer, i.e., carrying the substitution at the benzoyl or the hydroxylbenzyl moiety. However, the second, less stable, regioisomer is additionally formed to a certain extent.[150] As shown recently by Yamataka *et al.*,[151] a base-catalyzed rearrangement can lead to the formation of the regioisomer of benzoins with substitution at the aromatic rings. Thereby, it is assumed that a deprotonation in α-position is the determining step, leading to a ketol-rearrangement into the respective regioisomer. In the current thesis, such rearrangements were observed during the workup after the benzoin condensation steps. However, for both basic and acidic conditions. As a result, for FBz Iso a mixture of the regioisomers (FBz Iso and FBz) was obtained.

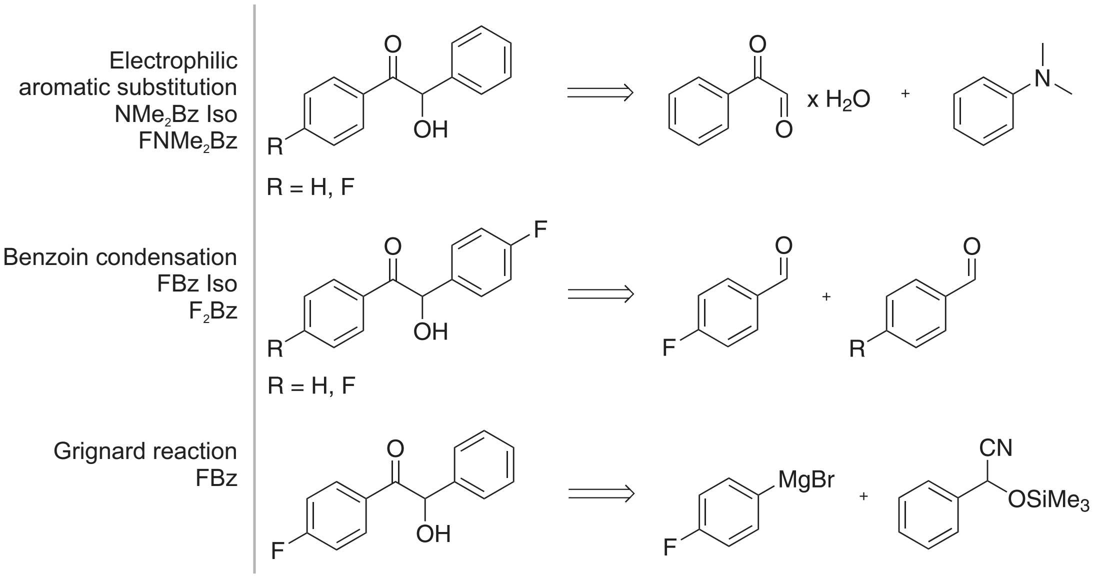

Figure 3.16.: The benzoin derivatives were obtained by the three illustrated synthetic pathways: electrophilic aromatic substitution, benzoin condensation, and Grignard reaction.

Thereby, FBz Iso is assumed to be the thermodynamically stable regioisomer, since it was formed in a higher ratio than FBz. Since chromatographic purification was not successful, FBz Iso was purified by manifold recrystallization steps.

Due to the performed rearrangement during and after benzoin condensation, the synthesis of FBz was performed via Grignard reaction. Thereby, trimethylsilylated cyanohydrin was reacted with fluorophenylmagnesium bromide as the Grignard reagent, resulting in a straightforward formation of pure FBz.

3.2.2. UV-Vis Spectroscopic Evaluation

As noted in the introduction of this chapter, the absorptivity of a photoinitiator is frequently correlated to its performance. A high extinction coefficient at the utilized irradiation wavelength can be beneficial. However, it is not mandatory, as will be concluded at the end of this chapter. Figure 3.17 depicts the extinction curves corresponding to the photoinitiator library and Table 3.4 summarizes the extinction coefficients at the employed wavelength in the PLP experiments (351 nm).

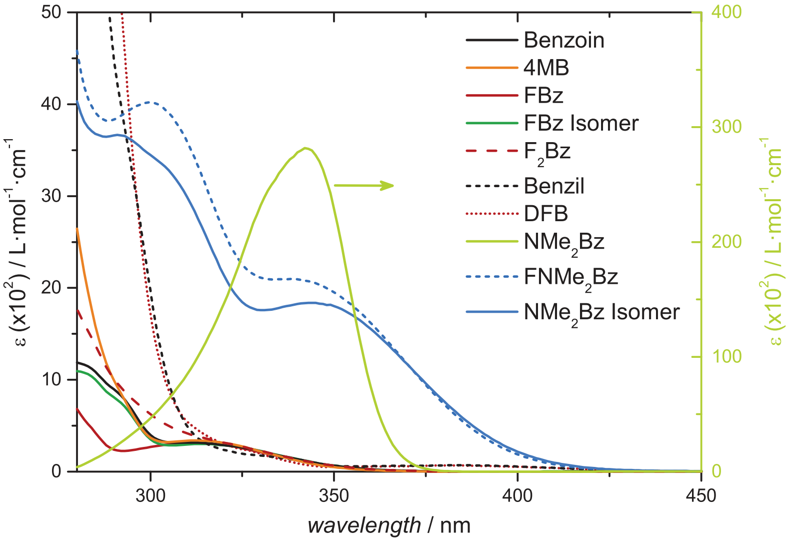

Figure 3.17.: Extinction curves of the photoinitiators depicted in Figure 3.15, measured in MIB. For clarity reasons the axis for the extinction of NMe_2Bz is situated on the right side of the graph.

The photoinitiators can be distinquished by their large differences in UV-vis absorbance. Benzoin itself shows a very low extinction coefficient (64 $L\cdot mol^{-1}\cdot cm^{-1}$) compared to its substituted derivatives. The benzoin derivatives with fluorine substitution, FBz, FBz Iso, and F_2Bz, exhibit extinction coefficients in a similar range (60, 66, and 63 $L\cdot mol^{-1}\cdot cm^{-1}$, respectively). The extinction of benzil and its derivative DFB is comparable to FBz and F_2Bz. The dimethylamine substituents have a strong influence on the absorption behavior and increase the extinction coefficient at 351 nm enormously, as observed for NMe_2Bz Iso and $FNMe_2Bz$ (1812 and 1950 $L\cdot mol^{-1}\cdot cm^{-1}$, respectively). NMe_2Bz shows a particularly increased extinction coefficient and an altered absorption curve compared to the other initiators.

3.2.3. Initiation Efficiencies via PLP-ESI-MS

The photoinitiators illustrated in Figure 3.15 were compared pairwise in so-called cocktail experiments. Thereby, different molar ratios of the photoinitiators were subject to PLP experiments. All initiators with a substitution at the benzoyl fragment were compared to benzoin. However,

Initiator	ε [L$\cdot$ mol^{-1}$\cdot$ cm^{-1}]^a	MMA conversion [%]^b	M_n [g$\cdot$mol^{-1}]	$Đ$
Benzoin	64	4.40	8500	2.01
4MB	52	6.00	8200	1.79
FBz	60	4.17	10000	2.05
FBz Iso	66	5.18	7900	1.90
F_2Bz	63	5.00	8900	2.15
NMe$_2$Bz	23400	0.25	–^{c}	–^{c}
NMe$_2$Bz Iso	1800	0.38	–^{c}	–^{c}
FNMe$_2$Bz	1950	0.53	13000	3.20
Benzil	63	0.39	–^{d}	–^{d}
DFB	59	1.58	16000	1.94

Table 3.4.: Extinction coefficients corresponding to the extinction curves depicted in Figure 3.17, monomer conversion in PLP experiments, and the respective molar masses and dispersities for the photoinitiators shown in Figure 3.15. ^{a}At 351 nm. ^{b}Determined by gravimetry. ^{c}No sufficient polymer output. ^{d}Not determined.

the initiators with substitution at the hydroxylbenzyl group cannot be compared to benzoin, due to their equal B fragment. For such initiators 4MB was chosen as the antagonist. Since the initiation efficiency ratio between benzoin and 4MB was determined in a previous study,[127] 4MB is well-known as an efficient initiator and can thus be employed for comparisons. Next to the cocktail experiments, the polymer output of all photoinitiators was investigated, the results are listed in Table 3.4. Thereby, the monomer conversion at specific PLP conditions (refer to the experimental part) and the molar mass and dispersity of the resulting polymer were determined by THF-SEC. High molar masses and low monomer conversions are characteristic for the generation of a small amount of radicals and vice versa. The achieved dispersities, all in the range of $Đ \approx 2$, are characteristic for an FRP process.

The determination of the respective initiation efficiencies was carried out in a similar way as described in the previous chapter (see 3.1.3). The mass bias-free ratio $G_{m/z,0}$ was calculated from the relative peak heights, Δh, of the respective disproportionation peaks and plotted against the employed initiator ratio. The ratio at which $G_{m/z,0}$ equals one corresponds to the initiation efficiency of the two compared initiator fragments. The graph in Figure 3.18 illustrates the determination of the mass bias-free ratio for the photoinitiators F_2Bz and benzoin and serves as an example. For the graphs of all other comparisons, the reader is referred to the Appendix. The initiation efficiency ratios determined in that way are provided in Table 3.5 and will be discussed in 3.2.5. However, for the dimethylamine-substituted species no initiation efficiency ratios could be determined, due to their very low polymer yields.

3.2.4. Additional Analytical Methods

Femtosecond Spectroscopy

In order to support the results obtained by PLP-ESI-MS, the photoinitiators were investigated by femtosecond pump-probe spectroscopy,[1] similar to the previous chapter. In a similar way, TA profiles for each photoinitiator were recorded at a pump pulse wavelength of 351 nm (as employed for the PLP experiments) and the population evolution of the excited states

---

[1] Experiments were carried out by Caroline Schweigert in the frame of a collaboration with PD Dr. Andreas-Neil Unterreiner, Physical Chemistry, Karlsruhe Institute of Technology

Compared fragments (initiators)		Initiation efficiencies PLP-ESI-MS
B (benzoin)	MB (4MB)	1 : 0.86
B (benzoin)	FB (FBz)	1 : 0.75
MB (4MB)	B (FBz Iso)	1 : 2.44
FB (FBz)	B (FBz Iso)	1 : 1.10
B (benzoin)	FB (F_2Bz)	1 : 1.09
MB (4MB)	FB (FBz)	1 : 1.23
BNMe$_2$ (NMe$_2$Bz)	B (benzoin)	n.d.[a]
B (NMe$_2$Bz Iso)	MB (4MB)	n.d.[a]
B (benzoin)	FB (FNMe$_2$Bz)	n.d.[a]
B (benzoin)	FB (DFB)	1 : 1.67

Table 3.5.: Overview of the compared initiators and the corresponding initiation efficiency ratios for the respective cocktail experiments. [a]Not determined due to substantial polymer yield differences of the compared photoinitiators.

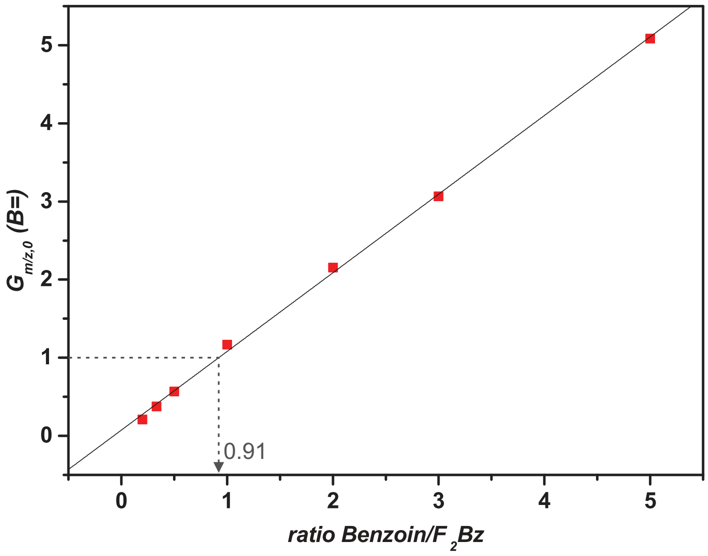

Figure 3.18.: Mass bias-free ratio plotted versus the molar ratio of the photoinitiators F_2Bz and benzoin.

was probed in the range of 500-600 nm wavelength. In contrast to the fs experiments in the previous chapter, no white-light continuum was employed for the probing. Thereby, the low extinction coefficients of some initiators at the utilized excitation wavelength, resulting in low amplitudes, were the decisive factor. Similar to the previous chapter, the TA profiles were fitted with triexponential functions to obtain the corresponding time constants τ_i and amplitudes A_i. Thereby, the time constant τ_1 corresponds to the combination of both IC and ISC processes. The time constant τ_2 represents dynamics of triplet states and radical formation. A detailed assignment to τ_3 is not possible within the scope of this work. Next to pump-probe experiments, ab initio calculation methods were employed to access information about the energetic position as well as the character of the singlet and triplet states involved in the important electronic transitions IC and ISC after excitation.

Calculations of Radical Reactivities

Next to the calculations regarding the orbitals involved in important electronic transitions, the reactivity of the generated initiator fragments was computed,[1] representing an important link between PLP-ESI-MS and femtosecond spectroscopy, since it helps understanding the underlying reasons for potential discrepancies between the two fields. For instance, radical reactivities can explain why poor initiation rates are found for an initiator that generates a large amount of radicals. Thereby, for each radical initiator fragment illustrated in Figure 3.15, the addition rate coefficient for the addition to the MMA double bond was computed. The photoinduced radical cleavage of a benzoin derivative generates two radical fragments with strongly differing reactivities. The acyl radical (referred to as benzoyl radical), with its sp^2 character, is unstable and thus highly reactive. Its radical is relatively localized and can thus be influenced in its reactivity by substitution in para-position via an inductive effect. The second – sp^3-type – hydroxybenzyl radical that is generated, is stabilized by its electronic structure and thus less reactive. The adjacent hydroxyl and phenyl functions stabilize the radical by electronic conjugation. A substituent in para-position can thus have an additional stabilizing influence, depending on its effect on the aromatic system.

The computed addition rate coefficients are summarized in Table 3.6. The reactivity of the radical fragments toward MMA can be listed in the following order: FB > B > MB > $BNMe_2$ » $BnNMe_2$ > Bn > BnF. The electron-donating dimethylamine substituent decreases the reactivity of the benzoyl radical, yet it increases the hydroxybenzyl radical reactivity. The latter can be explained by the relatively nucleophilic character of hydroxybenzyl radical that is additionally enhanced by the incorporation of an electron-donating group. A similar effect is observed for the fluorine group, an electron-withdrawing substituent: It increases the benzoyl radical reactivity, yet strongly decreases the reactivity of the corresponding hydroxybenzyl radical. Here, the electrophilic character of the benzoyl radical – resulting from its sp^2 type – is enhanced by the inductive effect of an electron-withdrawing group.

Radical fragment	k_{sol}
FB	16
B	6.3
MB	5.1
$BNMe_2$	4.2
$BnNMe_2$	0.14
Bn	0.02
BnF	0.01

Table 3.6.: Theoretically calculated rate coefficients ($\times\ 10^4\ L{\cdot}mol^{-1}{\cdot}s^{-1}$) for the addition of photoinitiator radical fragments to MMA, in bulk at -5°C.

In the further course of this work, the results of PLP-ESI-MS, femtosecond spectroscopic experiments, and theoretical methods are presented in separated groups consisting of structurally similar photoinitiators.

---

[1] Calculations were carried out by Benjamin B. Noble in the frame of a collaboration with Prof. Michelle L. Coote, Australian National University, Canberra.

3.2.5. Combined Photoinitiator Analysis

The behavior of the photoinitiators is discussed in the following, separated by substitution type. Thereby, the results from the three viewpoints PLP-ESI-MS, femtosecond spectroscopy, and theoretical calculations are summarized.

FBz, FBz Iso, and F_2Bz

Organic moieties carrying a halogen substituent are usually subject to both an inductive (-I) and mesomeric effect (+M), resulting from the electronegative group and its free electrons. The coexistence of both effects can be an interesting feature for photoinitiators. Thereby, fluorine plays a special role as the element with the highest electronegativity. The photoinitiator library compiled in this study, exhibits three benzoin derivatives with fluorine substitution: FBz carries a fluorine group in para-position of the reactive benzoyl moiety, FBz Iso – as the regioisomer – exhibits the fluorine group at the less reactive hydroxylbenzyl group, and F_2Bz carries two fluorine groups, one at each para-position.

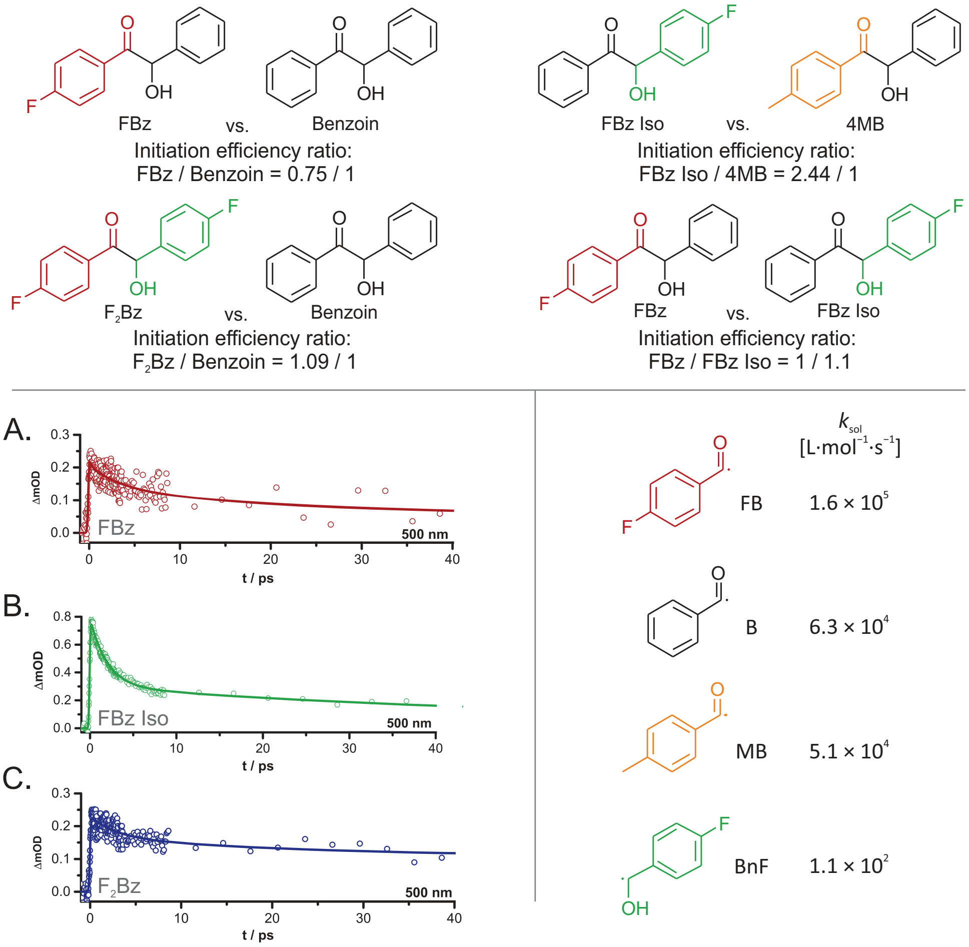

Figure 3.19.: Combined analytical results for the investigation of FBz, FBz Iso, and F_2Bz. Top: initiation efficiency ratios of FBz vs benzoin, FBz Iso vs 4MB, F_2Bz vs benzoin, and FBz vs FBz Iso determined by PLP-ESI-MS. Left: transients of FBz (A), FBz Iso (B), and F_2Bz (C) from femtosecond pump-probe experiments with probe pulses at 500 nm. Right: rate coefficients for the addition to MMA, k_{sol}, for the radical fragments of FBz, FBz Iso, F_2Bz, benzoin, and 4MB.

All three fluorine-substituted derivates discussed here exhibit relatively high monomer conversions in the PLP experiments, comparable to benzoin (see Table 3.4), serving as a first reference to their initiation behavior. Figure 3.19 summarizes the results obtained by PLP-ESI-MS, femtosecond spectroscopy, and calculation methods.

The comparison of FBz with benzoin via PLP-ESI-MS results in an initiaion efficiency ratio of 0.75 : 1 for the fragments FB : B. Hence, FBz shows a lower initiation efficiency compared to benzoin. FBz Iso cannot be compared to benzoin, due to their identical benzoyl fragment, and was thus compared to 4MB. The benzoyl fragment B originating from FBz Iso exhibits a clearly better performance than the methyl-benzoyl fragment, resulting in an initiation efficiency ratio of B : MB being 2.44 : 1. Interestingly, the obtained mass spectra from FBz Iso-initiated polymer showed no peaks originating from the fluorine-substituted hydroxylbenzyl fragment (BnF). The particularly low addition rate coefficient of BnF fragment, as shown in Table 3.6, is clearly responsible for this result. Subsequently, the two regioisomers were compared to each other, resulting in an initiation efficiency ratio of FB : B being 1 : 1.1. A better initiation performance is thus assigned to FBz Iso. Although the 1.1 times higher efficiency for the B fragment of FBz Iso is not greatly pronounced, the clear increase in efficiency from the comparison of FBz Iso to 4MB is evident. Additionally, a particularly high monomer conversion (approx. 5.2%) can be found for FBz Iso. The weak advantage of the B fragment originating from FBz Iso, compared to the FB fragment could be a result from a beneficial ionization behavior of FB-initiated chains due to the polar fluorine group. The comparison of F_2Bz to benzoin resulted in an initiation efficiency ratio of FB : B being 1.1 : 1, stating that the two fluorine substituents have a positive impact on the initiator performance.

All three fluorine-substituted derivatives show TA traces with a very low optical density. Further, their very fast decay is striking and suggests well-accessible deexcitation pathways. All three derivatives exhibit an excited singlet state S_1 around 350 nm with an $n\pi^*$ character. Two triplet states T_1 and T_2 (with partial $n\pi^*$ and $\pi\pi^*$ character) are in close energetic proximity to the S_1 state, as observed for benzoin and 4MB in the previous chapter. Based on the favorable position of the triplet states, a combination of IC and ISC processes presumably results in the fast decay that can be observed in the TA traces. The corresponding time constant τ_1 is in the range of 2-3 ps for all three fluorine-subsituted derivatives.

The reactivity calculations for the radical fragments show an increased reactivity for the FB fragment (found in FBz and F_2Bz) compared to the B fragment. Hence, FBz should perform better than benzoin. However, FBz presumably forms less radicals than benzoin and can thus not compete. The positive influence of the fluorine substituent on the benzoyl fragment is thus compensated by a lower probability to form radicals.

NMe_2Bz, NMe_2Bz Iso, and $FNMe_2Bz$

The functionalization of benzoin with amine groups has been previously reported in the literature.[150,152,153] Their electron-donating effect on the benzoin structure was the reason for choosing it as a substitutent for this study. The resulting dimethylamine-functionalized benzoin derivatives exhibit a strongly increased and red-shifted absorptivity compared to benzoin. Hence, they were expected to perform well in the PLP experiments.

However, after the first polymerizations it turned out that very poor polymer yields of the amine-substituted derivatives ($\leq$ 0.5%), compared to benzoin (approx. 4.5%), made it unfeasible to collect a sufficient amount of polymer that could be analyzed by ESI-MS. Subsequently, a fluorine-substituent was introduced, in addition to the amine-functionality, in order to improved the initiation performance. The resulting $FNMe_2Bz$ carries a dimethylamine substitutent in para-position at the hydroxylbenzyl fragment and a fluorine substituent in para-position at

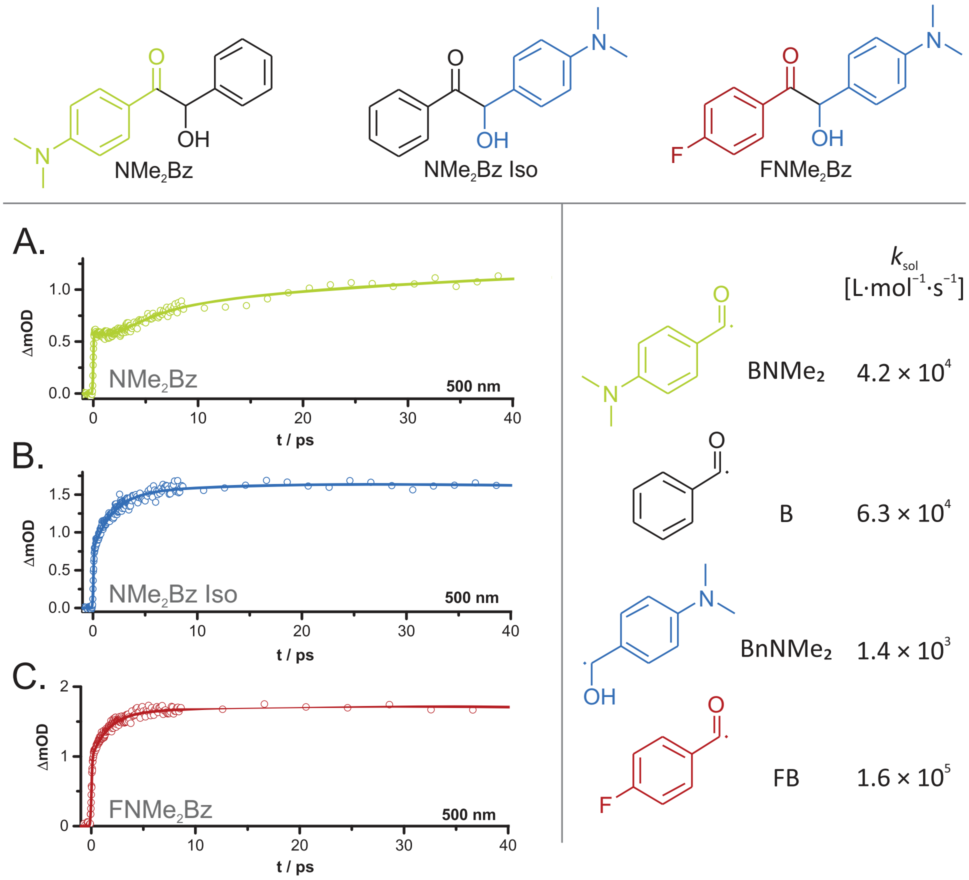

Figure 3.20.: Combined analytical results for the investigation of NMe_2Bz, NMe_2Bz Iso, and $FNMe_2Bz$. Transients of NMe_2Bz (A), NMe_2Bz Iso (B), and $FNMe_2Bz$ (C) from femtosecond pump-probe experiments with probe pulses at 500 nm. Right: radical fragments of NMe_2Bz, NMe_2Bz Iso, and $FNMe_2Bz$ and their corresponding rate coefficients for the addition to MMA.

the benzoyl fragment. However, no significant impact could be detected. $FNMe_2Bz$ exhibits the highest polymer yield of all amine-functionalized derivatives, nevertheless a comparison via PLP-ESI-MS could not be performed.

In contrast to PLP-ESI-MS, the investigation of the dimethylamine-substituted benzoin derivatives was unproblematic, since their high extinction coefficients entail high optical densities. The TA traces, as illustrated in Figure 3.20, exhibit particularly long delay times, showing no fast decay as observed for the fluorine-substituted species. Ab initio calculations showed that NMe_2Bz is excited into an S_1 state with $n\pi^*$ character upon irradiation with 351 nm. NMe_2Bz Iso and $FNMe_2Bz$ reach their S_2 state upon absorption of a photon. For all three derivatives a multitude of triplet states with $\pi\pi^*$ character and energetic approximation was found. Following the El-Sayed rule, the ISC from $n\pi^*$ into $\pi\pi^*$ states is an allowed process and thus favored. However, the large number of triplet states results in their overlay, illustrated by the long delay times of their TA traces. Inspection of the plateau-like shape of the TA traces shows that the amine-substituted benzoin derivatives form excited triplet states and subsequently show a longterm abidance in their triplets without deexcitation via radical scission. The latter serves as an explanation for the particularly high extinction coefficients found for NMe_2Bz, NMe_2Bz Iso, and $FNMe_2Bz$. Thus, the poor initiation performance – as seen from the femtosecond experiments – results from the low capability of radical formation, since after the ISC a large

number of triplet states is accessible. The radical scission is not the favored deexcitation pathway.
An alternative explanation for the poor initiation performance of the amine-substituted benzoin derivatives are the low radical reactivities that were found for the respective benzoyl fragment. The fragment $BNMe_2$ shows a 33% lower addition rate coefficient compared to the benzoyl fragment B. However, the high reactivity found for the FB fragment of $FNMe_2Bz$ cannot compensate the negative influence of the amine-substituent. The driving negative impact on the initiation performance of NMe_2Bz, NMe_2Bz Iso, and $FNMe_2Bz$ is assumed to be the multitude of accessible triplet states, preventing the excited molecules from performing radical scission. Thus, no sufficient amount of radicals is generated in order to initiate a polymerization.

DFB and Benzil

After observing the positive impact of fluorine substituents, their influence was further investigated for a different photoinitiator system: Benzil, structurally related to benzoin, is known to show poor initiation performance. Thus, the question arose if its initiation efficiency can be enhanced through the introduction of fluorine substituents. The newly synthesized difluorobenzil (DFB) derivative as well as benzil both generate two equal radical fragments that can initiate a polymerization. The combined analytical results are illustrated in Figure 3.21.

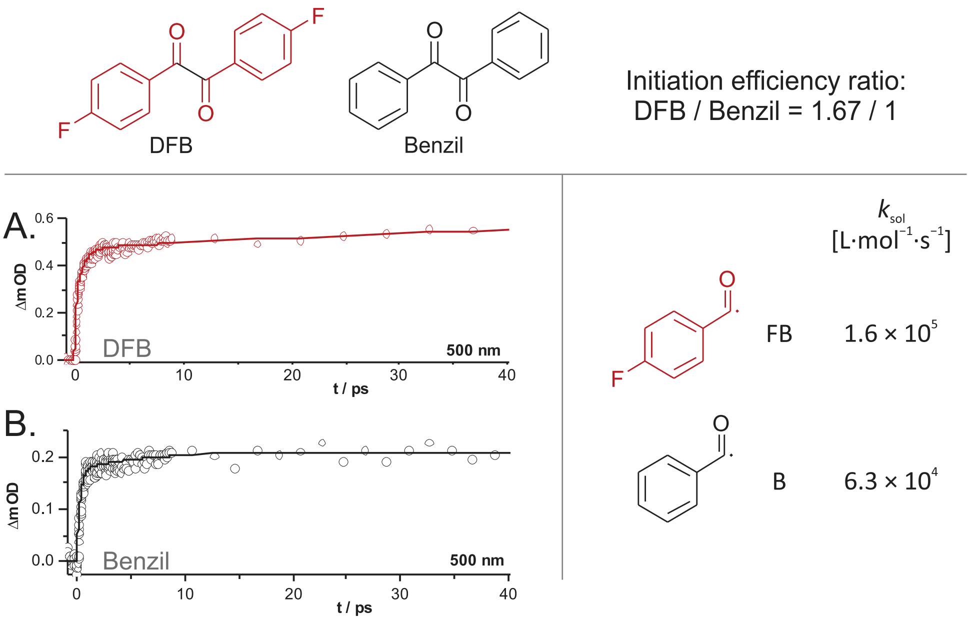

Figure 3.21.: Combined analytical results for the investigation of DFB and benzil. Top: initiation efficiency ratios of DFB vs benzil determined by PLP-ESI-MS. Left: transients of DFB (A) and benzil (B) from femtosecond pump-probe experiments with probe pulses at 500 nm. Right: rate coefficients for the addition to MMA, k_{sol}, for the radical fragments of DFB and benzil.

In the direct comparison via PLP-ESI-MS, an initiation efficiency ratio for the fragments FB : B was found to be 1.67 : 1. Consequently, the substitution has a positive influence.
In order to find an explanation, TA spectra were recorded and theoretical calculations performed for both benzil and DFB. It was found that both DFB and benzil are excited into an S_2 state with $n\pi^*$ character after irradiation with 351 nm. Below the S_2 state, in energetic proximity, six triplet states are situated. Thereby, T_1 and T_4 exhibit $n\pi^*$ character and are thus

not suitable for ISC. The other four triplet states have mixed or $\pi\pi^*$ character and are not appropriate states for radical scission. Consequently, the poor initiatior performance of benzil derivatives in general is presumably a result of the unfavored formation of radicals. Both DFB and benzil generate a small number of radicals, however the higher initiation efficiency of the fluorine-substituted derivate is most probably a result of the higher radical reactivity of the FB fragment compared to B.

3.2.6. Critical Evaluation of the PLP-ESI-MS Method

In the current work the comparison of initiator fragments regarding their initiation efficiency gave so-called initiation efficiency ratios for two fragments, respectively. The latter can be directly correlated to the amount of polymer chains that have been initiated by one single radical initiator fragment, compared to a second fragment. Assuming a quantitative comparison of the initiator fragments, the determined ratios should allow for a cross-comparison with other fragments. More precisely, if the initiation efficiency ratio for the fragments A : B and B : C is experimentally determined, the ratio of the fragments A : C should be predictable. This is demonstrated for the three initiator fragments B, FB (from FBz), and MB. The initiation efficiency ratio of B : FB equals 1.33 (FB from FBz) and the ratio of B : MB equals 1.16. Thus, the ratio of MB : FB should be possible to predict, as illustrated in Equations 3.9-3.12.

$$\frac{B}{MB} = \frac{1.16}{1} \quad \text{and thus} \quad MB = \frac{1.16}{B} \tag{3.9}$$

$$\frac{B}{FB} = \frac{1.33}{1} \quad \text{and thus} \quad FB = \frac{1.33}{B} \tag{3.10}$$

$$\frac{MB}{FB} = \frac{1.16}{B} \cdot \frac{B}{1.33} \tag{3.11}$$

$$\frac{MB}{FB} = \frac{0.85}{1} \tag{3.12}$$

As Table 3.5 shows, the initiation efficiency ratio of MB : FB equals 0.81 (1 : 1.23). Thus, the calculated value is in good agreement with the experimental value. However, the term "quantitative comparison" of polymers via ESI-MS should be always used with care. The ionization process of polymers is highly sensitive to changes in the molecular structure. Not only the polymer backbone should be equal for the compared polymers, yet also the end groups should not exhibit pronounced differences in size, electronic structure, and elemental composition. All the fragments compared in the current study exhibit a six-membered aromatic ring with a carbonyl function. The substitution along the aromatic ring is the only structural difference between the fragments. Thus, the comparison via PLP-ESI-MS performed in the current work is assumed to be quantitative, as shown for the cross-comparison in Equations 3.9-3.12.

3.2.7. Summary and Conclusion

As a summary, it can be stated that electron-withdrawing substituents have a negative impact on the initiation efficiency of benzoin-type photoinitiators. Regardless of the substituents' position – at the benzoyl or the hydroxylbenzyl fragment – the introduction of a dimethylamine group results in a lower initiation efficiency in comparison to benzoin. As seen for FNMe$_2$Bz, the negative impact of the dimethylamine substituent has a further deteriorating effect on fluorine-substituted derivatives.

The investigation of the fluorine-substitution showed that the fluorine-group has a positive influence on the initiation efficiency of the benzoin photoinitiator, if it is introduced at the unreactive hydroxylbenzyl moiety, as seen for FBz Iso. Although the radical para-fluoro benzoyl fragment is highly reactive, the fluorine-substituent has a slightly negative impact on the generation of radicals, i.e., delaying the radical bond scission.

Based on the aforementioned results, a set of important properties was compiled, summarizing the characteristics of a poor and a good benzoin-type photoinitiator.

First of all, the character of the electronic states involved in excitation and ISC is crucial. A poor benzoin-type photoinitiator exhibits a multitude of triplet states with a partial $\pi\pi^*$ character in energetic proximity to the excited singlet state. An excited system remaining in such overlapping triplet states consequently shows a high extinction coefficient at the excitation wavelength.

In contrary, a good benzoin-type photoinitiator is characterized by the following properties: (i) It exhibits a low extinction coefficient of approx. 60 $\mathrm{L \cdot mol^{-1} \cdot cm^{-1}}$. (ii) The excitation occurs into a singlet state with $n\pi^*$ character and the fast ISC (on a time scale of 2-4 ps) is performed into a triplet state with equal $n\pi^*$ character, since radical formation from such states are favored. The resulting violation of the El-Sayed rule is presumably necessary. (iii) The number of accessible triplet states should not exceed two, in order to avoid an overlap of triplet states. (iv) Radical cleavage should occur in the time frame of maximum 100 ps. (v) Finally, the generated radicals should posess a high reactivity for the addition to monomer.

4

Mechanistic Investigation of Copper-Mediated PhotoRDRP

Copper-mediated photoRDRP is the recent extension of ATRP and SET-LRP, implementing a light-triggered start of the polymerization. Thereby, as discussed in section 2.1.3, the catalyst $Cu^{II}Br_2/L$ is introduced in its oxidized state. Without the addition of any reducing agent, the polymerization is initiated solely by irradiation. Therefore, light is assumed to be involved in the reduction step, i.e., in the generation of the activator $Cu^{I}Br/L$.
Attempts were made by Anastasaki *et al.*[16] and Ribelli *et al.*[17] to investigate the mechanism of this process. Their studies, explained in detail in section 2.1.3, provided evidence that initiator and/or the ligand are involved in the reduction step. However, both studies lack detailed mechanistic information about how the individual compounds are involved in the photochemical process. For instance, an elucidation of the involved structures by nuclear magnetic resonance spectroscopy (NMR), mass spectrometry, or similar exact techniques is missing. Therefore, in this chapter, the mechanism of photoRDRP is elucidated on a molecular level. PLP was employed as polymerization technique and the resulting products were subsequently analyzed by ESI-MS, resulting in the illumination of the important processes in photoRDRP that lead to the efficient reduction of the deactivator $Cu^{II}Br_2/L$ and the initiation of the polymerization.

4.1. Stepwise Mechanism Elucidation via PLP-ESI-MS

PLP serves as the ideal polymerization method for the investigation of the mechanism, since it generates relatively short polymer chains that can be analyzed by ESI-MS. The latter provides exact information on the product structure such as the polymer end groups. Knowing the end group of a polymer chain helps identifying the initiating radical.
The two previously performed mechanistic studies employed MA as the monomer. However, in the current work MMA was chosen as the monomer, since it does not perform intramolecular chain transfer reactions (as observed for MA), results in shorter polymer chains due to its lower propagation rate coefficient compared to MA, and can thus be readily analyzed by ESI-MS. Similar to the previous studies, the composition of the photoRDRP reaction was varied by omitting single components and performing independent PLP experiments. Ethyl α-bromoisobutyrate (EBiB, initiator), copper (II) bromide, and tris-[2-(dimethylamino)ethyl]amine (Me_6TREN, ligand), typical ingredients for a photoRDRP reaction, were selected for the study. DMSO served as the solvent, since it showed a positive effect on the monomer conversion.[16]
As a first step, the initiator, ligand, and $CuBr_2$, respectively, were irradiated in a solution of monomer and DMSO, allowing for an understanding how these components behave under UV irradiation. Subsequently, PLP experiments with different combinations of the components

---

Parts of this chapter were reproduced from E. Frick, A. Anastasaki, D. M. Haddleton, C. Barner-Kowollik, *J. Am. Chem. Sci.* **2015**, *137*, 6889-6896.

were carried out, as summarized in Table 4.1. These experiments showed how the reactive species, generated under irradiation, interact with each other.

Entry	[M]:[I]:[$CuBr_2$]:[L]	MMA conversion [%]	M_n [g·mol^{-1}]	Đ
1	50 : - : - : -	-	-	-
2	50 : 1 : - : -	3.1	18000	1.56
3	50 : - : - : 0.06	0.6	20000	5.00
4	50 : - : 0.02 : -	-	-	-
5	50 : - : 0.02 : 0.06	3.3	14400	2.93
6	50 : 1 : - : 0.06	1.6	14000	2.21
7	50 : 1 : 0.02 : -	-	-	-
8	50 : 1 : 0.02 : 0.02	2.1	1900	1.28
9	50 : 1 : 0.02 : 0.03	3.8	2100	1.29
10	50 : 1 : 0.02 : 0.04	3.8	2100	1.28
11	50 : 1 : 0.02 : 0.08	5.3	2600	1.24

Table 4.1.: Summary of all experiments with varied compositions that were carried out by PLP. The experiments containing monomer (M), initiator (I), or ligand (L) were carried out in 30 vol % DMSO solutions and with 90 000 laser pulses. Entry 11 was carried out with 60 000 pulses.

Figure 4.1 illustrates all species that were detected by ESI-MS. Finally, in order to have complete evidence regarding the proposed structures, all measurements were additionally performed by high-resolution orbitrap mass spectrometry. In the following, the results are discussed in detail and, finally, summarized in the postulation of a new mechnism for photoRDRP.

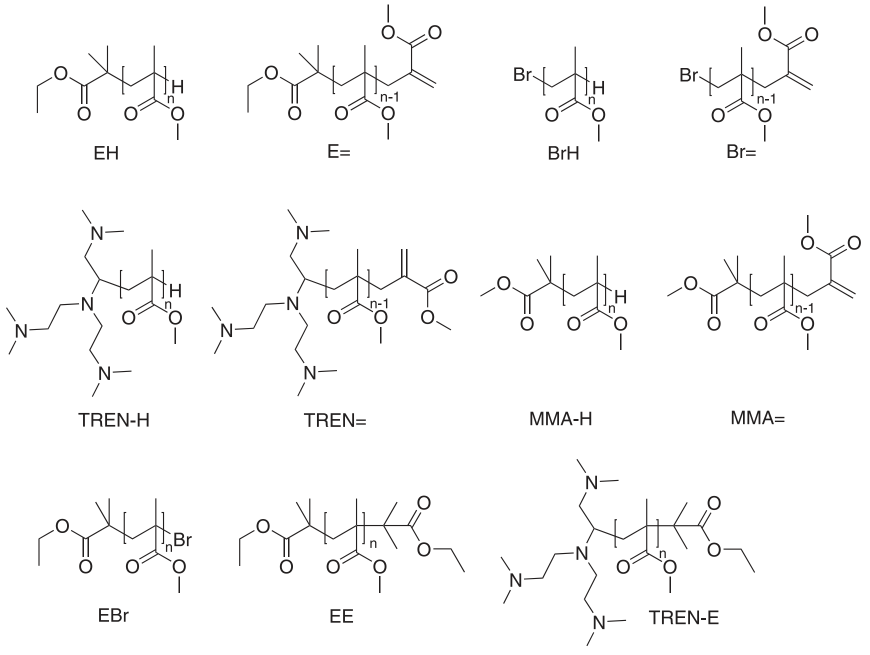

Figure 4.1.: Chemical structures found in ESI-MS, derived from variations in the composition.

4.1.1. PLP Experiments

Irradiation of EBiB/MMA

In the irradiation experiments with EBiB as the only component, next to monomer and solvent, polymerization was observed (see entry 2 in Table 4.1). Without copper or ligand being present, the polymerization was initiated by EBiB, an alkyl halide that performs a homolytic C-Br bond scission in the presence of the activator $Cu^{I}Br/L$. Thereby, the deactivator complex $Cu^{II}Br_2/L$ is formed next to an ethyl isobutyrate tertiary radical that can initiate the propagation of monomer. In general, EBiB – or other typical ATRP initiators – is not expected to generate radicals without the presence of the respective copper complex or to act as a radical photoinitiator. However, the present experiments clearly show that a radical cleavage into an ethyl isobuturate and a bromine radical is performed under irradiation. Both radicals initiate polymerization, as illustrated in Figure 4.2 and evidenced by the respective mass spectrum. Mass spectrometric analysis of the resulting polymer shows disproportionation peaks of poly(methyl methacrylate) (pMMA) that was initiated by an ethyl isobutyrate fragment (see peaks E= and EH) or by a bromine species (peaks Br= and BrH). The latter shows the characteristic isotopic pattern of a bromine-functionalized polymer. Additionally, the combination product EE can be detected. Hence, EBiB can obviously act as a photoinitiator at the employed wavelength of 351 nm.

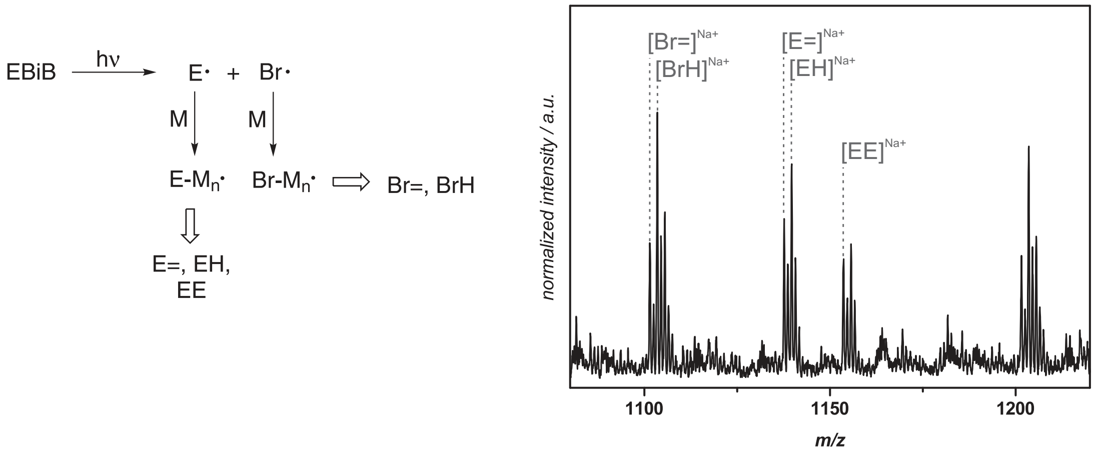

Figure 4.2.: Reaction pathway of EBiB after irradiation and the corresponding mass spectrum of pMMA synthesized with the combination of [MMA]:[EBiB]:[$CuBr_2$]:[Me_6TREN] = 50:1:0:0, entry 2 in Table 4.1.

Irradiation of Me_6TREN/MMA

A photoinitiated polymerization of MMA was observed in a solution of monomer, DMSO, and the ligand Me_6TREN (see entry 3 in Table 4.1). Thereby, in the subsequent mass spectrometric analysis, Me_6TREN-initiated chains (disproportionation peaks TREN= and TRENH, with ionization by sodium ions or protons) were found next to chains that were initiated by MMA itself, as illustrated in Figure 4.3. This finding shows that the ligand, an aliphatic tertiary amine, is a photoactive compound that generates radical species upon irradiation with UV light. Surprisingly, next to ligand-initiated chains, polymer that was initiated by the monomer itself was found. MMA alone is not known to be photoactive or to photochemically generate radicals, as shown by the lack of conversion in entry 1 of Table 4.1. An external radical source is necessary to initiate its propagation. An explanation for the formation of MMA-initiated polymer could be that photochemically excited Me_6TREN species experience a hydrogen abstraction in α-position to one of their amine groups by the monomer. Through the abstraction the monomer forms a radical that is well-suited for prapagation. Since, in addition, amines can form radical cations under irradiation, the reaction scheme in Figure 4.3 shows the respective Me_6TREN radical cations in brackets. In the further course of this work, the role of radical cations for the mechanism of photoRDRP will be discussed in more detail. In order to simplify the nomenclature, the short synonym TREN is utilized for Me_6TREN in reaction schemes and peak assignments.

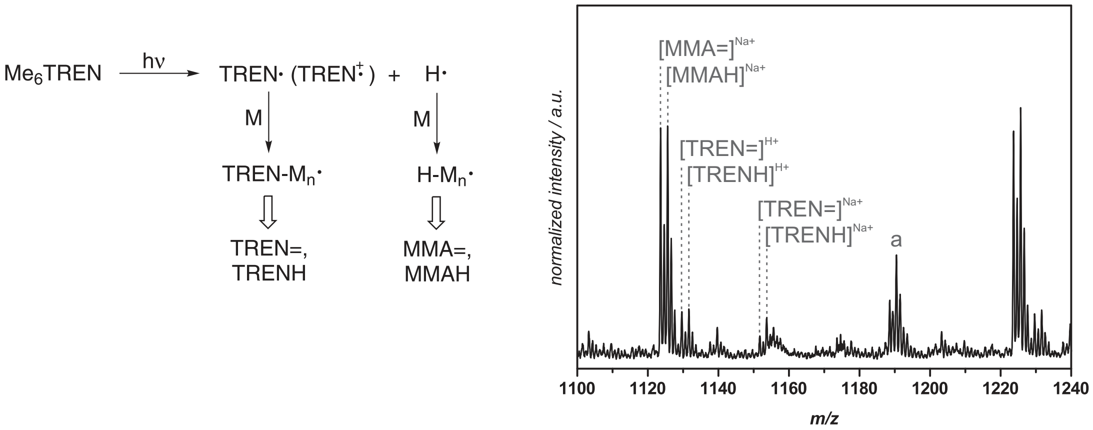

Figure 4.3.: Reaction pathway of Me_6TREN after irradiation and the corresponding mass spectrum of pMMA synthesized with the combination of [MMA]:[EBiB]:[$CuBr_2$]:[Me_6TREN] = 50:0:0:0.12, entry 3 in Table 4.1.

Irradiation of Me_6TREN/$CuBr_2$/MMA

PLP experiments performed with $CuBr_2$ and Me_6TREN show a relatively high monomer conversion of close to 3.3%. Remarkably, a color change was observed in the reaction solution from initially green to colorless after the irradiation. Thus, the activator complex $Cu^{II}Br_2/L$, formed by $CuBr_2$ and Me_6TREN, is most probably reduced to $Cu^{I}Br/L$ during the irradiation process.

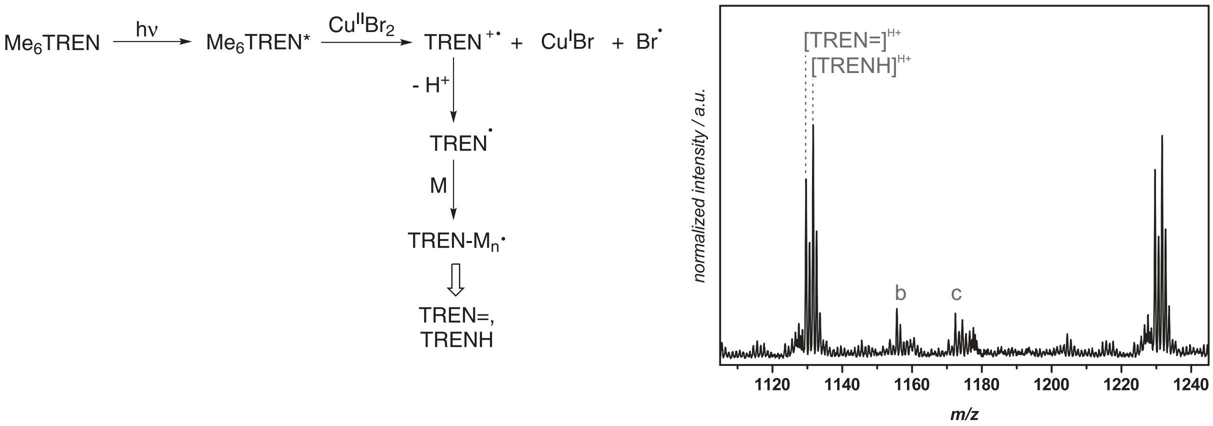

Figure 4.4.: Reaction pathway of Me_6TREN in the presence of $CuBr_2$ after irradiation and the corresponding mass spectrum of pMMA synthesized with the combination of [MMA]:[EBiB]:[$CuBr_2$]:[Me_6TREN] = 50:-:0.02:0.06, entry 5 in Table 4.1.

In the mass spectrometric analysis Me_6TREN-initiated chains appear as the exclusive product, while MMA-initiated chains are absent. The reduction of the copper complex – illustrated by the change of color – on the one hand and the lack of MMA-initiated chains on the other hand, are most probably connected. One suggestion could be that the photochemically excited ligand – present in excess compared to $CuBr_2$ – is able to reduce $CuBr_2$ species toward CuBr. Thereby, an amine radical cation (a so-called aminium radical) is generated that can subsequently form an α-aminoylkyl radical via deprotonation in the respective α-position. The resulting TREN radical, as illustrated in the reaction scheme in Figure 4.4, is most likely initiating the polymerization of MMA, forming the disproportionation products TREN= and TRENH that can be observed in the corresponding mass spectrum. The bromine radicals formed in the reduction process can further contribute to the generation of the activator Cu^IBr/L, as discussed in the further course of this work.

Irradiation of EBiB/Me_6TREN/MMA

A mixture of initiator, ligand, and monomer was irradiated in PLP experiments. Subsequent mass spectrometric analysis showed pMMA that was initiated by ethyl isobutyrate radical fragments (E= and EH) as well as by Me_6TREN radicals (TREN= and TRENH), as illustrated by Figure 4.5. Interestingly, no bromine- or MMA-initiated chains were detected. Thus, in this reaction mixture, bromine radicals most probably follow an alternative pathway. First, the bromine radical could perform a hydrogen abstraction from an excited ligand species, forming TREN radicals that subsequently initiate propagation. Second, bromine radicals may undergo a termination reaction with a growing polymer chain. In addition, a possible pathway for the bromide radical could be the formation of a ligand-bromide complex, as previously reported in metal-free ATRP.[12] Yet, such complexes are assumed to be unstable and decompose into the respective amine radicals that can initiate propagation. The peaks a, b and c, and d (found in Figures 4.3,4.4, and 4.5, respectively) were investigated by collision-induced dissociation (CID) experiments. While it was possible to find amine- and ethyl oxide-based fragments, an unambiguous assignment of the peaks revealed impossible. It must be noted that signal d does not appear in orbitrap ESI-MS measurements. It can therefore be assumed that the species is formed during the ionization process.

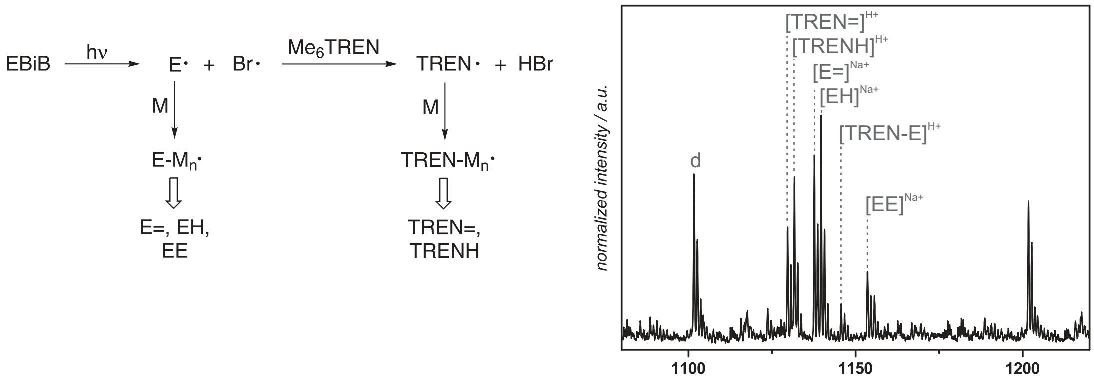

Figure 4.5.: Reaction pathway of EBiB and Me_6TREN after irradiation and the corresponding mass spectrum of pMMA synthesized with the combination of [MMA]:[EBiB]:[$CuBr_2$]:[Me_6TREN] = 50:1:-:0.06, entry 6 in Table 4.1.

Irradiation of EBiB/$CuBr_2$/MMA

After the irradiation of the mixture of EBiB, $CuBr_2$, and monomer, no polymer could be isolated. This result was surprising since the initiation of a polymerization solely via irradiation of EBiB and monomer was successful. Thus, the presence of $CuBr_2$ prevents the initiation step and acts as a radical quencher. Furthermore, the change of color of the solution from initially green to pale yellow serves as an indication for the reduction of the copper species. The yellow color could be an indication for the formation of small amounts of bromine. Thus, the following reaction is proposed: Both ethyl isobutyrate and bromine radicals are formed upon irradiation. However, as illustrated in Figure 4.6, the radicals are quenched by $CuBr_2$, resulting in the formation of CuBr in its reduced oxidation state as well as the original EBiB and bromine (Br_2).

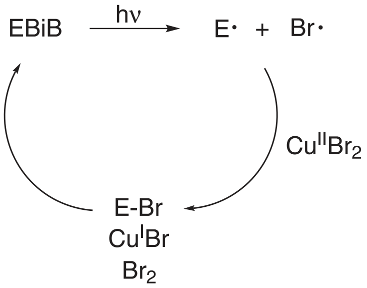

Figure 4.6.: Proposed reaction pathway of EBiB in the presence of $CuBr_2$ after irradiation, corresponding to the combination of [MMA]:[EBiB]:[$CuBr_2$]:[Me_6TREN] = 50:1:0.02:-, entry 7 in Table 4.1. No polymer could be isolated.

Irradiation of EBiB/$CuBr_2$/Me_6TREN/MMA (PhotoRDRP)

The irradiation of a solution containing all components of a photoRDRP (EBiB, $CuBr_2$, Me_6TREN, and monomer) resulted in a controlled-living polymerization of MMA with low molar masses and dispersities ($Đ \leq 1.3$). Hence, a clear difference can be identified compared to the free radical polymerizations that occured in the previously described combinations, resulting in polymer with a high molar mass and dispersities with $Đ \geq 2$.

Further, the linear correlation between the molar mass and the respective monomer conversion (or applied pulse number) indicates a living character (see Appendix, Figure A.12). Mass spectrometric analysis of the polymer shows ethyl isobutyrate-initiated chains with a bromine end group as the main product (EBr), as illustrated in Figure 4.7. The detection of ethyl isobutyrate-initiated polymer bearing a bromine end group (EBr) clearly indicates that the atom-transfer reaction occurs successfully during the pulsed-laser polymerization. However, next to the EBr product, disproportionation products initiated by an ethyl isobutyrate radical (E= and EH) and their respective combination products (EE) can be found to a smaller extent. No polymer can be found that was initiated by a Me_6TREN, a bromine, or an MMA radical. The PLP-ESI-MS technique gives insight mainly into the early steps of the polymerization, as underlined by the low MMA conversions of $\leq 3.8\%$. Therefore, the lack of ligand- and bromine-initiated chains illustrates the strong capability of the excited Me_6TREN moieties and the bromine radicals to act as reducing agents for $CuBr_2$ species. The rate coefficient for their reduction step is thus assumed to be significantly higher than for the addition onto the monomer molecule.

Next to the mass spectrometric analysis of the resulting polymer samples via quadrupole ESI-MS (see section 2.5), high-resolution orbitrap ESI-MS was employed in order to unambiguously

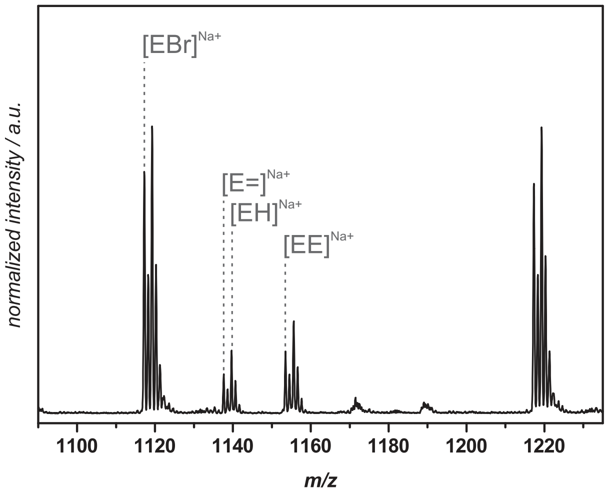

Figure 4.7.: Mass spectrum of pMMA synthesized with the combination of [MMA]:[EBiB]: [$CuBr_2$]:[Me_6TREN] = 50:1:0.02:0.08, entry 11 in Table 4.1. Ethyl isobutyrate-initiated chains with a bromine end group (EBr) are detected as well as ethyl isobutyrate-initiated chains showing disproportionation (E= and EH) or combination (EE) with a second chain.

identify the structures illustrated in Figure 4.1. Figure 4.8 illustrates the comparison of the high-resolution mass spectra with the respective mass spectrum derived from quadrupole ESI-MS. Additionally, the calculated mass spectrum for each structure is shown, confirming the existence of the proposed polymer structures (see Table 4.2).

Structure	Elemental formula	$(m/z)_{theo}$	$(m/z)_{exp}$	$\Delta\, m/z$
E=	$C_{56}H_{90}NaO_{22}^{+}$	1137.5816	1137.5881	0.0065
EH	$C_{56}H_{92}NaO_{22}^{+}$	1139.5973	1139.6031	0.0058
Br=	$C_{50}H_{79}BrNaO_{20}^{+}$	1101.4240	1101.4305	0.0065
BrH	$C_{50}H_{81}BrNaO_{20}^{+}$	1103.4397	1103.4466	0.0069
TREN=	$C_{57}H_{101}N_4O_{18}^{+}$	1129.7105	1129.7163	0.0058
TRENH	$C_{57}H_{103}N_4O_{18}^{+}$	1131.7262	1131.7313	0.0051
MMA=	$C_{55}H_{88}NaO_{22}^{+}$	1123.5660	1123.5701	0.0041
MMAH	$C_{55}H_{90}NaO_{22}^{+}$	1125.5816	1125.5840	0.0024
EBr	$C_{51}H_{83}BrNaO_{20}^{+}$	1117.4553	1117.4622	0.0069

Table 4.2.: Comparison of theoretical and experimentally determined molar mass for the significant structures found for various reagent compositions. TREN= and TRENH are ionized with H^+, respectively.

4.2. The Mechanism of PhotoRDRP

In order to elucidate the mechanism of photoRDRP, the information about how different combinations of initiator, $CuBr_2$, and ligand interact upon irradiation is merged into one picture. Giving insight into a complex mechanistic system, Figure 4.9 illustrates the proposed mechanism that leads to the initiation of a polymerization and – importantly – to the reduction of the $CuBr_2$ complex toward the activator.

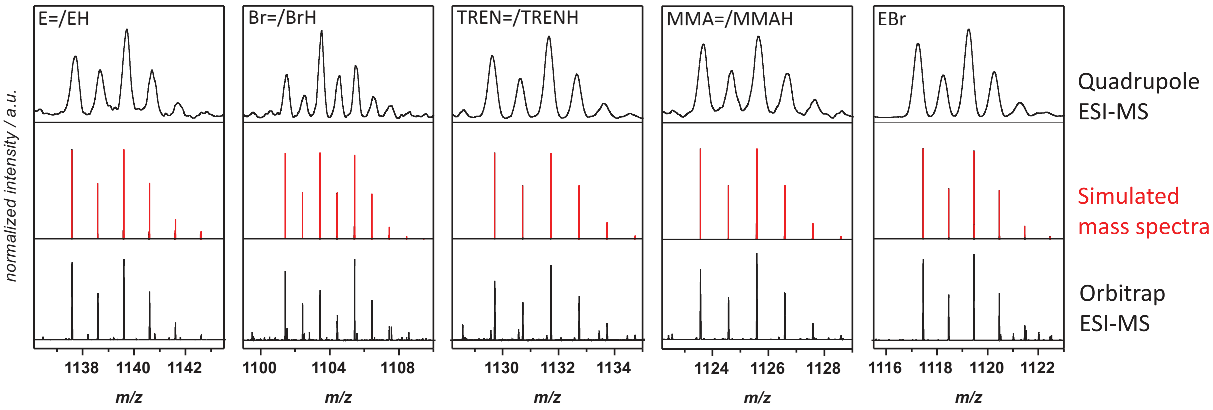

Figure 4.8.: Comparison of quadrupole ESI-MS (top row) and high-resolution orbitrap ESI-MS measurements (bottom row) with the simulated mass spectra (middle row) of the significant chemical structures found for various reagent compositions.

Irradiation results in the light-induced homolytic bond scission of the ATRP initiator into an alkyl and bromine radical. The alkyl radical adds onto a monomer molecule and, thus, initiates the polymerization. The bromine radicals act as reducing agents and react with $CuBr_2$. Thereby, the copper complex is oxidized, resulting in the formation of activator and bromine. It is assumed that the highly reactive bromine continues to react. Since this very first step results in propagating chains, the latter can react with the deactivator forming the activator Cu^IBr/L and bromine-terminated chains. Thus, already in the very first moments after beginning of the irradiation the controlled/living character of the polymerization is active. Moreover, since bromine radicals contribute to the formation of the activator Cu^IBr/L, the latter can perform an atom-transfer reaction with the initiator and form propagating radicals.

It is assumed that the atom-transfer reaction between the initiator and the activator serves as the main pathway for the generation of radicals that can propagate, as it is the case for conventional ATRP. The light-induced bond scission of the initiator is seen solely as a support for the reduction of $CuBr_2$ and the formation of the very first initiating radicals.

The main pathway for the generation of the deactiator species $Cu^{II}Br_2/L$ throughout the reaction is expected to be the reduction via the ligand. Thereby, two coexisting processes are presumably responsible. First, as shown in the previous experiments, the ligand can be photochemically excited and reduce the $CuBr_2$ toward CuBr, thereby forming a radical cation. On the other hand, the deactivator complex $CuBr_2/Me_6TREN$ could be excited as well upon irradiation and subsequently quenched by free ligand. Thereby, the activator complex Cu^IBr/Me_6TREN is formed next to the amine radical cation ligand. This second pathway is proposed in analogy to a similar mechanism that was recently published.[154] Thereby, a light-induced reduction process between a $Cu(phen)_2^+$ complex and triethylamine was observed. In summary, the ligand is a strong contributor to the continuous generation of activator species throughout the reaction. In addition, the contribution of the ligand prevents the accumulation of deactivator species during the polymerization and, thus, helps avoiding the occurence of the persistent radical effect.[155,156] The adjustment of the RDRP equilibrium, consisting of the dormant and the active state, is achieved more rapidly via the positive influence of the ligand. The fact that higher concentrations of ligand result in a faster polymerization,[16,17] confirms this observation.

The role of the ligand as reducing agent is additionally confirmed by the lack of ligand-initiated polymer (TREN= and TRENH) in the mass spectrum of the complete photoRDRP reaction, as shown in Figure 4.7. It is assumed that ligand radicals have a limited initiation ability and that Me_6TREN serves preferably as reducing agent.

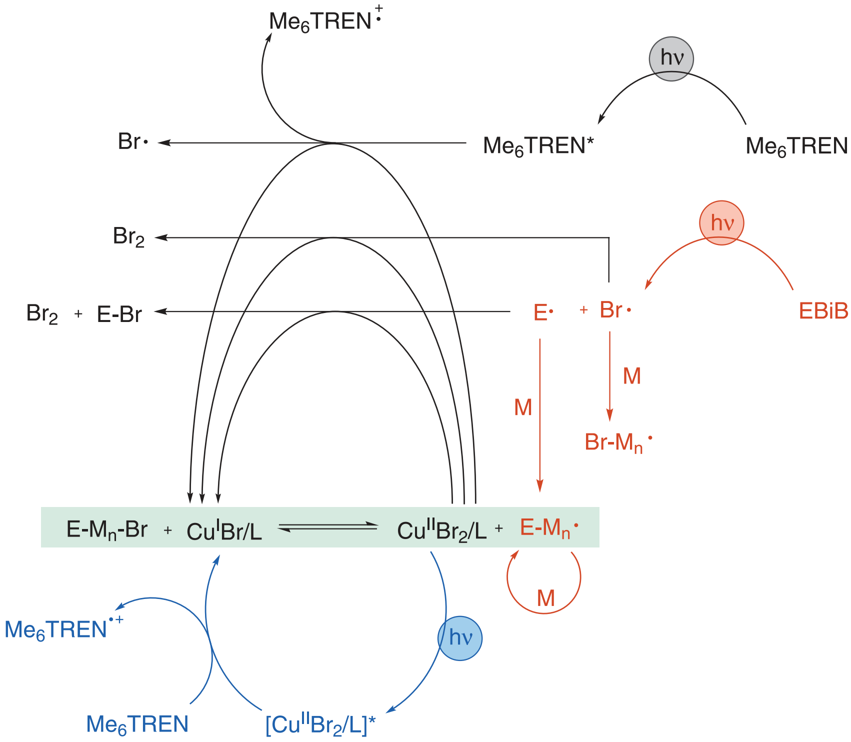

Figure 4.9.: Proposed mechanism of photoRDRP, based on structures found in ESI-MS for varied combinations of EBiB, Me_6TREN, $CuBr_2$, monomer, and solvent.

4.2.1. The Impact of the Ligand

In the previous experiments it was shown that the amine ligand performs a photoinduced electron transfer toward the $Cu^{II}Br_2/L$ species, resulting in the formation of the respective Cu^IBr/L complex. Such an electron donating process is enabled due to the photoexcitation of the respective electron donor, i.e., the amine ligand, resulting in a change of its redox properties. Thereby, the principle that a molecule in its electronically excited state is both a better reductant and oxidant than in its ground state is exploited.[157] The light-induced excitation of an electron from the low-energy orbital (HOMO) to the high-energy orbital (LUMO) implicates the decrease of the molecules' ionization potential as well as an increase of its electron affinity, as illustrated in Figure 4.10. Consequently, the transfer of an electron from the LUMO is energetically favored than from the HOMO. Thus, such electron donors act as sensitizers that are far better reductants in their excited state than in their ground state.[13,157–159] The latter explains why an amine ligand can act as a reducing agent for the $Cu^{II}Br_2/L$ complex upon irradiation.

It has been previously shown that amine derivatives can perform a light-induced electron transfer.[13,14,154,157–159] Thereby, a so-called aminium radical (a radical cation of an amine) is formed. The latter preferably reacts to an α-aminoalkyl radical after a deprotonation in α-position of an amine moiety, resulting in a radical that can, for instance, initiate the polymerization of a monomer. The observed deprotonation in α-position is preferably performed in the order of tertiary > secondary > primary > aromatic amines (if no steric hindrance occurs).[160,161] Thereby, the low deprotonation preference of aromatic amines explains the unsuccessful attempts to employ aromatic ligands, for instance 2,2'-bipyridine, for photoRDRP in the past.[16]

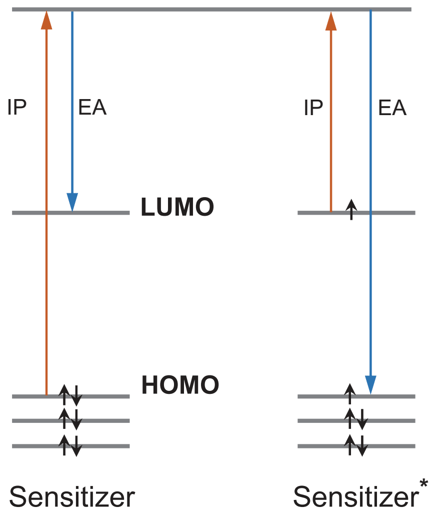

Figure 4.10.: Redox properties of a sensitizer in the excited and ground state, reproduced from ref.[159] ©Wiley-VCH Verlag GmbH & Co. KGaA, reproduced with permission. The reduced ionization potential (IP) after excitation is the reason why an amine ligand acts as a reductant upon irradiation. EA = electron affinity.

4.2.2. The Significance of UV-Vis Spectra for the Mechanistic Elucidation

UV-vis spectroscopic analysis of the reaction solution of photoRDRP played a significant role in previous studies of Anastasaki *et al.*[16] and Matyjaszewski and coworkers.[17] Thereby, the absorption of the reaction solution before and after irradiation was handled as key supporting data for the investigation of the mechanism. In detail, after irradiation the absorption of the $Cu^{II}Br_2/Me_6TREN$ complex in the range of 600-1000 nm decreased. The latter was interpreted as a proof for its reduction. Yet, the absorption spectrum of the respective $Cu^{I}Br/Me_6TREN$ complex was not reported. Figure 4.11 shows the UV-vis absorption spectra for a photoRDRP solution, recorded in the context of the current study. Thereby, as reported previously, a decrease in the absorption in the 600-800 nm range was observed after irradiation, assigned to d^9 d-d transitions of the Cu^{II} species. In the solution of CuBr with Me_6TREN three absorption maxima can be detected: in the 600-800 nm, 250-350 nm, and 400-500 nm range. Hence, the absorption at 400-500 nm of $Cu^{I}Br/Me_6TREN$, that does not appear in the spectrum of $Cu^{II}Br_2/Me_6TREN$, could be utilized for its detection. The same absorption band is detected in the study of Anastasaki *et al.*,[16] yet, it is not reported in the work of Matyjaszewski and coworkers.[17] The apparent experimental inconsistencies, presumably due to oxidation of the copper complex toward its higher oxidation state or due to low level impurities, show that UV-vis spectroscopic measurements have limitations regarding mechanistic conclusions. The high sensitivity of CuBr toward oxygen, as demonstrated by the distinct change of the absorption behavior of the $Cu^{I}Br/Me_6TREN$ complex in Figure 4.11 after a short time period, underlines that UV-vis measurements as an exclusive analytical method are somewhat unreliable. Hence, additional analytical methods need to be employed for the mechanistic elucidation, as were used in the current work.

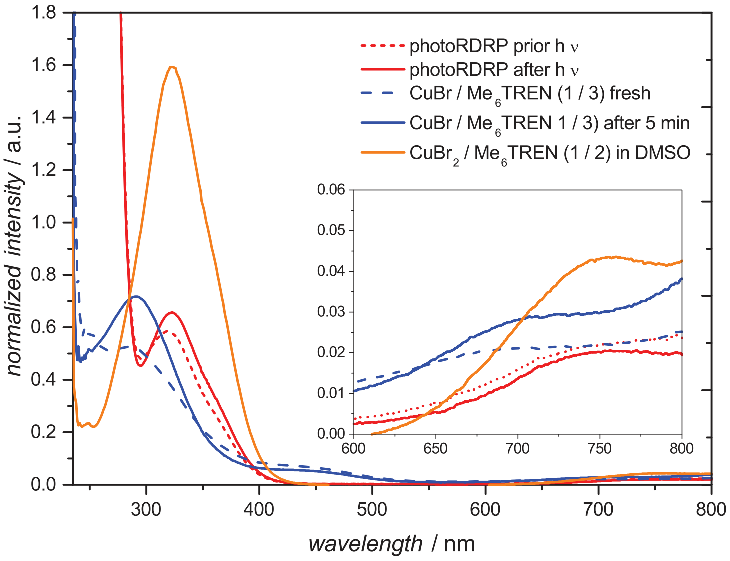

Figure 4.11.: UV-Vis spectra of [MMA]:[EBiB]:[$CuBr_2$]:[Me_6TREN] = 50:1:0.02:0.06 in DMSO prior (red dashed line) and after the PLP experiment (red solid line), [CuBr]:[Me_6TREN] = 1:3 in DMSO, freshly deoxygenated (blue dashed line) and after 5 min exposure to air in the open cuvette (blue solid line), [$CuBr_2$]:[Me_6TREN] = 1:2 in DMSO (orange line).

4.3. Summary and Conclusions

The mechanism of copper-mediated photoRDRP was investigated via a combination of pulsed-laser polymerization and high resolution mass spectrometry. The polymerization via PLP facilitates the generation of short polymer chains, while performing FRP. On the other hand, mass spectrometric analysis of the products allows for the unambiguous identification of the initiating species and, thus, the elucidation of the reactions occuring during irradiation. Hence, regardless of the free radical polymerization that occured for various combinations of the photoRDRP components, for instance when no initiator or no ligand was present, respectively, the generated polymer could be characterized regarding its structure. Thus, interactions between the reactive species during the irradiation could be identified.

It was found that the light-induced homolytic C-Br bond scission of the alkyle halide initiator generates the first initiating radicals that, on the one hand, commence the propagation of monomer as well as react with the deactivator copper species that are present in the reaction solution at the beginning. The continuous generation of activator copper species occurs via a light-induced electron transfer from the excited amine ligand to the deactivator species. In addition, the deactivator copper complex can be electronically excited. Thereby, free ligand species can perform a quenching reaction, generating the copper complex in its reduced state and an amine radical cation. In summary, the mechanism of photoRDRP consists of several complex interactions that contribute to the generation of activator species throughout the reaction. Thereby, the ligand plays a significant role as light-triggered reducing agent. Further investigations should therefore focus on the wavelength-dependency of the reducing steps as well as the homolytic bond scission of the initiator. Furthermore, the structure of the ligand should be analyzed regarding its efficiency to perform a light-induced electron transfer reaction.

5

Photoinitiator-Based Single-Chain Nanoparticle Formation

Single-chain nanoparticle (SCNP) technology aims at emulating single-chain architectures occuring in nature, for instance proteins with their three-dimensional structure, by means of synthetically synthesized polymers. As described in section 2.8.1, the three-dimensional structure is introduced into the polymer chain by either the collapse of the polymer chain via interactions of reactive sites within the repeating unit or the positioning of recognition units at predetermined places along the polymer chain, for instance at the end groups. To date, various chemical reactions have been employed for the bond formation, allowing the connection of distinct points along the chain. However, delicate procedures and, in general, numerous synthetic steps are necessary for the synthesis of such single chains. The facile radical formation of photoinitiators and their efficient radical termination in the absence of reactive units such as vinyl groups of monomers could facilitate a new synthetic approach for the formation of single-chain folding nanoparticles based on radical-radical termination events. Herein, photoinitiator functionalities are introduced into the polymer chain via the copolymerization of a functionalized monomer bearing a photoinitiator unit with a methyl methacrylate monomer unit. Irradiation with UV light is envisaged to efficiently form radicals along the chain and high dilution leads to the collapse of the chain into a nanoparticle.

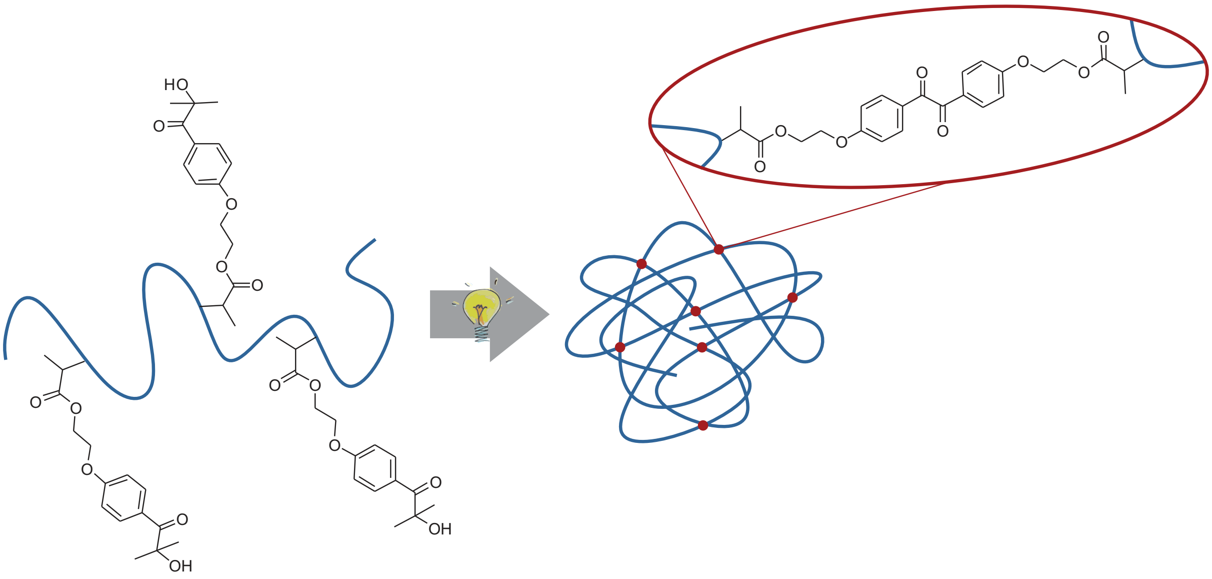

Figure 5.1.: Schematic illustration of single-chain folding into a nanoparticle triggered by the light-induced photoinitiator cleavage and subsequent radical-radical termination.

The work reported in this chapter was carried out at the University of Colorado Boulder (USA) in the laboratory of Prof. Dr. Christopher N. Bowman in the frame of a research stay.

Thereby, radical-radical termination events result in the formation of covalent bonds within the nanoparticle, as illustrated in Figure 5.1. Different chain lengths as well as different proportions of photoinitiator functionalities along the chain are expected to enable the fine tuning of the nanoparticle size and compactness. Altogether, the combination of photoinitiator chemistry and single-chain folding was expected to offer a facile method for the formation of nanoparticles.

5.1. Introduction of Photoinitiator Units along the Chain

In order to enable the formation of SCNPs based on radical-radical termination events, polymers carrying photoinitiator units along their chain were synthesized. Therefore, in a first step, a functional monomer bearing a photoinitiator moiety was synthesized. The well-known photoinitiator Irgacure 2959 (see Figure 5.2) was chosen as the functional species. It generates an easily accessible and reactive benzoyl-type radical fragment and a small hydroxyl propyl radical fragment.

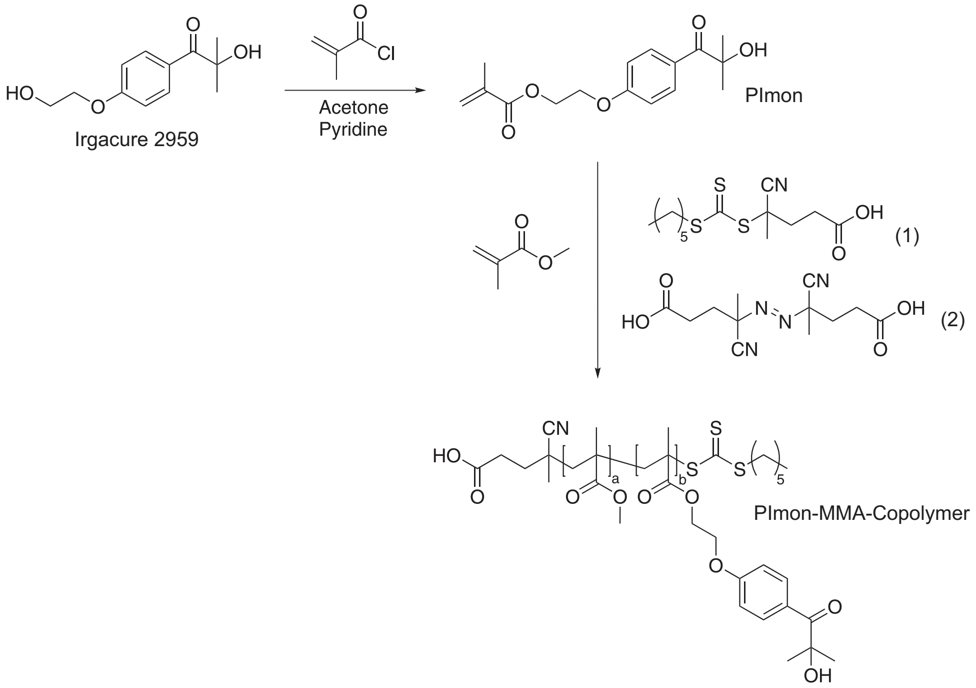

Figure 5.2.: Synthesis of the photoinitiator functionalized monomer PImon and the subsequent copolymerization with MMA via RAFT polymerization, employing a RAFT agent (1) and radical initiator (2).

Due to the activated hydroxyl group of the photoinitiator, its functionalization into a polymerizable monomer could be performed in a straightforward condensation reaction with methacryloyl chloride. Subsequently, the photoinitiator monomer (PImon) was copolymerized with MMA via reversible addition-fragmentation chain transfer (RAFT) polymerization, resulting in a single chain copolymer with statistical incorporation of photoinitiator units along the chain. The trithiocarbonate 4-cyano-4-(((hexylthio)carbonothioyl)thio)pentanoic acid [1] was employed as the RAFT agent. Figure 5.2 illustrates the synthetic pathway for the photoinitiator functionalized pMMA. The polymer was characterized by ^{1}H-NMR and SEC, showing a well-controlled polymerization behavior, as illustrated in Figure 5.3. In order to ensure the even introduction of the photoinitiator monomer along the chain, the conversion of both PImon and MMA was monitored for different reaction times. As Figure 5.3 shows, both monomers were introduced statistically and, thus, evenly throughout the polymerization.

---

[1] Synthesized and provided by Benjamin Fairbanks, University of Colorado Boulder.

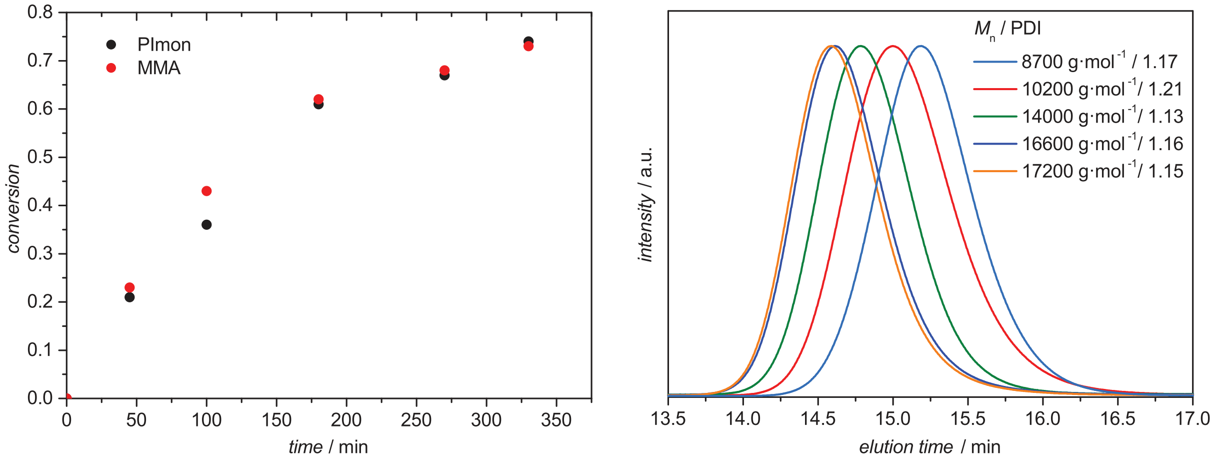

Figure 5.3.: Left: Time-conversion plot for the PImon-MMA-copolymer showing an equal incorporation of both monomers throughout the polymerization. Right: SEC traces for the PImon-MMA-copolymer for various polymerization times.

Variation of the ratio PImon/MMA in the range of 1/8 - 1/15 resulted in different incorporation densities of PImon in the chain. The effective ratio of PImon/MMA in the copolymer differed slightly from the experimentally employed ratio. For instance, the experimental ratio of PImon/MMA being 1/10 resulted in an actual incorporation ratio of 1/8.3 in the copolymer, determined by NMR spectroscopy. In addition, various polymer chain lengths in the range of 9000-18000 g·mol^{-1} were generated by varying the polymerization time. By adjusting both the ratio of photoinitiatur units compared to MMA as well as the chain length, the reactivity and folding behavior of the chain can be influenced. Higher amounts of photoinitiator moieties increase the number of reactive sites and can, thus, lead to a faster intramolecular reaction. Yet, with an increasing number of radicals along the chain, the probability of intermolecular reactions, i.e., crosslinking of the chains, is enhanced. In addition, long polymers are expected to increase the probability of crosslinking events. However, employing long polymer precursors facilitates the detection of the folding process, since the expected shift toward longer elution times in SEC is more pronounced for large polymers. Table 5.1 summarizes all copolymers that were synthesized with varied PImon content and polymer chain length.

5.2. Irradiation Experiments

In order to ensure the intramolecular reaction of the PImon-MMA-copolymer precursor, a wide range of experimental parameters were varied such as the solvent (mixture), polymer concentration, irradiation time, irradiation energy, wavelength range and reaction temperature. In the following, the results of the parameter variation will be discussed in detail.

5.2.1. Variation of the Solvent Mixture and Polymer Concentration

An entangled polymer chain promotes the intramolecular reaction in contrast to a polymer that exhibits a loose shape in solution with a large hydrodynamic radius. Thus, in the current work,

Entry	Ratio PImon/MMA	M_n (g·mol^{-1})	$Đ$
1	1/8	18200	1.16
2	1/8	16000	1.17
3	1/8	10200	1.21
4	1/8	14000	1.13
5	1/8	16600	1.16
6	1/8	17200	1.15
7	1/8	8700	1.17
8	1/11	13400	1.15
9	1/11	15700	1.15
10	1/12	18400	1.14
11	1/15	14800	1.17
12	1/15	17300	1.07

Table 5.1.: Summary of the PImon-MMA-copolymers that were prepared with different PImon/MMA ratios (the ratios were determined by NMR spectroscopy) and different chain lengths.

the focus of the solvent variation was on finding an appropriate solvent or solvent mixture that enhances the entanglement of the polymer chain. Hence, the solvent should dissolve the polymer sufficiently in order to prevent precipitation during irradiation and, at the same time, prevent the chains from being too well solvated and thus less compact.

Acetonitrile

In the first irradiation experiments acetonitrile was employed as the solvent due to the good solubility of the PImon-MMA-copolymer in the latter. For the first experiments, the copolymers from Entry 1 and 2 in Table 5.1 were employed. Thereby, as summarized by Table 5.2, a polymer concentration of 0.02 mg·mL^{-1} was irradiated for 10 min, 30 min, or 1 h with UV light that passed a 320-390 nm filter exhibiting an intensity of 80 mW·cm^{-2}. However, for all three irradiation times and both polymer chain lengths material with shorter elution time can be detected via SEC, as illustrated in Figure 5.4, assigned to crosslinked material.

Solvent	hν *Time*	Precursor	c_P (mg·mL^{-1})	*Intensity* (mW·cm^{-2})	λ (nm)
MeCN	1 h	Entry 1	0.02	80	320 - 390
MeCN	30 min	Entry 1	0.02	80	320 - 390
MeCN	10 min	Entry 1	0.02	80	320 - 390
MeCN	1 h	Entry 2	0.02	80	320 - 390
MeCN	30 min	Entry 2	0.02	80	320 - 390

Table 5.2.: Summary of the irradiation experiments in acetonitrile solution with different irradiation times and precursors. c_P = Precursor concentration. Entry 1 and 2 correspond to Table 5.1.

Dichloromethane (DCM)

In order to avoid crosslinking, DCM was employed as the solvent for the irradiation experiments. DCM was selected since it proved to be a suitable solvent in previous studies on SCNP

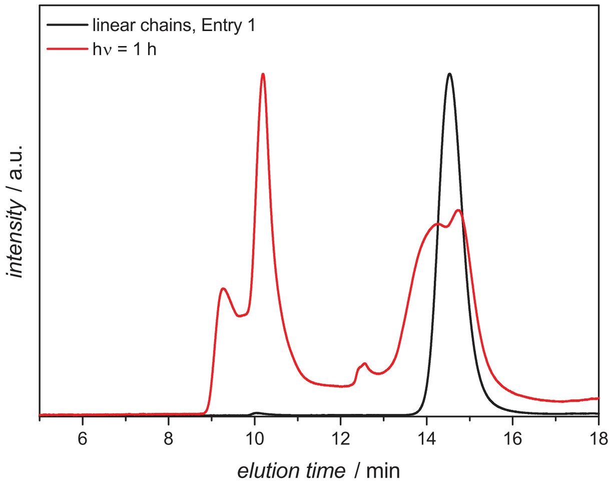

Figure 5.4.: Size-exclusion chromatogram of PImon-MMA-copolymer (Entry 1 in Table 5.1) in acetonitrile solution, irradiated for 1 h.

formation.[135,136,162] Irradiation experiments employing equal experimental parameters as for the aforementioned acetonitrile experiments, as illustrated in Table 5.3, show less crosslinking of the polymer in the SEC analysis.

Solvent	hν *Time*	Precursor	c_P (mg·mL^{-1})	*Intensity* (mW·cm^{-2})	λ (nm)
DCM	10 min	Entry 1	0.02	80	320 - 390
DCM	10 min	Entry 2	0.01	80	320 - 390
DCM	1 min	Entry 1	0.01	80	320 - 390
DCM	3 min	Entry 1	0.01	80	320 - 390
DCM	5 min	Entry 1	0.01	80	320 - 390
DCM	8 min	Entry 1	0.01	80	320 - 390

Table 5.3.: Summary of the irradiation experiments in DCM solution with different precursor concentrations c_P and irradiation times. Entry 1 and 2 correspond to Table 5.1.

In addition, next to a signal at shorter elution times in the SEC, a new signal at longer elution times appears, indicating that material with a smaller hydrodynamic radius was formed. Subsequently, the same irradiation experiment was performed with a lower polymer concentration (0.01 mg·mL^{-1}). Thereby, less material with short elution times (large hydrodynamic radius) is observed together with material that shows longer elution times. The latter is assigned to chain folding that occured after intramolecular termination reaction. Figure 5.5 illustrates the chromatograms for both polymer concentrations.

The experiments with a precursor concentration of c_P = 0.01 mg·mL^{-1} showed a clear improvement – a shift toward longer elution times and less material with large molar mass – compared to previous experiments. Thus, the precursor concentration was maintained and the irradiation was performed with shorter exposure times, as summarized by Table 5.3. Already for an irradiation time of 1 min the SEC trace exhibits a shift of its maximum toward longer elution times. However, even such short exposure results in the formation of, presumably, crosslinked material that is detected at shorter elution times. Figure 5.6 shows the SEC traces for the different exposure times next to the corresponding NMR spectra of the isolated material after irradiation. In the latter, two new resonances appear with increasing irradiation time

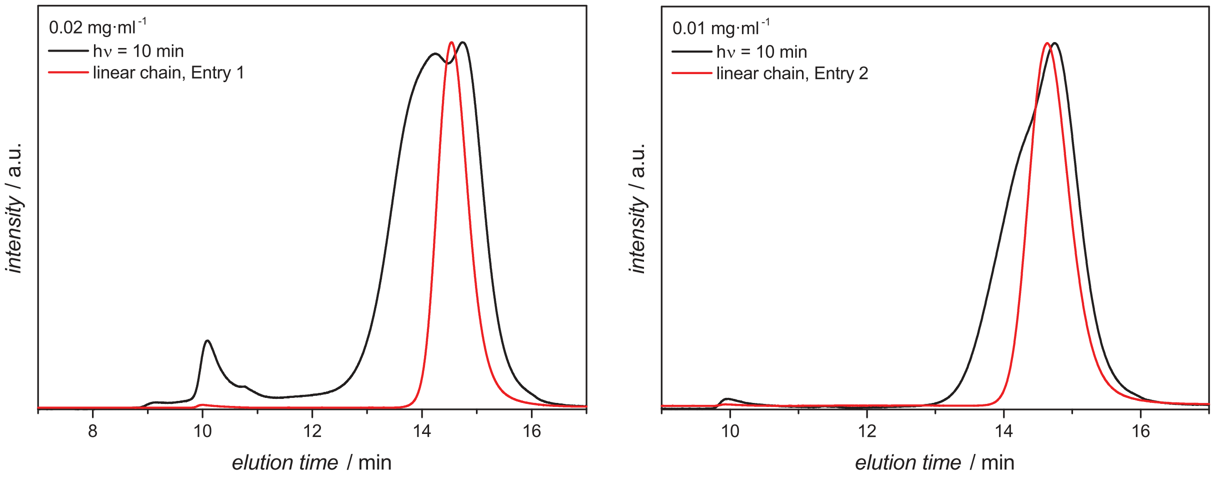

Figure 5.5.: Size-exclusion chromatograms of linear precursor irradiated in DCM 10 min with precursor concentrations of 0.02 mg·mL^{-1} (left) and 0.01 mg·mL^{-1} (right).

in the aromatic region (around 8 ppm). They could be assigned to the termination product between the two radical benzoyl fragments, as illustrated in Figure 5.1.

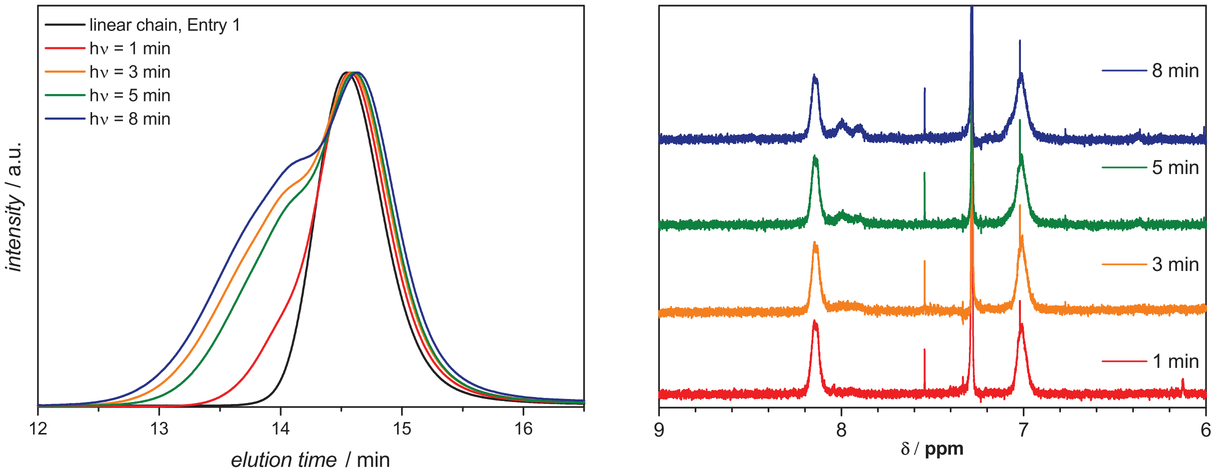

Figure 5.6.: Left: Size-exclusion chromatograms of PImon-MMA-copolymer irradiated in DCM for various exposure times. Right: The corresponding NMR spectra are shown, exhibiting two new peaks that appear in the aromatic region with increasing irradiation time.

Solvent Mixtures with Tetrahydrofuran (THF)

In order to identify a solvent that helps avoiding intermolecular reactions between the linear precursors, THF was employed, since its successful utilization in SCNP formation has been previously reported.[163] Thereby, pure THF and subsequently mixtures of THF and methanol were utilized. Parameters like the precursor concentration and irradiaton wavelength and intensity were maintained. Remarkably, no shift toward longer elution times could be observed. Yet, small amounts of crosslinked material appears in the SEC analysis. In addition, NMR spectra of the isolated material after irradiation in THF or THF mixtures exhibit a broad peak in the down-field region that could not be assigned, as illustrated in Figure 5.7.

Solvent	$h\nu$ *Time*	c_P (mg·mL^{-1})	*Intensity* (mW·cm^{-2})	λ (nm)
THF	3 min	0.01	80	320 - 390
THF/MeOH = 3.5/1	3 min	0.01	80	320 - 390
THF/MeOH = 2.5/1	3 min	0.01	80	320 - 390

Table 5.4.: Summary of the irradiation experiments in pure THF and THF-methanol solutions. Precursor from Entry 1 (refer to Table 5.1) was employed.

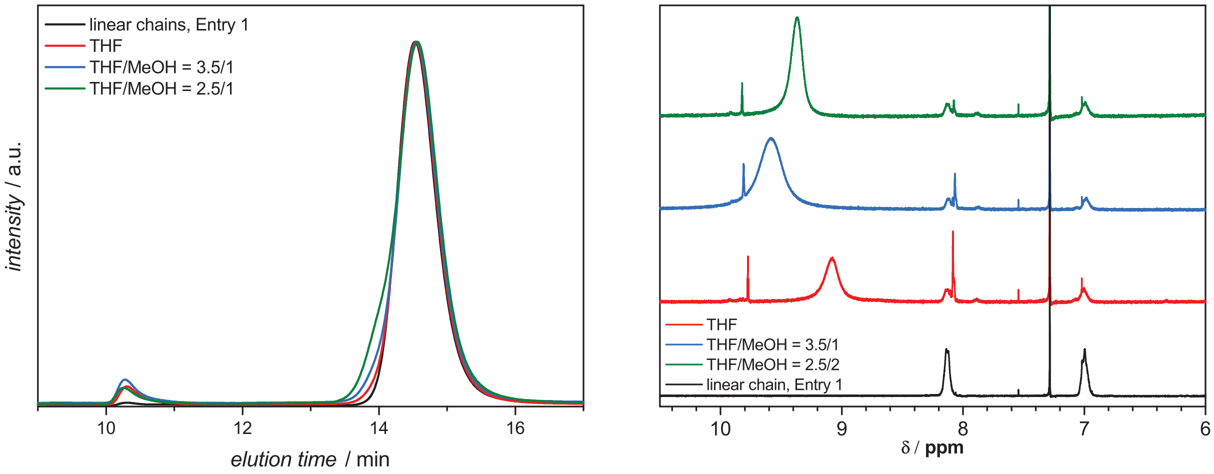

Figure 5.7.: Left: Size-exclusion chromatogram of PImon-MMA-copolymer irradiated in THF and THF mixtures for 3 min. Right: NMR spectra of the corresponding material that was isolated after irradiation. The broad peak in the down-field region that appears after exposure to light could not be assigned.

Solvent Mixtures with Dichloromethane

Since, from the previously reported solvents, DCM showed the most promising results, i.e., exhibiting a shift of the polymer distribution toward longer elution times and showing less crosslinked material, it was utilized for experiments with different solvent mixtures. Thereby, mixtures of DCM with methanol, THF, diethyl ether, and hexane were employed, as summarized in Table 5.5. None of the mentioned mixtures showed ideal results. However, the solvent mixture of DCM and diethyl ether resulted in a clear shift of the chromatogram toward longer elution times and showed the smallest amount of crosslinked material, as illustrated in Figure 5.8.

Solvent	$h\nu$ *Time*	c_P (mg·mL^{-1})	*Intensity* (mW·cm^{-2})	λ (nm)
DCM/MeOH = 2.5/2	3 min	0.01	80	320 - 390
DCM/THF = 2.5/1	3 min	0.01	80	320 - 390
DCM/Et$_2$O = 2.5/2	3 min	0.01	80	320 - 390
DCM/Hexane = 2.5/2	3 min	0.01	80	320 - 390

Table 5.5.: Summary of the irradiation experiments in various DCM solvent mixtures. Precursor from Entry 1 (refer to Table 5.1) was employed.

Due to the rather promising result for the solvent mixture of DCM and diethyl ether, further irradiation experiments were performed in the same medium, as summarized in Table 5.6. Thereby, a small amount of DCM was used to dissolve the polymer. Subsequently, the DCM solution was added into a large amount of diethyl ether. The described procedure was envis-

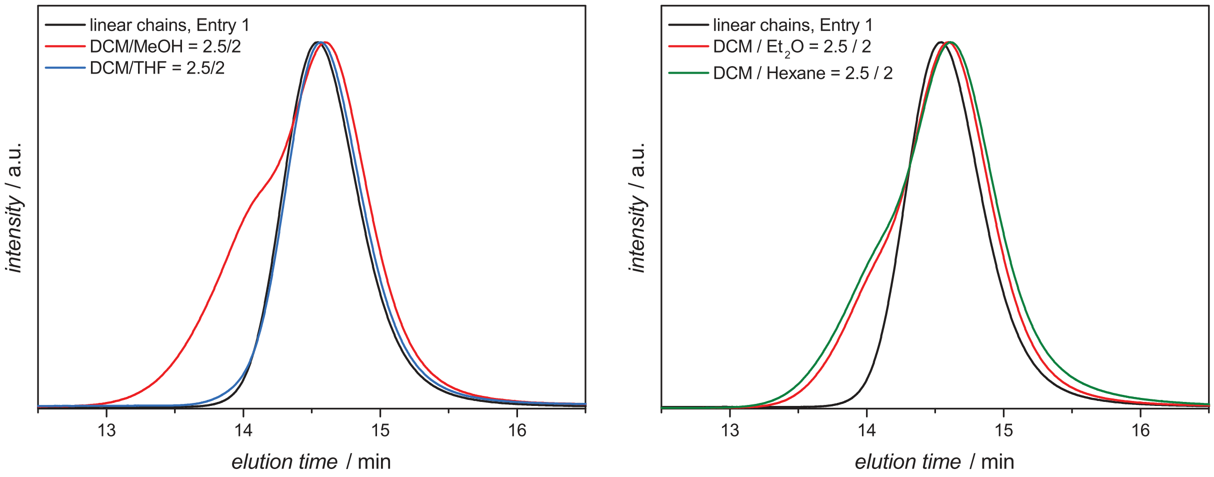

Figure 5.8.: Size-exclusion chromatograms of PImon-MMA-copolymer irradiated in DCM mixtures with methanol, THF, diethyl ether, and hexane, respectively.

aged to help obtaining polymer chains in an entangled state since – prior to the irradiation experiments – the PImon-MMA-copolymer precursor was precipitated in diethyl ether. Hence, diethyl ether is a poor solvent for the employed precursor.

Solvent	hν *Time*	Precursor	c_P (mg·mL^{-1})	*Intensity* (mW·cm^{-2})	λ (nm)
DCM/Et$_2$O = 1/8	3 min	Entry 1	0.01	80	320 - 390
DCM/Et$_2$O = 1/8	6 min	Entry 1	0.01	80	320 - 390
DCM/Et$_2$O = 1/8	3 min	Entry 10	0.01	80	320 - 390
DCM/Et$_2$O = 1/8	6 min	Entry 10	0.01	80	320 - 390
DCM/Et$_2$O = 1/8	10 min	Entry 10	0.01	80	320 - 390

Table 5.6.: Summary of the irradiation experiments in DCM/diethyl ether mixtures. Precursors from Entry 1 and 10 (refer to Table 5.1) were employed.

Figure 5.9 (left) shows the results for the irradiation experiments with a DCM/diethyl ether = 1/8 solvent mixture, employing linear precursors with a PImon/MMA ratio of 1/8. Thereby, a clear shift toward longer elution times can be detected. However, a small shoulder at shorter elution times remains, presumably resulting from crosslinked precursor.

Additional experiments were performed with linear precursor carrying a smaller number of photoinitiator units with a PImon/MMA ratio of 1/12 (Entry 10 in Table 5.1). The results illustrated in Figure 5.9 (right) are similar compared to the results of the irradiation exeriments employing precursors with a PImon/MMA ratio of 1/8: a clear shift of the elution curve toward longer elution times is detected, yet a small shoulder – assigned to crosslinked material – remains.

In the noted chromatograms a small signal at very short elution times (10-11 min) can be detected. However, this small signal appears in the irradiated samples as well as in the sample containing non-irradiated linear precursor. It could not be clarified if this high molar mass material is a result of unintentional light-induced crosslinking within the SEC sample or if it is a contamination of the employed SEC device. However, it is assumed that this signal corresponds to a negligible amount of material, since the detected intensity is not proportional

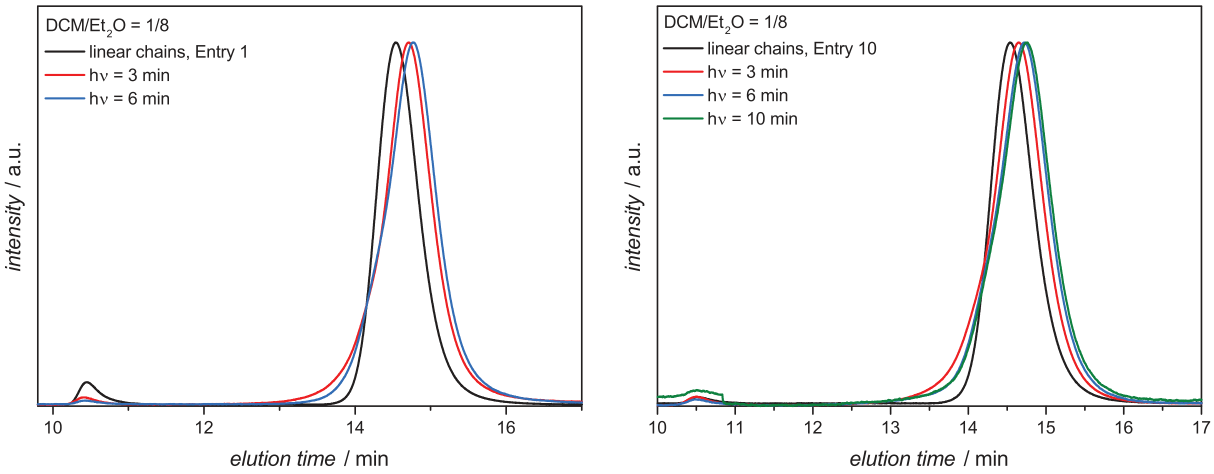

Figure 5.9.: Size-exclusion chromatograms of PImon-MMA-copolymer irradiated in DCM/diethyl ether mixtures for linear precursor with PImon/MMA ratio of 1/8 (left, Entry 1) and a PImon/MMA ratio of 1/12 (right, Entry 10).

to the number of detected chains. In general, very large polymers show a particularly high signal intensity in SEC, an analytical method reporting a weight distribution.

5.2.2. Addition of Radical Inhibitor

In order to decrease the probability of intermolecular reactions and, thus, to avoid crosslinking events, the radical inhibitor MEHQ (4-methoxyphenol) was added prior to irradiation. Thereby, 5 mol% and 10 mol% of MEHQ per photoinitiator unit was employed. The irradiation experiments were carried out in a solvent mixture of DCM/diethyl ether = 1/8 and other reaction parameters, such as light intensity and precursor concentration, were maintained, as illustrated in Table 5.7. Thereby, as shown in Figure 5.10, the formation of crosslinked material, illustrated by the small shoulder at shorter elution times, could be reduced compared to previous experiments. In addition, a distinct shift in the maximum of the elution curve is detected, assigned to the formation of polymer with a smaller hydrodynamic radius and, thus, to successful SCNP formation. The shift of the elution curve is underlined by the corresponding shift in molar mass, as shown in Table 5.7. Thereby, the difference in molar mass detected by SEC is at least 3300 g·mol^{-1} and, thus, a clear indication for SCNP formation. However, the dispersity of the irradiated sample increased compared to the linear precursor, most probably resulting from the shoulder in the elution curve.

Solvent	hν *Time*	MEHQ (mol%)	Precursor	M_n (g·mol^{-1})	Đ
-	-	-	Entry 10	18400	1.14
DCM/Et$_2$O = 1/8	10 min	5	Entry 10	15100	1.25
DCM/Et$_2$O = 1/8	10 min	10	Entry 10	15500	1.22

Table 5.7.: Performed irradiation experiments in DCM/diethyl ether = 1/8 with addition of radical inhibitor MEHQ and the corresponding molar mass and dispersity, determined by SEC. A precursor concentration of c_P = 0.01 mg·mL^{-1} and a light intensity of 80 mW·cm^{-2} at a wavelength of 320-390 nm were employed. The first line corresponds to the non-irradiated precursor.

An efficient folding of a linear precursor into an SCNP is characterized by a decrease of the dispersity, resulting from a more compact structure of the chain. Thus, a complete folding process is not occurring in the observed system. Since no particular difference between 5 mol% or 10 mol% added MEHQ could be observed, further irradiation experiments were performed with an addition of 5 mol% MEHQ.

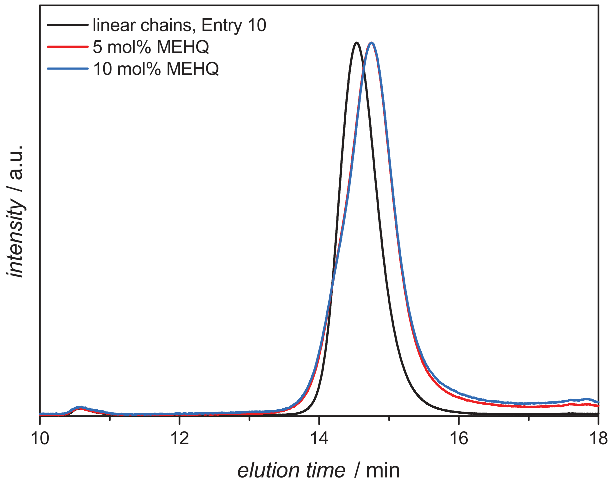

Figure 5.10.: Size-exclusion chromatograms of PImon-MMA-copolymer irradiated in DCM/diethyl ether = 1/8 with addition of 5 mol% and 10 mol% of radical inhibitor MEHQ, in relation to photoinitiator units in the linear precursor.

5.2.3. Variation of the DCM/Diethyl Ether Solvent Mixture

Since the solvent mixture of DCM/diethyl ether showed promising results, yet crosslinking could still occur, the ratio of the two solvents was further varied. In order to improve the solubility of the linear precursor in the medium, the DCM content was increased to DCM/diethyl ether = 1/5.4 and 1/3.5, respectively. The irradiation experiments that were carried out with these solvent mixtures are summarized in Table 5.8 and the corresponding size-exlusion chromatograms are shown in Figure 5.11. Thereby, a strong increase of crosslinking could be observed for both solvent mixtures. Thus, a higher DCM content, i.e., a better solubility of the linear precursor, increases the probability for intermolecular termination between the chains.

Solvent	hν *Time*	*Intensity* (mW·cm^{-2})	Precursor	c_P (mg·mL^{-1})
DCM/Et$_2$O = 1/3.5	6 min	80	Entry 10	0.01
DCM/Et$_2$O = 1/3.5	10 min	80	Entry 10	0.01
DCM/Et$_2$O = 1/3.5	6 min	40	Entry 10	0.01
DCM/Et$_2$O = 1/3.5	10 min	40	Entry 10	0.01
DCM/Et$_2$O = 1/5.4	1 min	40	Entry 10	0.01
DCM/Et$_2$O = 1/5.4	5 min	40	Entry 10	0.01
DCM/Et$_2$O = 1/5.4	1 min	80	Entry 10	0.01
DCM/Et$_2$O = 1/5.4	5 min	80	Entry 10	0.01

Table 5.8.: Performed irradiation experiments with varied DCM/diethyl ether ratio at a wavelength of 320-390 nm. Entry 10 corresponds to Table 5.1.

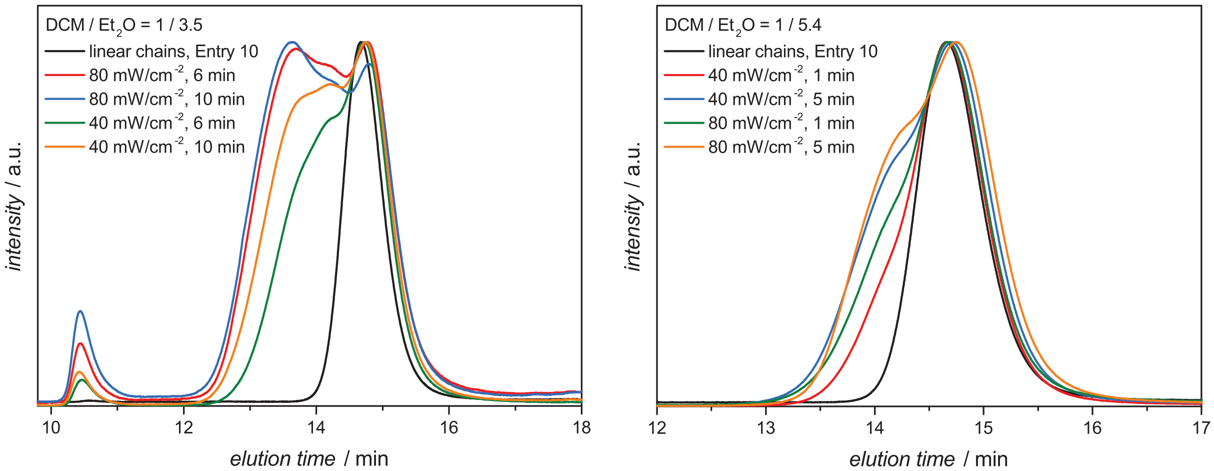

Figure 5.11.: Size-exclusion chromatograms of PImon-MMA-copolymer irradiated in different DCM/diethyl ether ratios with addition of 5 mol% MEHQ. Left: DCM/diethyl ether = 1/3.5. Right: DCM/diethyl ether = 1/5.4. For detailed experimental conditions see Table 5.8.

5.2.4. Variation of Irradiation Intensity and Time

Further experiments with reduced irradiation energy were performed in order to reduce the occurrence of crosslinking events. Therefore, the light intensity was reduced to 40 mW·cm^{-2}, as summarized by Table 5.9. The experiments were performed in DCM/diethyl ether in the ratio of 1/8 and with addition of 5 mol% MEHQ. The results are shown in Figure 5.12 (left). Thereby, the sample that was irradiated with lower energy shows a very similar elution curve compared to the irradiation with 80 mW·cm^{-2}, yet with a smaller shift toward longer elution times. Hence, lower irradiation intensities seem to retard the radical-radical termination reaction. A reduced amount of crosslinked material is not observed, since the elution curves still exhibit a shoulder at shorter elution times. In addition, the dispersities of the samples are increasing after irradiation. Hence, a successful SCNP formation was not achieved.

Solvent	hν *Time*	*Intensity* (mW·cm^{-2})	Precursor	M_n (mg·mL^{-1})	$Đ$
-	-	-	Entry 12	16900	1.16
DCM/Et$_2$O = 1/8	6 min	80	Entry 12	15500	1.26
DCM/Et$_2$O = 1/8	10 min	80	Entry 12	15400	1.25
DCM/Et$_2$O = 1/8	10 min	40	Entry 12	15400	1.29
-	-	-	Entry 12	16500	1.19
DCM/Et$_2$O = 1/8	15 min	80	Entry 12	14400	1.25
DCM/Et$_2$O = 1/8	20 min	80	Entry 12	14100	1.27

Table 5.9.: Performed irradiation experiments with varied light intensity at a wavelength of 320-390 nm and irradiation time. The first and fifth line correspond to the non-irradiated precursors, measured prior to the irradiated samples. Entry 12 corresponds to Table 5.1.

Further experiments were carried out with the PImon-MMA-copolymer exhibiting a ratio of PImon/MMA = 1/15 (Entry 12 in Table 5.1). Thereby, the effect of longer irradiation times on the folding behavior was investigated, as summarized in Table 5.9. However, as Figure 5.12 (right) shows, no positive influence on the elution curve could be achieved. Next to a clear shift

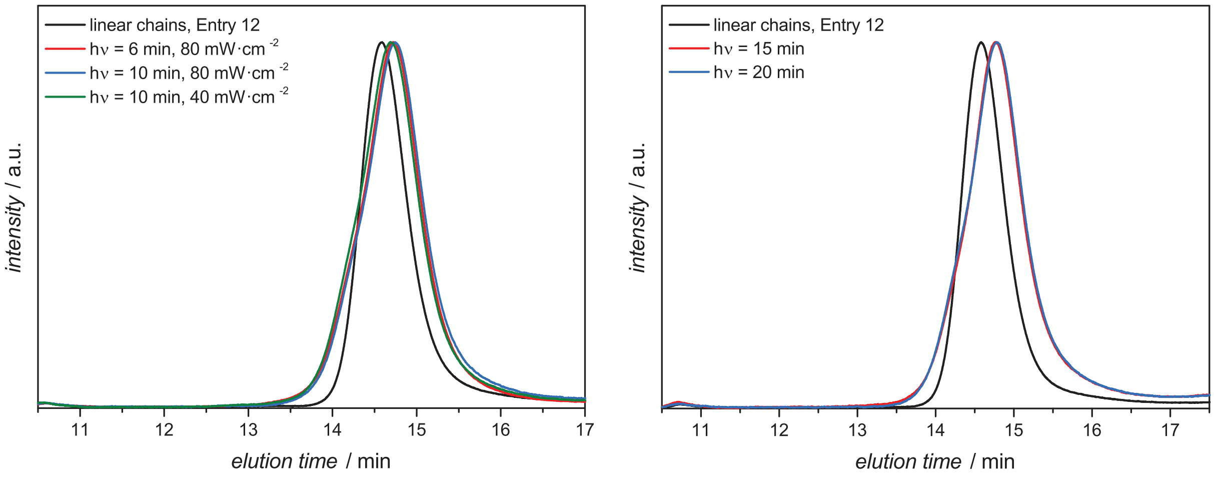

Figure 5.12.: Size-exclusion chromatograms of PImon-MMA-copolymer irradiated in DCM/diethyl ether = 1/8 at two different irradiation intensities (left) and two different irradiation times (right).

of the determined molar mass, i.e., the elution time, a shoulder at shorter elution times was detected.

5.2.5. Variation of the Precursor Chain Length

As was shown in the previous experiments, a polymer chain that takes up a rather entangled state in the irradiated medium, undergoes less termination reactions with other chains. Therefore, short PImon-MMA-copolymer chains were employed in irradiation experiments with molar masses of M_n = 13400 g·mol^{-1} and M_n = 8700 g·mol^{-1}. Short polymers are assumed to posses a more compact shape in solution than long polymer chains and, thus, have a lower probability of interacting with other chains. The experimental conditions are summarized in Table 5.10 and the corresponding size-exclusion chromatograms are shown in Figure 5.13. In contrast to the expected results, short precursors seem to undergo more intermolecular termination reactions. For both chain lengths, next to a shift of the absorption maximum to longer elution times, a strong signal at shorter elution times was detected.

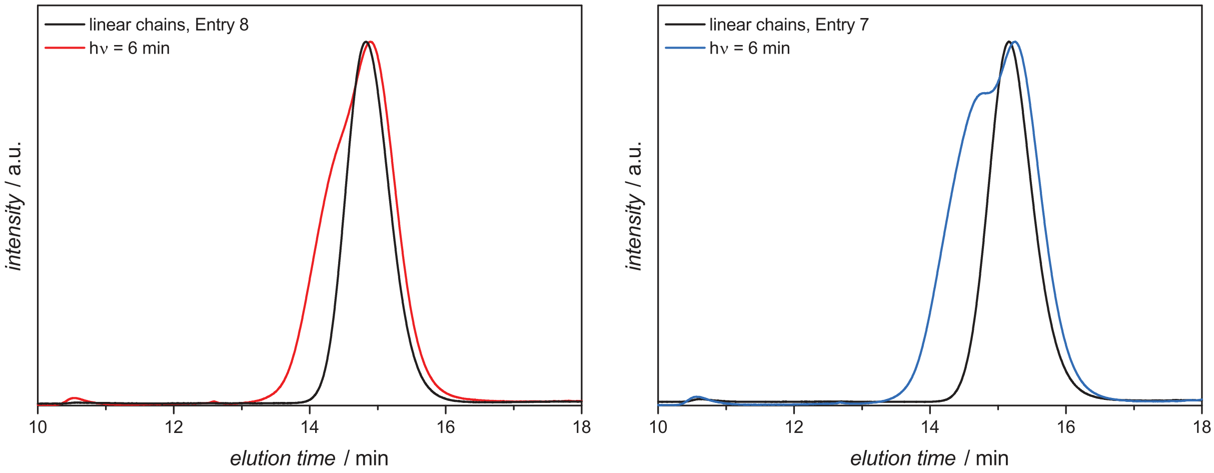

Figure 5.13.: Size-exclusion chromatograms of two irradiated (short) PImon-MMA-Copolymers. Left: M_n = 13400 g·mol^{-1}. Right: M_n = 8700 g·mol^{-1}.

Solvent	hν *Time*	*Intensity* (mW·cm^{-2})	Precursor	c_P (mg·mL^{-1})
DCM/Et$_2$O = 1/8	6 min	80	Entry 8	0.01
DCM/Et$_2$O = 1/8	6 min	80	Entry 7	0.01

Table 5.10.: Performed irradiation experiments with varied DCM/diethyl ether ratio at a wavelength of 320-390 nm. Entry 7 and 8 correspond to Table 5.1.

5.2.6. Irradiation at Higher Dilution and Lower Temperature

An additional method to reduce the probability of termination events between single precursors is to decrease their concentration in the irradiated medium. Therefore, the concentration of precursor was reduced to c_P = 0.005 mg·mL^{-1}, i.e., 4.5 mg of polymer were diluted in 900 mL of solvent. The experimental conditions are given in detail in Table 5.11 and the corresponding size-exclusion chromatogram is shown in Figure 5.14 (left). Surprisingly, such high dilution of the precursor still resulted in crosslinking of the chains.

All previous irradiation experiments were carried out at ambient temperature. Therefore, in order to decrease the mobility of the precursor chains in the solvent and, thus, decrease the probability of intermolecular interaction, the precursor solution was cooled down to -1°C prior to irradiation. All other experimental parameters were maintained. The corresponding size-exclusion chromatogram, illustrated in Figure 5.14 (right), shows that the decrease of the reaction temperature has a negative effect on the elution curve: a strong signal at shorter elution times can be detected, assigned to crosslinked material.

Solvent	hν *Time*	*Intensity* (mW·cm^{-2})	Precursor	c_P (mg·mL^{-1})	Temp. (°C)
DCM/Et$_2$O = 1/8	2 min	80	Entry 9	0.005	a.t.
DCM/Et$_2$O = 1/8	6 min	80	Entry 9	0.005	a.t.
DCM/Et$_2$O = 1/8	6 min	80	Entry 9	0.01	-1

Table 5.11.: Irradiation experiments performed with high dilution of the linear precursor and low temperature, respectively. Irradiation was carried out employing a wavelength of 320-390 nm and after addition of 5 mol% MEHQ. Entry 9 corresponds to Table 5.1.

5.2.7. Variation of the Normalization Method

In all previously shown size-exclusion chromatograms the evaluation was performed in such way that the intensities (the y-axis) of the respective elution curves were normalized to their peak heights. Thus, all maxima of the elution curves show an identical peak height. However, with this procedure shoulders that, for instance, are observed at shorter elution times, receive an excessive weight. As a result, small shoulders that correspond to a negligible amount of crosslinked material, could be overestimated. Hence, a different evaluation was performed, focusing on the area below an elution curve instead of on its peak height. Thereby, the area below the main peak of the elution curve of the precursor was calculated following the trapezoidal rule. Subsequently, all elution curves that were compared in one graph were normalized to the calculated area, respectively. As a result, the area below all compared elution curves remained constant, yet the peak heights varied. It is assumed that the described procedure gives a more realistic picture of the actual composition of a polymer sample. Figure 5.15 compares both normalization to peak height as well as to area. Thereby, the size-exclusion chromatograms showing the result of the irradiation experiment in Table 5.7, line two, were utilized.

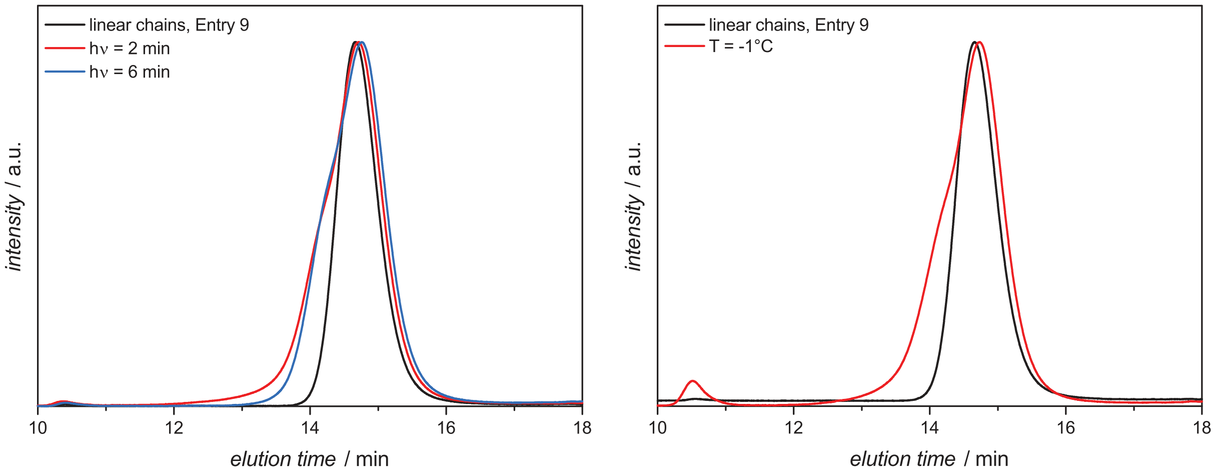

Figure 5.14.: Size-exclusion chromatograms for PImon-MMA-copolymers irradiated in high dilution: c_P = 0.005 mg·mL^{-1} (left) and low temperature: -1 °C (right). For experimental parameters see Table 5.11.

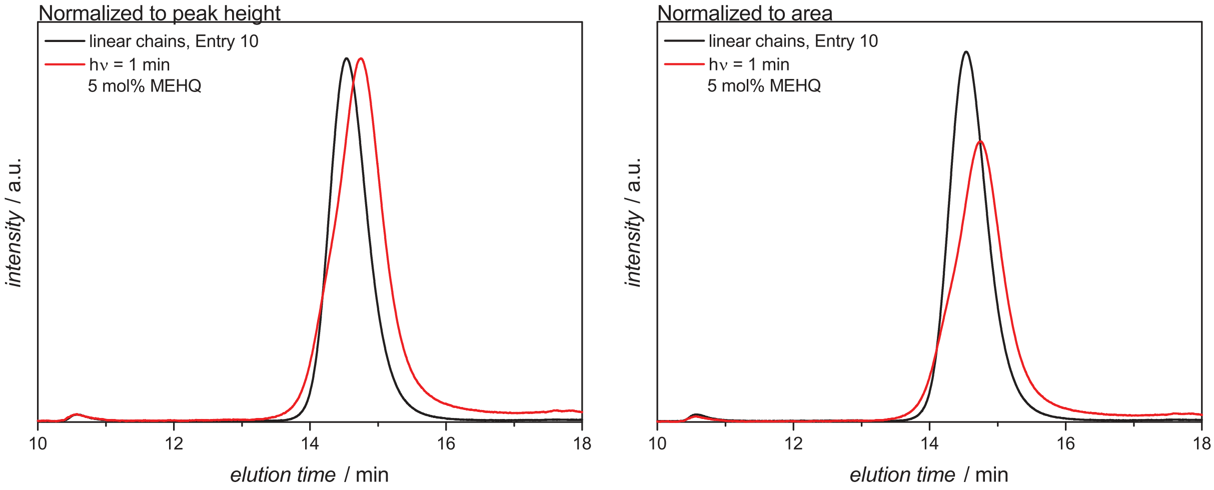

Figure 5.15.: Illustration of two different normalization methods for the evaluation of size-exclusion chromatograms. Left: Normalization to peak height. Right: Normalization to peak area.

Clearly, a shift of the curve toward longer elution times can be detected. However, precursor chains with higher molar masses (the left part of the curve) seem to remain in their unfolded state. Furthermore, material with a larger molar mass – presumably crosslinked chains – still remains as a shoulder at shorter elution times.

5.2.8. Variation of Irradiation Wavelength

An irradiation wavelength range of 320-390 nm was employed in all previous experiments. This wavelength range was selected, since the employed photoinitiator units show good absorbance in this area. As an additional parameter, the irradiation wavelength was changed to 365 nm, by using a corresponding filter. In Figure 5.16 the results of both wavelength ranges are compared. Thereby, the previously employed 320-390 nm range achieves a stronger shift of the elution curve toward longer elution times. Hence, more SCNP formation can be expected. On the other hand, irradiation with 365 nm results in no particular reduction of crosslinked material.

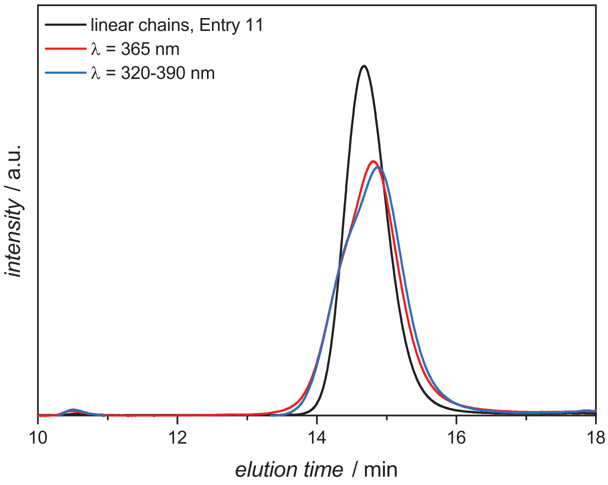

Figure 5.16.: Size-exclusion chromatogram (normalized to peak area) of PImon-MMA-copolymer irradiated with different wavelengths. Experimental conditions are equal to line 2 in Table 5.7.

5.2.9. Performance of Test Reactions

In order to exclude any influence of the RAFT end group, the latter was removed. Therefore, the PImon-MMA-copolymer was refluxed with the radical initiator AIBN, resulting in a polymer carrying an initiator-derived functionality in both α- and ω-position.[164] Subsequently, irradiation experiments were performed with the precursor carrying no RAFT group. Table 5.12 summarizes the experimental conditions and Figure 5.17 shows the corresponding elution curves. The results show that the RAFT group has no influence on the folding or crosslinking behavior of the precursor chains. The polymer without RAFT group undergoes intermolecular reactions in a similar manner as the polymer with intact RAFT functionality.

Solvent	hν *Time*	*Intensity* (mW·cm^{-2})	Precursor	c_P (mg·mL^{-1})
DCM/Et$_2$O = 1/8	1 min	80	Entry 8 w/o RAFT	0.01
DCM/Et$_2$O = 1/8	3 min	80	Entry 8 w/o RAFT	0.01
DCM/Et$_2$O = 1/8	6 min	80	Entry 8 w/o RAFT	0.01
DCM/Et$_2$O = 1/8	6 min	80	pMMA/PI	0.01

Table 5.12.: Performed irradiation experiments with precursor without RAFT end group and with pure pMMA (without photoinitiator units) in the presence of free photoinitiator (PI), respectively. Irradiation with a wavelength of 320-390 nm and after addition of 5 mol% MEHQ. Entry 8 corresponds to Table 5.1.

The test reaction, employing precursor without RAFT group, was complemented by an irradiation experiment of pure pMMA – without photoinitiator units – in the presence of free photoinitiator (Irgacure 2959). Thereby, a molar ratio of photoinitiator species to MMA of 1/10 was employed. The aim of this experiment was to show that photoinitiator radicals are not able to attack the polymer backbone and, thus, to form radical sites along the chain. Such a reaction could drastically increase the probability for intermolecular termination events and could thus be the reason for the shoulder that appeared in all size-exclusion chromatograms shown in the current work. The shoulder was assigned to crosslinked material. The right graph in Figure

5.17 shows the elution curve of the pMMA before irradiation (black) and after irradiation in the presence of photoinitiator (red). Although the change is minimal, a slight shoulder in the red curve can be detected. Hence, it is likely that the intermolecular termination reactions occur based on photoinitiator-generated radicals along the backbone. Thereby, radical sites could be generated along the polymer backbone – possibly formed by the second (and small) hydroxyl propyl radical of the photoinitiator. Intermolecular termination events could result in crosslinked material.

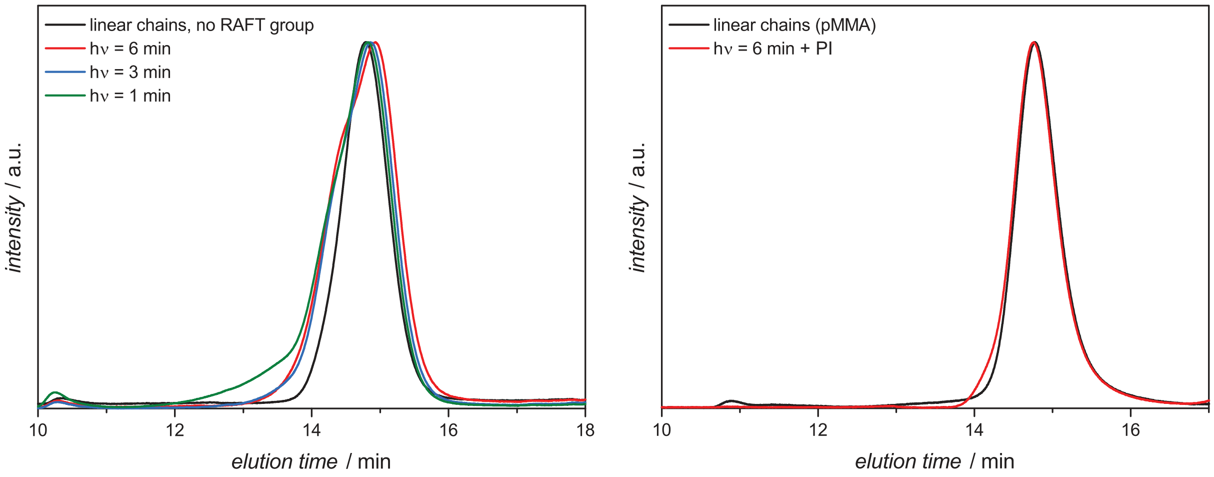

Figure 5.17.: Size-exclusion chromatograms of irradiated PImon-MMA-copolymers. Left: performed with PImon-MMA-copolymer without RAFT end group. Right: Performed with pMMA and added photoinitiator Irgacure 2959. Experimental conditions for both graphs according to Table 5.6, line five.

5.3. Characterization via DOSY

Diffusion ordered spectroscopy (DOSY), discussed in detail in section 2.8.2, is an NMR technique that measures the translational diffusion coefficient D of a molecule in solution. Since the hydrodynamic radius of a polymer particle can be directly correlated to its diffusion coefficient, DOSY serves as an ideal analytical method for the evaluation of folding processes within a polymer chain. In order to gain better insight into the processes occuring during the irradiation experiments of the PImon-MMA-copolymer precursors, DOSY measurements were performed for two selected experiments.[1] In both experiments, PImon-MMA-copolymer with a ratio of PImon/MMA = 1/11 was irradiated. Thereby, two different polymer chain lengths were selected: precursors with M_n = 13400 g·mol^{-1} and M_n = 15700 g·mol^{-1}, respectively (Entry 8 and 9 in Table 5.1). The experimental conditions are summarized in Table 5.13.

Figures 5.18 and 5.20 show the results of the DOSY analysis of the precursors prior to irradiation. The upper graph depicts the complete DOSY spectrum and the lower graph shows a zoom into the main signals. The spectra of the two non-irradiated precursors exhibit very narrowly distributed diffusion coefficients of D = 1.1-1.2 m^2·s^{-1} (Entry 8) and D = 1.0-1.2 m^2·s^{-1} (Entry 9). However, the DOSY spectra of the irradiated samples, illustrated in Figures 5.19 and 5.21, show many components that are larger or smaller than the precursor molecules. Thereby, in both experiments peaks from aromatic compounds, i.e., the photoinitiator units,

---

[1] DOSY measurements were performed by Richard K. Shoemaker from the University of Colorado Boulder.

Solvent	hν *Time*	*Intensity* (mW·cm^{-2})	Precursor	c_P (mg·mL^{-1})	MEHQ (mol%)	λ (nm)
DCM/Et$_2$O = 1/8	10 min	80	Entry 8	0.01	5	320-390
DCM/Et$_2$O = 1/8	10 min	80	Entry 9	0.01	5	320-390

Table 5.13.: Performed irradiation experiments with subsequent characterization via DOSY. For Entry 8 and 9 refer to Table 5.1.

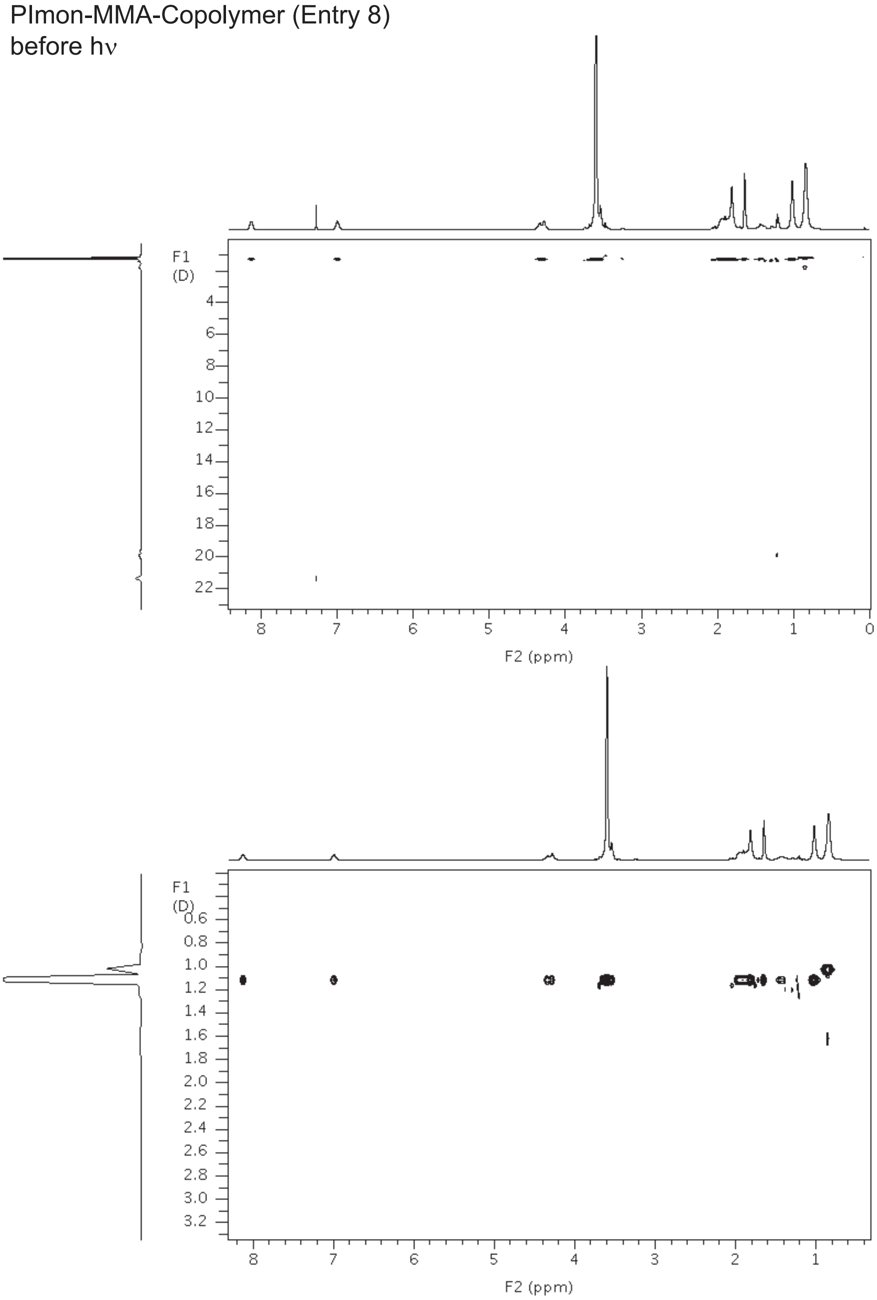

Figure 5.18.: DOSY spectrum of the PImon-MMA-copolymer precursor with a PImon/MMA ratio of 1/11 (Entry 8 in Table 5.1), before irradiation.

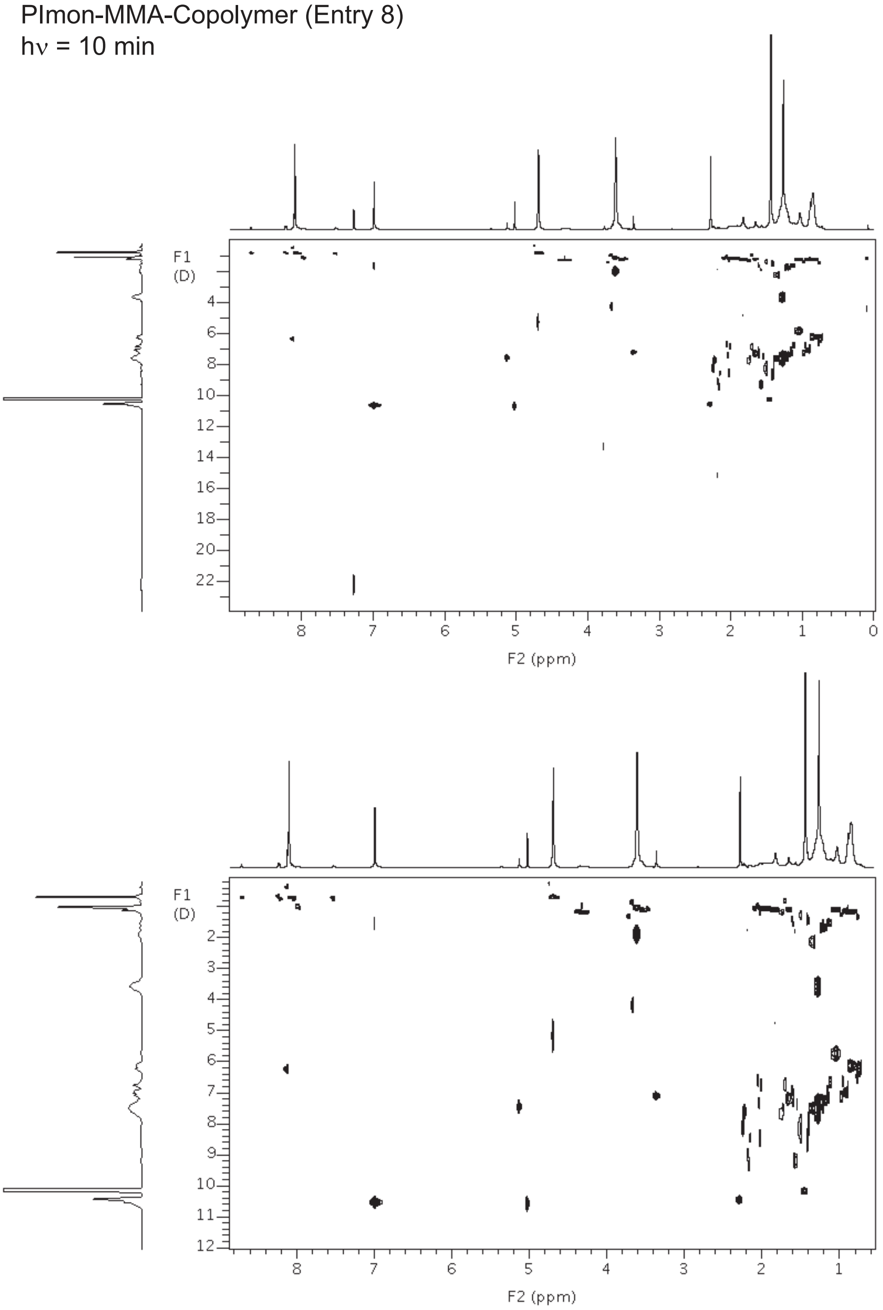

Figure 5.19.: DOSY spectrum of an irradiated PImon-MMA-copolymer precursor. Experimental conditions are listed in Table 5.13, line one.

as well as aliphatic compounds, originating from the polymer backbone, can be found with small, similar as well as larger diffusion coefficients compared to the linear precursor. For instance, the spectrum in Figure 5.21 (Entry 9 irradiated) shows components that are larger (exhibiting a smaller diffusion coefficient), nearly the same, or much smaller – with a ten-fold larger diffusion coefficient – compared to the non-irradiated polymer of Entry 9. Thereby, the smaller components, with D = 10 $m^2{\cdot}s^{-1}$ are nevertheless larger than the solvent molecules with a diffusion coefficient of about 22 $m^2{\cdot}s^{-1}$.

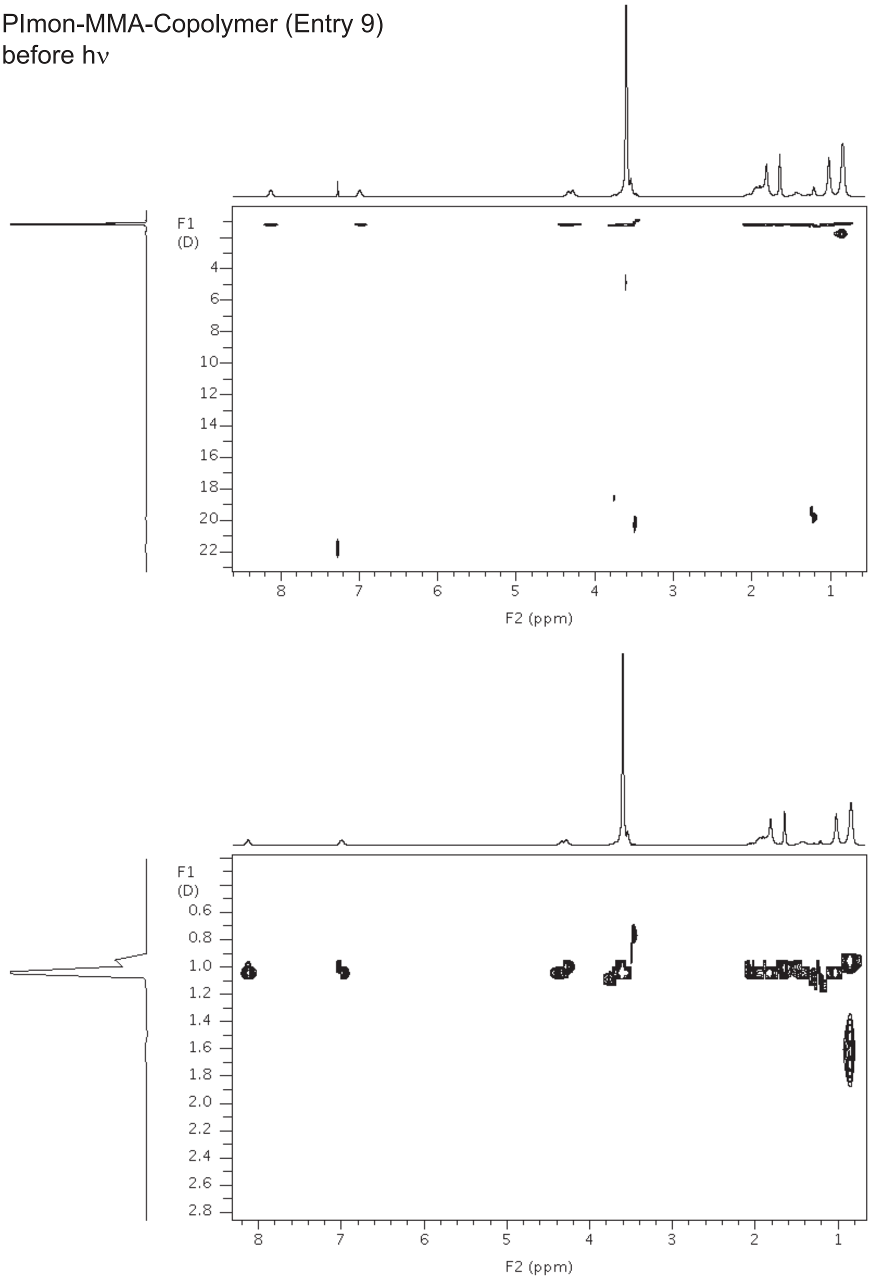

Figure 5.20.: DOSY spectrum of the PImon-MMA-copolymer precursor with a PImon/MMA ratio of 1/11 (Entry 9 in Table 5.1), before irradiation.

5.4. Conclusions and Outlook

Combining the results from SEC and DOSY measurements, it can be stated that the radical photoinitiator-induced formation of SCNPs could not be performed successfully. Although a clear shift in the size-exclusion chromatogram toward longer elution times could be detected, the formation of material at longer elution times, i.e., larger molar masses, could not be prevented by changing various experimental parameters. Varying the solvent mixture, photoinitiator unit density along the polymer chain, irradiation time, irradiation intensity and wavelength, and precursor concentration did not result in a folding of the polymer chains into

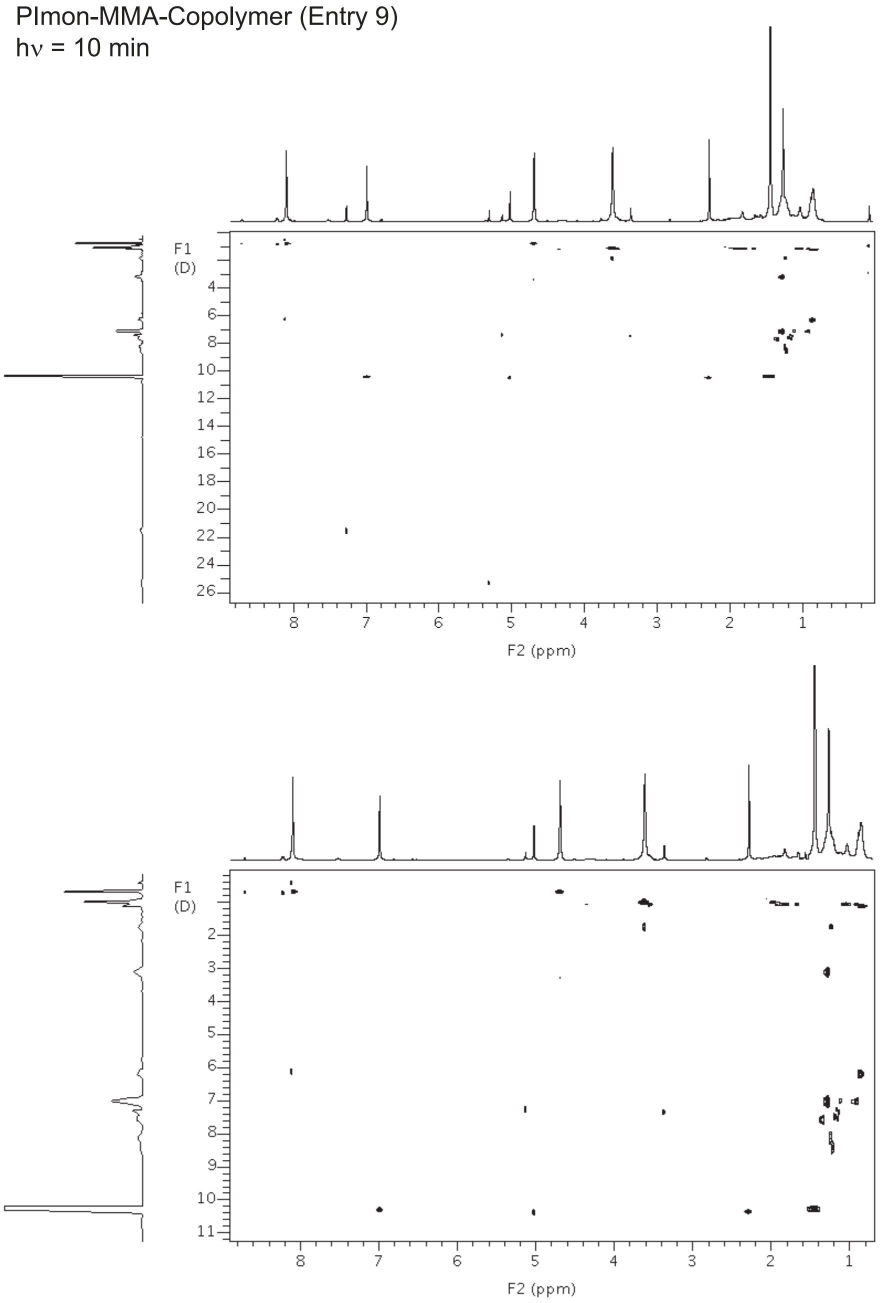

Figure 5.21.: DOSY spectrum of an irradiated PImon-MMA-copolymer precursor. Experimental conditions are listed in Table 5.13, line two.

nanoparticles without formation of crosslinked material.
DOSY measurements could not prove the formation of nanoparticles, since no components with a slightly larger diffusion coefficient were detected – as it is expected for successful SCNP formation. Components with larger diffusion coefficients, presumably corresponding to crosslinked material, as well as components with much smaller diffusion coefficients were detected. The latter presumably result from disintegration processes – performed during the irradiation – that are induced by radical abstraction reactions. Giving a clear picture of the processes occuring during the irradiation experiment is not feasible. However, it is assumed

that the high reactivity of the formed radicals results in several termination and abstraction processes that do not allow for an efficient and exclusive intramolecular termination reaction. An important factor may be the formation of the small hydroxyl propyl radical after the radical cleavage of the photoinitiator unit. It can contribute to radical abstraction processes that lead to disintegration of polymer chains. However, since radicals are usually formed in an even number, the formation of a second radical – in addition to the desired radical species – cannot be avoided. Yet, based on the structure of the photoinitiator, the second radical could be designed as a stable radical, stabilized by, for instance, a tertiary structure or a mesomeric impact. Due to their lower reactivity such stable radicals are assumed to contribute less in radical abstraction reactions.

Although a wide range of experimental parameters was varied in the current work, additional experiments could be performed to achieve an efficient SCNP formation. The following parameters could be varied: First, the irradiation performed in the current work was carried out using a glass fiber cable that directed the light onto the flask containing the precursor solution. The small outlet of the cable, with an area of approx. 1 cm^2, resulted in a narrow light beam passing through the solution. Hence, only a relatively small solution volume was constantly irradiated. The system could be improved by irradiating the complete solution evenly. Thereby, large vertical lamps could be employed as irradiation sources. A further improvement could be to irradiate the precursor solution in a flow reactor. Thereby, a highly-diluted solution could be pumped through a system that is irradiated at a certain position for a very short time. This method could facilitate applying lower precursor concentrations (no handling of large flasks) with short irradiation times. As the reported experiments show, the generated radicals are highly reactive and crosslinking events occur already after irradiation times as short as 1 min. Hence, irradiation times in the time range of seconds could be sufficient to induce radical formation that could lead to intramolecular termination and SCNP formation.

6

Conclusions and Outlook

In the current thesis, the main goal was to enhance the initiation behavior of radical photoinitiators and to investigate mechanistic aspects of the photoinitiation step. In Chapter 3 radical photoinitiators were studied via a combination of PLP-ESI-MS, femtosecond spectroscopy, and theoretical calculations. PLP-ESI-MS gave valuable insights into the initiation efficiency of single radical fragments. Particularly, the initiation efficiency of various initiator fragments – with distinct substitution patterns – was quantitatively compared to the benzoyl or 4-methyl benzoyl fragment of benzoin and 4-methyl benzoin, respectively. It was shown that benzoin-derivatives with fluorine-substitution at the hydroxyl benzyl position posses the best initiation efficiency. In contrast, introduction of a dimethylamine-substituent results in a very poor initiation performance of benzoin-derived radicals.

In the frame of a collaboration, the investigation via PLP-ESI-MS was accompanied by employing femtosecond spectroscopy as well as computational methods. Femtosecond spectroscopic investigation of the photoinitiators gave a complete picture of the electronic processes molecules undergo upon irradiation. In detail, lifetimes of electronically excited singlet and triplet states were determined as well as their energetic positioning. Thus, valuable information about the possibilities to perform intersystem crossing and radical formation were obtained. Computational methods were employed for the determination of radical reactivities towards methyl methacrylate. Combining the findings of PLP-ESI-MS, femtosecond spectroscopy, and theoretical calculations resulted in the determination of key parameters characterizing a good radical photoinitiator of benzoin-type structure. Notably, the introduction of electron-withdrawing substituents showed the most promising results. In addition, it was shown that the absorption behavior of the respective photoinitiators is by no means a measure of its reactivity. On the contrary, benzoin-derivatives exhibiting a strong absorption at the employed irradiation wavelength showed poor initiation efficiencies.

In order to improve the efficiency of photoinitiating systems, it is important to understand the underlying processes and the approach presented in the current thesis is therefore an important step in this direction. Further studies should be performed focussing on the introduction of additional fluoride substituents along the aromatic rings of benzoin and other electron-withdrawing groups such as a triflate group. Substituents that enhance the mesomeric effect, such as the polycyclic aromatic moieties pyrene or anthracene, may be interesting regarding their influence on the initiation efficiency as well as molecular dynamics of the benzoin derivative.

The light-induced copper-mediated reversible-deactivation radical polymerization (photoRDRP), a photoinitiated polymerization that is not based on the radical cleavage of photoinitiators, yet on a light-induced electron transfer reaction was investigated in Chapter 4. The mechanism of this recently developed polymerization method was elucidated by means of PLP-ESI-MS. Various combinations of typical photoRDRP components were irradiated in PLP experiments. ESI-MS analysis of the formed material provided information on the nature of the initiating fragments and the reactions occuring upon irradiation. A critical evaluation of all reaction steps resulted in the postulation of a mechanism of photoRDRP that is verified on a molecular level, i.e., the involved species were unambiguously identified. Importantly, the photoexcited amine ligand was identified as the main reducing agent for the deactivator species $Cu(II)Br_2/L$ to $Cu(I)Br/L$, two copper complexes that govern the equilibrium between active (propagating) radical chains and dormant polymer chains carrying a bromine end group. The elucidation of the photoRDRP mechanism enabled not only the understanding of how the reaction can be initiated by light, but the important parameters which enhance the living character of the polymerization have been identified. In further investigations the focus should be placed on the impact of structurally different initiators and ligands as well as employing different irradiation wavelengths. An investigation of the respective alkyl halides and amine ligands via femtosecond spectroscopy should provide deeper insight into their molecular dynamics and electronic processes that occur upon irradiation. A detailed study on the influence of various irradiation wavelengths in the UV as well as visible range should be performed in order to find the most suitable light source that enhances the formation of radicals and the performance of reduction steps. In such a way, additional parameters could be identified that may further improve photoRDRP with regard to its polymerization rate and living character.

Next to the mechanistic investigation of photoinitiated polymerization processes, Chapter 5 described a study that was carried out with the aim of linking polymer segments intramolecularly. Thereby, radical photoinitiators – introduced along the polymer backbone – were examined in their ability to generate covalent bonds based on radical-radical termination events. High dilution of the respective photoinitiator-functionalized polymers was supposed to result in intramolecular reactions and, thus formation of so-called single-chain nanoparticles (SCNPs). The radical combination reaction – known as a very fast and efficient reaction – was envisaged to provide a new and facile synthetic pathway for SCNP formation. However, although to date a wide range of different chemical reaction types was reported to successfully generate SCNPs, the radical combination reaction did not result in an efficient intramolecular folding of the chains. Intermolecular crosslinking of the polymer chains and radical abstraction reactions occurred, even after varying a wide range of experimental conditions. Such a result demonstrates the high reactivity of radicals and their affinity to abstraction reactions compared to, for instance, the two reactants of a Diels–Alder reaction, a reaction type that was previously successfully employed for SCNP formation. In order to gain control over the radical combination step and its high rate coefficient, elaborate experimental parameters may be required. For instance, utilization of a flow reactor would allow highly diluted conditions, yet without large reaction flasks, and very short irradiation times. In addition, the radical reactivity should be reduced by, for instance, employing photoinitiator moieties with a lower tendency to perform radical formation. Nevertheless, the generated radicals should provide a higher ability to perform combination than abstraction reactions. Furthermore, the second radical moiety – not covalently linked to the polymer chain – should exhibit a high stability in order to avoid abstraction reactions. Finally, the flexibility of the precursor should be enhanced with regard to a better entanglement of the chain, for instance by appropriate monomer selection.

7

Experimental Section

7.1. Photoinitiator Investigation

7.1.1. Materials and Instrumentation

Materials

Methyl methacrylate (MMA, Sigma-Aldrich, 99%) was freed from inhibitor by passing through a column of activated basic alumina (Merck). Benzoin (Bz, Sigma-Aldrich, 98%) and 2-methyl-4-(methylthio)-2-morpholinopropiophenone (MMMP, Sigma-Aldrich, 98%) were recrystallized twice in ethanol prior to use. 4-Methyl benzoin (4MB) was synthesized according to the literature.[124]

1-[4-(Dimethylamino)phenyl]-2-hydroxy-2-phenylethanone (NMe_2Bz, Sigma-Aldrich), 4,4'-difluorobenzil (DFB, Merck, 98%), phenylglyoxal monohydrate (Sigma-Aldrich, 97%), 4-fluorophenylglyoxal monohydrate (Carbolution Chemicals, 98%), *N*,*N*-dimethylanilin (Merck, 99%), methylisobutyrate (MIB, Sigma-Aldrich, 99%), dichloromethane (DCM, Normapur, VWR), benzene (anhydrous, Alfa Aesar, 99.8%) and sodium sulfate (Na_2SO_4, Carl Roth, 99%), and Benzil (Sigma-Aldrich, 98%) were used as purchased.

For the ESI-MS measurements sodium trifluoroacetate (Sigma-Aldrich, 99%), toluene (Carl Roth, Rotisolv HPLC grade), tetrahydrofuran (THF, Scharlau Multisolvent, GPC grade) and methanol (VWR, Chromanorm) were employed as received. Methylisobutyrate (MIB, Sigma Aldrich, 99%) was used as purchased.

PLP Experiments

All PLP samples (volume approx. 0.5 mL) contained MMA and a mixture of photoinitiators (PI) with a concentration of $c_{PI} = 5 \cdot 10^{-3}$ mol$\cdot$ L^{-1}. The samples were freed from oxygen prior to laser irradiation by purging the reaction mixture with nitrogen for 2 min. Each sample vial was subsequently placed into a sample holder, which was held at a constant temperature of -5°C using a thermostat (1196D, VWR, Darmstadt, Germany). The temperature was independently measured at the sample holder. The sample temperature was allowed to equilibrate for 5 min before starting the polymerization. Photoinitiation was achieved by an excimer laser system (Coherent Xantos XS-500, XeF, frequency variable from 1 to 500 Hz, operating at a wavelength of 351 nm with a pulse width of approx. 20 ns) at 100 Hz for an overall polymerization time of 90 000 laser pulses ($\approx$ 15 min). A custom-built metal filter (fine-mesh metal grid) was implemented next to the radiation exit window to obtain a reduced laser energy of $\approx$ 0.35 mJ per pulse. The laser beam was redirected to illuminate the vial from the bottom (the detailed laser setup is described in literature[122]).

ESI-MS Measurements

For section 3.1, direct infusion ESI-MS measurements were performed in a toluene/methanol (3 : 2 v/v) mixture with 300 mM sodium trifluoroacetate (NaTFA) to avoid H^+ ionization of the polymer chains containing the morpholino end group (N). For section 3.2, direct infusion ESI-MS measurements were performed in a THF/methanol (3:2 v/v) mixture with 100 μM sodium trifluoroacetate (NaTFA). For both studies, a polymer concentration of 0.4 $\text{mg}\cdot \text{mL}^{-1}$ was applied for the measurements. ESI-MS spectra were recorded using an LXQ mass spectrometer (ThermoFisher Scientific, San Jose, CA, USA) equipped with an atmospheric pressure ionization source operating in the nebulizer assisted electrospray mode. The instrument was calibrated in the m/z range 195-1822 using a standard containing caffeine, Met-Arg-Phe-Ala acetate (MRFA) and a mixture of fluorinated phosphazenes (Ultramark 1621) (all from Aldrich). A constant spray voltage of 4.5 kV was used and nitrogen at a dimensionless sweep gas flow rate of 2 (approx. 3 $\text{L}\cdot\text{min}^{-1}$) and a dimensionless sheath gas flow rate of 12 (approx. 1 $\text{L}\cdot\text{min}^{-1}$) were applied. The capillary voltage, the tube lens offset voltage, and the capillary temperature were set to 6 kV, 110 V, and 300°C, respectively.

Size-Exclusion Chromatography (SEC)

Size exclusion chromatography (SEC) measurements were performed on a Polymer Laboratories (Varian) PL-GPC 50 Plus Integrated System, comprising an autosampler, a PLgel 5 mm bead-size guard column (50 x 7.5 mm), one PLgel 5 mm Mixed E column (300 x 7.5 mm), three PLgel 5 mm Mixed C columns (300 x 7.5 mm), and a differential refractive index detector using THF as the eluent at 35°C with a flow rate of 1 $\text{mL}\cdot \text{min}^{-1}$. The SEC system was calibrated using linear poly(styrene) standards ranging from 160 to $6\cdot10^6$ $\text{g}\cdot\text{mol}^{-1}$ and linear poly(methyl methacrylate) standards ranging from 700 to $2\cdot10^6$ $\text{g}\cdot\text{mol}^{-1}$. The resulting molecular weight distributions were determined by universal calibration using Mark-Houwink parameters for polystyrene ($K = 14.1\cdot10^{-5}$ $\text{dL}\cdot\text{g}^{-1}$, $\alpha = 0.7$).[165]

UV-Vis Spectroscopy

All UV-Vis steady-state spectra of the presented photoinitiators, as well as their determined extinction coefficients were recorded on a Varian Cary 500 spectrometer. The absorption spectra and resulting extinction coefficients were measured along a wavelength range of 200-800 nm in quartz glass SUPRASIL cuvettes (Hellma) and methylisobutyrate (MIB) as solvent. For section 3.2, a dilution series was performed using cuvettes with different optical path lengths (1, 10, 20, and 50 mm).

NMR Spectroscopy

The synthesized compounds were analyzed via ^{1}H-NMR and ^{19}F-NMR spectroscopy using a Bruker Avance 400 spectrometer (400 MHz). Samples were dissolved in $CDCl_3$. The δ-scale was referenced with tetramethylsilane ($\delta = 0.00$) as internal standard. Abbreviations used in the description of the photoinitiator syntheses include singlet (s), doublet (d), triplet (t), and unresolved multiplet (m).

Femtosecond Spectroscopy

The photophysical and photochemical properties of the photoinitiators were studied by femtosecond transient absorption spectroscopy. The employed setup is shown in Figure 7.1, similar to a state-of-the-art femtosecond transient spectrometer described by Riedle et al.[166] Laser pulses with 1.6 mJ per pulse at a central wavelength of 775 nm, a typical pulse duration of 150 fs and a repetition rate of 1 kHz were generated using a CPA 2210 laser system (Clark-MXR).[132,167]

For Section 3.1, a portion of the fundamental beam (250 mJ per pulse) was split into two parts by a beam splitter (BS) on the one hand to operate a NOPA (non-collinearly optical parametric amplifier) system in the visible region and on the other hand to generate a white light (WL) continuum. In order to excite the photoinitiators in the UV region, the visible pulses generated by the NOPA system were dispersion optimized using a prism compressor (PC) and subsequently upconverted into UV by frequency doubling using a BBO crystal. Since this method allows for pump wavelengths in a tunability range between 240 nm and 360 nm, the photoinitiators were investigated at two selected pump wavelengths (325 nm and 351 nm, respectively) with pulse energies of about 0.3 and 0.25 mJ per pulse. A computer-controlled delay stage in combination with a retro reflector was employed for measuring at different delay times. The second portion of the fundamental laser output, employed for WL generation, was focused into a sapphire plate (1 mm (4)) after passing through an iris (1), a neutral density filter (2), and a lens (3). After recollimation, the seed-wavelength was removed from the WL spectrum using a custom-made dielectric filter (Laser Components). Thus, the generated WL covers the large wavelength range of 430 nm to 710 nm employed for probing the molecules. The pump pulse and WL were focused into the sample under magic angle conditions. Behind the sample the transmitted WL was split in a prism-based polychromator and detected using a CCD camera (Linescan 2000, Ingenieurbüro Stresing). For efficient exploitation of the detector's dynamic range, the dispersed WL was attenuated using a variable neutral density filter in front of the camera. The repetition rate of the laser pulses was reduced using a chopper wheel to allow for measuring the change of the optical density ΔOD, where $I(\lambda,t)$ and I_0 are the transmitted probe light through the excited and non-excited sample and ΔOD_0 the optical density of the non-excited sample.

$$\Delta OD(\lambda,t) = log\left(\frac{I_0}{I(\lambda,t)}\right) - \Delta OD_0 \tag{7.1}$$

The CCD camera was aligned using small bandwidth interference filters inserted into the WL beam path at the position of the sample. The temporal overlap between the pump and the probe beam (time zero) was adjusted by the dye molecule 7-diethylamino-3-thenoylcoumarin (DETC). The samples were continuously pumped through a fused silica cuvette with an optical path length of 1 mm to avoid decomposition by radiation. Data acquisition was performed using a home-made software in a Labview environment. Furthermore, the transient data are corrected for the chirp of the white light caused by group velocity dispersion due to optical components in the The CCD camera was aligned using small bandwidth interference filters inserted into the WL beam path at the position of the sample. The temporal overlap between the pump and the probe beam (time zero) was adjusted by the dye molecule 7-diethylamino-3-thenoylcoumarin (DETC). The samples were continuously pumped through a fused silica cuvette with an optical path length of 1 mm to avoid decomposition by radiation. Data acquisition was performed using a home-made software in a Labview environment. Furthermore, the transient data are corrected for the chirp of the white light caused by group velocity dispersion due to optical components in the probe beam. Thereby, the chirp correction is based on the determination of the coherent artifact characterized by the temporal overlap of the pump pulse with a certain frequency component of the white light continuum.[166]

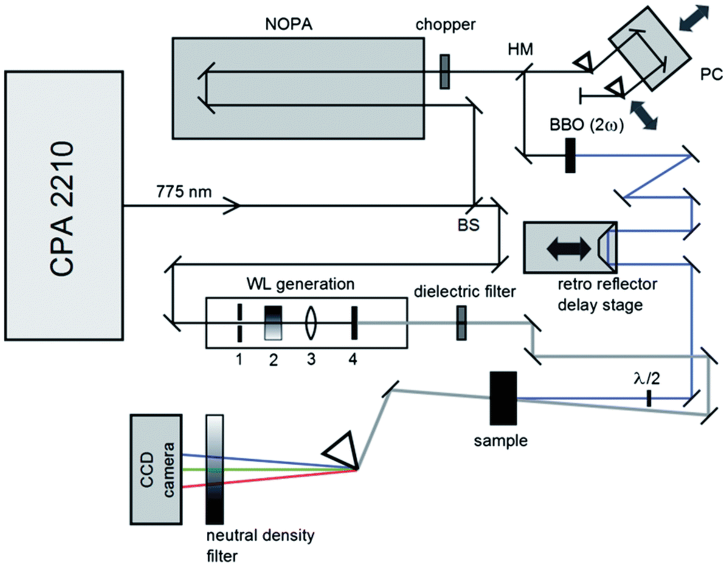

Figure 7.1.: Scheme of the employed transient spectrometer consisting of a half mirror (HM), a prism compressor (PC), and a beam splitter (BS).

For section 3.2, the generated pulses resulting from the higher pumped NOPA system served for a sum-frequency mixing process with a central wavelength of 775 nm in order to generate pump pulses in the UV region (300-360 nm). The smaller portion of the fundamental laser output was employed to pump a second NOPA system, producing probe pulses in the wavelength range of 470-750 nm. The pump and probe pulses were focused into the sample for a temporal and spatial overlap of both beams under magic angle (54.7°) conditions to avoid anisotropic effects. In order to measure different delay times between exciting and probing the sample a computer-controlled translation stage (Physik Instrumente) was employed for delaying the probe pulses with respect to the pump pulses. The experimental time resolution was around 100-150 fs. The change of optical density (ΔOD) was recorded as a function of delay time, by measuring with and without a pump pulse, practically realized by a mechanical chopper. All samples were prepared in MIB solutions and measured in a 1 mm quartz glass SUPRASIL flow cell up to a maximum delay of 600 ps.

Theoretical Methods

For section 3.1, DFT calculations as well as TD-DFT calculations for excited states were performed employing the TURBOMOLE V6.3 program package.[168] The geometries of the ground states were optimized using BP86/def2-SV(P).[169–178] Energies at the optimized geometries as well as singlet and triplet excitations[179–181] and associated oscillator strengths were computed by B3LYP/aug-ccpVDZ.[169–173,175–177,182–184]

For section 3.2, the high-level composite ab initio G3(MP2)-RAD[185] method was used in conjunction with M06-2X[186] thermochemistry to obtain accurate gas-phase energies. The SMD[187] method was used to model implicit solvation effects using methyl propanoate (for comparison with the polymerizations) and acetonitrile (for benchmarking against available experiment) as the solvents. Similar methodology has been previously shown to predict accurate values for the kinetics and thermodynamics of a wide range of including propagation[188–190] and rate coefficients for addition reactions involving acyl radicals.[191] In the present work we benchmark this methodology against experiment for two related reactions and show that it reproduces the experimental rate coefficients to within a factor of 3 or better (see supporting information). All standard ab initio molecular orbital theory and density functional theory (DFT) calculations were carried out using Gaussian 09[192] and Molpro 2012,[193] software packages. A full set of obtained results can be found in the ESI. Excited state properties were computed using DFT as well as TD-DFT, both calculations were performed applying the TURBOMOLE V6.3 program package.[168] Optimization of the geometries for the ground states were carried out by BP86/def2-SV(P).[169–178] B3LYP/aug-cc-pVDZ[169–173,175–177,182–184] was used to calculate the energies of the optimized geometries as well as for singlet and triplet excitations[179–181] and their related oscillator strengths.

7.1.2. Syntheses

Synthesis of NMe$_2$Bz Iso

Phenylglyoxal monohydrate (2.000 g, 13.2 mmol) and *N*,*N*-dimethylanilin (1.594 g, 13.2 mmol) were mixed with benzene (18 mL). The reaction mixture was refluxed at 80°C for 2 h. The solvent was evaporated under vacuum to give an orange oil. Recrystallization in ethanol gave green crystals (150 mg, 4.5%). ^{1}H-NMR (400 MHz, CDCl$_3$, δ, ppm): 2.84 (s, 6H, N(CH_3)$_2$), 4.32 (d, 1H, CHOH), 5.81 (d, 1H, CHOH), 6.56 (d, 2H, CH_{ar}CH), 7.09 (d, 2H, CH_{ar}CHCN), 7.31 (t, 2H, CH_{ar}CHCH), 7.42 (t, 1H, CH_{ar}CHCH), 7.84 (d, 2H, CH_{ar}CCO).

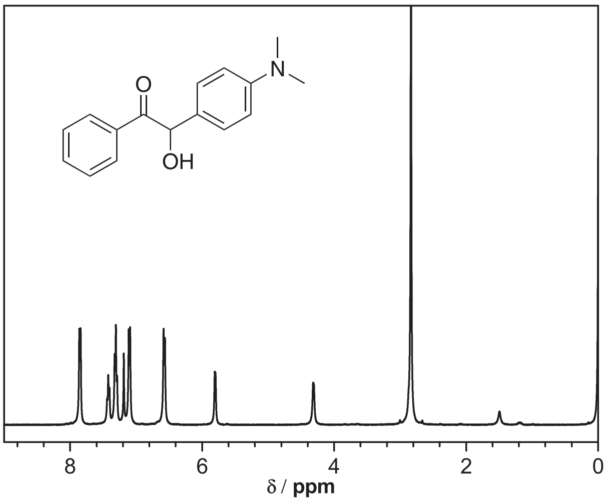

Figure 7.2.: ^{1}H-NMR spectrum of NMe$_2$Bz Iso.

Synthesis of FNMe$_2$Bz

4-Fluorophenylglyoxal monohydrate (0.200 g, 1.18 mmol) and *N*,*N*-dimethylanilin (0.142 g, 1.18 mmol) were mixed with benzene (5 mL). The reaction mixture was refluxed at 80°C for 6 h. The solvent was evaporated under vacuum to give an orange oil. Recrystallization in ethanol gave yellow crystals (59.9 mg, 18.6%). ^{1}H-NMR (400 MHz, CDCl$_3$, δ, ppm): 2.84 (s, 6H, N(CH_3)$_2$), 4.28 (s, 1H, CHOH), 5.75 (s, 1H, CHOH), 6.56 (d, CH_{ar}CH), 6.97 (t, 2H, CH_{ar}CHCF), 7.07 (d, 2H, CH_{ar}CHCN), 7.86-7.90 (m, 2H, CH_{ar}CCO). ^{19}F-NMR (400 MHz, CDCl$_3$, δ, ppm): -103.7 (s, 1F, C$_{ar}$F).

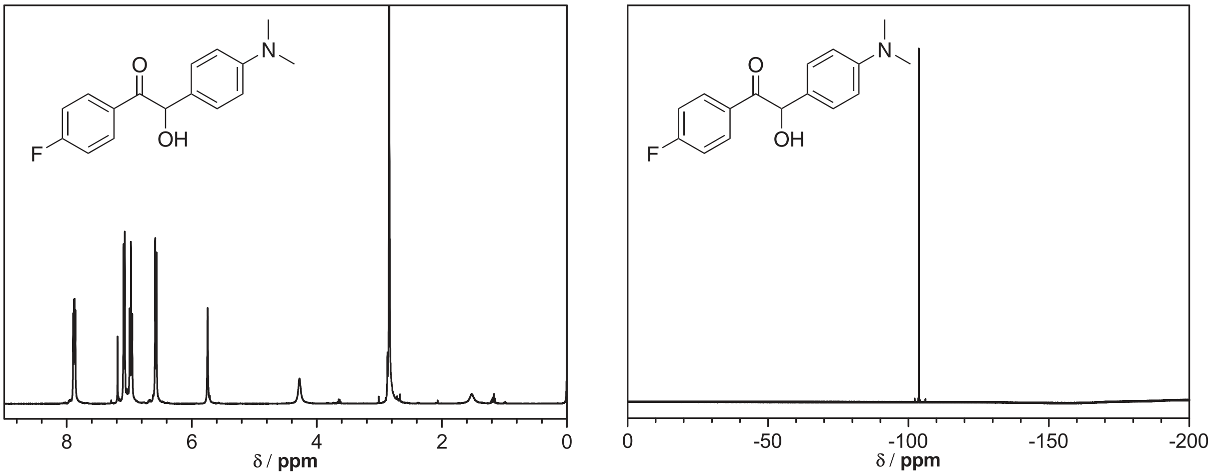

Figure 7.3.: ^{1}H-NMR (left) and ^{19}F-NMR spectrum (right) of $\mathrm{FNMe_2Bz}$.

Synthesis of FBz

4-Fluorophenylmagnesium bromide (1.2 mL, 2.38 mmol, 0.474 g) was dissolved in absolute diethyl ether (4 mL) under a nitrogen atmosphere. Trimethylsilylated cyanohydrin (0.5 mL, 2.38 mmol, 0.489 g) was dissolved in absolute diethyl ether (4 mL) and degassed by nitrogen bubbling for 15 min. Subsequently, the solution was added to the Grignard solution during a period of 10 min and the reaction mixture was stirred for 2 h. The reaction mixture was poured into a separating funnel containing 1 mL of concentrated sulfuric acid dissolved in 30 mL of cold water. The phases were separated and the ether layer was extracted with aqueous hydrochloric acid (5%, 2 x 5 mL). The combined aqueous solutions were left standing over night at ambient temperature to afford a white crystalline solid (98.5 mg, 18%). ^{1}H-NMR (400 MHz, $\mathrm{CDCl_3}$, δ, ppm): 4.25 (s, 1H, CHOH), 5.83 (s, 1H, CHOH), 6.98 (t, 2H, CH_arCHCH), 7.18-7.28 (m, 5H, CH_arCHCH and CH_arCHCF), 7.85-7.89 (m, 2H, CH_arCCO). ^{19}F-NMR (400 MHz, $\mathrm{CDCl_3}$, δ, ppm): -102.93 (s, 1F, $\mathrm{C_{ar}F}$).

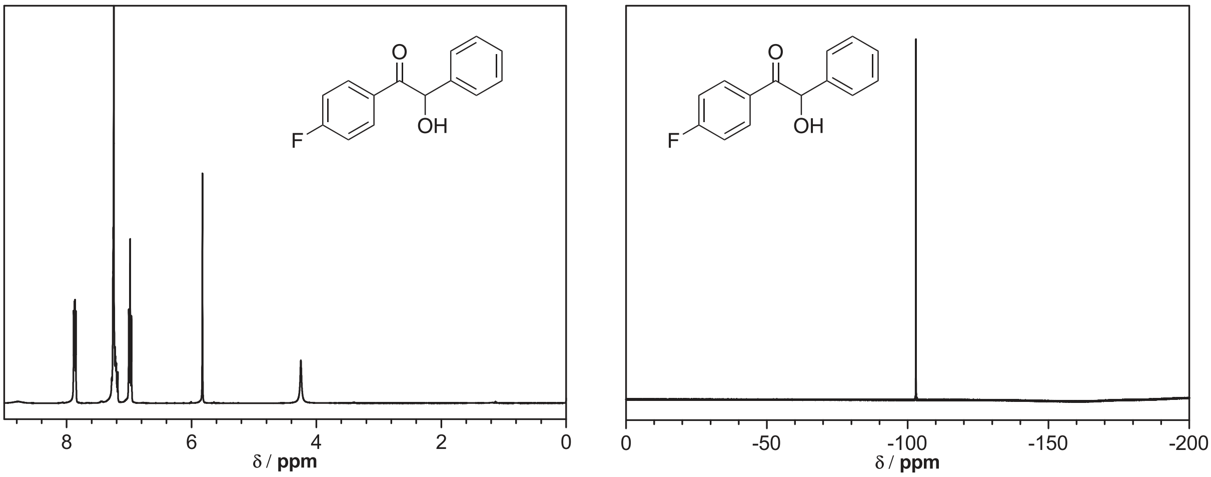

Figure 7.4.: ^{1}H-NMR (left) and ^{19}F-NMR spectrum (right) of FBz.

Synthesis of FBz Iso

Fluorobenzaldehyde (10.000 g, 80.6 mmol) was dissolved in ethanol (20 mL) at ambient temperature and an aqueous solution of sodium cyanide (1.185 g, 24.2 mmol in 9.4 mL water) was added. The solution was stirred for 10 min. Subsequently, benzaldehyde (8.551 g, 80.6 mmol) was dissolved in ethanol (20 mL) and added to the fluorobenzaldehyde solution. The reaction mixture was refluxed (80°C) for 5 h. The mixture was allowed to reach ambient temperature. After addition of water (10 mL) the reaction mixture was extracted with DCM (4 x 30 mL), the organic phase was dried over Na_2SO_4, and the solvent was evaporated to give an oily solid. Fivefold recrystallization in ethanol gave needle-like off-white crystals (461 mg, 2.5%). ^{1}H-NMR (400 MHz, $CDCl_3$, δ, ppm): 4.48 (s, 1H, CHOH), 5.88 (s, 1H, CHOH), 7.18-7.27 (m, 4H, CH_{ar}CF and CH_{ar}CH), 7.31 (t, 2H, CH_{ar}CHCH), 7.44 (t, 1H, CH_{ar}CHCH), 7.83 (d, 2H, CH_{ar}CCO). ^{19}F-NMR (400 MHz, $CDCl_3$, δ, ppm): -112.93 (s, 1F, C_{ar}F).

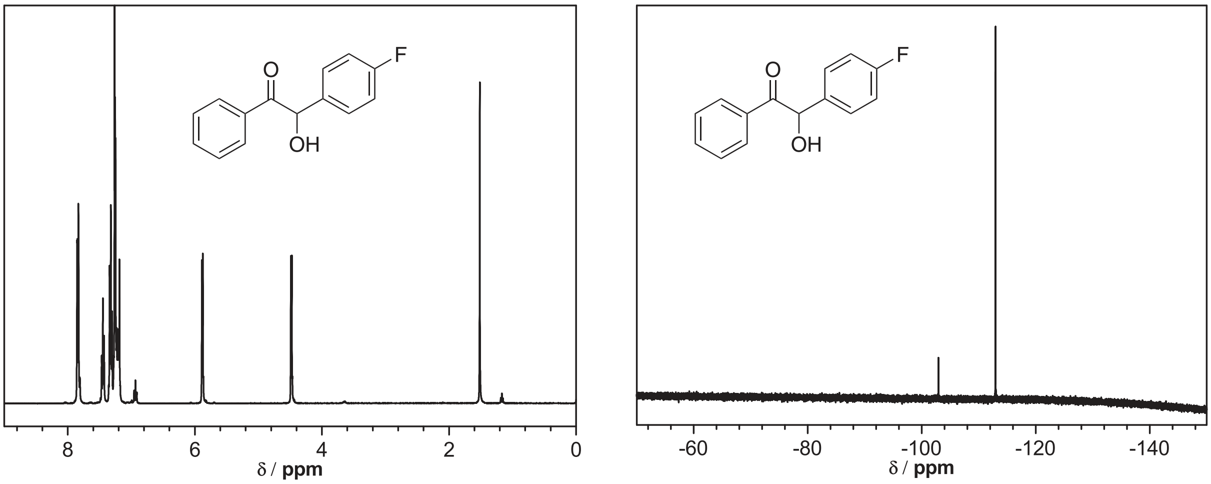

Figure 7.5.: ^{1}H-NMR (left) and ^{19}F-NMR spectrum (right) of FBz Iso.

Synthesis of F_2Bz

Fluorobenzaldehyde (5.000 g, 40.29 mmol) was dissolved in ethanol (20 mL) at ambient temperature and an aqueous solution of sodium cyanide (0.5924 g, 12.09 mmol in 4.7 mL water) was added dropwise. The solution was refluxed (85°C) for 5 h and was then allowed to reach ambient temperature. After addition of water (10 mL) the reaction mixture was extracted with DCM (4 x 15 mL), the organic phase was dried over $MgSO_4$, and the solvent was evaporated to give an orange oil. Purification by column chromatography (silica gel, *c*-hexane/ethyl acetate 4/1 v/v) and subsequent recrystallization in methanol gave yellow needle-like crystals (283 mg, 5.6%). ^{1}H-NMR (400 MHz, $CDCl_3$, δ, ppm): 4.44 (d, 1H, CHOH), 5.83 (d, 1H, CHOH), 6.93-7.03 (m, 4H, CH_{ar}CF and CH_{ar}CH), 7.19-7.25 (m, 2H, CH_{ar}CF), 7.84-7.87 (m, 2H, CH_{ar}CCO). ^{19}F-NMR (400 MHz, $CDCl_3$, δ, ppm): -102.57 (s, 1F, C_{ar}F), -112.61 (s, 1F, C_{ar}F).

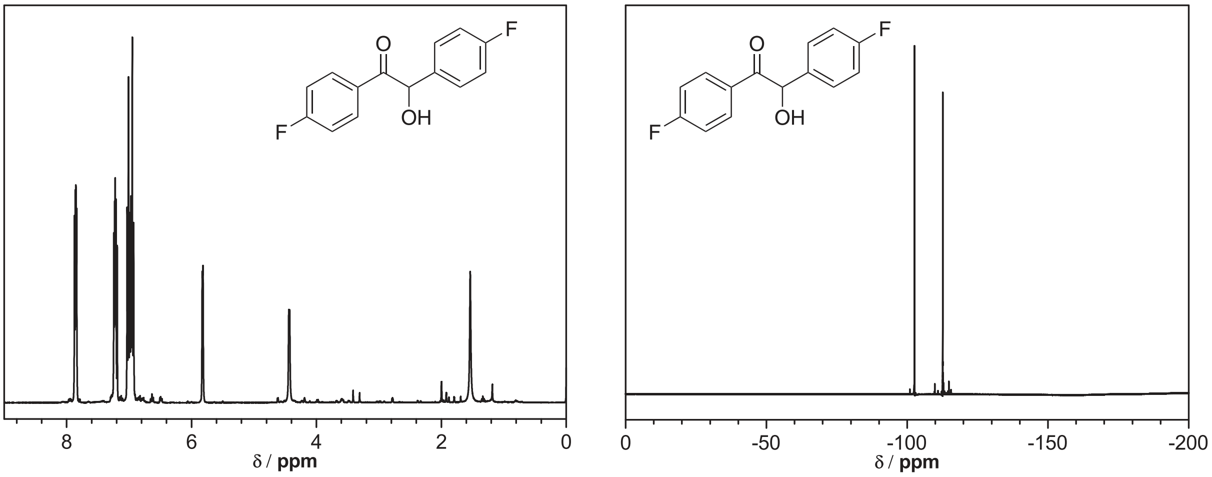

Figure 7.6.: ^{1}H-NMR (left) and ^{19}F-NMR spectrum (right) of F_2Bz.

7.2. PhotoRDRP

7.2.1. Materials and Instrumentation

Materials

Methyl methacrylate (MMA, Sigma-Aldrich, 99%) was freed from inhibitor by passing through a column of activated basic alumina (Merck). Ethyl isobutyrate (EBiB, abcr, 98%), tris[2-(dimethylamino)ethyl]amine (Me_6TREN, Sigma-Aldrich, 97%), copper(II) bromide ($CuBr_2$, Fluka Analytical, $\geq$ 99%), and dimethyl sulfoxide (DMSO, Fisher Scientific UK) were used as received. Copper(I) bromide (CuBr, Fluka) was purified by sequential washing with acetic acid, ethanol, and diethyl ether, followed by drying under reduced pressure and storage under nitrogen atmosphere. For the ESI-MS measurements sodium trifluoroacetate (Sigma-Aldrich, 99%), tetrahydrofuran (THF, multisolvent, 250 ppm BHT, Scharlau), and methanol (VWR, Chromanorm) were used as received.

PLP Experiments

All PLP samples (volume approx. 0.5 mL) contained MMA and a mixture of EBiB, Me_6TREN, $CuBr_2$, and DMSO, depending on the experiment. The samples were freed from oxygen prior to laser irradiation by purging the reaction mixture with nitrogen for 2 min. Each sample vial was subsequently placed into a sample holder, which was held at a constant temperature of 10°C using a thermostat (1196D, VWR, Darmstadt, Germany). The temperature was independently measured at the sample holder. The sample temperature was allowed to equilibrate for 5 min before starting the polymerization. Photoinitiation was achieved by an excimer laser system (Coherent Xantos XS-500, XeF, frequency variable from 1 to 500 Hz, operating at a wavelength of 351 nm (pulse width approx. 20 ns) and a laser energy of 5.0 mJ) at 250 Hz for an overall polymerization time of 90 000 laser pulses ($\approx$ 7 min). The laser beam was redirected to illuminate the vial from the bottom (the detailed laser set-up is described in literature[122]).

Quadrupole ESI-MS Measurements

Direct infusion ESI-MS measurements were performed in a THF/methanol (3:2 v/v) mixture with 300 μM sodium trifluoroacetate (NaTFA). A polymer concentration of 0.4 mg·mL^{-1} was utilized for the measurements. For further technical details see section 7.1.1.

Orbitrap ESI-MS Measurements

Mass spectra were recorded on a Q Excative (Orbitrap) mass spectrometer (ThermoFisher Scientific, San Jose, CA, USA) equipped with an atmospheric pressure ionization source operating in the nebulizer assisted electrospray mode. The instrument was calibrated in the m/z range 150-2000 using a standard containing caffeine, Met-Arg-Phe-Ala acetate (MRFA) and a mixture of fluorinated phosphazenes (Ultramark 1621) (all from Aldrich). A constant spray voltage of 3.5 kV and a dimensionless sheath gas of 6 and a sweep gas flow rate of 2 were applied. The capillary voltage and the S-lens RF level were set to 68.0 V and 320°C, respectively.

Size-Exclusion Chromatography (SEC)

See section 7.1.1.

UV-Vis Spectroscopy

UV-Vis spectra were measured on an Epoch 2 microplate spectrophotometer. All measurements were carried out in DMSO in a disposable plastic UV cuvette with a thickness of 10 mm at a temperature of 25°C.

General Procedure for Pulsed-Laser Polymerization (PLP) Experiments

$CuBr_2$ (0.00396 g, 17.72 μmol, 0.02 eq) was weighed in a vial and dissolved in DMSO (1.4 mL). Me_6TREN (14.2 μL, 0.53 μmol, 0.06 eq), EBiB (0.13 mL, 88.5 mmol, 1 eq) and deinhibited MMA (4.737 mL, 44.29 mmol, 50 eq) were added. The solution was aliquoted in 2-3 glass vials for PLP experiments ($V \approx 0.5$ mL) and deoxygenated by nitrogen bubbling for 2 min. The vials were allowed to reach 10°C for 5 min prior to irradiation. For those experiments not containing all ingredients the exact same procedure was executed. All experiments were performed in triplicate in order to exclude experimental errors.

7.3. SCNP Formation

7.3.1. Materials and Instrumentation

Methyl methacrylate (MMA, Sigma-Aldrich, 99%) was freed from inhibitor by passing through a column of activated basic alumina (Sigma-Aldrich). Irgacure 2959 was obtained from BASF. DMF, methacryloyl chloride, pyridine, acetone, Na_2SO_4, concentrated hydrochloric acid, 4,4'-azobis(4-cyanovaleric acid) ($\geq$ 98%), acetonitrile, tetrahydrofuran, methanol, dichloromethane, *n*-hexane, hydroquinone monomethyl ether (MEHQ), diethyl ether, 2'-azobis (2-methylpropionitrile) (AIBN), and dimethyl sulfoxide were purchased from Sigma-Aldrich as used as received. 4-Cyano-4-(((hexylthio)carbonothioyl)thio)pentanoic acid (RAFT agent) was synthesized by Benjamin Fairbanks (University of Colorado Boulder).

Size-Exclusion Chromatography

The molar mass of the polymer was determined by a Tosoh EcoSEC GPC system (HLC-8320) with DMSO as the mobile phase at a flow rate of 0.350 mL·min^{-1} at 50°C. Column sets: two TSKgel SuperHM-H, 3 μm, 6.0 mm i.d. x 15 cm columns. Molar masses were calculated based on a calibration with narrow polydispersity poly(methyl methacrylate) standards.

NMR Spectroscopy

^{1}H-NMR measurements were performed in $CDCl_3$ and d-DMSO to determine the purity and degree of functionalization of the synthesized molecules, using a Bruker Avance-III-400 NMR spectrometer. The number of transients is 16 and a relaxation time of 1 s was used for the integrated intensity determination of ^{1}H-NMR spectra.

DOSY Measurements

DOSY NMR experiments were performed on a Varian INOVA 500 NMR spectrometer operating at 499.60 MHz for ^{1}H-NMR observation. Calibrated 90°excitation pulses of 6.70 microseconds were used. Convection Compensated Double Pulsed Field Gradient Stimulated Echo experiments were performed using the DgcsteSL cc pulse sequenc in the VNMRJ 3.2A (Agilent Technologies) software, with Non-Uniform Gradient correction applied to remove errors from gradient nonlinearity across the length of the detection coil in the probe. The sample temperature was regulated at 23.0°C. (+/- 0.5°C). An exponential gradient array of 32 discreet calibrated gradient strengths for 1.99 to 52.0 Gauss/CM were used to measure signal attenuation vs. gradient strength, providing adequate data for sample components with high diffusion coefficients (i.e., solvents), and very small diffusion coefficients (large molecules) within the same sample.
Other key parameters used in setting up the DOSY experiment are as follows:
Diffusion Delay (Δ, parameter"del") = 110 msec (0.110 sec)
Gradient time (δ, parameter = "gt1") = 3.0 msec (0.003 sec)
Number of scans per gradient value = 32 (interleaved every 4 scans to distribute any systematic instrument errors evenly throughout all 32 individual spectra)
Relaxation delay = 2.0 with acquisition time of 3.0 s, giving a repetition time of 5.0 s per scan.

Irradiation Source

Photo reactions were carried out with an Acticure 4000 mercury lamp with a 320-390 nm bandpass filter. The light intensity was determined with a UV light detector.

UV-Vis Spectroscopy

UV-Vis spectra were recorded on UV-Vis spectrophotometer (Thermo-Fischer Scientific). All sample solutions were examined in quartz glass cuvettes with 1 cm light path lengths. Absorbance data was collected in absorbance mode with a bandwidth of 2 nm and a scan speed of 240 nm/min.

7.3.2. Synthesis

Synthesis of Photoinitiator-functionalized Methacrylate Monomer PImon

Irgacure 2959 (3.000 g, 13.4 mmol) was dissolved in 25 mL acetone and cooled down to 0°C. Pyridine (2.544 g,2.60 mL, 32.2 mmol) and, subsequently, methacryloyl chloride (1.404 g, 1.30 mL, 13.4 mmol) were added dropwise via syringe. The reaction solution was stirred in an ice-bath for 6 h, allowing the solution to slowly reach ambient temperature. The reaction mixture was poured on ice containing concentrated hydrochloric acid. The aqueous phase was extracted with diethyl ether (3 x 30 mL) and the combined organic phase was dried over Na_2SO_4. The solvent was evaporated under reduced pressure to give a yellow oil. The crude product was purified by column chromatography (siliga gel, *n*-hexane/ethyl acetate = 2/1 v/v, R_f = 0.42). The solvent was removed at ambient temperature under high vacuum and protected from light by aluminum foil. Complete removal of the solvent was not feasible, due to polymerization of the product. Thus, the product was isolated as a visous, colorless oil (2.16 g, 55% yield).
^{1}H-NMR (400 MHz, $CDCl_3$, δ, ppm): 1.61 (s, 6H, $C(CH_3)_2OH$), 1.97 (s, 3H, CCH_3), 4.28-4.30 (m, 2H, CH_2OCH_2), 4.50-4.52 (m, 2H, CH_2OCH_2), 5.59 (s, 1H, CC*H*), 6.13 (s, 1H, CC*H*), 6.96-6.97 (m, 2H, $COCH_{ar}$), 8.06 - 8.08 (m, 2H, $COCCH_{ar}$).

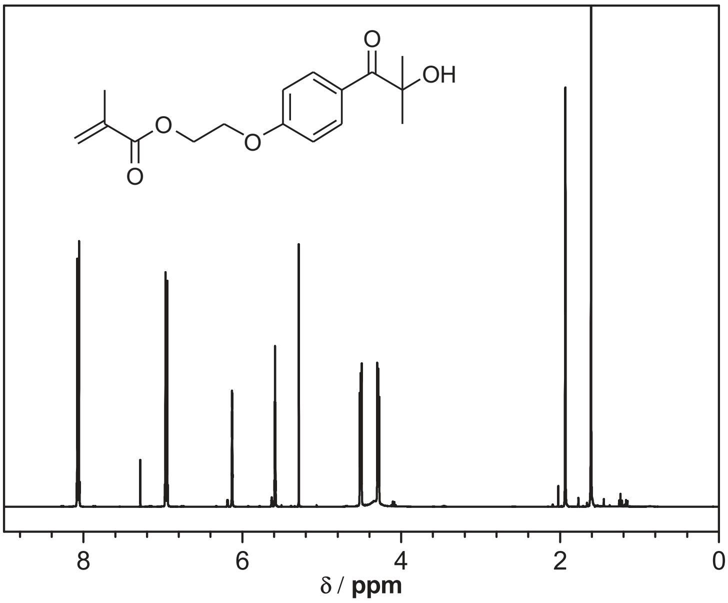

Figure 7.7.: ^{1}H-NMR of the photoinitiator-functionalized methacrylate monomer PImon.

Synthesis of the Photoinitiator-functionalized Linear Precursor Copolymers Exemplified for a PImon/MMA Ratio of 1/10

PImon (1.198 g, 4.1 mmol) was dissolved in MMA (4.104 g, 4.39 mL, 41.0 mmol). 4-Cyano-4-(((hexylthio)carbonothioyl)thio)pentanoic acid (0.092 g, 0.29 mmol) was dissolved in 4.39 mL DMF and 4,4'-azobis(4-cyanovaleric acid) (0.008 g, 28.7 μmol) was added. The solutions were combined and aliquoted into five glass vials that were sealed with a rubber septum. Each vial was bubbled with argon for 12 min in an ice bath. Subsequently, the vials were submerged in an oil bath at 75°C and polymerized for 45 min, 1 h 40 min, 3 h, 4 h 30 min, and 5 h 30 min, respectively. The conversion was determined by NMR spectroscopy and are listed in Table 7.1 as well as the corresponding molar masses and dispersities. The polymer was purified by two-fold precipitation in diethyl ether at ambient temperature and the molar mass was determined by DMSO-SEC. ^{1}H-NMR (400 MHz, $CDCl_3$, δ, ppm): 0.85-1.03 (2 bs, 30.6H, $\mathrm{C}(\mathrm{C}H_3)$ and $\mathrm{C}(\mathrm{C}H_2)$), 1.65 (s, 6.44H, $\mathrm{C}(\mathrm{C}H_3\mathrm{C}H_3)\mathrm{COH}$), 3.61 (s, 25H, OCH_3), 4.32 (d, 4.7H, $\mathrm{C}H_2\mathrm{OC}H_2$), 7.00 (m, 2H, $\mathrm{COC}H_{ar}$), 8.12 (m, 2H, $\mathrm{COCC}H_{ar}$).

Time	Conversion MMA (%)	Conversion PImon (%)	M_n ($g \cdot mol^{-1}$)	Đ
45 min	23	21	8750	1.17
1 h 40 min	43	36	10220	1.21
3 h	62	61	14000	1.26
4 h 30 min	68	67	16630	1.16
5 h 30 min	73	74	17190	1.15

Table 7.1.: Summary of the monomer conversions, molar masses, and dispersities for the copolymerization of PImon and MMA for the ratio PImon/MMA = 1/10. Conversions were determined by NMR spectroscopy, molar masses and dispersities were determined by DMSO-SEC.

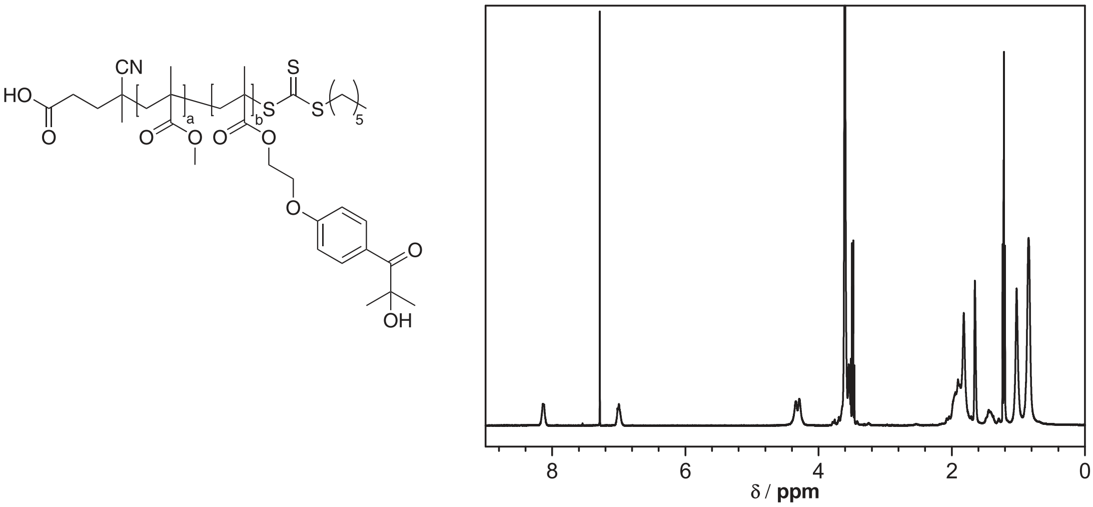

Figure 7.8.: ^{1}H-NMR of the PImon-MMA-copolymer for a PImon/MMA ratio of 1/10.

Synthesis of pMMA via RAFT for Test Reactions

4-Cyano-4-(((hexylthio)carbonothioyl)thio)pentanoic acid (0.0189 g, 59.5 μmol) was dissolved in 1.0 mL DMF and 4,4'-azobis(4-cyanovaleric acid) (0.0017 g, 5.95 μmol) was added. MMA

(0.936 g, 1.00 mL, 9.35 mmol) was added. The vial was sealed with a rubber septum and the solution was bubbled with argon in an ice bath for 15 min. Subsequently, the vial were submerged in an oil bath at 75°C and polymerized for 7.5 h. The molar mass was determined by DMSO-SEC, giving M_n = 15500 g·mol^{-1} and Đ = 1.13.

RAFT Group Removal of PImon-MMA-Copolymer

PImon-MMA-Copolymer (150 mg, 11.2 μmol) with PImon/MMA = 1/11 (Entry 8 in Table 5.1) was dissolved in 30 mL acetonitrile. 2,2'-Azobis(2-methylpropionitrile) (18.4 mg,0.11 mmol) were added and the solution was bubbled with argon for 15 min. Subsequently, the solution was refluxed at 70°C for 2 h. The solvent was evaporated and the polymer was precipitated in diethyl ether at ambient temperature. The molar mass was determined by DMSO-SEC, giving M_n = 15100 g·mol^{-1} and Đ = 1.18.

Irradiation Experiments

Various concentrations, solvent mixtures, irradiation energies, and irradiation times were employed for the light-induced SCNP formation. Therefore, the following irradiation experiment serves as an exemplary procedure. The PImon-MMA-copolymer precursor (4 mg) was dissolved in 49 mL of DCM and 1 mL of MEHQ stock solution (23.2 μg in DCM) was added. The polymer solution was added slowly into a 500 mL round-bottom flask containing 400 mL diethyl ether. The solution was bubbled with argon for 1 h at ambient temperature. Subsequently, the flask was placed in a UV reactor (schematically illustrated in Figure 7.9) with a distance of 2 cm between the lamp outlet and the outside of the flask and irradiated for 10 min with UV light in the range of 320-390 nm and 80 mW/cm^2. The solvent was removed under reduced pressure. Photoinitiator conversions were determined by NMR spectroscopy and the molar masses were measured by DMSO-SEC.

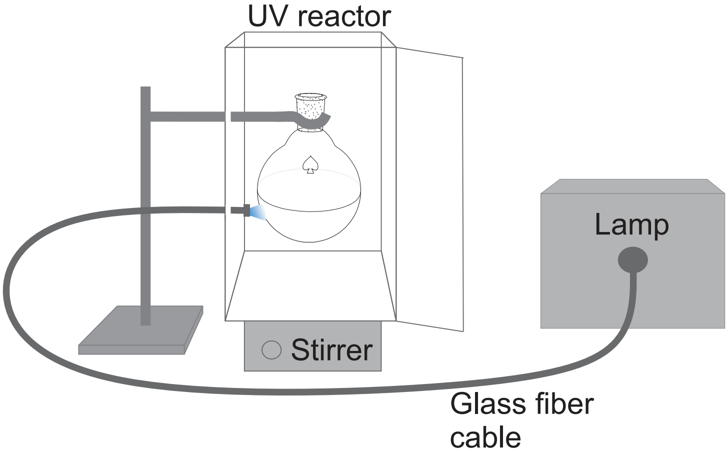

Figure 7.9.: Schematical illustration of the UV reactor employed for the irradiation experiments.

Bibliography

[1] C. Decker, *J. Coating. Technol.* **1987**, *59*, 97–106.

[2] S. Allakhverdiev, *Photosynthesis: A New Approach to the Molecular, Cellular, and Organismal Levels*, Wiley, **2015**.

[3] W. A. Green, *Industrial Photoinitiators : A Technical Guide*, CRC Press, Boca Raton, **2010**.

[4] Y. Yagci, S. Jockusch, N. J. Turro, *Macromolecules* **2010**, *43*, 6245–6260.

[5] K. S. Anseth, S. M. Newman, C. N. Bowman in *Biopolymers II, Vol. 122* (Eds.: N. Peppas, R. Langer), Springer, Berlin Heidelberg, **1995**, pp. 177–217.

[6] J. L. Aparicio, M. Elizalde, *Packag. Technol. Sci.* **2015**, *28*, 181–203.

[7] M. A. Lago, A. R.-B. de Quiros, R. Sendon, J. Bustos, M. T. Nieto, P. Paseiro, *Food Addit. Contam. A* **2015**, *32*, 779–798.

[8] K. Van Den Houwe, A. Van Heyst, C. Evrard, J. Van Loco, F. Bolle, F. Lynen, E. Van Hoeck, *Packag. Technol. Sci.* **2016**, *29*, 121–131.

[9] K. Dietliker, T. Jung, J. Benkhoff, H. Kura, A. Matsumoto, H. Oka, D. Hristova, G. Gescheidt, G. Rist, *Macromol. Sy.* **2004**, *217*, 77–98.

[10] J.-P. Fouassier, *Photoinitiators for Polymer Synthesis: Scope, Reactivity and Efficiency*, Wiley-VCH, Weinheim, **2012**.

[11] C. Dietlin, S. Schweizer, P. Xiao, J. Zhang, F. Morlet-Savary, B. Graff, J.-P. Fouassier, J. Lalevee, *Polym. Chem.* **2015**, *6*, 3895–3912.

[12] N. J. Treat, H. Sprafke, J. W. Kramer, P. G. Clark, B. E. Barton, J. R. de Alaniz, B. P. Fors, C. J. Hawker, *J. Am. Chem. Soc.* **2014**, *136*, 16096–16101.

[13] G. J. Kavarnos, N. J. Turro, *Chem. Rev.* **1986**, *86*, 401–449.

[14] J. Xu, S. Shanmugam, H. T. Duong, C. Boyer, *Polym. Chem.* **2015**, *6*, 5615–5624.

[15] Z. Guan, , B. Smart, *Macromolecules* **2000**, *33*, 6904–6906.

[16] A. Anastasaki, V. Nikolaou, Q. Zhang, J. Burns, S. R. Samanta, C. Waldron, A. J. Haddleton, R. McHale, D. Fox, V. Percec, P. Wilson, D. M. Haddleton, *J. Am. Chem. Soc.* **2014**, *136*, 1141–1149.

[17] T. G. Ribelli, D. Konkolewicz, S. Bernhard, K. Matyjaszewski, *J. Am. Chem. Soc.* **2014**, *136*, 13303–13312.

[18] S. Mavila, O. Eivgi, I. Berkovich, N. G. Lemcoff, *Chem. Rev.* **2016**, *116*, 878–961.

[19] G. Odian, *Principles of Polymerization*, Wiley-Interscience, Hoboken, NJ, 4th ed., **2004**.

[20] G. Ayrey, M. Humphrey, R. Poller, *Polymer* **1977**, *18*, 840–844.

[21] G. Bonta, B. M. Gallo, S. Russo, C. Uliana, *Polymer* **1976**, *17*, 217–220.

[22] D. R. Hensley, S. D. Goodrich, A. Y. Huckstep, H. J. Harwood, P. L. Rinaldi, *Macromolecules* **1995**, *28*, 1586–1591.

[23] M. Szwarc, *Nature* **1956**, *178*, 1168–1169.

[24] R. P. Quirk, B. Lee, *Polym. Int.* **1992**, *27*, 359–367.

[25] G. Litvinenko, A. H. E. Müller, *Macromolecules* **1997**, *30*, 1253–1266.

[26] M. K. Georges, R. P. N. Veregin, P. M. Kazmaier, G. K. Hamer, *Macromolecules* **1993**, *26*, 2987–2988.

[27] C. J. Hawker, *Accounts Chem. Res.* **1997**, *30*, 373–382.

[28] C. J. Hawker, A. W. Bosman, E. Harth, *Chem. Rev.* **2001**, *101*, 3661–3688.

[29] J. Nicolas, Y. Guillaneuf, C. Lefay, D. Bertin, D. Gigmes, B. Charleux, *Prog. Polym. Sci.* **2013**, *38*, 63–235.

[30] G. Moad, E. Rizzardo, S. H. Thang, *Polymer* **2008**, *49*, 1079–1131.

[31] J. Chiefari, Y. K. B. Chong, F. Ercole, J. Krstina, J. Jeffery, T. P. T. Le, R. T. A. Mayadunne, G. F. Meijs, C. L. Moad, G. Moad, E. Rizzardo, S. H. Thang, *Macromolecules* **1998**, *31*, 5559–5562.

[32] *Handbook of RAFT Polymerization*, (Ed.: C. Barner-Kowollik), Wiley-VCH, Weinheim, **2008**.

[33] K. Matyjaszewski, *Macromolecules* **2012**, *45*, 4015–4039.

[34] V. Percec, A. V. Popov, E. Ramirez-Castillo, M. Monteiro, B. Barboiu, O. Weichold, A. D. Asandei, C. M. Mitchell, *J. Am. Chem. Soc.* **2002**, *124*, 4940–4941.

[35] V. Percec, T. Guliashvili, J. S. Ladislaw, A. Wistrand, A. Stjerndahl, M. J. Sienkowska, M. J. Monteiro, S. Sahoo, *J. Am. Chem. Soc.* **2006**, *128*, 14156–14165.

[36] A. P. Haehnel, S. Fleischmann, P. Hesse, K.-D. Hungenberg, C. Barner-Kowollik, *Macromol. React. Eng.* **2013**, *7*, 8–23.

[37] A. Anastasaki, C. Waldron, P. Wilson, R. McHale, D. M. Haddleton, *Polym. Chem.* **2013**, *4*, 2672–2675.

[38] D. Konkolewicz, Y. Wang, M. Zhong, P. Krys, A. A. Isse, A. Gennaro, K. Matyjaszewski, *Macromolecules* **2013**, *46*, 8749–8772.

[39] D. Konkolewicz, Y. Wang, P. Krys, M. Zhong, A. A. Isse, A. Gennaro, K. Matyjaszewski, *Polym. Chem.* **2014**, *5*, 4396–4417.

[40] W. Tang, Y. Kwak, W. Braunecker, N. V. Tsarevsky, M. L. Coote, K. Matyjaszewski, *J. Am. Chem. Soc.* **2008**, *130*, 10702–10713.

[41] W. Jakubowski, K. Matyjaszewski, *Angew. Chem. Int. Edit.* **2006**, *45*, 4482–4486.

[42] K. Matyjaszewski, W. Jakubowski, K. Min, W. Tang, J. Huang, W. A. Braunecker, N. V. Tsarevsky, *P. Nat. Acad. Sci. USA* **2006**, *103*, 15309–15314.

[43] D. Konkolewicz, A. J. D. Magenau, S. E. Averick, A. Simakova, H. He, K. Matyjaszewski, *Macromolecules* **2012**, *45*, 4461–4468.

[44] T. Pintauer, K. Matyjaszewski, *Chem. Soc. Rev.* **2008**, *37*, 1087–1097.

[45] A. J. D. Magenau, N. C. Strandwitz, A. Gennaro, K. Matyjaszewski, *Science* **2011**, *332*, 81–84.

[46] A. J. D. Magenau, N. Bortolamei, E. Frick, S. Park, A. Gennaro, K. Matyjaszewski, *Macromolecules* **2013**, *46*, 4346–4353.

[47] M. A. Tasdelen, M. Uygun, Y. Yagci, *Macromol. Rapid Comm.* **2011**, *32*, 58–62.

[48] J. Mosnaček, M. Ilčikova, *Macromolecules* **2012**, *45*, 5859–5865.

[49] D. Konkolewicz, K. Schröder, J. Buback, S. Bernhard, K. Matyjaszewski, *ACS Macro Lett.* **2012**, *1*, 1219–1223.

[50] S. Dadashi-Silab, M. A. Tasdelen, Y. Yagci, *J. Polym. Sci. A* **2014**, *52*, 2878–2888.

[51] T. Zhang, D. Gieseler, R. Jordan, *Polym. Chem.* **2016**, *7*, 775–779.

[52] J. V. Crivello, E. Reichmanis, *Chem. Mater.* **2014**, *26*, 533–548.

[53] S. C. Ligon-Auer, M. Schwentenwein, C. Gorsche, J. Stampfl, R. Liska, *Polym. Chem.* **2016**, *7*, 257–286.

[54] H.-B. Sun, S. Kawata in *NMR, 3D Analysis, Photopolymerization*, *Vol. 170*, Springer, Berlin Heidelberg, **2004**, pp. 169–273.

[55] T. F. Scott, B. A. Kowalski, A. C. Sullivan, C. N. Bowman, R. R. McLeod, *Science* **2009**, *324*, 913–917.

[56] K. B. Kockler, A. P. Haehnel, T. Junkers, C. Barner-Kowollik, *Macromol. Rapid Commun.* **2016**, *37*, 123–134.

[57] V. N. Genkin, V. V. Sokolov, *Dokl. Akad. Nauk SSSR* **1977**, *234*, 94–96.

[58] A. P. Aleksandrov, V. N. Genkin, M. S. Kitai, I. M. S. V. V. Sokolov, *J. Quant. Electron.* **1977**, *4*, 976–981.

[59] O. F. Olaj, I. Bitai, F. Hinkelmann, *Makromolekul. Chem.* **1987**, *188*, 1689–1702.

[60] O. Olaj, I. Schnöll-Bitai, *Eur. Polym. J.* **1989**, *25*, 635–641.

[61] S. Beuermann, M. Buback, *Prog. Polym. Sci.* **2002**, *27*, 191–254.

[62] S. Beuermann, M. Buback, T. P. Davis, N. Garcia, R. G. Gilbert, R. A. Hutchinson, A. Kajiwara, M. Kamachi, I. Lacik, G. T. Russell, *Macromol. Chem. Physic.* **2003**, *204*, 1338–1350.

[63] J. M. Asua, S. Beuermann, M. Buback, P. Castignolles, B. Charleux, R. G. Gilbert, R. A. Hutchinson, J. R. Leiza, A. N. Nikitin, J.-P. Vairon, A. M. van Herk, *Macromol. Chem. Physic.* **2004**, *205*, 2151–2160.

[64] R. G. W. Norrish, F. W. Kirkbride, *J. Chem. Soc.* **1932**, 1518–1530.

[65] C. H. Bamford, R. G. W. Norrish, *J. Chem. Soc.* **1935**, 1504–1511.

[66] B. Ganster, U. K. Fischer, N. Moszner, R. Liska, *Macromol. Rapid Comm.* **2008**, *29*, 57–62.

[67] R. Kuhlmann, W. Schnabel, *Angew. Makromol. Chem.* **1978**, *70*, 145–157.

[68] S. Dadashi-Silab, C. Aydogan, Y. Yagci, *Polym. Chem.* **2015**, *6*, 6595–6615.

[69] P. Xiao, J. Zhang, F. Dumur, M. A. Tehfe, F. Morlet-Savary, B. Graff, D. Gigmes, J. P. Fouassier, J. Lalevee, *Prog. Polym. Sci.* **2015**, *41*, 32–66.

[70] M. A. Tehfe, F. Louradour, J. Lalevee, J.-P. Fouassier, *Appl. Sci.* **2013**, *3*, 490.

[71] D. S. Esen, N. Arsu, J. P. Da Silva, S. Jockusch, N. J. Turro, *J. Polym. Sci. A* **2013**, *51*, 1865–1871.

[72] P. K. Sengupta, S. K. Modak, *J. Macromol. Sci. A* **1983**, *20*, 789–805.

[73] P. K. Sengupta, S. K. Modak, *Makromolekul. Chem.* **1985**, *186*, 1593–1604.

[74] S. Jockusch, M. S. Landis, B. Freiermuth, N. J. Turro, *Macromolecules* **2001**, *34*, 1619–1626.

[75] M. Buback, A. Kuelpmann, *Macromol. Chem.* **2003**, *204*, 632–637.

[76] T. Sumiyoshi, W. Schnabel, *Makromolekul. Chem.* **1985**, *186*, 1811–1823.

[77] T. Sumiyoshi, W. Schnabel, A. Henne, *J. Photochem.* **1986**, *32*, 119–129.

[78] L. Gonsalvi, M. Peruzzini, *Angew. Chem. Int. Edit.* **2012**, *51*, 7895–7897.

[79] B. Ganster, U. K. Fischer, N. Moszner, R. Liska, *Macromolecules* **2008**, *41*, 2394–2400.

[80] N. Moszner, U. K. Fischer, B. Ganster, R. Liska, V. Rheinberger, *Dent. Mater.* **2008**, *24*, 901–907.

[81] Y. Y. Durmaz, N. Moszner, Y. Yagci, *Macromolecules* **2008**, *41*, 6714–6718.

[82] A. Borer, R. Kirchmayr, G. Rist, *Helv. Chim. Acta* **1978**, *61*, 305–324.

[83] J. P. Fouassier, D. J. Lougnot, *J. Chem. Soc. Faraday Trans. 1* **1987**, *83*, 2935–2952.

[84] L. Cokbaglan, N. Arsu, Y. Yagci, S. Jockusch, N. J. Turro, *Macromolecules* **2003**, *36*, 2649–2653.

[85] M. Aydin, N. Arsu, Y. Yagci, S. Jockusch, N. J. Turro, *Macromolecules* **2005**, *38*, 4133–4138.

[86] D. K. Balta, N. Arsu, Y. Yagci, S. Jockusch, N. J. Turro, *Macromolecules* **2007**, *40*, 4138–4141.

[87] J. Jakubiak, X. Allonas, J. Fouassier, A. Sionkowska, E. Andrzejewska, L. Linden, J. Rabek, *Polymer* **2003**, *44*, 5219–5226.

[88] Y.-C. Chen, J. L. Ferracane, S. A. Prahl, *Dent. Mater.* **2007**, *23*, 655–664.

[89] A. Lauer, D. E. Fast, A.-M. Kelterer, E. Frick, D. Neshchadin, D. Voll, G. Gescheidt, C. Barner-Kowollik, *Macromolecules* **2015**, *48*, 8451–8460.

[90] M. Planck, *Verhandl. Dtsch. phys. Ges.* **1900**, *2*, 237–245.

[91] A. Einstein, *Ann. Phys.* **1905**, *17*, 132–148.

[92] A. Jablonski, *Nature* **1933**, *131*, 839–840.

[93] M. Kasha, *Discuss. Faraday Soc.* **1950**, *9*, 14–19.

[94] J. Franck, E. G. Dymond, *Trans. Faraday Soc.* **1926**, *21*, 536–542.

[95] E. Condon, *Phys. Rev.* **1926**, *28*, 1182–1201.

[96] P. Atkins, J. de Paula, M. Bär, A. Schleitzer, C. Heinisch, *Physikalische Chemie*, Wiley-VCH, Weinheim, **2006**.

[97] V. Balzani, P. Ceroni, A. Juris, *Photochemistry and Photophysics: Concepts, Research, Applications*, Wiley-VCH, Weinheim, **2014**.

[98] G. Wedler, H.-J. Freund, *Lehrbuch der physikalischen Chemie*, Wiley-VCH, Weinheim, 6th ed., **2012**.

[99] *Einführung in die Photochemie*, (Ed.: H. G. O. Becker), Dt. Verl. d. Wiss., Berlin, 3rd ed., **1991**.

[100] M. A. El-Sayed, *J. Chem. Phys.* **1963**, *38*, 2834–2838.

[101] Z. Pawelka, E. S. Kryachko, T. Zeegers-Huyskens, *Chem. Phys.* **2003**, *287*, 143–153.

[102] *Femtosecond Laser Pulses: Principles and Experiments*, (Ed.: C. Rulliere), Springer, New York, 2nd ed., **2005**.

[103] P. Weinberger, *Phil. Mag. Lett.* **2008**, *88*, 897–907.

[104] J. H. Gross, *Mass Spectrometry: A Textbook*, Springer, Berlin, **2004**.

[105] *Mass Spectrometry in Polymer Chemistry*, (Ed.: C. Barner-Kowollik), Wiley-VCH, Weinheim, **2012**.

[106] *Mass Spectrometry of Polymers*, (Ed.: G. Montaudo), CRC Press, Boca Raton, Fla., **2002**.

[107] M. Yamashita, J. B. Fenn, *J. Phys. Chem.* **1984**, *88*, 4451–4459.

[108] K. Tanaka, H. Waki, Y. Ido, S. Akita, Y. Yoshida, T. Yoshida, T. Matsuo, *Rapid Commun. Mass Sp.* **1988**, *2*, 151–153.

[109] M. Karas, F. Hillenkamp, *Anal. Chem.* **1988**, *60*, 2299–2301.

[110] J. N. Smith, R. C. Flagan, J. L. Beauchamp, *J. Phys. Chem. A* **2002**, *106*, 9957–9967.

[111] M. W. F. Nielen, *Rapid Commun. Mass Sp.* **1996**, *10*, 1652–1660.

[112] L. Prokai, *Int. J. Polym. Anal. Ch.* **2001**, *6*, 379–391.

[113] M. M. Wolff, W. E. Stephens, *Rev. Sci. Instrum.* **1953**, *24*, 616–617.

[114] A. Makarov, *Anal. Chem.* **2000**, *72*, 1156–1162.

[115] Q. Hu, R. J. Noll, H. Li, A. Makarov, M. Hardman, R. Graham Cooks, *J. Mass Spectrom.* **2005**, *40*, 430–443.

[116] T. Gruendling, S. Weidner, J. Falkenhagen, C. Barner-Kowollik, *Polym. Chem.* **2010**, *1*, 599–617.

[117] T. Gruendling, K. K. Oehlenschlaeger, E. Frick, M. Glassner, C. Schmid, C. Barner-Kowollik, *Macromol. Rapid Comm.* **2011**, *32*, 807–812.

[118] J. O. Mueller, F. G. Schmidt, J. P. Blinco, C. Barner-Kowollik, *Angew. Chem. Int. Edit.* **2015**, *54*, 10284–10288.

[119] J. O. Mueller, N. K. Guimard, K. K. Oehlenschlaeger, F. G. Schmidt, C. Barner-Kowollik, *Polym. Chem.* **2014**, *5*, 1447–1456.

[120] T. Gruendling, M. Guilhaus, C. Barner-Kowollik, *Anal. Chem.* **2008**, *80*, 6915–6927.

[121] T. Gruendling, M. Guilhaus, C. Barner-Kowollik, *Macromolecules* **2009**, *42*, 6366–6374.

[122] F. Günzler, E. H. H. Wong, S. P. S. Koo, T. Junkers, C. Barner-Kowollik, *Macromolecules* **2009**, *42*, 1488–1493.

[123] D. Voll, T. Junkers, C. Barner-Kowollik, *Macromolecules* **2011**, *44*, 2542–2551.

[124] D. Voll, A. Hufendiek, T. Junkers, C. Barner-Kowollik, *Macromol. Rapid Comm.* **2012**, *33*, 47–53.

[125] D. Voll, T. Junkers, C. Barner-Kowollik, *J. Polym. Sci. A* **2012**, *50*, 2739–2757.

[126] D. Voll, D. Neshchadin, K. Hiltebrandt, G. Gescheidt, C. Barner-Kowollik, *Macromolecules* **2012**, *45*, 5850–5858.

[127] E. Frick, H. A. Ernst, D. Voll, T. J. A. Wolf, A.-N. Unterreiner, C. Barner-Kowollik, *Polym. Chem.* **2014**, *5*, 5053–5068.

[128] E. Frick, A. Anastasaki, D. M. Haddleton, C. Barner-Kowollik, *J. Am. Chem. Sci.* **2015**, *137*, 6889–6896.

[129] E. Frick, C. Schweigert, B. B. Noble, H. A. Ernst, A. Lauer, Y. Liang, D. Voll, M. L. Coote, A.-N. Unterreiner, C. Barner-Kowollik, *Macromolecules* **2016**, *49*, 80–89.

[130] T. Wolf, PhD thesis, Karlsruhe Institute of Technology (KIT), Karlsruhe, **2013**.

[131] H. A. Ernst, PhD thesis, Karlsruhe Institute of Technology (KIT), Karlsruhe, **2015**.

[132] T. J. A. Wolf, D. Voll, C. Barner-Kowollik, A.-N. Unterreiner, *Macromolecules* **2012**, *45*, 2257–2266.

[133] O. Altintas, E. Lejeune, P. Gerstel, C. Barner-Kowollik, *Polym. Chem.* **2012**, *3*, 640–651.

[134] O. Shishkan, M. Zamfir, M. A. Gauthier, H. G. Borner, J.-F. Lutz, *Chem. Commun.* **2014**, *50*, 1570–1572.

[135] J. Willenbacher, O. Altintas, P. W. Roesky, C. Barner-Kowollik, *Macromol. Rapid Comm.* **2014**, *35*, 45–51.

[136] J. Willenbacher, O. Altintas, V. Trouillet, N. Knofel, M. J. Monteiro, P. W. Roesky, C. Barner-Kowollik, *Polym. Chem.* **2015**, *6*, 4358–4365.

[137] J. Willenbacher, B. V. K. J. Schmidt, D. Schulze-Suenninghausen, O. Altintas, B. Luy, G. Delaittre, C. Barner-Kowollik, *Chem. Commun.* **2014**, *50*, 7056–7059.

[138] K. F. Morris, C. S. J. Jr., *J. Am. Chem. Soc.* **1992**, *114*, 3139–3141.

[139] S. Peresada, A. Tonielli, R. Morici, C. Johnson, *Prog. Nucl. Magn. Res. Sp.* **1999**, *34*, 203–256.

[140] E. O. Stejskal, J. E. Tanner, *J. Chem. Phys.* **1965**, *42*, 288–292.

[141] M.-A. Tehfe, F. Dumur, B. Graff, J.-L. Clement, D. Gigmes, F. Morlet-Savary, J.-P. Fouassier, J. Lalevee, *Macromolecules* **2013**, *46*, 736–746.

[142] P. Xiao, W. Hong, Y. Li, F. Dumur, B. Graff, J. P. Fouassier, D. Gigmes, J. Lalevee, *Polymer* **2014**, *55*, 746–751.

[143] J. Zhang, M. Frigoli, F. Dumur, P. Xiao, L. Ronchi, B. Graff, F. Morlet-Savary, J. P. Fouassier, D. Gigmes, J. Lalevee, *Macromolecules* **2014**, *47*, 2811–2819.

[144] S. Hu, R. Popielarz, D. C. Neckers, *Macromolecules* **1998**, *31*, 4107–4113.

[145] *A Compilation of Photoinitiators: Commercially Available for UV Today*, (Ed.: K. A. Dietliker), SITA Technology Ltd.: London, **2002**.

[146] J. Yang, F. Xu, S. Shi, J. Nie, *Photochem. Photobiol. Sci.* **2012**, *11*, 1377–1382.

[147] J. Hutchison, A. Ledwith, *Polymer* **1973**, *14*, 405–408.

[148] *CRC Handbook of Chemistry and Physics*, (Ed.: D. R. Lide), CRC Press, Boca Raton, 86th ed., **2005**.

[149] W. G. Barb, *J. Polym. Sci.* **1953**, *11*, 117–126.

[150] C. Simion, A. M. Simion, *U.P.B. Sci. Bull. Series B* **2007**, *69*, 49–56.

[151] M. Karino, D. Kubouchi, K. Hamaoka, S. Umeyama, H. Yamataka, *J. Org. Chem.* **2013**, *78*, 7194–7198.

[152] R. L. Patel, *J. Chem. Soc. C* **1966**, 801–802.

[153] R. Herold, J.-P. Fouassier, *Angew. Makromol. Chem.* **1981**, *97*, 137–152.

[154] Q. Yang, F. Dumur, F. Morlet-Savary, J. Poly, J. Lalevee, *Macromolecules* **2015**, *48*, 1972–1980.

[155] H. Fischer, *Macromolecules* **1997**, *30*, 5666–5672.

[156] H. Fischer, *Chem. Rev.* **2001**, *101*, 3581–3610.

[157] M. Julliard, M. Chanon, *Chem. Rev.* **1983**, *83*, 425–506.

[158] J. Dileep Kumar, S. Das, *Res. Chem. Intermed.* **1997**, *23*, 755–800.

[159] S. Das, V. Suresh, *Electron-transfer Reactions of Amines*, Wiley-VCH, Weinheim, **2008**, pp. 379–456.

[160] Y. L. Chow, W. C. Danen, S. F. Nelsen, D. H. Rosenblatt, *Chem. Rev.* **1978**, *78*, 243–274.

[161] W. Horspool, F. Lenci, *CRC Handbook of Organic Photochemistry and Photobiology, Volumes 1 & 2, Second Edition*, Taylor & Francis, **2003**.

[162] O. Altintas, J. Willenbacher, K. N. R. Wuest, K. K. Oehlenschlaeger, P. Krolla-Sidenstein, H. Gliemann, C. Barner-Kowollik, *Macromolecules* **2013**, *46*, 8092–8101.

[163] J. Willenbacher, K. N. R. Wuest, J. O. Mueller, M. Kaupp, H.-A. Wagenknecht, C. Barner-Kowollik, *ACS Macro Letters* **2014**, *3*, 574–579.

[164] S. Perrier, P. Takolpuckdee, C. A. Mars, *Macromolecules* **2005**, *38*, 2033–2036.

[165] A. Rudin, H. L. W. Hoegy, *J. Polym. Sci. A* **1972**, *10*, 217–235.

[166] U. Megerle, I. Pugliesi, C. Schriever, C. F. Sailer, E. Riedle, *Appl. Phys. B* **2009**, *96*, 215–231.

[167] K. Tamura, C. R. Doerr, L. E. Nelson, H. A. Haus, E. P. Ippen, *Opt. Lett.* **1994**, *19*, 46–48.

[168] R. Ahlrichs, M. Bär, M. Häser, H. Horn, C. Kölmel, *Chem. Phys. Lett.* **1989**, *162*, 165–169.

[169] A. D. Becke, *Phys. Rev. A* **1988**, *38*, 3098–3100.

[170] P. A. M. Dirac, *P. Roy. Soc. Lond. A Mat.* **1929**, *123*, 714–733.

[171] K. Eichkorn, O. Treutler, H. Öhm, M. Häser, R. Ahlrichs, *Chem. Phys. Lett.* **1995**, *240*, 283–290.

[172] K. Eichkorn, O. Treutler, H. Öhm, M. Häser, R. Ahlrichs, *Chem. Phys. Lett.* **1995**, *242*, 652–660.

[173] K. Eichkorn, F. Weigend, O. Treutler, R. Ahlrichs, *Theor. Chem. Acc.* **1997**, *97*, 119–124.

[174] A. Schäfer, H. Horn, R. Ahlrichs, *J. Chem. Phys.* **1992**, *97*, 2571–2577.

[175] J. C. Slater, *Phys. Rev.* **1951**, *81*, 385–390.

[176] O. Treutler, R. Ahlrichs, *J. Chem. Phys.* **1995**, *102*, 346–354.

[177] S. H. Vosko, L. Wilk, M. Nusair, *Can. J. Phys.* **1980**, *58*, 1200–1211.

[178] F. Weigend, *Phys. Chem. Chem. Phys.* **2006**, *8*, 1057–1065.

[179] R. Bauernschmitt, R. Ahlrichs, *J. Chem. Phys.* **1996**, *104*, 9047–9052.

[180] R. Bauernschmitt, R. Ahlrichs, *Chem. Phys. Lett.* **1996**, *256*, 454–464.

[181] S. Grimme, F. Furche, R. Ahlrichs, *Chem. Phys. Lett.* **2002**, *361*, 321–328.

[182] A. D. Becke, *J. Chem. Phys.* **1993**, *98*, 5648–5652.

[183] C. Lee, W. Yang, R. G. Parr, *Phys. Rev. B* **1988**, *37*, 785–789.

[184] R. A. Kendall, T. H. Dunning, R. J. Harrison, *J. Chem. Phys.* **1992**, *96*, 6796–6806.

[185] D. J. Henry, M. B. Sullivan, L. Radom, *J. Chem. Phys.* **2003**, *118*, 4849–4860.

[186] Y. Zhao, D. G. Truhlar, *Theor. Chem. Acc.* **2007**, *120*, 215–241.

[187] A. V. Marenich, C. J. Cramer, D. G. Truhlar, *J. Phys. Chem. B* **2009**, *113*, 6378–6396.

[188] E. I. Izgorodina, M. L. Coote, *Chem. Phys.* **2006**, *324*, 96–110.

[189] B. B. Noble, M. L. Coote, *Int. Rev. Phys. Chem.* **2013**, *32*, 467–513.

[190] C. Y. Lin, E. I. Izgorodina, M. L. Coote, *Macromolecules* **2010**, *43*, 553–560.

[191] S. H. Kyne, C. Y. Lin, I. Ryu, M. L. Coote, C. H. Schiesser, *Chem. Commun.* **2010**, *46*, 6521–6523.

[192] M. J. Frisch, G. W. Trucks, H. B. Schlegel, G. E. Scuseria, M. A. Robb, J. R. Cheeseman, G. Scalmani, V. Barone, B. Mennucci, G. A. Petersson, H. Nakatsuji, M. Caricato, X. Li, H. P. Hratchian, A. F. Izmaylov, J. Bloino, G. Zheng, J. L. Sonnenberg, M. Hada, M. Ehara, K. Toyota, R. Fukuda, J. Hasegawa, M. Ishida, T. Nakajima, Y. Honda, O. Kitao, H. Nakai, T. Vreven, J. A. Montgomery, Jr., J. E. Peralta, F. Ogliaro, M. Bearpark, J. J. Heyd, E. Brothers, K. N. Kudin, V. N. Staroverov, R. Kobayashi, J. Normand, K. Raghavachari, A. Rendell, J. C. Burant, S. S. Iyengar, J. Tomasi, M. Cossi, N. Rega, J. M. Millam, M. Klene, J. E. Knox, J. B. Cross, V. Bakken, C. Adamo, J. Jaramillo, R. Gomperts, R. E. Stratmann, O. Yazyev, A. J. Austin, R. Cammi, C. Pomelli, J. W. Ochterski, R. L. Martin, K. Morokuma, V. G. Zakrzewski, G. A. Voth, P. Salvador, J. J. Dannenberg, S. Dapprich, A. D. Daniels, . Farkas, J. B. Foresman, J. V. Ortiz, J. Cioslowski, D. J. Fox, *Gaussian 09 Revision E.01*, Gaussian Inc. Wallingford CT 2009.

[193] H.-J. Werner, P. J. Knowles, G. Knizia, F. R. Manby, M. Schütz, *WIREs Comput. Mol. Sci.* **2012**, *2*, 242–253.

A

Appendix

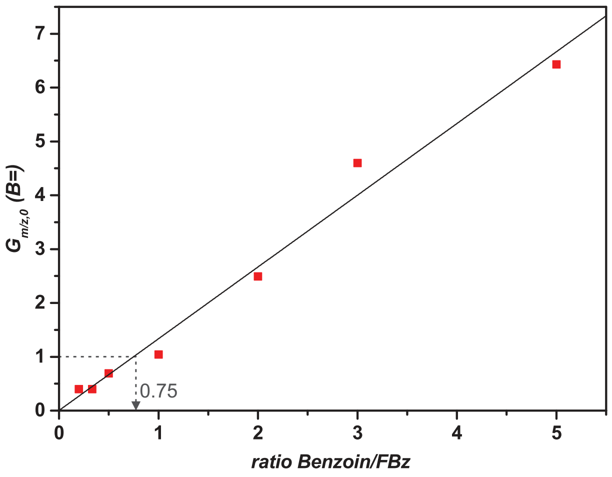

Figure A.1.: Mass bias-free ratio $G_{m/z,0}$ plotted versus the molar ratio of the photoinitiators FBz and benzoin, resulting in an initiation efficiency ratio of FB : B being 0.75 : 1.

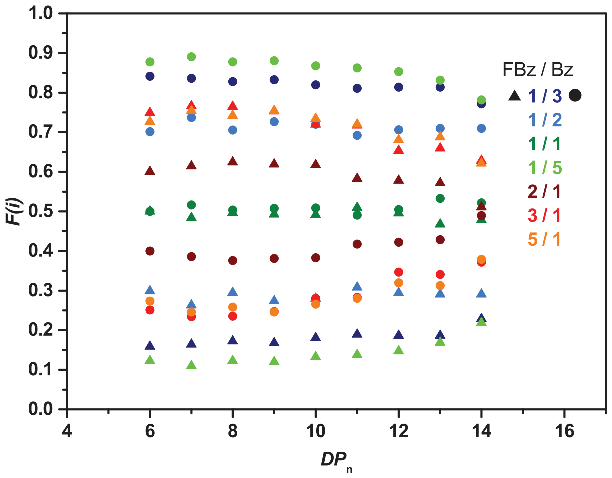

Figure A.2.: Plot of the mole fractions of the disproportionation peaks FB= (triangles) and B= (circles) versus the degree of polymerization for different ratios of FBz and benzoin.

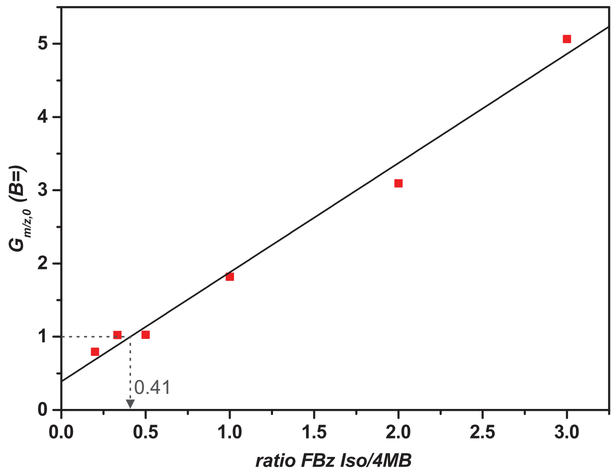

Figure A.3.: Mass bias-free ratio $G_{m/z,0}$ plotted versus the molar ratio of the photoinitiators FBz Iso and 4MB, resulting in an initiation efficiency ratio of B : MB being 2.44 : 1.

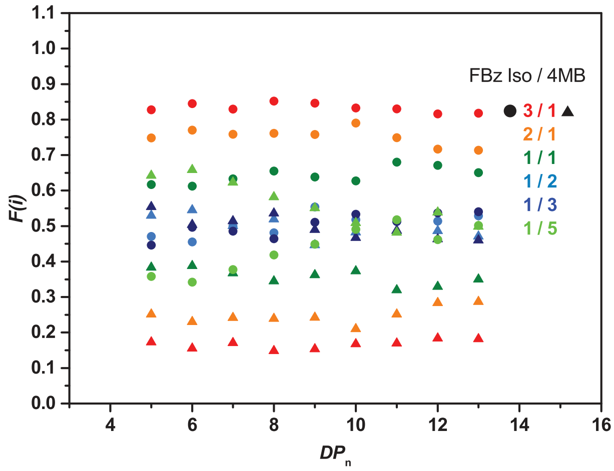

Figure A.4.: Plot of the mole fractions of the disproportionation peaks B= (circles) and MB= (triangles) versus the degree of polymerization for different molar ratios of FBz Iso and 4MB.

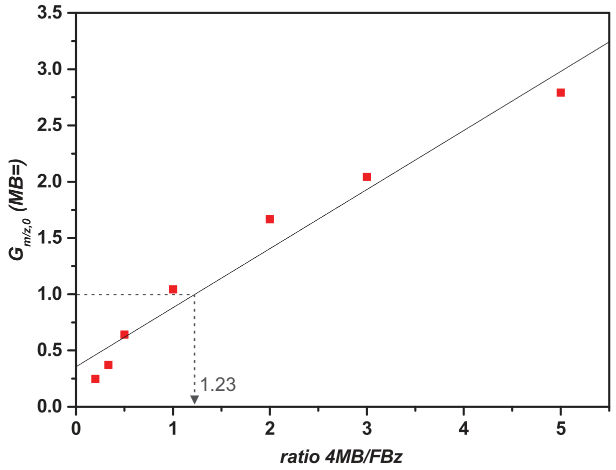

Figure A.5.: Mass bias-free ratio $G_{m/z,0}$ plotted versus the molar ratio of the photoinitiators FBz and 4MB, resulting in an initiation efficiency ratio of MB : FB being 1 : 1.23.

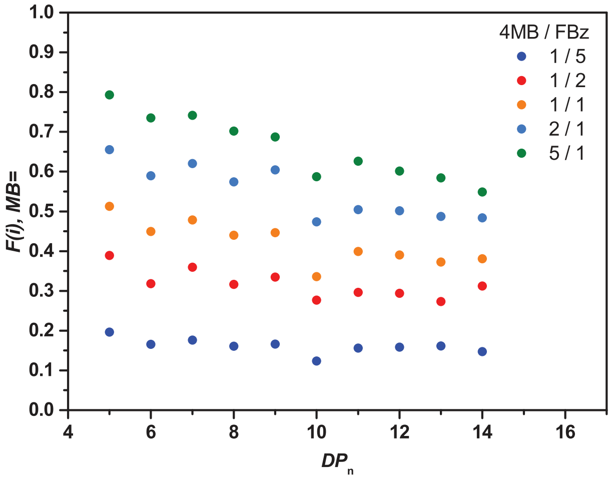

Figure A.6.: Plot of the mole fractions of the disproportionation peaks MB= (circles) versus the degree of polymerization for different molar ratios of FBz and 4MB.

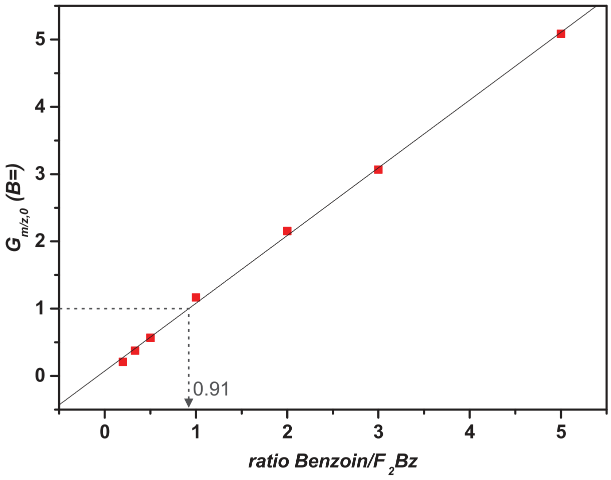

Figure A.7.: Mass bias-free ratio $G_{m/z,0}$ plotted versus the molar ratio of the photoinitiators F_2Bz and benzoin, resulting in an initiation efficiency ratio of FB : B being 1.1 : 1.

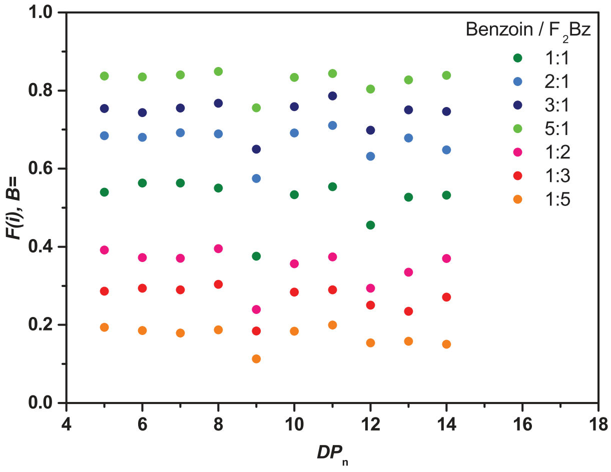

Figure A.8.: Plot of the mole fractions of the disproportionation peaks of B= versus the degree of polymerization for different molar ratios of benzoin and F_2Bz.

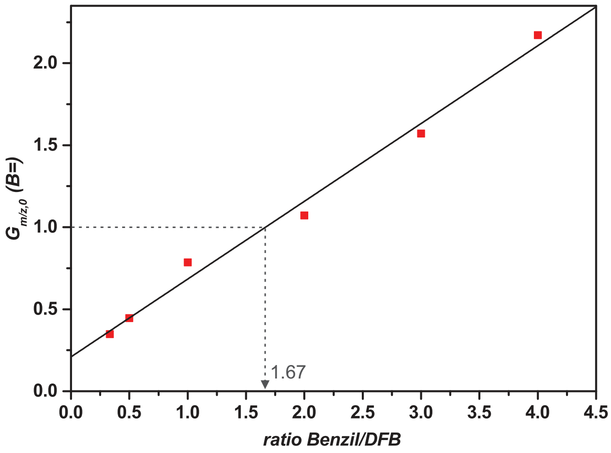

Figure A.9.: Mass bias-free ratio $G_{m/z,0}$ plotted versus the molar ratio of the photoinitiators DFB and benzil, resulting in an initiation efficiency ratio of FB : B being 1.67 : 1.

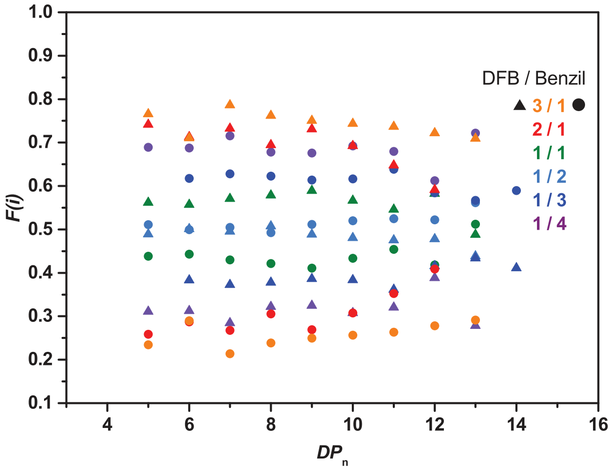

Figure A.10.: Plot of the mole fractions of the disproportionation peaks FB= (triangles) and B= (circles) versus the degree of polymerization for different molar ratios of DFB and benzil.

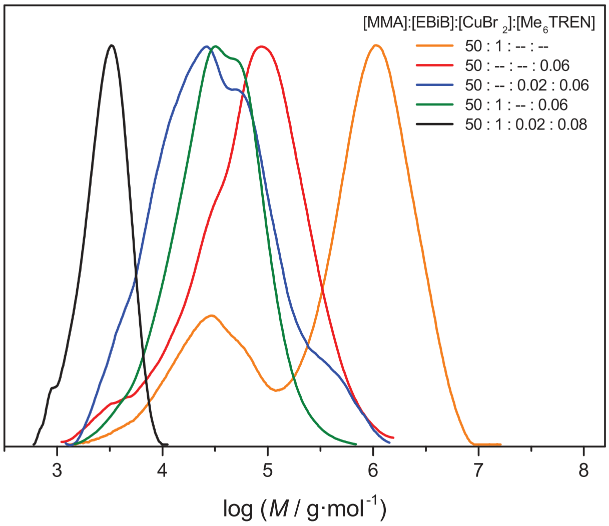

Figure A.11.: Molar mass distribution for various reaction compositions of the photoRDRP components.

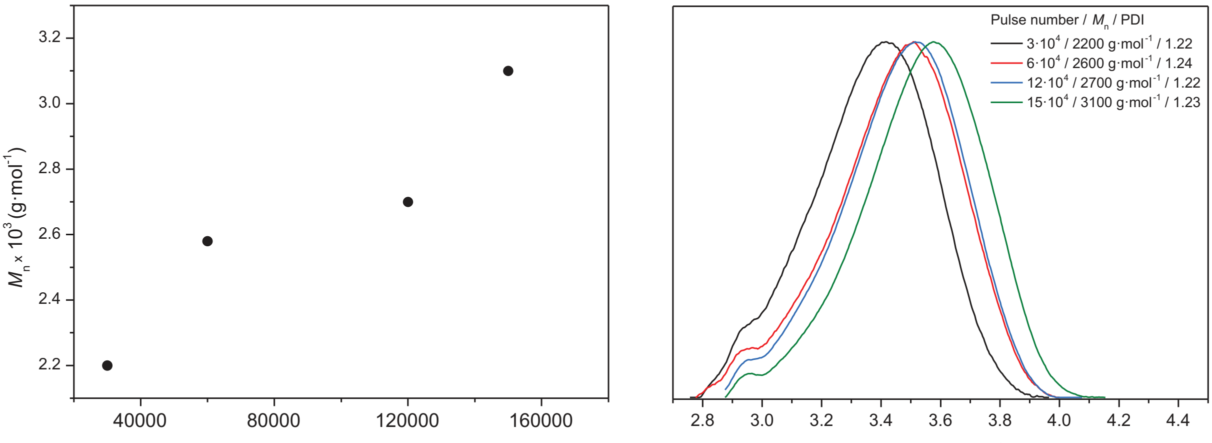

Figure A.12.: Molar mass (left) and molar mass distribution (right) of a photoRDRP reaction ([MMA]:[EBiB]:[$CuBr_2$]:[Me_6TREN] = 50:1:0.02:0.08 and 30 vol% DMSO) for different pulse numbers.

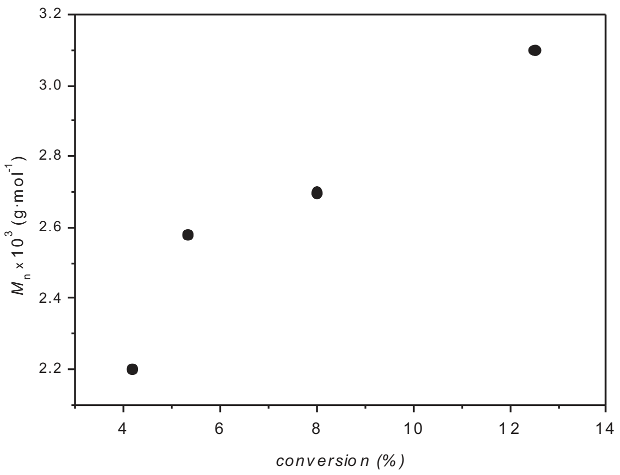

Figure A.13.: Molar mass of a photoRDRPreaction ([MMA]:[EBiB]:[$CuBr_2$]:[Me_6TREN] = 50:1:0.02:0.08 and 30 vol% DMSO) at different monomer conversions, corresponding to the pulse numbers in Figure A.12.

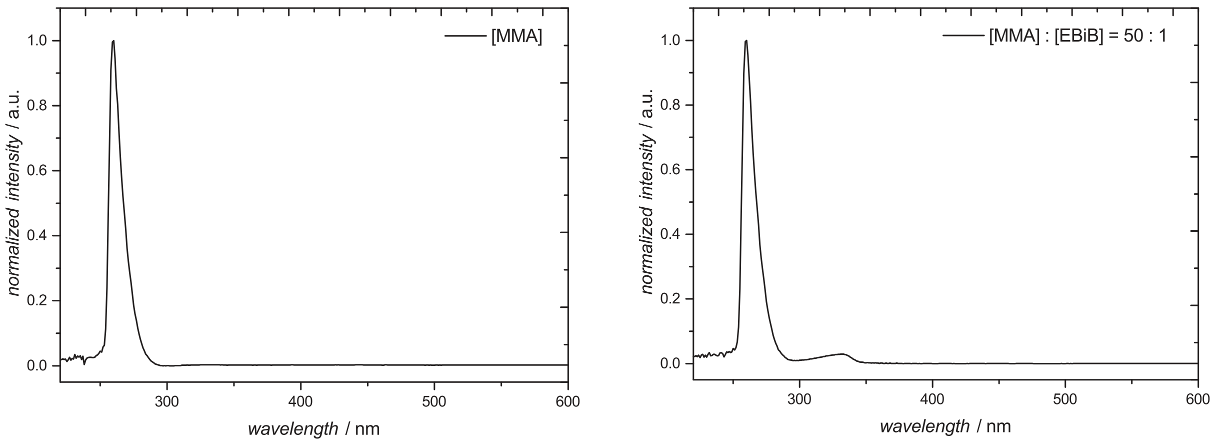

Figure A.14.: Right: UV-vis spectrum of Entry 1 (Table 4.1): [MMA]:[EBiB]:[$CuBr_2$]:[Me_6TREN] = 50:0:0:0 in DMSO. Left: UV-vis spectrum of Entry 2: [MMA]:[EBiB]:[$CuBr_2$]: [Me_6TREN] = 50:1:0:0 in DMSO.

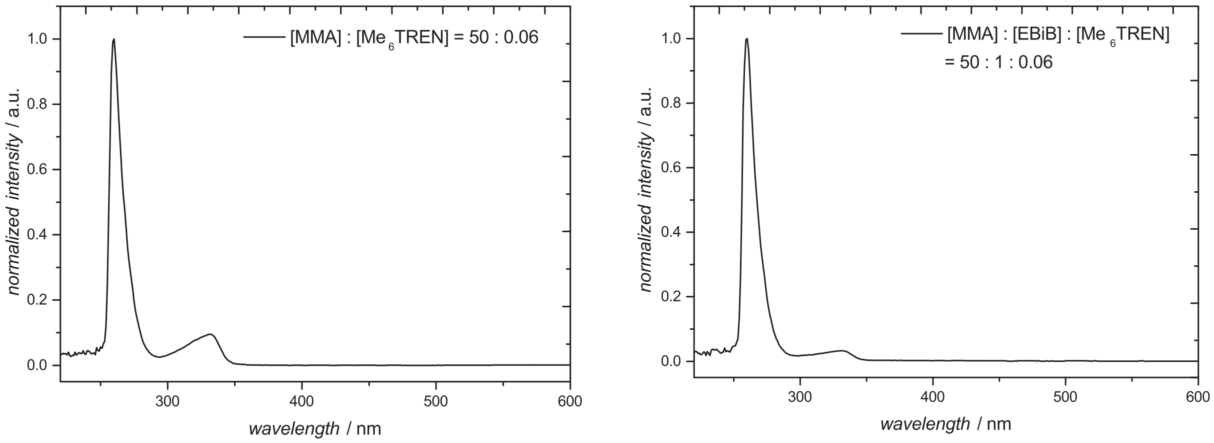

Figure A.15.: Right: UV-vis spectrum of Entry 3 (Table 4.1): [MMA]:[EBiB]:[$CuBr_2$]:[Me_6TREN] = 50:0:0:0.06 in DMSO. Left: UV-vis spectrum of Entry 6: [MMA]:[EBiB]:[$CuBr_2$]:[Me_6TREN] = 50:1:0:0.06 in DMSO.

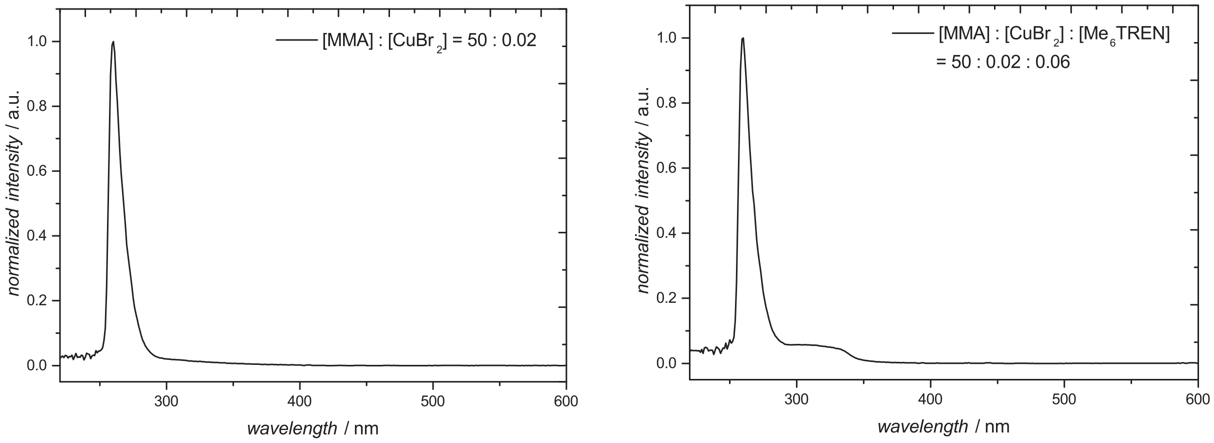

Figure A.16.: Right: UV-vis spectrum of Entry 4 (Table 4.1): [MMA]:[EBiB]:[$CuBr_2$]:[Me_6TREN] = 50:0:0.02:0 in DMSO. Left: UV-vis spectrum of Entry 5: [MMA]:[EBiB]:[$CuBr_2$]:[Me_6TREN] = 50:0:0.02:0.06 in DMSO.

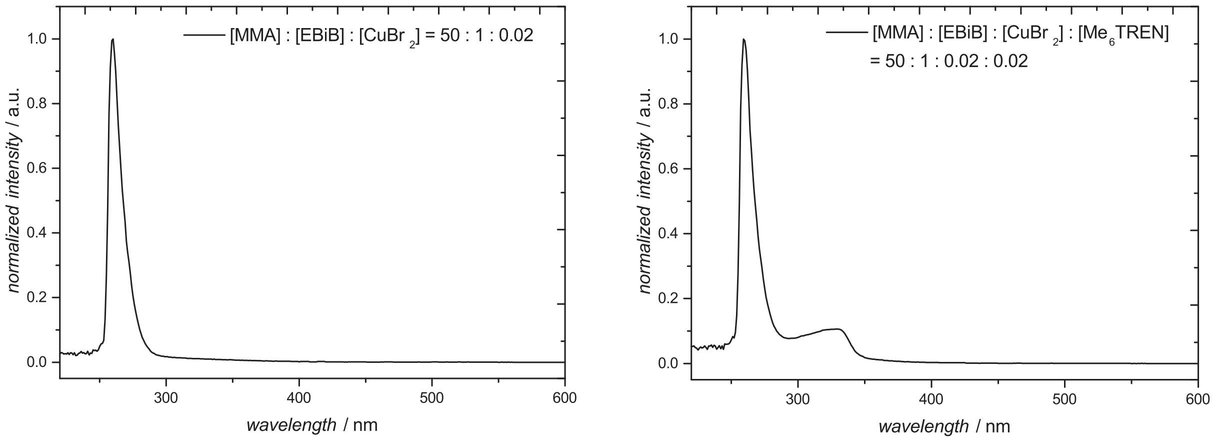

Figure A.17.: Right: UV-vis spectrum of Entry 7 (Table 4.1): [MMA]:[EBiB]:[$CuBr_2$]:[Me_6TREN] = 50:1:0.02:0 in DMSO. Left: UV-vis spectrum of Entry 8: [MMA]:[EBiB]:[$CuBr_2$]:[Me_6TREN] = 50:1:0.02:0.06 in DMSO.

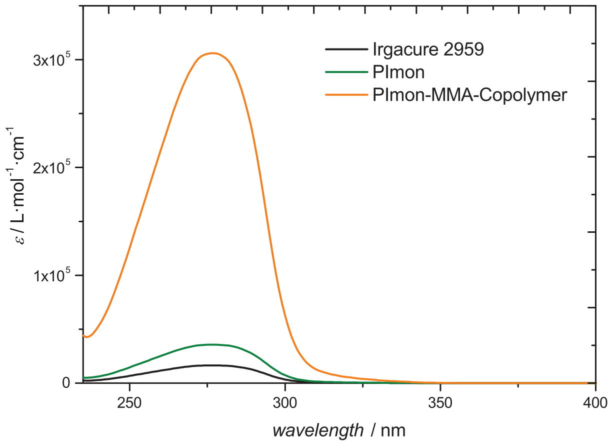

Figure A.18.: UV-vis spectrum of Irgacure 2959, PImon, and the PImon-MMA-copolymer (PImon/MMA = 1/12) in dichloromethane.

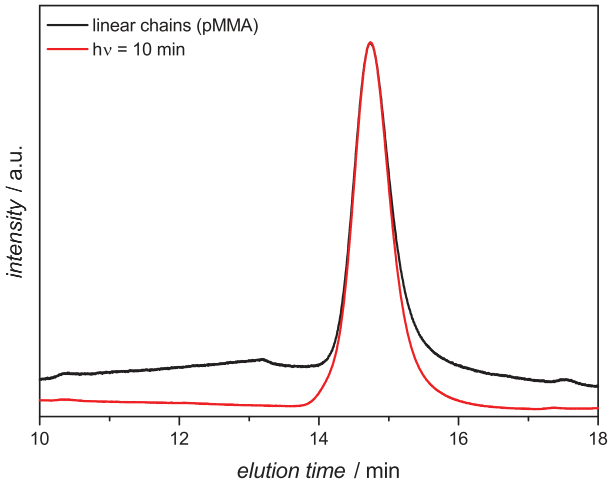

Figure A.19.: Size-exclusion chromatogram of irradiated pMMA without photoinitiator units. Experimental conditions were according to Table 5.6, line five.

Abbreviations

4MB	4-methyl benzoin
A_i	amplitude
AIBN	2,2'-azobis(2-methylpropionitrile)
a.t.	ambient temperature
ATRP	atom-transfer radical polymerization
CID	collision-induced decay
CPA	chirped pulse amplification
$CuBr_2$	copper(II) bromide
Da	dalton
DCM	dichloromethane
DFT	density functional theory
DMSO	dimethyl sulfoxide
DOSY	diffusion ordered spectroscopy
DP_n	degree of polymerization
EBiB	ethyl α-bromoisobutyrate
eq	equivalent
ESI	electrospray ionization
ESI-MS	electrospray ionization-mass spectrometry
ESR	electron spin resonance
fs	femtosecond
FRP	free radical polymerization
HOMO	highest occupied molecular orbital
HCl	hydrochloric acid
IC	internal conversion
IR	infrared
ISC	intersystem crossing
laser	light amplification by stimulated emission of radiation
LUMO	lowest unoccupied molecular orbital
M	monomer
MA	methyl acrylate
Me_6TREN	tris[2-(dimethylamino)ethyl]amine
MeCN	acetonitrile
MIB	methyl isobutyrate
MMA	methyl methacrylate
MO	molecular orbital
MS	mass spectrometry
m/z-ratio	mass-to-charge ratio
NaTFA	sodium trifluoro acetate
NMP	nitroxide-mediated polymerization
NMR	nuclear magnetic resonance
NOPA	noncollinear optical parametric amplifier
OD	optical density
PFG	pulsed field gradient
PI	photoinitiator

PLP	pulsed-laser polymerization
PLP-ESI-MS	pulsed-laser polymerization and subsequent product analysis by ESI-MS
pMMA	poly(methyl methacrylate)
RAFT	reversible addition-fragmentation chain transfer
RDRP	reversible-deactivation radical polymerization
S	singlet state
SCNP	single-chain nanoparticle
SEC	size-exclusion chromatography
SET-LRP	single electron transfer living radical polymerization
T	triplet state
τ	time constant
TA	transient absorption
TD-DFT	time-dependent density functional theory
THF	tetrahydrofuran
UV	ultraviolet
UV-vis	ultraviolet and visible light

Hiermit bestätige ich wahrheitsgemäß, dass ich die vorliegende Arbeit im Rahmen der Betreuung durch Prof. Dr. Christopher Barner-Kowollik selbstständig verfasst und keine anderen Quellen und Hilfsmittel als die angegebenen verwendet habe. Wörtlich oder inhaltlich übernommene Stellen sind als solche kenntlich gemacht und die Satzung des Karlsruher Instituts für Technologie (KIT) zur Sicherung guter wissenschaftlicher Praxis wurde beachtet. Desweiteren erkläre ich, dass ich mich derzeit in keinem weiteren laufenden Promotionsverfahren befinde und keine vorausgegangenen Promotionsversuche unternommen habe.

Elena Frick

Karlsruhe, den 08.03.2016

Curriculum Vitae

Date of Birth	06.09.1986
Place of Birth	Mihajlowka, Omsk region, Russia
Nationality	German

Education

10/2006 – 09/2012	**Diploma in Chemistry (eq. MSc)** Polymer Chemistry as elective Karlsruhe Institute of Technology (KIT)
09/1997 – 06/2006	**University-entrance Diploma (Abitur)** Albertus-Magnus-Gymnasium, Ettlingen

Research

12/2012 – 04/2016	**PhD Studies in Chemistry** under the supervision of Prof. Christopher Barner-Kowollik Karlsruhe Institute of Technology (KIT), Germany "Mechanistic Investigation of Photoinitiation Processes via PLP-ESI-MS"
09/2015 – 12/2015	**University of Colorado, Boulder, USA** Research stay in the group of Prof. Christopher N. Bowman "Photoinitiator-Based Single-Chain Nanoparticle Formation
03/2012 – 09/2012	**Karlsruhe Institute of Technology (KIT)** Diploma thesis under the supervision of Prof. Christopher Barner-Kowollik, in collaboration with BASF Ludwigshafen "Preparation of Photoreactive Polymers and Nanoparticles and their Subsequent UV-Induced Crosslinking"
04/2011 – 07/2011	**Carnegie Mellon University, Pittsburgh, USA** Research internship in the group of Prof. Krzystof Matyjaszewski "Electrochemically Mediated ATRP: Synthesis of Star Polymers in Aqueous Media and Polymerization of BA, MMA, and Styrene"
08/2010 – 10/2010	**Karlsruhe Institute of Technology (KIT)** Research internship in the group of Prof. Christopher Barner-Kowollik "Photoinduced Diels–Alder Conjugation via Photoenol Chemistry"

Acknowledgements

An erster Stelle möchte ich mich bei meinem Doktorvater Christopher Barner-Kowollik sehr herzlich bedanken. Du hast mich immer mit Ratschlägen und Aufmunterung tatkräftig unterstützt und in allen Phasen an mich geglaubt. Durch Deine Hilfe und Dein Vertrauen konnte ich wertvolle Erfahrungen bei zwei Auslandsaufenthalten machen, denn auch vor meiner Promotion hast Du Dich schon für mich eingesetzt und dafür bin ich sehr dankbar! Ganz besonders ist es beeindruckend mit welcher Energie und Hingabe Du Deine Gruppe führst! Vielen Dank dafür!

Weiterhin möchte ich mich herzlich bei meinen Kooperationspartnern aus der Physikalischen Chemie, Andreas-Neil Unterreiner, Caroline Schweigert, Hanna Ernst, Yu Liang und Thomas Wolf bedanken! Es hat Spaß gemacht mich Euch zu arbeiten und ich habe wahrlich viel gelernt von Euch und ich glaube wir haben uns ziemlich gut ergänzt bei unserem Projekt. Insbesondere danke ich Caroline für ihren tatkräftigen Einsatz und die gute Stimmung!

I would like to thank my cooperation partners Michelle Coote and Benjamin Noble from the Australian National University (Canberra) for their great work and their reliability. It was easy to work with you and your input was very valuable for our publication!

Furthermore, I would like to thank Dave Haddleton and Athina Anastasaki from the University of Warwick in UK for our fruitful collaboration. Our project was kind of a surprise and I really enjoyed working with you. Especially, I thank Athina for the helpful discussions and the easy communication!

I thank Christopher N. Bowman for hosting me at the University of Colorado Boulder for my research stay and giving me both freedom and advice during my time there. It was a great experience for me and I really enjoyed my time in Boulder!

Ein großes Dankeschön an alle aus der macroarc-Gruppe, die sich stets dafür einsetzen, dass der Laden läuft! Hier möchte ich insbesondere Maria Schneider danken für ihren großen Einsatz für die Gruppe und den tiptop-Zustand aller Geräte! Anja Goldmann, Evelyn Stühring, Vincent Schüler und auch Peter Gerstel vielen Dank für Euren Einsatz und das Organisationstalent! Weiterhin ein Danke an alle Geräte-Verantwortlichen aus der Gruppe, dafür dass alles am Laufen bleibt und schnell repariert ist wenn es mal brennt!

Danke an alle meine Kollegen für die schöne Zeit die ich mit Euch verbracht habe, wie z.B. in den Kaffeepausen oder Eispausen im Sommer, den Grillabenden und den vielen Doktorfeiern! Danke für die Unterstützung bei allen möglichen Fragen des täglichen Büro- und Laborlebens sowie für höchst kreativen und direkten Input was Poster, ToC-Figures und Synthesen angeht! Hierbei gilt mein Dank besonders Andrea L., Astrid, Carolin, Johannes, Jan M., Kim, Alex Q., Alex S., Corinna, Jan S., Kai H., Dominik, Kai P., Nils und Thomas G., dem ich noch dazu sehr dankbar bin für seine PC-Rettungsversuche und die Übernahme der Laborverantwortung für 322! Danke auch an Johannes und Eva für die schöne Zeit während der gemeinsamen Konferenzen in Gent und Boulder! Vielen Dank an Dominik für die Grundsteinlegung des Photoinitiatorprojekts und das Schreiben des DFG-Antrags, der mein Projekt erst ermöglicht hat!

Many thanks to the members of the Bowman group in Boulder for their warm welcome, interesting conversations, and our great hikes in the Rocky Mountains!

Vielen Dank auch an Helena Hörig und Wolfgang Arbogast für die Aufwertung all der endlosen Stunden die ich an der Waage verbracht habe durch unsere interessanten und witzigen Gespräche!

Zum Schluss, aber doch am Bedeutendsten, möchte ich den wichtigsten Menschen im Leben danken, meinen Freunden und meiner Familie! Danke an Katharina fürs Zuhören, für das Lachen und den großen Zuspruch!
Ein ganz großes Danke an meine Eltern und an Andrej, Olja und die kleine Lena für Eure Unterstützung, Euer Verständnis und dass Ihr immer an mich geglaubt habt! Ihr seid der Grund dafür, dass ich an dieser Stelle nun endlich angekommen bin!

Last, but not least, danke ich Guillaume von ganzem Herzen! Danke für Deine Unterstützung, Zuversicht und die Ermunterungen! Thank you for our past, present, and future!